Stabilization and motility mechanism of blebs in cancer cells

Juan Manuel García Arcos

Université de Paris

École doctorale 474 Frontières de l'Innovation en Recherche et Education

Laboratoire CNRS UMR 144, Institut Curie

Stabilization and motility mechanism of blebs in cancer cells

Mécanisme de stabilisation et motilité des blebs dans les cellules cancéreuses

Par Juan Manuel GARCÍA ARCOS

Thèse de doctorat de Biophysique

Spécialité: Biologie moléculaire et structurale et biochimie, biophysique

Dirigée par Matthieu PIEL

Présentée et soutenue publiquement le 30 novembre 2020 devant un jury composé de :

M. Karsten KRUSE, Professeur, Université de Genève, Rapporteur, Président ;

M. Guillaume CHARRAS, Professeur, University College London, Rapporteur ;

M^{me} Anne-Cécile REYMANN, CR CNRS, IGBMC Université de Strasbourg, Examinatrice ;

M. Guillaume ROMET-LEMONNE, DR CNRS, Institut Jacques Monod, Examinateur,

M. Matthieu PIEL, DR1 CNRS, Institut Curie, Directeur de thèse ;

M. Damien CUVELIER, Maître de conférence HDR, UPMC, Institut Curie.

Thesis title in English:

Stabilization and motility mechanism of blebs in cancer cells

Keywords in English:

Actin flows, Cell polarity, Myosin, Actin, Microfluidics, Amoeboid migration, Bleb

Abstract in English:

Previously associated with apoptosis, blebs have arisen in the past decade as **important structures for amoeboid cell migration**, particularly for cancer cells. Blebs form when the plasma membrane detaches from the actomyosin cortex. They retract, exerting friction forces and allowing cells to migrate. A few independent studies have reported large and stable blebs in cells under non-adhesive confinement in recent years. This universal switch to bleb-based migration has been found in amoeba, choanoflagellates, immortalized cell lines, and primary cultures. Unlike previously described blebs, they can overcome retraction and **stabilize a constant** flow. Stable blebs are a new type of cellular structures that amoeboid cells use to migrate, **analogous to filopodia or lamellipodia** for mesenchymal cells. In a single cell, multiple blebs form and compete against each other, so that eventually, a single bleb drives the migration. Thus, it is essential to know how single blebs stabilize to understand how single-bleb amoeboid cells polarize. More generally, stable actomyosin flows constitute the basis of fast migration in numerous cell types, including also immune cells.

During my Ph.D. I studied bleb morphogenesis and bleb stabilization **in confined cancer cells**, using advanced **microfluidic techniques** to control the confinement of cells. The first part of my project describes the **bleb formation** as an immediate response of cells to confinement and what differentiates it from a classical retracting bleb. The second part of my project focuses on the **mechanism leading to the establishment of retrograde flow**. Based on the results I obtained with my experiments, we propose that bleb stabilization depends on 1) the depletion of actin from the front by myosin contractility and 2) the particular actin filament arrangement at the bleb tip caused by the membrane topology of a confined cell. I completed this work with advanced high-resolution imaging, which allowed observation of single actin filaments and tagged cytoskeleton-associated molecules at the bleb tip, under different perturbations. My results show three cortex regimes in blebs: 1) **Assembling loose cortex**: localized at the front, composed of single filaments poorly attached to the membrane. If this region is lost, the bleb retracts. 2) **Crosslinked cortex**: actin filaments and fibers bind together to form a network that gradually gets denser and reticulated but does not contract (this region is devoid of Myosin II motors). 3) **Contractile cortex**: towards the base of the bleb. Myosin-II starts to get enriched, contracting the dense actin network, driving the entire retrograde actin flow up to the tip of the bleb, generating new actin free regions at the front and pressurizing the bleb, leading to membrane protrusion at the very front.

This unique set of observations allowed to complete a model for the stabilization of motile blebs, with conclusions that can be generally applied to any flowing actomyosin cortex. My results present a negative role of actin-membrane attachment in protrusion persistence and contribute to the recent findings in the cell migration field, pointing in this direction. They also introduce an additional role for NMIIA contractility, which is essential for maintaining intracellular pressure and depleting actin from the cell front.

Titre de la thèse en français :

Mécanisme de stabilisation et motilité des blebs dans les cellules cancéreuses

Mots-clés en français :

Flux d'actine, Polarité cellulaire, Myosine, Actine, Microfluidique, Migration amiboïde, Bleb

Résumé en français :

Auparavant associées à l'apoptose, les blebs sont apparus au cours de la dernière décennie en tant que **structures importantes pour la migration des cellules amiboïdes**, en particulier pour les cellules cancéreuses. Les blebs se forment lorsque la membrane plasmique se détache du cortex d'actomyosine. Ils se rétractent en exerçant des forces de friction et en permettant aux cellules de migrer. Ces dernières années, quelques études indépendantes ont observé des **blebs volumineux et stables** dans des cellules sous confinement et en absence d'adhésion. Ce changement universel vers la migration à base de blebs a été observé chez les amibes, les choanoflagellés, les lignées cellulaires immortalisées et les cultures primaires. Contrairement aux blebs précédemment décrits, ils sont capables de surmonter leur rétraction et de maintenir un **flux d'actomyosine constant**. Les blebs stables forment un nouveau type de structures cellulaires que les cellules amiboïdes utilisent pour migrer, **analogues aux filopodes ou lamellipodes** pour les cellules mésenchymateuses. Dans une seule cellule, plusieurs blebs se forment et se font concurrence, de telle sorte que finalement un seul bleb entraîne la migration. Ainsi, il est important de savoir comment les blebs simples sont stabilisés pour comprendre comment les cellules amiboïdes se polarisent. Plus généralement, des flux d'actomyosine stables constituent la base d'une migration rapide pour de nombreux types de cellules, comprenant également des cellules immunitaires.

Pendant mon doctorat, j'ai étudié la morphogenèse et la stabilisation des blebs dans des **cellules cancéreuses confinées**, en utilisant des **techniques microfluidiques**

avancées pour contrôler le confinement des cellules. La première partie de mon projet décrit la **formation de blebs** comme une réponse immédiate des cellules au confinement et ce qui les différencie des blebs rétractables classiques. La deuxième partie de mon projet se concentre sur le **mécanisme conduisant à l'établissement d'un flux rétrograde**. Sur la base des résultats que j'ai obtenus avec mes expériences, nous proposons que la stabilisation d'un bleb dépend de 1) l'épuisement de l'actine par la contractilité de la myosine et 2) la disposition particulière des filaments d'actine à l'extrémité du bleb causée par la topologie de la membrane. J'ai complété ce travail avec une imagerie avancée qui a permis l'observation de filaments d'actine uniques et des molécules associées au cytosquelette à l'extrémité du bleb, sous différentes perturbations. Cet ensemble unique d'observations a permis de compléter un modèle pour la stabilisation des blebs motiles, avec des conclusions qui peuvent être plus largement appliquées à tout flux de cortex d'actomyosine.

Mes résultats montrent **trois régimes de cortex** dans les blebs : 1) Assemblage de **cortex lâche** : localisé à l'extrémité, composé de filaments simples mal fixés à la membrane. Si cette région est perdue, le bleb se rétracte. 2) **Cortex réticulé** : les filaments et les fibres d'actine se lient pour former un réseau qui se densifie et se réticule progressivement mais ne se contracte pas (cette région est dépourvue de moteurs Myosine-II). 3) **Cortex contractile** : vers la base du bleb. La myosine-II commence à s'enrichir en contractant le réseau dense d'actine, entraînant tout le flux d'actine rétrograde jusqu'à l'extrémité du bleb, générant de nouvelles régions sans actine à l'extrémité et comprimant le bleb, conduisant à une avancée de la membrane à l'avant.

To the whole family of coronaviruses,

To Henrietta Lacks,

To my family, boyfriend, and friends, for being supportive,

To my teachers and my thesis supervisor, for being available, inspiring and trustworthy,

To my dearest philosophy and science heroes: Søren Kierkegaard, Hannah Arendt, Antonio Gramsci, Marie Curie, Richard Feymann Albert Szent-Gyorgi…

To my lab colleagues and master students, for teaching me so much,

To the people at PBoC course at MBL in Woods Hole, for their inspiration and enthusiasm for good values and good science

To my collaborators, for their help, trust, and teaching,

To the institute staff, being indispensable,

To the funding agencies and university, for their trust and material means,

To the Ph.D. advisory board members and the jury members for their generosity and availability,

And to you, the reader.

Table of contents

List of acronyms by alphabetical order

AFM: Atomic force microscopy.
AMP: adenosine 3'-monophosphate.
ARHGEF11: Rho Guanine Nucleotide Exchange Factor 11.
Arp2/3: actin-related proteins-2/3.
ATP: adenosine 3'-triphosphate.
CAD: catecholaminergic-a-differentiated cells.v
Cdc42: Cell division control protein 42 homolog.
CEN: cytoskeleton excitable network.
CIBN: N-terminus of cryptochrome-interacting basic-helix-loop-helix from *A. thaliana*.
cPLA2: Cytosolic phospholipase A2.
CRY2: cryptochrome 2 from *Arabidopsis thaliana*.
DIC: Differential interference contrast microscopy.
DMD: digital micromirror device.
DMEM: Dulbecco's Modified Eagle Medium.
ECM: extracellular matrix.
EMT: epithelial-to-mesenchymal transition.
Eps8: Epidermal Growth Factor Receptor Pathway Substrate 8.
Erk: Extracellular signal-regulated kinase.
ERM: ezrin-radixin-moesin.
FCS: Fluorescence correlation spectroscopy.
FRET: fluorescence resonance energy transfer.
GEF: Guanine nucleotide exchange factor.
GPCRs: G protein-coupled receptors.
Hem-1: Hematopoietic protein 1, a component of the WAVE2 complex.
High NA TIRF: high numerical aperture total internal reflection fluorescence microscopy.
H2B: histone H2B.
iRFP: Infrared fluorescent protein.
LEGI: Local-excitation, global-inhibition.
LEGI-BEN: LEGI-biased excitable network.
MAT: mesenchymal-to-amoeboid transition.
NMIIA/B/C: non-muscle myosin II A/B/C.
MAT: mesenchymal-to-amoeboid transition.
MEF : Mouse embryonic fibroblast.
mDia1 : Diaphanous-related formin-1, Diaph1.

MMP: Matrix metalloproteinase.
MRLC : Myosin regulatory light chain.
mTORC2: mammalian target of rapamycin complex 2.
PDMS: Polydimethylsiloxane.
PIP2: phosphatidylinositol-(3,4,5)-*bis*-phosphate.
PIP3: phosphatidylinositol-(3,4,5)-*tris*-phosphate.
PIP3K: phosphatidylinositol 3-kinase.
PIV: Particle image velocimetry.
PLC: Phospholipase C.
PLD2: phospholipase D2.
PLL: poly-L-lysine.
PLL-*g*-PEG: random graft co-polymer with a poly(L-lysine) backbone and poly(ethylene glycol) side-chains.
PDMS: poly(dimethylsiloxane).
PMN: polymorphonuclear leukocytes.
PTEN: Phosphatase and tensin homolog.
Rac1: Ras-related C3 botulinum toxin substrate 1.
RhoA: Ras homolog family member A.
ROCK / ROK: Rho-associated protein kinase
ROI: region of interest.
SPIN90: SH3 protein interacting with Nck, 90 kDa.
STEN : signal transduction excitable network.
STORM: stochastic optical reconstruction microscopy.
TIAM1: T-cell lymphoma invasion and metastasis 1.
TIRF: Total internal reflection fluorescence microscopy.
WAVE2 / SCAR: Wiskott-Aldrich syndrome protein family Verprolin-homologous protein.

Contributions to this work

I acknowledge my thesis director, **Matthieu Piel**, for his sustained supervision, for his role in conceptualizing the project together with me, for funding acquisition for reagents, materials, and travelling, and for his help on commenting, writing and reviewing the results and discussion sections of this manuscript.

I acknowledge the Piel lab for their support: **Raffele Attia**, **Jian Shi**, and **Li Wang** provided molds for the confinement devices and training in photolithography, **Damien Cuvelier** provided interesting feedback and support, **Guilherme Nader** and **Yanyun Liu** (now in Fudan university, Shanghai) for the training on confinement techniques at the beginning of PhD and feedback on the project, **Nicolas Carpi** for his advice on Python programming, for amplifying the plasmids, and for taking care of the lab, **Alexis Lomakin**, for his feedback and supervision on the first months of PhD**, Matthieu Deygas**, **Nishit Srivastava**, **Ido Lavi**, **Aastha Mathur**, **Larisa Venkova**, **Pablo Sáez**, **Pablo Vargas**, **Clotilde Cadart**, **Lucie Barbier, Mathilde Bernard, Alice Williart** were always open to discuss science, sharing techniques, protocols, and provide feedback, and the rest of the team for their support and creating a good working atmosphere for research. In addition, Guilherme Nader, Larisa Venkova, and Mathieu Deygas provided valuable feedback for the introduction section of this manuscript.

I acknowledge in particular **Kevin Gateau** and **Gaurav Shajepal**, the master students who decided to come to the lab to work with me, helped with experiments shown in this manuscript. Kevin worked on the development of the agarose confiner, and Gaurav on the image analysis of single blebs in the AFM confocal movies.

I acknowledge the **microfabrication facilities** at IPGG and ICFO, the **imaging facilities** in CRG, ICFO, Curie Institute and IPGG, the **cell culture facilities** at ICFO and CRG, as well as the image analysis engineers **Anne-Sophie Macé** and **Mathieu Maurin** for their technical support. Mathieu assisted me in the early development of the bleb analysis and Anne-Sophie in the early development of the PIV reader.

I want to thank my Woods Hole Physical Biology of the Cell course mentors: **Hernán García**, **Jane Kondev**, **Julie Theriot**, **Rob Phillips**, the enormous help of course assistants **Rikki Garner** and **Vahe Galystan,** and the whole promotion for their help in understanding biophysics and quantitative cell biology. I believe the PBoC course was a marking and intense experience that changed the course of my PhD and inspired the research in the last year.

Collaborations

The work presented on this manuscript has been done a collaboration with many other colleagues, which I list below. I am extremely thankful to have worked with all of them. This has significantly enriched my personal and professional perspectives throughout these four years of PhD work.

Loïc Reymond in the lab of **Verena Ruprecht** at CRG (Barcelona, Spain) and **Johannes Ziegler**, in the lab of **Stefan Wieser** at ICFO (Castelldefels, Spain) for their support in the High NA TIRF imaging. Johannes and Loïc built the custom setups used in the image acquisition and trained me to use the setup. Stefan hosted me at ICFO during three months thanks to an EMBO short-term scholarship and Verena hosted me at CRG during one month. I want to thank the Ruprecht and Wiser labs for their warm welcome in Barcelona, in particular **Valeria Venturini**, which provided interesting discussions, and the technical support of Valeria, **Christian Knapp**, **Senda Jiménez Delgado, Fabio Pezzano, Merche Rivas Jiménez**, and the personnel at ICFO.

Alexis Lomakin former postdoc in our lab (now at Children's Cancer Research Institute, Vienna, Austria) and **Cédric Cattin**, in the lab of **Daniel Müller** at ETH Basel (Basel, Switzerland) provided the unpublished raw data used in figure 26 (AFM confinement).

Kotryna Vaidžiulytė, in the lab of **Matthieu Coppey** at Institut Curie helped me to set up a "High NA TIRF" replica in Curie, and helped with the optogenetic experiments, the image acquisition, and discussing and interpreting the results. Kotryna made the lentiviral transfections of the optogenetic cell lines.

Manos Mavrakis, group leader at Fresnel Institute (Marseille, France) trained me on using the polarized light spinning and interpreting and analyzing the results. He hosted me for two days at Fresnel Institute.

Jérémie Francfort helped with the cross-correlation and PIV flow analysis, translating the model equations into programming routines. He was always open to help and discuss maths and physics with me, which was fundamental to complete the project.

Funding

My PhD salary in the first three years has been covered an individual fellowship from INSERM ITMO Cancer Plan Cancer 2015-2020, after a report from the PhD selection committee of CRI (Center for Research and Interdisciplinarity of Paris).

The salary in the 4th year was covered by an individual fellowship from Fondation ARC no. DOC20190508743.

My stay in the lab of Dr. Stephan Wieser in the Institute of Photonic Sciences ICFO (September - December 2018) was funded an individual short-term EMBO fellowship no. 7873.

My attendance to the course “Physical Biology of the Cell” in Woods Hole (USA), and to the Gordon conference “Motile and contractile systems” in New London (USA) was supported by a Boehringer Ingelheim Fonds travel grant (for the course fees), Bourses doctorales de mobilité de l'université (BDMU), and a fellowship from Horace W. Stunkard Scholarship Fund.

This work has received the support of "Institut Pierre-Gilles de Gennes" (laboratoire d’excellence, “Investissements d’avenir” program ANR-10-IDEX-0001-02 PSL and ANR-10-LABX-31.).

This work has received the support of "Institut Pierre-Gilles de Gennes" (équipement d’excellence, “Investissements d’avenir” program ANR-10- EQPX-34).

This work received support from the LabEx CelTisPhyBio (ANR-11-LABX-0038).

Part II: Introduction

Chapter 2: The molecular machines of cell migration.

ells are intriguing, beautiful, and complex systems. This thesis's topic is cell migration, which is a **fundamental behavior of cells in every ecological niche**, including higher metazoans. Even when a cell is not producing forces for movement, it can be pulled by others like in wound healing events or just pushed by the growth of the bulk in a tissue. The morphogenesis of multicellular organisms includes both cell-autonomous and collective migration, such as the development of central nervous systems in mammals. In prokaryotes or single-cell organisms, cell migration becomes essential for survival. Inhomogeneities in food sources make it vital for many cells to be able to be attracted by gradients. **Prokaryotic migration is controlled by flagella and cilia**, which can control the rate and direction of beating to direct the cell. Simple "run and tumble" migration trajectories can yield efficient chemotaxis and collective behavior strategies such as the establishment of colonies and biofilms. In contrast, **metazoan cell migration is far more complex and relies on cytoskeletal scaffolds** of the scale of the cell and membrane-substrate interactions.

Mammalian cells migrate thanks to a dynamic scaffold called the cytoskeleton, and an army of crosslinkers, active motors, and modulators of cytoskeleton dynamics. The cytoskeleton comprises three main components: actin, microtubules, and intermediate filaments such as vimentin. Briefly, cells will need to push their membrane forward and retract the rear to move. However, there is a diversity of physical strategies to achieve this goal, and the motors and the specific molecules for each different cell type vary. **The two main force generation mechanisms are polymerization** (Dogterom et al., 2005; Footer et al., 2007), **and contraction or transport by molecular motors**, such as myosins or kinesins. **Membrane anchoring for cytoskeleton proteins is fundamental to transmit forces** and **a coupling mechanism** to the outside.

The cellular structure most relevant for this work is the cortex, an active viscoelastic material beneath the membrane whose primary scaffold is actin. The active properties of actin depend on motors such as myosins. Non-muscular myosin II-A (NMIIA) is a plus-end actin motor that assembles into force dipoles contracting the actin network. We often refer to the cortex as a composite material called "actomyosin." For this reason, actin is a central player in cell migration (Olson and Sahai, 2008) and a highly conserved among species. As the topic of my Ph. D. thesis involves the assembly of the cytoskeleton at the

front of a cell, I will introduce the molecular machines involved in cell migration, particularly related to the actin cytoskeleton.

Actin as a polymer

Actin is the most abundant intracellular protein in a eukaryotic cell, and it is the one with most protein-protein interactions known. It typically comprises 10 percent by weight of the total cell protein in muscle cells and 1 to 5 percent of the other cells' protein. Actin exists in a soluble globular form called G-actin and in an F-actin filamentous form (**Figure 1**). Cells typically bear concentrations of ~1mM of polymerized actin and few tens of µM of globular actin (Abraham et al., 1999). Compared to microtubules (1-10 mm), actin is much more **flexible** (10 µm of actin versus 1-10 mm persistence length of microtubules), **thinner** (6 nm diameter of actin versus 25 nm for microtubules), and forms generally **shorter filaments** (35 nm in the erythrocyte cortex to 10–100 µm in ear hair cells for actin versus <1 µm in *S. pombe*, 100 µm in *R. norvegicus* to even >1 mm in insect sperm cells for microtubules). Actin can produce forces to push membranes thanks to

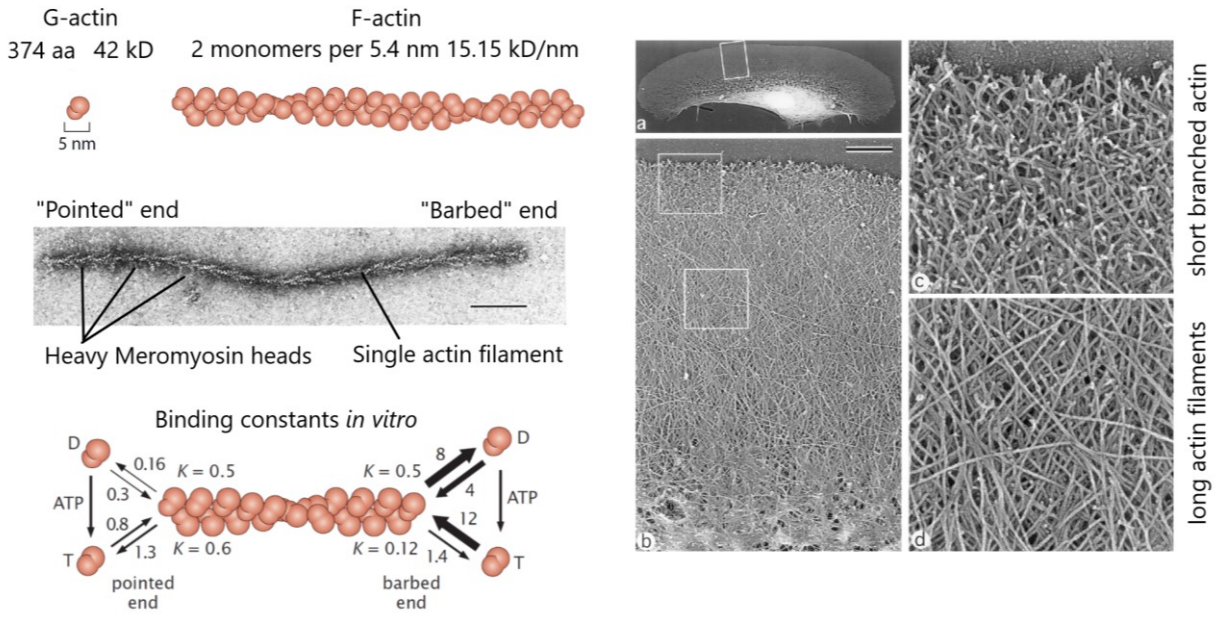

***Figure 1: Molecular aspects of actin assembly**. Left top: actin monomers are relatively small proteins of a few hundred aminoacids that assemble into filaments. Left middle: Actin filament decorated with human meromyosin and photographed with uranyl acetate 1% by EM, scale bar = 0.1 µm. Left bottom: assembly rates of ADP-actin and ATP-actin from the barbed ends as measure* in vitro. *The barbed ends polymerize spontaneously at lower concentration than the pointed end. Right: molecular structure of the actin network in the lamellipodium of a fish keratocyte, as shown by EM of detergent-extracted cells. The front of the lamellipodium has a dense network of actin filaments oriented +35/-35 degrees respective to the cell front. The network remodels as it flows back, so that the back of the lamellipodium has longer filaments which are arranged by tropomyosin and myosins. Scale bar in (b) = 1 mm. Adapted from (Milo and Phillips, 2016; Phillips et al., 2013; Pollard, 1986; Svitkina et al., 1997; Woodrum et al., 1975)*

polymerization at the filament ends, but can also **stall above a specific force applied by membrane tension** (7.7 ±1.3 $pN/\mathrm{filament}$). Filaments can withstand forces, but also **rupture if subjected to stress** (~3.5 N/m^2) (Abraham et al., 1999; Janmey et al., 1991).

As microtubules, actin filaments have a polarity and have a "pointed" end and a "barbed" end. These were called this way due to the shape of heavy meromyosin heads decorating actin in vitro, which look like arrows pointing towards one end (**Figure 1**). Actin monomers can be **ATP-bound or ADP-bound**. Typically, ADP-bound monomers are more prone to stay in the globular form than ATP-bound monomers. The binding affinities of ATP- and ADP-bound monomers to the pointed and barbed ends of a filament have been well characterized *in vitro* (**Figure 1**). We also know that the actin filaments keep an ATP-bound cap, which controls polymerization (Carlier, 1990; Jégou and Romet-Lemonne, 2016; Korn et al., 1987; Neuhaus et al., 1983; Pollard, 1986; Vavylonis et al., 2005). Pure actin monomers can spontaneously polymerize *in vitro* above a critical concentration, which is lower for barbed ends. However, the cells keep monomeric **concentration for up to 1500 times higher than the critical concentration of 0.1 µM**. G-actin in a cell is **sequestered by** proteins such as **thymosin-beta-4 and profilin**, making it available to actin nucleators to be polymerized in specific places. The sequestering prevents spontaneous actin polymerization in a disorganized manner. For this reason, profilin is a crucial regulator of actin and lamellipodial cell migration, broadly modulating actin polymerization (Funk et al., 2019; Pernier et al., 2016).

Cellular control of actin polymerization

The *in vitro* behavior of actin is very well studied, but it is less understood how this translates to situations inside the cell. As mentioned previously, actin is the protein with the most known protein-protein **interactions**. These interactions **modulate polymerization** rates, **mechanical properties**, and **interaction with** other **filaments** (Pollard, 2016; Pollard et al., 2000; Welch and Mullins, 2002). Rather than a network of actin filaments, cellular actin structures are composite materials of actin with many accessory proteins, crosslinkers, and the membrane. For example, spontaneous nucleation of actin *in vitro* has a costly initiation step. Analogous to the polymerization core of microtubules, actin monomers need to form a core of few elements before polymerizing steadily. However, spontaneous formation of a nucleation core *in vivo* is skipped by nucleators proteins. **Arp2/3 complex** contains a variant of G-actin monomers that can **branch on the side of an existing filament**, creating a new filament without the need of a nucleating core. The other prominent family of nucleators is **formins**, a

group of dimeric proteins involved in actin polymerization, associated with the barbed end. They can promote the elongation of pre-existing filaments by removing barbed end capping proteins and capable of actin nucleation. Nucleators can be cell type-specific. In Hela cells, the **two main actin nucleators** are the formin **mDia1 and Arp2/3**. Increases in one nucleating factor can **partially compensate** for the other's depletion, suggesting that both factors cooperate in building the cortex (Isogai et al., 2015). However, there are some differences: **mDia1 can nucleate F-actin twice as fast** (Bovellan et al., 2014), and mDia1 typically participate in elongating filaments linearly, whereas Arp2/3 in branching new filaments.

There exists a rich regulation of actin barbed ends (Shekhar et al., 2016). **Actin cappers bind barbed ends to block further addition of monomers**. They are divided into **Capping protein** versus proteins of the gelsolin family (Ca^{2+}-dependent), such as gelsolin, adseverin, villin, advillin, supervillin, flightless I homolog, and CapG in mammals. Capping protein is the main capper in mammalian cells, being very abundant (1-2 μM). As expected by its function, it binds with high affinity to barbed ends and dissociates very slowly. **Capping-protein-interacting proteins** control the capping protein activity and can "uncap" actin to allow for actin nucleation. Given the affinity and the concentration of capping protein in a cell, if there were no **negative regulators of actin capping,** polymerization would be frozen inside a cell (Hug et al., 1995).

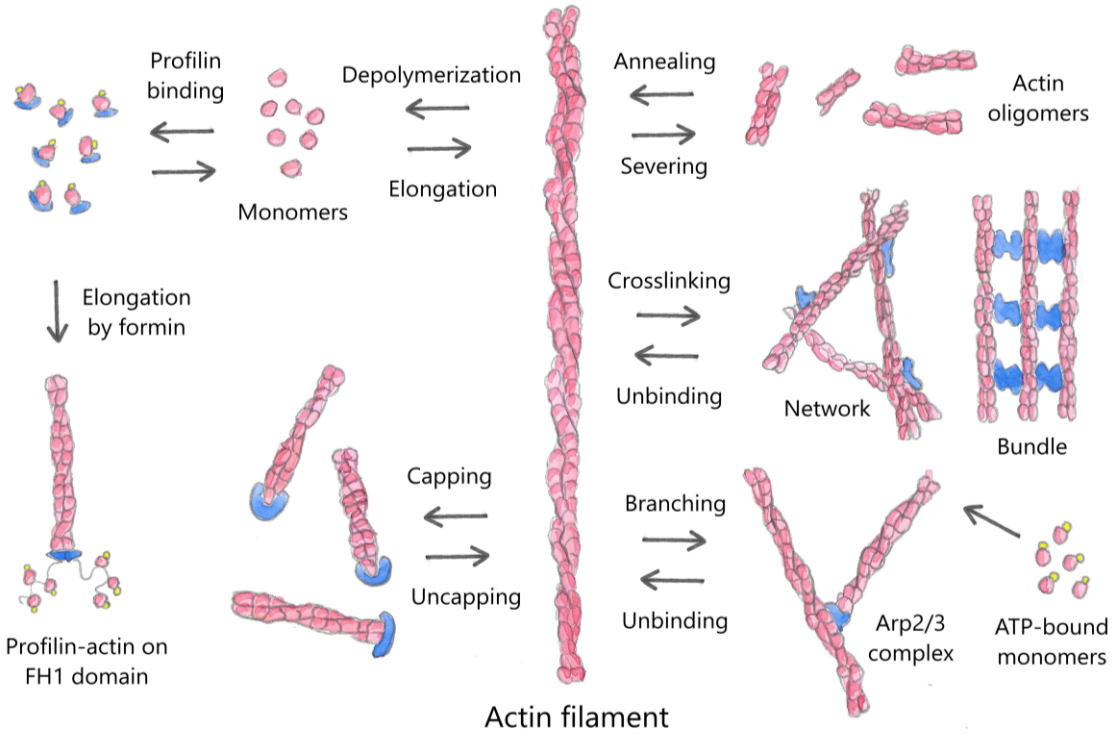

***Figure 2: Overview of functions of actin-binding proteins**. This includes: monomer binding, filament polymerization, capping, severing, cross-linking, and branching. Filaments can joint end-to-end (annealing), but not proteins are yet known to perform this function. Adapted from Pollard, 2016.*

While we know the individual functions of barbed-end-binding proteins, the interaction between the different nucleators inside a cell is still an intense research area. For example, the nucleation-promoting factor WishDIP/spin90 and Arp2/3 could also start polymerization with no pre-existing actin filament (Wagner et al., 2013). Recently, a novel **interaction between Arp2/3 and mDia1** was identified through the nucleation-promoting factor SPIN90. Recruitment of mDia1 to SPIN90–Arp2/3 nucleated filaments or formation of a ternary SPIN90–Arp2/3–mDia1 complex can yield rapid nucleation of filaments bearing mDia1 at their barbed ends and SPIN90–Arp2/3 at their pointed ends (Cao et al., 2020).

The Rho family of small GTPases such as RhoA, Rac1, and Cdc42 control the assembly and organization of actin upstream of the nucleators. They are small (~21 kDa) signaling G proteins belonging to the Ras superfamily. They are the main "molecular switches" that control cell migration, polarity, and cytoskeleton dynamics. RhoA activation by calcium (via calmodulin) or other pathways has implications both in myosin activity (via phosphorylation of MRLC) and in actin (via cofilin inactivation) (Figure 5). Moreover, most formins are **Rho-GTPase effector proteins**. Recently, the development of the FRET-based sensors has allowed for live measurements of the different GTPases'

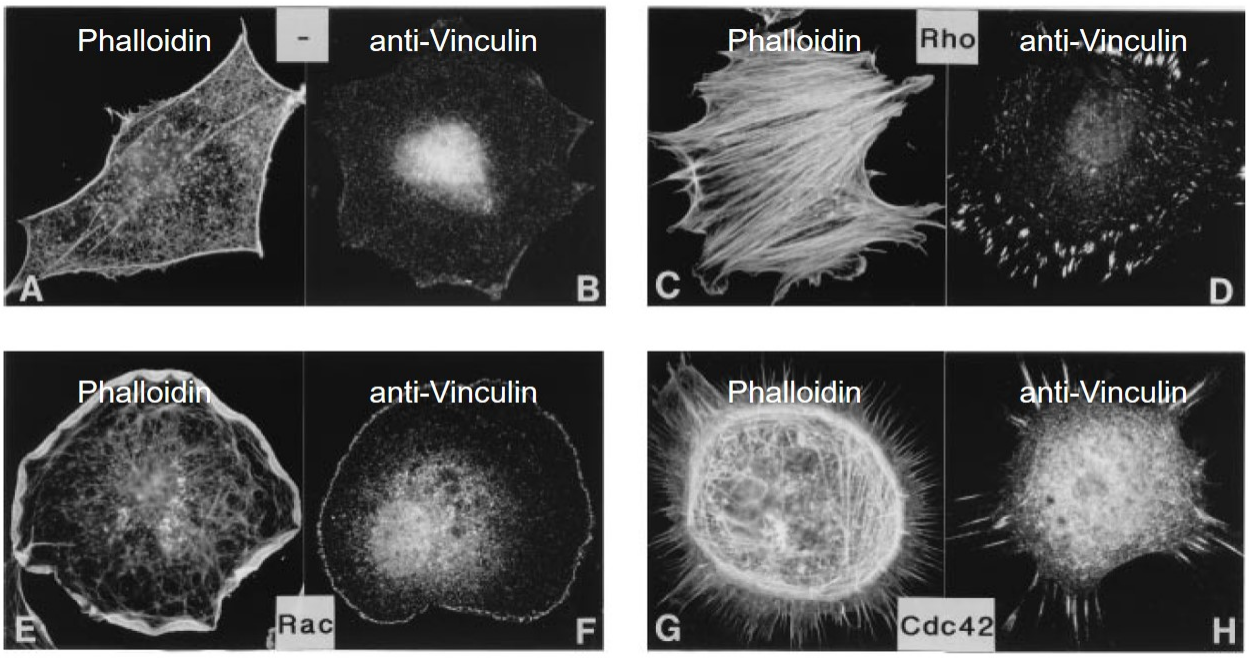

Figure 3: RhoA, Rac1, and Cdc42 control the assembly and organization of the actin cytoskeleton. *Quiescent, serum-starved Swiss 3T3 fibroblasts with overexpression of different small GTPases, and stained for actin (phalloidin) and vinculin (anti-vinculin). RhoA overexpression creates thick ventral tress fibers and large focal adhesions. Rac1 overexpression increases the actin at the lamellar regions, and decreases the size of focal adhesions. Cdc42 promotes the creation of filopodia and the rounding of the cell. Adapted from (Hall, 1998).*

activity. The three GTPases are active at the leading edge of fibroblasts, where their activity is finely controlled temporally and spatially (Machacek et al., 2009; Martin et al., 2016). The development of optogenetics has allowed for precise tuning of their activity in live cells by recruiting specific GEFs and GAPs to the membrane and establishing gradients of activity within cells (de Beco et al., 2018): ArhGEF11 for RhoA, TIAM1 for Cdc42, and intersectin (ITSN) for Rac1. In migrating RPE1 or HeLa cells, RhoA activation will cause edge retraction, whereas Rac1 activation will generate an actin-rich protrusion. Extraordinarily, in suspended leukocytes, optogenetic activation of RhoA/Rac1 at the membrane creates a flow that can drive an adhesion-independent swimming migration purely by hydrodynamic interactions (O'Neill et al., 2018)

As a summary, purely free G-actin is absent from the cell, as is always bound to sequestering proteins that control nucleation. Nucleation is mainly restricted to signaling factors located at membranes. Even in what is often called "bulk filament assembly," as in fish oocytes, the actin nucleation happens at the surface of small vesicles (Montaville et al., 2014). As the filament forms, they tend to be capped, although some elements can negatively regulate capping. There is a particular "time" for actin stability, which is the exchange of the ATP-bound to ADP-bound states for the F-actin monomers. ABP (actin-binding proteins) such as ADF/cofilin preferentially attack ADP–actin and compromise the stability of the ADP-bound F-actin portions. All these factors cooperate to form a constant actin network treadmilling from the tip of a lamellipodium to the rear, and from the membrane towards the center of a non-migrating cell. This way, actin polymerization occurs on the membrane and disassembly in bulk. The flow creates an equilibrium so that the cortex keeps an equilibrium density and thickness depending on the activity of small GTPases and actin-binding proteins. As an exception at larger scales, researchers described that regions of the cell periphery with high negative curvature display actin anterograde flow, as actin fibers that push towards the membrane (Chen et al., 2019).

Actin crosslinkers

Actin crosslinkers are essential proteins that define the mechanical properties of actin bundles and the network properties. Actin filaments can buckle in force and length-dependent fashion: the force of actin **polymerization can buckle actin filaments** longer than 700 nm (Kovar and Pollard, 2004). **Crosslinkers increase the bending stiffness** of the network filaments by bundling filaments or forming a network. Actin crosslinkers

have a **broad range of sizes and functions**, and some results even suggest that they can work synergistically to define cell mechanical properties (Tseng et al., 2005). Motors such as myosins also join actin filaments together, but they are not defined as crosslinkers because they consume ATP and move. Smaller globular crosslinkers (e.g., **fascin**) or crosslinkers with more than one actin-binding site (e.g., **fimbrin, alpha-actinin dimers**) will more likely form actin bundles. In contrast, larger crosslinkers (e.g., **spectrin, filamin, dystrophin**) can allow more space between filaments and form actin networks.

Crosslinkers can have different expression levels and functions related to a specific cell type, protrusion, or model organism. Crosslinkers can have alternative genes that encode for different versions of the protein that are tissue-specific. For example, **filamin and fimbrin drive cellularization in *Drosophila*** embryos. Filamin facilitates hexagonal patterning of actin fibers, and fimbrin promotes the hexagonal network's remodeling into contractile rings (Krueger et al., 2019). In budding yeast, **fimbrin is phosphorylated by** metaphase cyclin-dependent kinase 1 (**Cdk1**), promoting actin cable assembly. In **HeLa cells** migrating by a "**stable ble**" or "leader bled" migration, the crosslinkers Eps8, **filamin, and alpha-actinin are fundamental** to maintaining the bleb structure (Logue et al., 2015). Still, the reason why they contribute to bleb migration is not yet known. Cellular signaling regulates crosslinkers: **Erk activates Eps8** at the front of leader bleb cells (Logue et al., 2015). *In vitro* studies on Eps8 activation show that it can have a double activity: bundling when activated, and capping when inactivated. These results suggest that **Eps8 might promote different actin organizations in the front versus the rear of migrating blebbing cells, but this has not yet been shown** in cells. The consequences of the crosslinker activity in actin organization in stable blebs and the mechanism by which crosslinking contributes to cell migration are one of the topics of my Ph.D. thesis.

Actin crosslinkers and motors share some functional characteristics. **Myosins** have **a catch-bond with actin** so that the dissociation lifetime increases with the tensile force applied to the bond (Guo and Guilford, 2006; Inoue and Adachi, 2013). Similarly, it was recently reported that the crosslinking time of α-actinin-4 homodimers increases twofold within the typical range of cortical tension found in cells (Hosseini et al., 2020). Crosslinking can support the activity of motors by modulating the connectivity and the order of the actin network (Ennomani et al., 2016). In fish egg extracts, actin crosslinkers, and not only myosin motor activity, can trigger contractile waves (Field et al., 2011).

Actin-membrane attachment

The crosslinking of actin with the plasma membrane is ensured mainly by the **ERM protein family**, including **ezrin**, **radixin**, and **moesin**. ERM proteins have **actin-binding domains** and **FERM domains.** FERM domains contain binding motifs with integral proteins at the membrane, such as receptors, and can exist in closed or open (active) conformations. Ezrin (also known as cytovillin or villin-2) is encoded in humans by the *EZR* gene and is one of the main ERM proteins. It **binds** the sodium-hydrogen exchanger regulatory factor (**NHERF**) once it is in the active open state. The **activation** of ezrin involves two steps: first, **binding** of the N-terminal domain to **PIP_2** and second, **phosphorylation** of **threonine T567** in the C-terminal domain by Rho-kinase and several PKC isoforms (Fievet et al., 2004). Ezrin is a **major regulator of membrane tension**: constitutively active ezrin or an increase of PIP_2 levels increases membrane tension in epithelial cells and lymphocytes, and a decrease of ezrin phosphorylation will promote the formation of blebs and decrease in membrane tension (Liu et al., 2012; Rouven Brückner et al., 2015). Similarly, microinjection of constitutively active ezrin (T567D) into filamin-deficient M2 cells stops blebbing (Charras et al., 2006).

The regulation of actin-cortex attachment and membrane protrusion is tightly linked to the regulation of the lipid composition, in particular, the presence of PIP_2 and PIP_3 at the plasma membrane. The activation of **PI3K phosphorylates PIP_2 to yield PIP_3** at the plasma membrane. This is often upregulated in cancer cells, and it is associated with cell motility and local inactivation of ezrin (Insall and Weiner, 2001). The enzyme performing the reverse reaction, the phosphatase and tensin homolog (**PTEN**), is considered a tumor suppressor. Other enzymes regulating PIP_2 levels at the membrane are responsible for the detachment and inactivation of ezrin, such as **PLC**, which hydrolyzes PI (Hao et al., 2009). Supplementary to their role in cortex-membrane attachment, ERM proteins can bind to microtubules and have a role in regulating spindle organization (Solinet et al., 2013). In *D. discoideum,* microtubules indirectly regulate cortex-membrane attachment and ERM activity, positioning the enzyme PI3K on the cortex and promoting lamellipodia. Without microtubules, the absence of PIP_3 and the upregulation of PIP_2 increases cortical contractility and promotes bleb-based migration (Sugiyama et al., 2015).

Nonmuscle myosin II: a fundamental motor for cell migration

Albert Szent-Györgyi, Bruno Straub, and colleagues discovered the molecular nature of muscle contraction by experiments with rabbit muscle extracts performed during WWII

in Szeged, Hungary. One year after his 1937 Nobel prize award, Szent-Györgyi began work on the biophysics of muscle movement. His team found that muscles contain actin, which contracts when combined with myosin and ATP (Kühne and Kühne, 1864; Rall, 2018; Szent-Györgyi, 1942; Szent-Györgyi, 1968). This discovery preceded in 30 years the discovery of the cross-bridge mechanism of contraction of muscle myosin (Huxley, 1969), and the discovery of nonmuscle myosin II (NMII) in platelets (Adelstein and Conti, 1975) and amoebae (Pollard and Korn, 1973a, 1973b).

Myosins contain 18 classes of proteins. Some classes are well studied, such as myosin I and V, ubiquitous proteins that participate in vesicle transport. Other myosins classes, such as III and XII, are less explored. Some classes are absent from animals such as myosin VIII. Most myosin molecules are composed of a head, neck, and tail domain that typically dimerizes. The **head domain binds F-actin** and uses ATP hydrolysis to generate a power stroke to move on the filament. The **neck domain** acts as a linker to transduce the force from the motor domain and as a **binding site for the myosin light chains**, which form a molecular complex with the heavy chain. The **tail domain** can play a role in regulating **motor activity**, binding to cargo, or **interacting with other myosin subunits**. Nonmuscle myosin II (NMII) is a major motor-related to cell migration and has three heavy chain isoforms named **NMIIA**, **NMIIB**, and **NMIIC**, encoded in mammals by the genes *MYH9*, *MYH10*, and *MYH14,* respectively. The heavy chain determines the type of paralog, but the light chain types are shared. NMII is analogous to the conventional muscle myosin but found in the cortex of all cells. Myosin II motors are hexamers with two heavy chain subunits containing the head and tail domains and four light chain subunits, belonging to a family of calcium-binding proteins and necessary for the assembly of the macromolecular complexes, named minifilaments (**Figure 4**).

Compared to other myosins, **class II myosins** are **non-processive motors**. They have a high ATPase rate and a low duty ratio, which means they spend only a small fraction of the ATPase cycle attached to its track. NMIIA motors **need to work together in a bipolar minifilament to perform their function**. In human cells, motors assemble to a stereotypic size of 30 molecules, corresponding to a rod of approximately 300 nm long (Billington et al., 2013; Niederman and Pollard, 1975), which is a considerable size for the scale of an actin cortex (100-350 nm thick).

NMIIA and NMIIB are broadly expressed, while the expression of NMIIC is restricted to some differentiated tissues. These paralogs have a very similar amino acid sequences but bear significant differences in motor kinetics, structure, and regulation (Shutova and

Svitkina, 2018): for example, NMIIA is a faster motor than NMIIB. **NMIIA is required specifically to drive membrane retraction in blebs in HeLa cells, particularly** the motor domain and nonhelical tailpiece of NMIIA (Taneja and Burnette, 2019). The two paralogs are also regulated in different ways, depending on the cellular context. For example, the metastasis-associated protein mts1 specifically regulates the assembly of NMIIA in vitro and is known to change cancer cells' migration properties (Ford and Zain, 1995; Li et al., 2003). The most common regulators of myosin II activity in cells, Rho-associated protein kinase (ROCK) (**Figure 5**) and Myosin light chain kinase (MLCK) discriminate between NMIIA and NMIIB.

In fibroblasts, ROCK preferentially regulates phosphorylation of MLC20, which is associated with NMIIA. In these cells, MLCK activity is concentrated at the cell periphery and ROCK at the cell center. As in fibroblasts, ROCK-mediated contractility promotes stress fibers and focal adhesions rather than protrusions. Rho-kinase inhibition prevents the formation of focal adhesions and accelerates fibroblast migration (Sandquist et al., 2006; Totsukawa et al., 2000). In SV1 cells (immortalized fibroblasts), NMIIA localizes to stress fibers throughout cells, while NMIIB is excluded from the peripheral region. This pattern occurs at the level of individual minifilaments: in U2OS cultured cells, **NMIIA, and NMIIB isoforms coassemble**. Still, there is a **gradient in** the relative quantity of

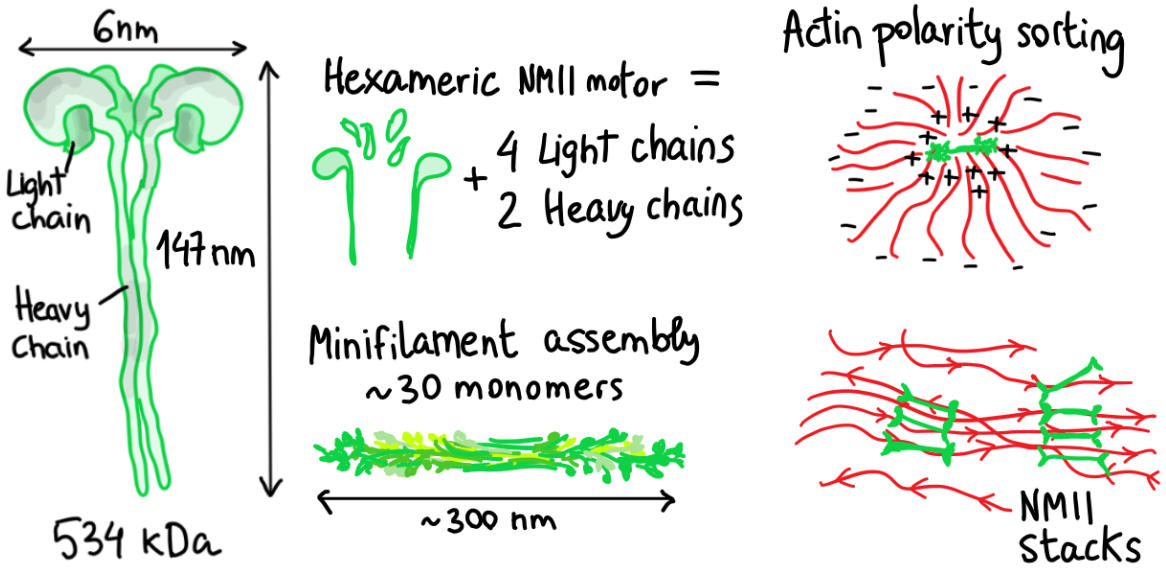

***Figure 4: Molecular organization of myosin motors and of actin-myosin arrays**. A NMII motor consists of two heavy chains (230 kDa), two regulatory light chains (20 kDa) controlling the myosin activity, and two essential light chains (17 kDa), stabilizing the structure. Myosin assembly then into large macromolecular motors called minifilaments which enhance motor processivity. Myosin is a plus-oriented motor, so it is able to sort actin filaments by polarity, forming asters. Myosin bipolar minifilaments can also have supramolecular interactions with other minifilaments and form stacks, somewhat analogous to what myosin organization in muscle cells.*

NMIIA/NMIIB from the periphery to the cell center (**Figure 6**). Similarly, in migrating keratocytes, MLCK activity influences cell polarity by increasing myosin accumulation in lamellipodia. In contrast, ROCK regulates myosin accumulation at the cell rear and does not determine protrusion size (Lou et al., 2015).

Myosin assembly

The polymerization of NMII molecules into minifilaments is fundamental for its function, and assembly is regulated to control contractility. The phosphorylation of the light chains and the heavy chains (Dulyaninova and Bresnick, 2013) can set the myosin molecules into an open conformation, at which they will be able to polymerize. The interaction of myosin molecules depends on parallel and anti-parallel interactions between rod domains, specifically at *assembly competence domains* (ACD1 and 2) at the end of the heavy chain (Ricketson et al., 2010; Shutova and Svitkina, 2018).

Several **cooperative effects** occur **at the level of myosin assembly**. First, minifilaments can change *in vitro* the conformation of closed myosins and recruit them. Second, myosin minifilaments will change the actin network structure and **create asters** (Wollrab et al., 2019). Myosin is a plus-end-oriented motor, so actin's plus-ends will be at the center of the aster (**Figure 4**) (Kreten et al., 2018). This arrangement will direct new motors that come in contact with actin towards the filaments at the aster's center.

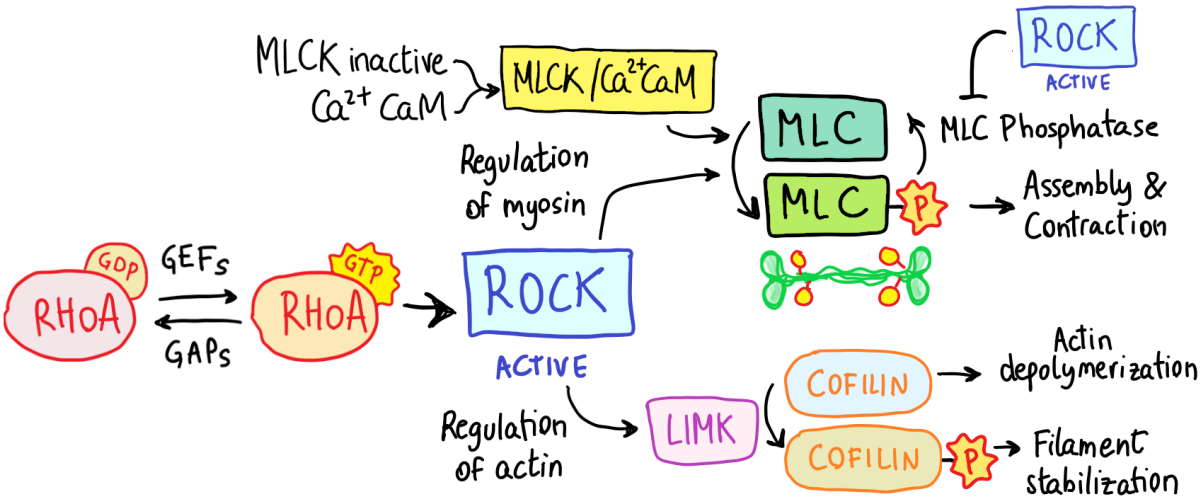

Figure 5: ***Regulation of myosin and actin by ROCK****. Rho small GFPases are a family of proteins regulating a large number of cellular processes. Their activity is controlled by guanine nucleotide exchange factors (RhoGEFs) and GTPase-activating proteins (RhoGAPs), which mediate the GTP/GDP state of the protein. RhoA, Cdc42 and Rac1 are the most known small GTPases in humans. RhoA activates ROCK, which in turn can have a double effect: i) activating contractility through MLC phosphorylation and ii) stabilizing actin filaments, through cofilin inactivation by LIMK phosphorilation.*

Myosins' force is so important that it can bend and break actin filaments *in vitro* (Vogel et al., 2013). Gradually, an actomyosin network evolves from a disorganized state to a mature state where the **myosin organizes in sequential stacks**, analogous to muscle myosins (Fenix et al., 2016; Fenix and Burnette, 2018; Hu et al., 2017). Other proteins such as myosin 18 and alpha-actinin cooperate to establish sarcomeric NMIIA arrays in U2OS cells, and alpha-actinin and fimbrin (also a large molecule like myosin) collaborate with myosin II to organize actomyosin bundles during contractile-ring assembly in *S. pombe* (Laporte et al., 2012).

Moreover, the long-range stresses in contractile networks can create **convective flows** that attract other filaments, which is the more classical network assembly mechanism by contraction. Convective flows have been observed in migrating cells and reproduced *in vitro*, where myosin clusters can undergo active coarsening, attracting each other at ~18 µm/min (Soares e Silva et al., 2011). Finally, NMIIA displays **mechano-accumulative behavior** (Schiffhauer et al., 2016). Theory predicts that increasing actin concentration and network tension can promote minifilament assembly due to the myosin-actin interaction's catch-bond properties, by actively lowering the critical aggregation concentration of the monomers (Grewe and Schwarz, 2020).

As an example of this cooperative behavior, **single myosin nucleation events** can **nucleate minifilaments**. In MEFs and U2OS cells, minifilaments can partition,

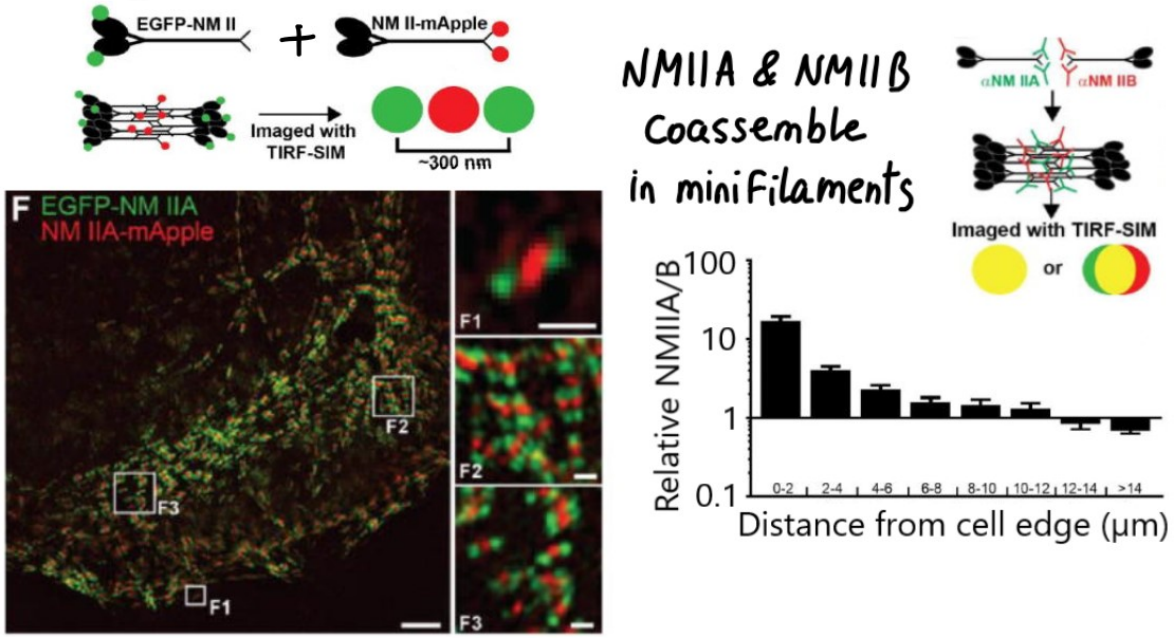

***Figure 6: Myosin organization in stacks in U2OS cells**. NMIIA and NMIIB can assemble togehter in minifilaments while keeping a gradient in the cell, so that NMIIA is relatively more abundant at the cell periphery and NMIIB at the cell center. SIM images from from Beach et al., 2014.*

concatenate, and spread to the neighboring cortex (Fenix et al., 2016). Interestingly, the partition and maturation of minifilaments are spatially regulated in MEFs by ROCK and MLCK, so that MLCK-dependent filament assembly in the lamella competes with ROCK filament assembly at stress fibers (Beach et al., 2017).

All these mechanisms are not mutually exclusive, and they could happen at the same time. There is currently a discussion in the field over the relative importance of the **expansion-concatenation mechanism** of myosin filament arrays **versus the contraction-convection model**. It might be possible that the dominant mechanism for cluster formation depends on the cellular context (Fenix and Burnette, 2018). Without being my main focus, I will address some aspects of NMIIA assembly in blebs in the present thesis, in particular the role of convection versus expansion.

The molecular interaction of actin with myosin monomers or minifilaments in cells is an intense area of research, particularly the **role of steric hindrance** in the behavior of actomyosin networks. Recent theoretical work suggested that **myosin and actin layering** is necessary to recapitulate cortex patterning and aster formation (Das et al., 2020). They proposed **that only the cortex's top layer is accessible by myosin II minifilaments** and other large molecules such as certain actin crosslinkers. A myosin II minifilament can be up to 0.3µm, which is less than the thickness of a lamellipodium, leading to a steric hindrance to reaching the tip (Svitkina et al., 1997). *In* vitro actomyosin reconstitutions on supported bilayers with continuous turnover confirmed the role of stratification, but it has not yet been observed in cells (Sonal et al., 2018). Some works suggest a role of steric hindrance in the localization of actin crosslinkers, particularly large actin bundlers accessing the thin lamellipodial network. In FRAP experiments on the lamellipodium of NG108-15 (a hybrid of mouse neuroblastoma N18TG2 and rat glioma C6-BU-1 cells), it was observed that the recovery of actin fluorescence was from the edge of the lamellipodium. In contrast, the recovery of the bundlers (fascin) was from the base (Nakagawa et al., 2006).

The molecular machines that compose the cytoskeleton cooperate to produce forces and control cell migration. The essential components such as actin and myosin are common to all cells, but they can give rise to very different cell behaviors depending on their dynamics and organization. In the next chapter, we describe the different migration modes and how they produce forces to achieve locomotion.

Chapter 3: Crawling or blebbing, that is the question

Crawling and blebbing are complementary and coexisting migration modes

enerally, there are **two strategies for cells to migrate: amoeboid migration and mesenchymal migration** (Clark and Vignjevic, 2015; te Boekhorst et al., 2016). These two modes are sometimes referred to as **friction- versus adhesion-based or bleb- versus lamellipodium-based**. Migrating cells are often divided into these two rather broad categories based on cell shape, cytoskeleton organization, mechanism of force generation, and type of interaction with the substrate (Friedl and Wolf, 2010). Cell types, protrusions, and typical morphologies are also conceptually placed in one of these two categories (Table 1, **Figure 7**).

	Cell types	Protrusions	Cell characteristics
Mesenchymal modes	Fibroblasts Fish keratocytes Neural crest cells Sarcoma cells Dedifferentiated cancer cells	Lamellipodia Filopodia Invadopodia	"**Crawling**" motion Elongated or irregular cells Slow-motion (0.1-1µm/min) Spiky or fan-shaped front Strong substrate adhesion Actin stress fibers
Amoeboid modes	*D. discoideum* Zebrafish prim. germ cells Confined HeLa cells Immune cells (dendritic cells, neutrophils)	Pseudopods Blebs	"**Blebbing**" motion Rounded cells Fast shape changes Fast motion (1-10µm/min) Friction-based migration Uropod formation

Table 1: General classification into "amoeboid" and "mesenchymal" categories of cell types, protrusions, morphology, or modes of migration.

This dichotomy in cell motility and cell morphology of "blebbing" versus "ruffling" was already identified in 1980 (Albrecht-Buehler, 1980). Amoebae were an early study model for cell biologists. The study of other single cells such as zebrafish melanocytes, keratocytes, or mammalian embryonic cells revealed that they have different shapes and migration dynamics, so cells with a migration cycle similar to amoeba were called "**amoeboid.**" The term "mesenchymal migration" initially referred to the migration of cells in the mesenchyme during development (Lewis, 1923). The mesenchyme is a connective

tissue found mostly during embryonic development of bilateral animals, composed mainly of ECM with few cells. In the 1980s, **EMTs (epithelial-to-mesenchymal transition)** and **METs (mesenchymal-to-epithelial transition)** were described **in embryonic development**. It was not until the 2000s when the term "mesenchymal migration" acquired more attention due to the research done in cancer cell biology and the factors triggering metastasis. Cancer cells go through a process of "**dedifferentiation**" that involves an EMT and a **MAT (mesenchymal-to-amoeboid transition)** (Sahai, 2007). In cancer, specific molecular and genetic changes define these transitions.

Mesenchymal modes often display slower velocities, strong cell-substrate adhesions in the form of focal adhesions with emanating actin stress fibers, and actin-rich protrusions such as lamellipodia, filopodia, or invadopodia (Gardel et al., 2010). The mesenchymal modes are exemplified by fish keratocytes (Keren et al., 2008) or fibroblasts. Mesenchymal migration is dominated by **actin-rich protrusions such as filopodia, lamellipodia, or invadopodia**, and amoeboid migration by **actin-depleted protrusions such as blebs**. Lamellipodia are at the front of some adhesion-based cells, such as keratocytes. They constitute thin sheets of branched actin networks covered by the membrane. Actin polymerization pushes the front of the membrane, where the network

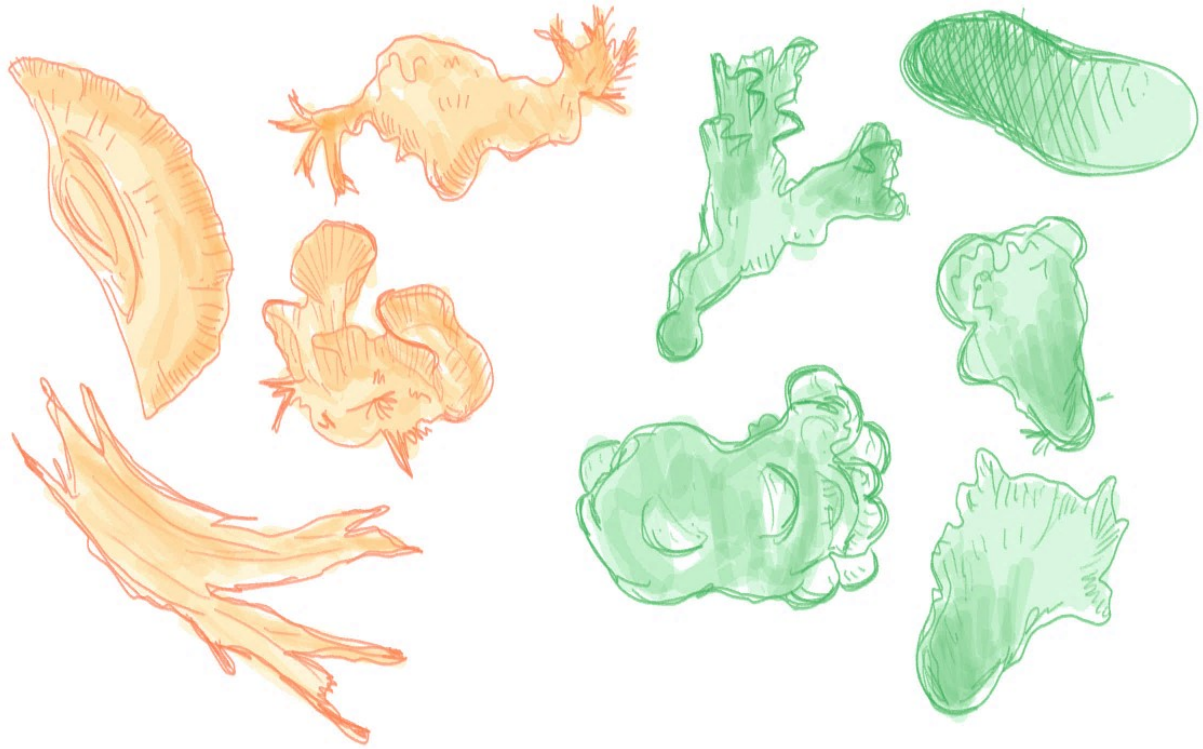

Figure 7: Typical morphologies of stereotypical mesenchymal (yellow) and amoeboid (green) cells. *Mesenchymal mode shapes include a fish keratocyte, a fibroblast, and cancer cells inside a collagen matrix. Amoeboid shapes include a dendritic cell inside a collagen matrix, a zebrafish germ cell, an amoeba, and a blebbing melanoma cell. Shadows in the filling color aim at representing F-actin density.*

assembles. There is a constant retrograde flow of actin, which helps to exert forces on the substrate thanks to focal adhesions at the lamellipodium base. Invadopodia are also actin-rich protrusions present in cancer cells associated with the degradation of the extracellular matrix during cancer cell migration and metastasis. The signaling defining front and back could differ between migration modes (Sahai and Marshall, 2003). **In mesenchymal migration, PIP_3 signal and activated Rac and Cdc42 are predominant at the front, and activated ROCK and myosin II contractility at the back**. This signaling triggers a multistep cycle of protrusion, adhesion formation, and stabilization, as described by Abercrombie (Abercrombie et al., 1970a). During mesenchymal migration, the cytoskeleton rearranges to push the cell forward and often secrete matrix metalloproteinases (MMPs) at the leading edge that degrade extracellular matrix components.

The amoeboid modes display ~10x faster migration (Liu et al., 2015), lower adhesion to the substrate, which results in weaker traction forces exerted on the substrate (Bodor et al., 2020; Yip et al., 2015), and absence of stress fibers (Lämmermann and Sixt, 2009). Whereas the term "fiction-based" could be used interchangeably with "amoeboid," the term "blebbing migration" is more specific than amoeboid motility. Amoeboid migration is not based on focal adhesions, but rather on the contraction of the cell's rear, like in human T cells. The front of the cell forms a protrusion, sometimes with actin-rich protrusions such as **pseudopods**, sometimes with actin-depleted protrusions such as **blebs**. Actomyosin mediates contraction of the cell body in the back, which pushes the cell body to the front (Yoshida and Soldati, 2006). Cells move by squeezing their cell body through extracellular matrix gaps (Fritz-Laylin et al., 2017a). The **uropod** is an essential structure for maintaining the polarity in migrating immune cells, similar to the keel of a boat (Hind et al., 2016; Lorentzen et al., 2011). It contains a high concentration of the membrane-cortex linking group of proteins from the ERM family (ezrin, radixin, and moesin), other transmembrane proteins, and cell surface receptors. Different migrating cell types contain uropod-like structures as well (Liu et al., 2015). The molecular mechanisms and signaling underlying amoeboid migration are generally less understood.

Strikingly, cells are versatile: they **can switch from amoeboid migration to mesenchymal or vice versa,** and they can also bear both types of protrusions at the same time (Bergert et al., 2015; Chikina et al., 2019; Liu et al., 2015; Ruprecht et al., 2015; Zatulovskiy et al., 2014). This phenomenon was already described very early on amoeba (Trinkaus, 1973), where blebs cooperate with actin-rich protrusions. Similarly, cell fragments from the same cell can reproduce mesenchymal or amoeboid phenotypes

(Albrecht-Buehler, 1980). The transition between migration phenotypes is referred to in cancer cell biology as migration plasticity. In the present work, we use confinement in a non-adhesive environment to induce amoeboid migration in HeLa cells, which would otherwise display a mesenchymal phenotype when cultured on a petri dish.

Forces in crawling and blebbing migration modes

Generally, cells need to extend their leading edge to migrate. A simple way to see the differences between mesenchymal and amoeboid modes is the protrusion's main driver: actin polymerization versus cortical flows and intracellular pressure. While bleb migration is dependent on NMIIA activity, keratocyte and keratocyte fragments can migrate after NMIIA inhibition (Barnhart et al., 2011; Okimura et al., 2018). Both modes rely on actin flows (Callan-Jones and Voituriez, 2016), but their origin might diverge in different migration modes. Generally, flows originate due to either contractility (Bray and White, 1988) or polymerization unbalance arising from polarity establishment. So, if amoeboid cells rely more on membrane protrusion and flow initiation driven by contractility, mesenchymal cells rely on actin polymerization unbalance and polymerization forces to extend their leading edge.

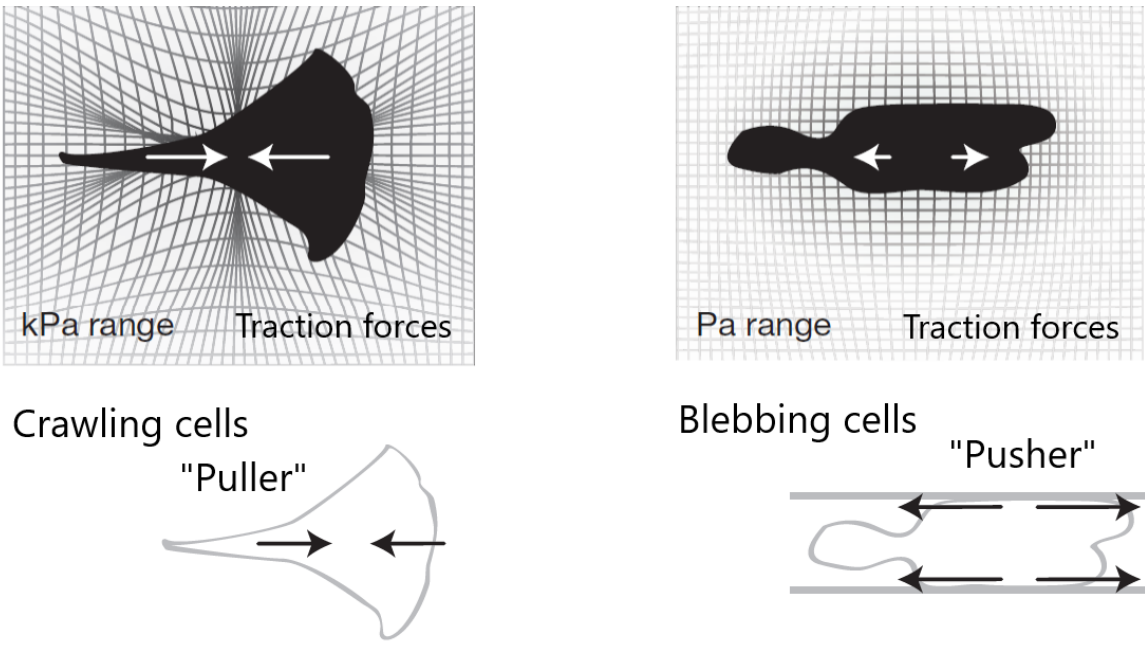

Figure 8: Magnitude and direction of forces exerted on the substrate by friction-based and adhesion-based cells. *Adapted from Bergert et al. 2015.*

Amoeboid and mesenchymal cells differ in the magnitude and orientation of forces exerted on the substrate (Figure 8). **Adhesive, mesenchymal cells** make large stresses that induce **strong contractile deformations (kPa range)** on their environment. **Friction-based amoeboid** cells exert small stresses that induce **weak extensile deformations (Pa range)** (Bergert et al., 2015; Yip et al., 2015). Focal adhesion restricts the trailing edge's detachment, limiting cell velocity, and explaining why the stresses exerted on the substrate need to be considerably higher (Gupton and Waterman-Storer, 2006). Due to this, cells migrating by focal adhesions will have a maximal cell speed at intermediate friction, but cells migrating through friction reach a speed plateau at middle friction value (Paluch et al., 2016). Consequently, the rearrangements that cells produce on the extracellular matrix and their influence in the migration of other cells can be different. For example, mesenchymal cells will bundle collagen fibers and create trails that guide other cells' migration.

More precisely, several physical mechanisms of force generation and transmission have been proposed for amoeboid migration: **swimming** migration, cell-substrate **intercalation**, **chimneying** force transmission, and **flow-friction**-driven force transmission (Paluch et al., 2016) (**Figure 9**). Flow-friction-driven force transmission differs from adhesion-based migration, mostly in the strength and lifetime of the molecular interactions with the substrate. Still, the other mechanisms of force transmission are entirely different. The nature of friction of mesenchymal migration has been exceptionally well studied and involves integrins in focal adhesion complexes (Gardel et al., 2010). However, the nature of friction of amoeboid migration is not yet well understood. One possibility is that the friction is due to weak transient molecular adhesions, but it is also possible that the friction happens without molecular interactions, due to lubricated friction. This friction is caused by the frictional viscous resistance to the motion of the lubricating fluid between the surfaces (Paluch et al., 2016).

Membrane tension

Membrane tension is another critical parameter to understand forces in cells. Tether pulling experiments have been used to understand membrane dynamics and measure its tension. The measured force has a contribution from the tension itself and the friction of the membrane and the cytoskeleton, which resist the pulling. Typically, membrane tension in cells (3-276 pN/μm) is much lower than the rupture membrane tension (3000-10000 pN/μm) (Sens and Plastino, 2015). Apparent membrane tension or cell tension (σ) is defined as the sum of intrinsic in-plane tension (T_m) and cytoskeleton adhesion (γ)

and can be measured by membrane tether pulling. **Membrane tension causes mechanical feedbacks to regulate the actin cytoskeleton at the level of nucleation, elongation, and disassembly**. Actin polymerization is force-dependent: at higher opposing forces, the filament will stall and stop its growth. Increasing membrane tension will prevent nucleation of filaments pointing towards the membrane. Increasing tension will also change actin nucleators' binding to the membrane, such as SCAR/WAVE complex, which will disassemble at high tension. Membrane tension can also trigger the opening of mechanosensitive Ca^{2+} channels, which activate contractility and actin disassembly. Through these interactions, membrane tension has been proposed to act as a global negative modulator to confine protrusive signaling exclusively to the cell front (Houk et al., 2012).

In fibroblasts, endothelial cells, and muscle cells, **membrane tension** seems to be determined and regulated by the **availability of membrane reservoirs**. For example, endothelial cells undergoing rapid membrane tension increase disassemble caveolae and other membrane reservoirs to decrease it (Gauthier et al., 2011; Morris and Homann, 2001; Raucher and Sheetz, 1999; Sinha et al., 2011). Another factor that can largely determine membrane tension is the **interaction between the membrane and the**

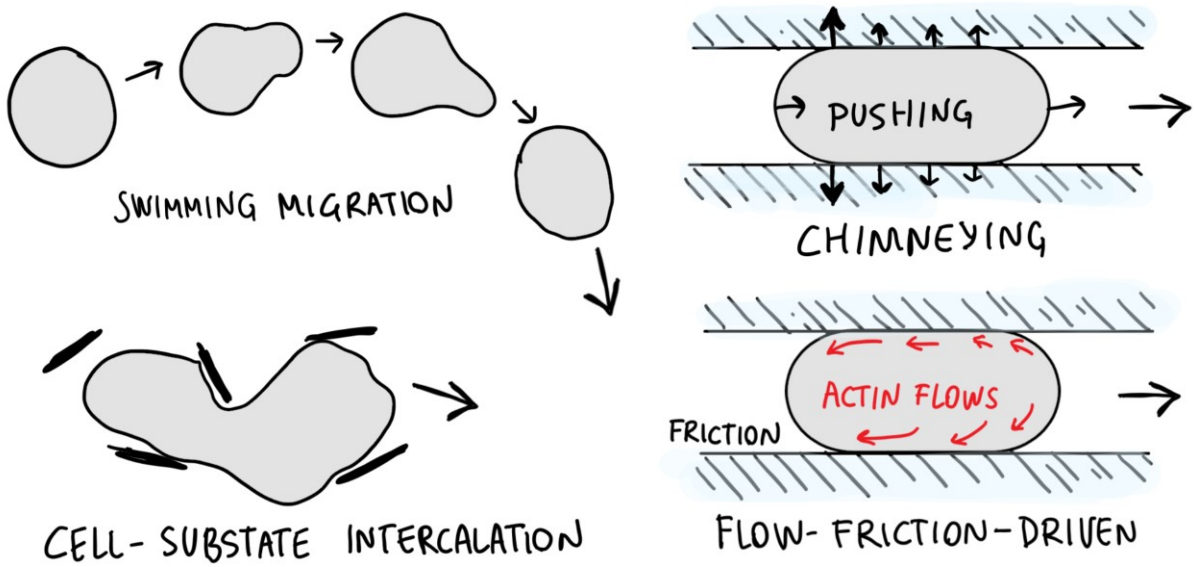

***Figure 9: Physical mechanisms of force generation and transmission for amoeboid migration**. **Swimming** migration combines asymmetric bleb retractor with hydrodynamic interactions in the fluid to move the cell. **Intercalation** of protrusions into lateral gaps can serve as supports for migration. **Chimneying** cells have a gradient of lateral pushing forces against the surrounding substrate, allowing for protrusion expansion at the front and contractility at the rear. For **flow-friction-driven migration**, forces generated by actomyosin flows are transmitted to the substrate by non-specific transient interactions. Drawings adapted from (Paluch et al., 2016).*

cytoskeleton (Sheetz et al., 2006). Decreasing the adhesion between the plasma membrane and the cytoskeleton reduces the apparent membrane tension and promotes bleb formation. This effect is related to the presence of PIP_2 at the membrane, which can be enhanced by phosphatidylinositol phosphate kinases (PIPKs) or decreased by phospholipase C (PLC) in NIH-3T3 mouse fibroblast cells (Raucher et al., 2000).

Researchers have tried to interpret the relative contribution of in-plane tension and cytoskeleton adhesion to the apparent membrane tension by doing tether-pulling experiments in blebs. Blebs are devoid of the actin cortex while forming, so tether-pulling measurements should only have the contribution from the membrane in-plane tension and not the friction with the cytoskeleton beneath. In general, the coupling between the membrane and the actin cortex is the main contributor to effective membrane tension (Sens and Plastino, 2015). Similarly, **bleb apparent membrane tension increases 2-fold during the stalling and retraction phases compared to the growth phase**, when the cortex forms again (Charras et al., 2008; Peukes and Betz, 2014).

Interestingly, **in keratocytes, the in-plane tension is one of the main determinants of cell tension** since the tether force of blebs is similar to that measured at the cortex. Membrane tension in motile keratocytes is **determined by cytoskeletal forces**, and not by the membrane surface availability. There, the typical value for **membrane tension is approximately the stalling force of actin filaments,** and perturbing actin polymerization decreases membrane tension. Increasing the actin pushing forces, increasing adhesion, or decreasing myosin contractility leads to a decrease in membrane tension measured by tube pulling, but **a considerable increase of available membrane in keratocytes by GUV fusion does not change the speed of the retrograde flow or the membrane tension** (Lieber et al., 2013). Remarkably, tension is maintained constant regardless of a two-fold increase in the projected area after fusion with a GUV (Lieber et al., 2013), which indicated that the membrane reservoirs in a cell are dynamically adjusted. The quantity of F-actin increases to the same extent as the increased projected area, suggesting cells modulate the actin polymerization. Equally, **dendritic cells migrating over different adhesion substrates will retain the same protrusion speed while modulating the retrograde actin flow**. In conditions with low adhesion, the friction is weak therefore decreasing the force exerted on the actin pushing at the front. This suggests that actin is polymerizing at the fastest possible speed and that the protrusion of the cell is given by the force balance at the front, perhaps limited by the cortex-membrane friction or membrane flows (Renkawitz et al., 2009).

The lipid bilayer can be considered a 2D fluid, where gradients of membrane tension generate membrane flows from regions of low tension towards high tension regions, equilibrating membrane tension over the cell rapidly. The timescale of propagation of such flows will depend on the membrane's viscosity and generally is fast, on the order of milliseconds. Therefore, in static cells, the tension is uniform. However, migratory cells maintain gradients, consistent with the observation of persistent membrane flows toward

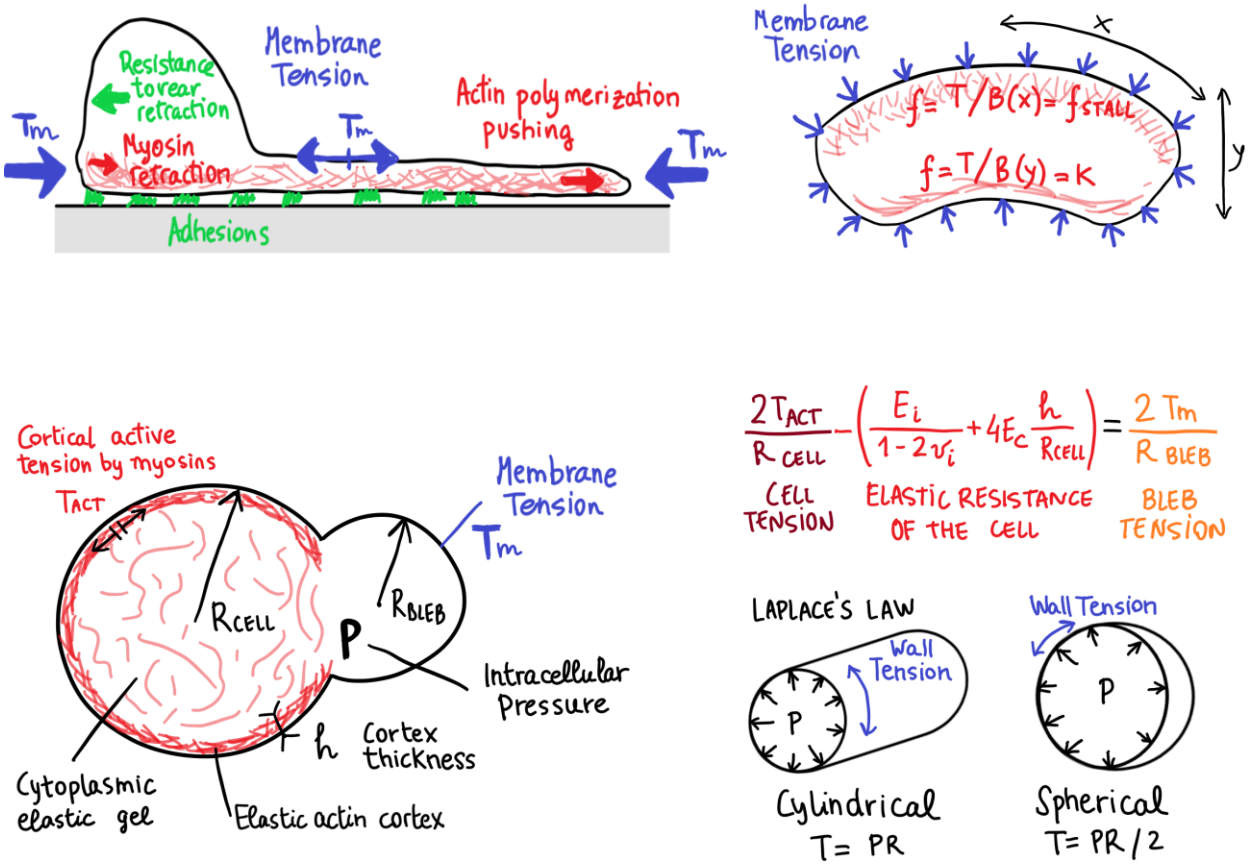

Figure 10: Force balances determining the shape of a keratocyte (top) and a blebbing cell (bottom).

Top: In a migrating keratocyte, membrane tension (T_m) contributes to myosin retraction of the rear and counteracts cell adhesion, whereas at the front stalls the pushing forces from actin polymerization. Membrane tension generates a force along the keratocyte perimeter. At the front corners, the force per filament (tension divided by filament density) reaches the stall force (f_{stall}). At the rear boundary, the force needed to crush the actin network (k) is equal to the membrane tension. The rate of actin disassembly and the membrane tension determines the distance between the front and the back of the cell.

Bottom: In a blebbing cell, the growth of a bleb is determined by the balance between the membrane and cortical tension and the elastic resistance of cellular structures. The pressure in the bleb is imposed by the membrane tension of a sphere ($P = 2T/R$), as described in Laplace's law. In the cell body membrane tension is substituted by cortical tension, which also takes into account the cortical contractility driven by motors. The total elastic resistance of the cell to compression will decrease the radius of the bleb at equilibrium, and has been determined experimentally to be $\left(\frac{E_i}{1-2\nu_i} + 4E_c\frac{h}{R_{cell}}\right)$ ≈ 6850 Pa. Adapted from Lieber et al., 2013, Ofer et al., 2011 and Tinevez at al., 2009.

the anterior side of cells. Also, membrane tension is generally higher in migratory cells. There is a steady gradient of apparent membrane tension measured by tether pulling in migrating keratocytes, about **30% higher at the leading edge** (Lieber et al., 2015). Similar results are obtained with keratocyte fragments.

There is a **force balance between the actin polymerization at the front, cell adhesion, and membrane tension** in crawling cells **(Figure 10)**. Substrate adhesion and membrane tension oppose actin polymerization at the front. At the cell rear, membrane tension and myosin contraction contribute to retraction. This force balance determines the actin polymerization rate and cell shape. **In contrast, membrane tension does not hinder actin polymerization in blebs**. The available membrane and the concentration of nucleators control net actin polymerization. The bare membrane will recruit actin up to certain cortex thickness, at which there is a dynamic turnover of actin that maintains the typical thickness (100-300 nm) while renewing the actin every few minutes. In blebs, actin polymerization does not result in membrane protrusion, but cortex formation inwards and membrane retraction.

The differences in tension inside the cell between the amoeboid and the mesenchymal modes are not yet understood. **Nevertheless, membrane tension also plays a role in blebbing migration.** Membrane tension determines the shape of blebs, as described by Laplace's law. There is a **force balance between the intracellular pressure produced by cortical contractility and the membrane tension (Figure 10)**. For a spherical bleb with no cortex, the membrane tension ($mN/\mu m$) will be proportional to the internal pressure ($mN/\mu m^2$, or Pa) and the radius (μm): $\boldsymbol{T = P \times R/2}$**.** At constant pressure, increasing membrane tension will increase the radius of the bleb. For example, to hang a mass from a cable with less sag, one will need to put more tension on the cable. Are there any general differences in membrane tension values between crawling and blebbing cells? If a cell increases contractility, blebs form and prevent that the intracellular pressure rises. Blebs are known to release intracellular pressure and decrease membrane tension while increasing cell surface area. As mentioned above, membrane reservoirs ensure a homeostatic membrane tension within a range (Pietuch et al., 2013), but stable blebs might deplete the cell's membrane reservoirs and hinder cells' ability to regulate membrane tension. It is not clear whether membrane tension could be higher in cells with stable blebs, or whether cells that move by blebbing also have gradients in membrane tension since the sparser cytoskeleton of bleb fronts could allow for a faster equilibration. In my Ph.D. work, we focus on the interaction of actin filaments and

membrane at the cell front to understand the role of actin-membrane attachment and membrane in-plane tension in the stability of a bleb protrusion.

Blebbing is a fundamental mode of animal cell locomotion

Blebbing is a **fundamental mode of metazoan cell migration, conserved across evolutionarily divergent organisms**. Historically, we find early evidence of blebbing migration in embryonic development in fish (Trinkaus, 1973) and amoeba (Jennings, 1904). Jennings described how amoebae move with round protrusions at the front, with a static membrane at the bottom and forward flow at the top membrane. Since then, cells migrating with round protrusions at the front, a typical feature of amoeboid or adhesion-free migration, have been identified in many systems

Some researchers proposed that adhesion-free migration might be the default mode for animal cells, predating focal adhesion-based migration (Bodor et al., 2020; Fritz-Laylin et al., 2017b). Moreover, bleb-based, adhesion-independent migration may require less energy than focal-adhesion-based motility because it does not have to counteract the strong adhesive forces from focal adhesions (Bodor et al., 2020). This is particularly relevant in 3D: whereas blebbing cells in 2D cannot migrate through friction, they can use it to migrate in 3D (Ruprecht et al., 2015). In 2D, cells need strong adhesion to counteract membrane thermal fluctuations and maintain cell-substrate contact. 3D migration can happen independently from adhesion and actin-rich protrusions, with the notable exception of *Dictyostelium*, which can migrate in 2D without focal adhesions (Leithner et al., 2016; Reversat et al., 2019) (**Figure 11**).

When did the components of the migratory machine in animals appear in evolution? As described above, cells can switch to an amoeboid phenotype and migrate through blebs when confined or prevented from forming focal adhesions. This switch has been described for cancer cells, primary immune human and murine cells, zebrafish germ cells, and *Dictyostelium* cells. Remarkably, while conserving this switch, amoeba and animals belong to two different kingdoms, so the similarities might represent either reflects common ancestry or evolutionary convergence. Recently, the switch to bleb-based migration after confinement was also described in different species of animals' closest relatives in the evolutionary tree, choanoflagellates (Brunet et al., 2020). Choanozoa is the clade of opisthokont eukaryotes that contains choanoflagellates (Choanoflagellatea) and animals (Animalia, Metazoa). Choanoflagellates subjected to

confinement retract their flagella and microvilli, generating blebs, activating myosin, and switching reversibly to amoeboid motility while the confinement is maintained. These results suggest that the **duality between the epithelial and amoeboid phenotypes** and the **myosin-mediated phenotypic switch** was probably present in their last common ancestors and that confinement-induced blebbing migration is a **well-conserved feature**.

Blebbing migration is relevant for cancer and human disease

In humans, we find numerous examples of physiological processes controlled by bleb-based cell migration (Paluch and Raz, 2013). Defects can result in immune-related diseases due to the importance of cell migration in the immune system (Alvarez et al., 2008). Another **consequence of misregulated cell migration is metastasis of carcinomas**. During metastasis, cancer cells migrate away from the tumor through the stroma to reach out to blood or lymph vessels and colonize other tissues. Metastasis is the leading cause of mortality in cancer patients (Hanahan and Weinberg, 2011). There is evidence of single-cell blebbing migration in cancer from intravital microscopy (Alexander et al., 2013; Headley et al., 2016; Weigelin et al., 2012). The flexibility of phenotypes that cancer cells can display to optimize their metastatic spreading makes it challenging to find cures or targets to stop them. For example, inhibition of integrin-binding or production of metalloproteases promotes mesenchymal-to-amoeboid transition (Sahai and Marshall, 2003; Wolf et al., 2003). The signaling network complexity challenges the pharmacological strategy against cancer migration to consider the amoeboid modes that rely less on cell-matrix interaction and degradation (Logue and Morrison, 2012; Ullo and Logue, 2018).

Following its evolutionary importance, blebbing migration is also relevant in human physiological processes (e.g., embryonic and brain development) and diseases (e.g., immune disorders, cancer). Previously associated only with apoptosis, **blebs are essential structures for cell migration of amoeboid cells** (Charras and Paluch, 2008; Fackler and Grosse, 2008). One of the first unequivocal studies that showed that adhesion-free migration happens *in vivo* and *in vitro* reported the migration of immune cells without integrins and talins, required for focal adhesions (Lämmermann et al., 2008). As another example, the satellite cells responsible for muscle tissue repair after damage use an amoeboid-based mechanism and dynamic blebbing to migrate to damaged sites

(Otto et al., 2011). In fibroblasts migrating in murine dermal explants, intracellular signaling defines two distinct modes of 3D cell migration regulated by RhoA, ROCK, myosin II, and the elastic behavior of the 3D extracellular matrix (Petrie et al., 2012).

Despite the diversity in signaling and physical mechanisms, there is a unifying feature: all cells polarize before starting locomotion. Both amoeboid and mesenchymal cells break symmetry from a homogeneous state to a polarized state, giving rise to two opposing poles. Cell polarity is a condition *sine qua non* for cell migration: an asymmetry of forces arising from cell polarity is needed to move. The study of cell polarity, its emergence, maintenance, and consequences is a major focus of modern cell biology. Effectively, the force amplitude is not as important as their asymmetry. In the next chapter, we will outline the major mechanisms cells use to polarize, with a particular focus on the mechanisms arising from actomyosin contractility, which are fundamental for bleb stabilization in confined cells.

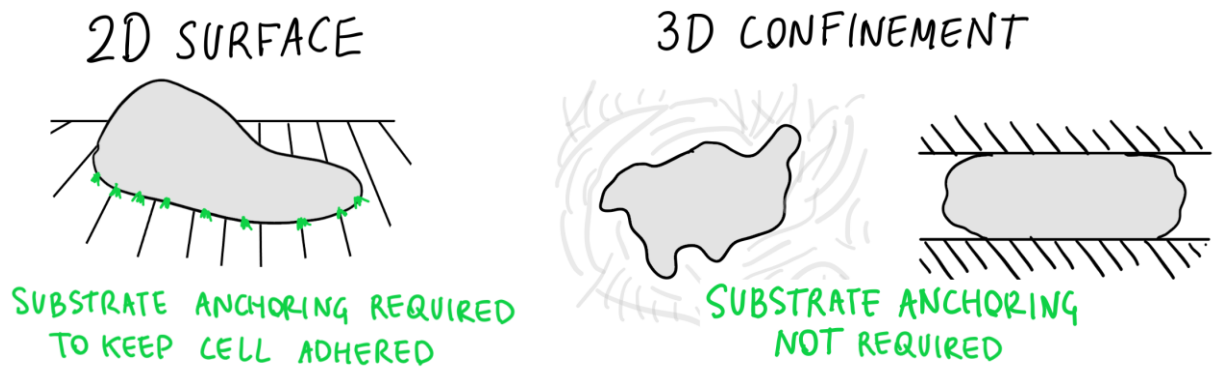

Figure 11: Adhesion requirements for migration in 2D and 3D environments. *Migration in 2D substrate requires strong anchoring in order to counteract Brownian forces, with the great exception of Dictyostelium. Conversely, in a 3D environment cell-substrate contact is ensured by confinement and strong substrate anchoring is not required. Drawings adapted from (Paluch et al., 2016).*

Chapter 4: On cell polarity

Meinhardt and Gierer first conceptualized cell polarity in their 1972 model (Gierer and Meinhardt, 1972), also termed "**LEGI**" (**Local Excitation, Global Inhibition**). This model assumes the presence of an activator with a non-linear local effect and an inhibitor with a long-range impact. This simple model has served to describe the excitable behavior of signaling networks involved in signaling transduction and actin polymerization: the **signal transduction excitable network (STEN) and the cytoskeleton excitable network (CEN),** respectively (Devreotes et al., 2017; Ma et al., 2004; Miao et al., 2019, 2017). STEN is the best studied in terms of molecular details and overall behavior. An expansion of this model is the **LEGI-BEN (local-excitation global-inhibition biased excitable network**), accounting for the interactions of the chemotactic LEGI mechanism, CEN, STEN, and other regulatory networks (Xiong et al., 2010) (Figure 12). The model contains four basic modules to account for cell polarity:

1. **Chemotactic bias**. This module represents the local excitation global inhibition model for receptor occupancy and G-protein coupled receptors (GPCR) signaling in chemotaxis. External chemical gradients trigger it.

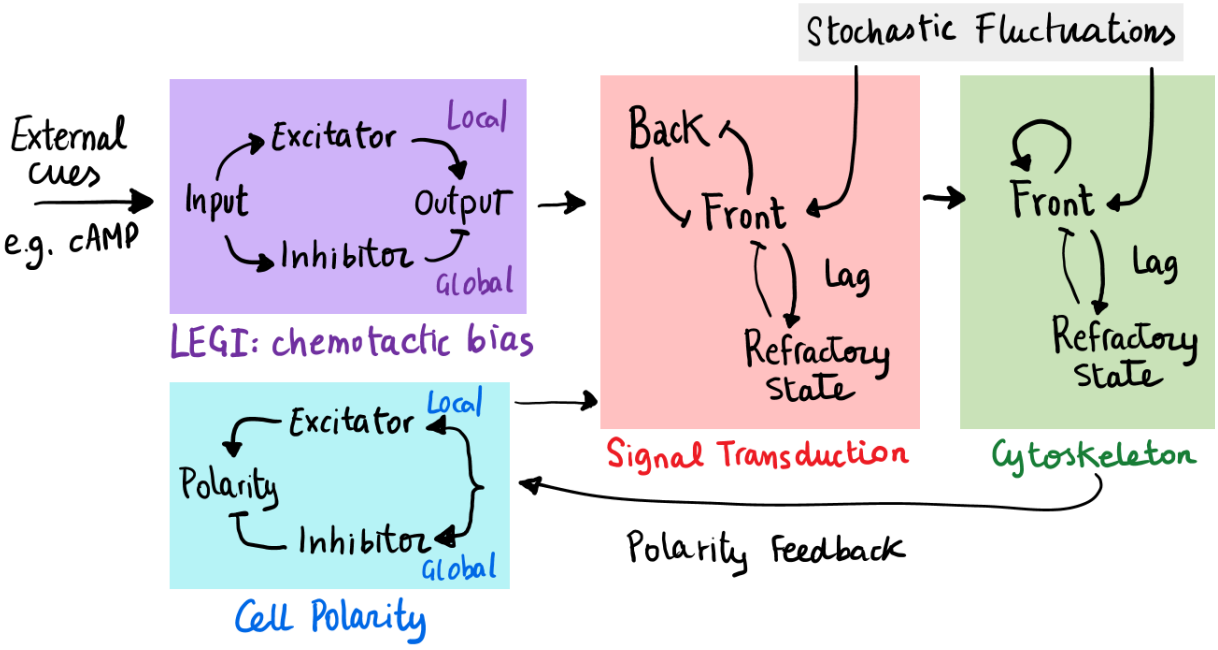

Figure 12: Conceptual representation of the regulation loops contributing to cell migration. *The polarity and the chemotactic modules function as LEGI systems with a self-enhanced activator and a long range inhibitor, whereas the signal transduction network and the cytoskeleton work as excitable systems with an active (denoted as front), inactive (back) and refractory states. Adapted from (Devreotes et al., 2017).*

2. **Signal transduction**. This module is the **signal transduction excitable network (STEN)**, responsible for the signaling at the membrane mediating between GPCRs and cytoskeleton in chemotactic cells.
3. **Cytoskeleton**. This module is the **cytoskeleton excitable network (CEN)**, responsible for the polymerization of actin at the membrane and the formation of actin waves, a feature of an excitable system.
4. **Cell polarity**. This module is related to factors that mediate cell polarity, responsible for maintaining cell persistence in the absence of chemotactic cue. The polarity cue relates to the coupling of cell speed and persistence.

The work to build this model has been performed mainly in *D. discoideum.* Although the general principles might be conserved, there are molecular differences such as in myosin II regulation: in *D. discoideum*, this is controlled by cGMP, whereas in mammalian cells, it is regulated by ROCK and MLCK. Therefore, for mammalian cells, the network structure does not represent specific molecular mechanisms, but it helps to conceptualize, model cells' behavior, and make theoretical predictions.

Actin polymerization waves can drive cell motility

Actin waves are cellular events that exemplify the excitable behavior of the cortex. **Actin waves form spontaneously in many cell types**: *D. discoideum* cells (Asano et al., 2008; Brzeska et al., 2014), keratocytes (Barnhart et al., 2011), leucocytes (Hepper et al., 2012; Weiner et al., 2007), fibroblasts (Johnson et al., 2015; Vicker, 2002), neurons (Flynn et al., 2009; Toriyama et al., 2006), cancer cells like melanoma or osteosarcoma cells (Case and Waterman, 2011; Vicker, 2002), oocytes, and *C. elegans* embryos (Bement et al., 2015). The **STEN-CEN waves provide a coordination mechanism to form actin structures at a much larger scale than a single filament.** CEN and STEN waves' duration and intensity dictate the shape of a protrusion or the lack of response in the cortex. For waves persistent and localized in one place, the cell will have thin and long protrusions, and moving waves will have shorter and wider actin protrusions.

The local activator and global inhibitor of actin polymerization

The mathematical description of an excitable system that can produce activity waves is consensual and includes a global inhibition and local activation, based on the Meinhardt-Gierer model. For actin polymerization, multiple nodes have self-enhancing

characteristics and could play a role in the local activation. Rho GTPases activate actin assembly driven by Arp2/3 by recruiting nucleation promoting factors such as WAVE or WASP in ways that can depend on actin assembly itself, generating positive feedback loops. For example, a positive feedback loop requiring Rac activity/actin polymerization and PI3K mediates the polarity of PIP_3 in the plasma membrane (Inoue and Meyer, 2008; Srinivasan et al., 2003; Weiner et al., 2002). Furthermore, an activator of Rac1/Cdc42 called PLEKHG3 has autocatalytic recruitment (Nguyen et al., 2016).

In contrast, **the molecular details of the global inhibitor are not entirely understood.** Meinhardt and others were inspired by the chemical reaction-diffusion processes to propose soluble factors. As discussed earlier, the global inhibition effect could be due to a **depletion of a hypothetical substrate** needed by the activator **or a "poison" or inhibitor produced by the front**. Importantly, in both cases, the molecules need to diffuse at a much higher rate than the typical reaction times. Cortical (cytoskeletal) or membrane tension have been proposed as mechanisms to fulfill the global inhibitor's role. However, some works argue against a global effect of tension (Shi et al., 2018). Their respective importance varies across different systems. In *D. discoideum*, myosin II's cortical tension plays a dominant role in maintaining protrusions restricted to the front. Myosin II inhibition decreases cortical tension dramatically (Pasternak et al., 1989), stimulates lateral protrusions (Wessels et al., 1988), and Ras activation (Lee et al., 2010). However, in keratocytes, inhibition of myosin II does not perturb the polarization or affect migration significantly (Yam et al., 2007).

Membrane tension, and not the cortical tension, was proposed to restrict protrusions in the back of keratocytes by applying a homogeneous load throughout the cell contour. Since the filaments' density is higher at the front than at the back, the load per filament in the back is expected to higher and restrict actin polymerizing. This logic is analogous to the average receptor occupancy acting as the global inhibitor in LEGI chemotactic models. However, this gradient of filament density would still require a different actin assembly in the front and the back through some signaling (Keren et al., 2008; Kozlov and Mogilner, 2007). Houk et al. proposed that as in keratocytes, **membrane tension plays the role of the global inhibitor of protrusions in neutrophils, following the Meinhardt-Gierer terminology.** They split neutrophils into two parts connected by a thin membrane tube to restrict the diffusion between the front and the back. Arguing against the hypothesis of a diffusion-based inhibitory mechanism, they found that the cell remained polarized and bearing a single front. This result excluded the possibility that the global inhibitory mechanism used

intracellular diffusion. Moreover, a sudden increase in surface tension by pipette aspiration led to an overall inactivation of WAVE2 activity. Conversely, a hypertonic shock increases protrusive activity everywhere in the cell (Houk et al., 2012). Both cases cause severely affected cell migration, as cells need to remain polarized to migrate. Furthermore, membrane tension triggers additional feedback cascade that negatively affects actin assembly through PLD2 and mTORC2 (Diz-Muñoz et al., 2016). This regulation closes the loop between biochemical signaling and membrane tension and suggests that overlapping regulation mechanisms of different nature work together to coordinate a migrating cell's shape and forces (Figure 14). It is not clear what is the role of membrane tension in stable bleb migration.

Authors differ on the **particularities of actin polymerization waves compared to other excitable networks**. Some studies describe them as waves purely driven by chemical activities, such as the Hem-1 actin waves in neutrophils, while others **incorporate** elements such as **polarity and order of the filaments** to account for some particular behavior (Doubrovinski and Kruse, 2011; Dreher et al., 2014). These models are based on self-enhanced actin nucleators that can be active if bound to the membrane, or inactive, if cytoplasmic. Active nucleators bind cooperatively to the membrane, where they polymerize actin with a certain polarity. Actin filaments, in turn, inactivate actin nucleators (Figure 13). The Hem-1 component of the Scar/WAVE complex in human neutrophils shows cooperative binding effects and actin-mediated detachment. These two elements constitute the core of the wave generator, which moves at 3-5 μm/min (Weiner et al., 2007, 2006). In models incorporating polarity, the actin polarity field and the actin density can predict membrane dynamics and migration trajectories in **dendritic cells** using a phase-field approach to describe boundary dynamics. This model could predict that by changing parameters related to actin dynamics – such as actin nucleation or polymerization rates – dendritic cells can switch from a diffuse to a directed migration

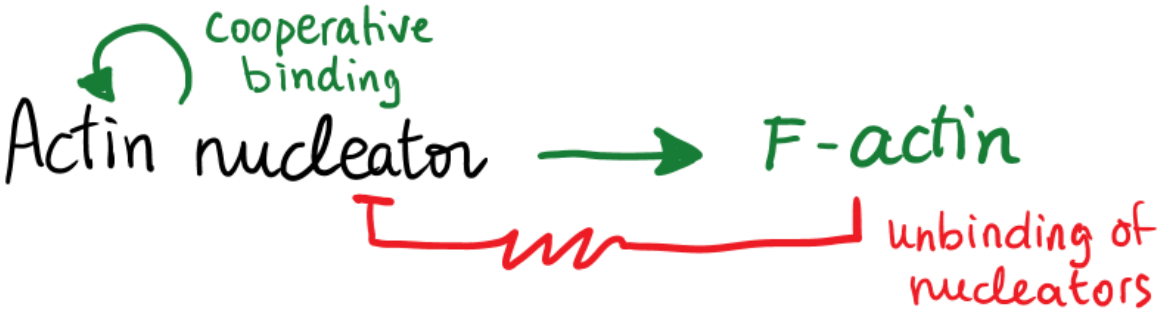

Figure 13 Basic oscillator model for actin waves at the ventral plasma membrane. *It consists of a self-enhanced element (actin nucleators) and a repressor with a time delay (actin filaments is promoting the unbinding of nucleators). Adapted from (Stankevicins et al., 2020).*

state (Stankevicins et al., 2020). As another example, in **neuronal growth cones**, the propagation of actin waves is dependent on adhesion molecules and molecular clutch components, with a wave propagation speed proportional to that of actin polymerization. In this case, actin filaments are attached parallel to the membrane, aligned, and pointing their plus ends towards the end of the axon, so that the wave is directional (Inagaki and Katsuno, 2017; Katsuno et al., 2015).

Since actin polymerization does not drive blebs, how does the signaling network regulate cell polarity in blebbing migration? **The research on blebs and chemotaxis is limited**, but there are some clues dispersed in the literature. When stimulated with uniform concentrations of chemoattractant, amoeba cells experience a series of morphological changes: i) increase, ii) decrease in F-actin, iii) transient blebbing, iv) formation of pseudopods, and v) migration (Langridge and Kay, 2006). During the transient blebbing phase, blebs are restricted in size and number by Arp2/3 activity and promoted by myosin II activity. On the other hand, in a **gradient of chemoattractant, amoeba produce blebs in the direction of the gradient** (Zatulovskiy et al., 2014). Progenitor germ cells in zebrafish embryos use blebs to move to specific sites during embryogenesis and perturbing blebbing results in a wrong localization during development (Blaser et al., 2006). In melanoma cells, actin polymerization and blebbing co-occur at the front of the cell. This enables coordination between the short time scale of blebbing and the longer time scale of cell migration (Welf et al., 2020). PIP_2 enrichment at the back and PIP_3 enrichment at the front, and the advection of actin-membrane linkers caused by blebbing (Olguin-Olguin et al., 2021) weakens actin-membrane attachment and increases the probability of bleb formation at the front, on the direction of chemokine gradients.

As will be discussed later, **some studies point that bleb and pseudopod generation cooperate.** Pseudopods in *Amoeba proteus* are a direct consequence of cortical contraction (GręObecki, 1994; Yanai et al., 1996). **In *D. discoideum*, actin-rich**

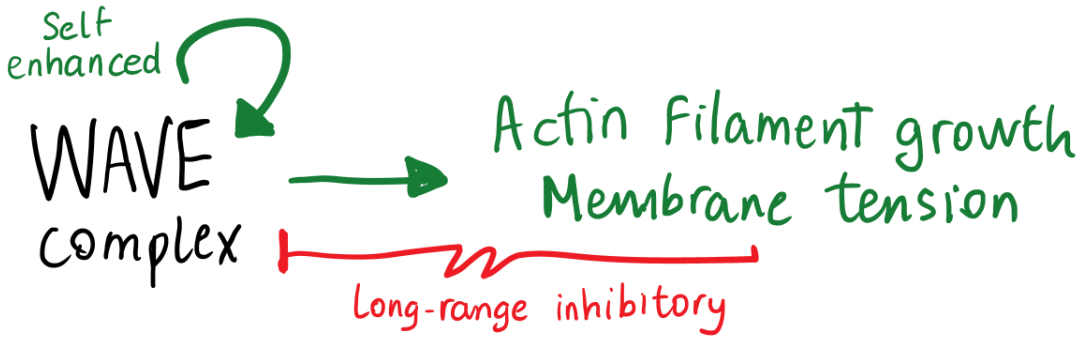

Figure 14: Basic oscillator model of for actin nucleation at the leading edge. *It consists of a self-enhanced element (WAVE and a long-range repressor (membrane tension).*

protrusions often arise from blebs. It is speculated that membrane-cortex detachment by intracellular pressure and membrane-cortex detachment by PIP_3 signaling and FERM/ezrin disengagement can cooperate to maintain a protrusive front during chemotactic migration (Bisaria et al., 2020; Zatulovskiy et al., 2014). Furthermore, and blebs could cooperate through local membrane tension: blebs often form at areas of negative membrane curvature, on the flanks of earlier projections. In the chemical gradient direction, pseudopods show a unimodal distribution in chemotactic cells with a single peak at 0°. In contrast, blebs show a bimodal distribution with two peaks at ±30° (Figure 15). This observation explains the bimodal distribution found in blebs forming at the flanks of pseudopods and suggests a role for membrane tension in bleb formation. This can indicate that the same **pathways** described to **drive lamellipodium-based chemotaxis** in mammalian cells **can promote directed bleb migration** if blebbing is favored (Welf et al., 2020).

Topology and cell shape bias actin dynamics

The organization of actin polymerization in excitable waves of activity implies that they are biased by cell shape and membrane topology. For this reason, physical extracellular cues in the form of substrate topology can promote cell migration by inducing symmetry-breaking or maintaining polarity. As a consequence, cells display contact guidance on adhesive nanogrooves or aligned fibers (**Figure 16**). This means that they migrate parallel to the grooves and bias the orientation of focal adhesions or actin fibers. The term "**contact guidance**" was first coined by Paul Weiss in 1931, but the first observations of this phenomenon date back at least to the dawn of the 20th century. Ross

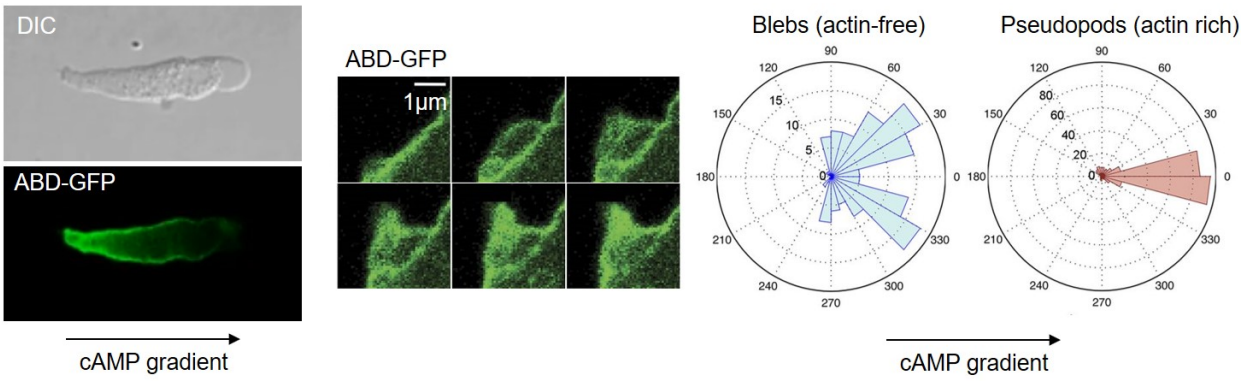

Figure 15: Actin-rich pseudopods and actin-free blebs cooperate in D. discoideum to direct cell migration towards cAMP gradients. *Adapted from (Zatulovskiy et al., 2014).*

G. Harrison (Yale University), Alexis Carrel, and Montrose T. Burrows (Rockefeller Laboratory) described in 1911 how **embryonal or adult tissues of mammals align in culture along fibers** made of glass, cotton, or even spider webs. Harrison wrote: *"the behavior of the cells with reference to the surface of the coverslip and spider web shows not only that the surface of a solid is a necessary condition but also that when the latter has a specific linear arrangement, as in the spider web, it has an action in influencing the direction of the movement, as well as upon the form and the arrangement of cells"* (Harrison, 1914). Harrison pointed out the potential importance of this phenomenon in cancer and wound healing. Remarkably, oriented collagen guides tumor extravasation *in vivo* (Han et al., 2016)., indicating that matrix remodeling can be a central event in the initial steps of metastasis.

Contact guidance has been widely reported (Figure 16). Many examples include rat myocytes (Kim et al., 2010), SV40-immortalized or primary human corneal epithelial cells (Karuri, 2004; Teixeira et al., 2003), NIH 3T3 fibroblasts (Kim et al., 2009), human pancreatic cancer cells (Holle et al., 2017), and amoeboid migrating cells such as confined T cells (Kwon et al., 2012) and *D. discoideum* (Driscoll et al., 2014). **The exact mechanism** of contact guidance of cells on nanogrooves **is still debated** (Bettinger et al., 2009). **Actin polymerization patterns can bend membranes** (Carlsson, 2018), and **membrane curvature can guide actin polymerization** (Gov, 2018). Amoeba cells migrating on nanogrooves nucleate actin polymerization waves that propagate parallel to

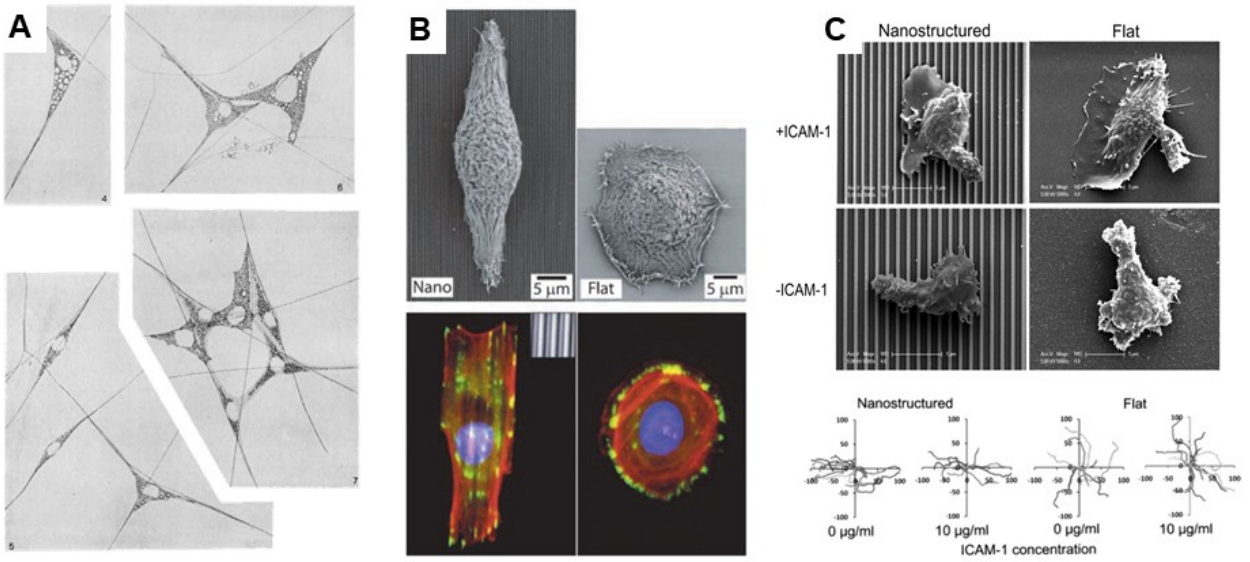

Figure 16: Different examples of in vitro contact guidance. *A: chicken embryonic cells plated over spider webs (Harrison R G et al. Os Zoöl Lab Yale 1911). Epithelial cells plated on top on silicon nanogrooves (Bettinger et al. Angew Chem. 2009). T cells on silicon nanogrooves under confinement of an agarose pad (Keon Woo Kwon et al. J Immunol 2012)*

the grooves, orienting cell migration (Driscoll et al., 2014). Similarly, when plated on a microperforated film, actin forms rings around the perforation in what appears to be both formin and Arp2/3-driven polymerization (Jasnin et al., 2016). These cues are sufficient to drive protrusions or the direction of the whole cell. Proposed mechanisms include membrane curvature sensing proteins or an effect of cortical flows stopped by the topology.

The effects of surface nanogrooves in stable bleb migration are yet unexplored. The mechanisms of biasing filopodia and actin polymerization could not apply to blebs. Blebs do not normally nucleate in the cell's bottom plane and are not induced by actin polymerization. However, grooves could stabilize blebs retracting perpendicularly, guide as rails the protrusion of blebs parallel to grooves, or just change cortex organization in blebs. A less common phenomenon is **“perpendicular” or “inverted” contact guidance**, where cells move or grow perpendicularly to grooves. This effect has only been reported in neurons so far, like small inhibitory cerebellar interneurons or central nervous system neuroblasts from rodents (Hekmat et al., 1989; I. Nagata et al., 1993; Isao Nagata et al., 1993). The mechanism is still not elucidated but could play a relevant role in neuronal development.

Cell shape and local membrane topology have further implications on cell behavior, modulating membrane signaling, regardless of whether the cell shape is produced by an external constraint (surface topology, confinement) or by the cellular forces (cytoskeleton organization). Curvature can be sensed by proteins, which can, in turn, provide mechanical feedback to maintain the curvature or enhance it. Curvature sensing proteins such as septins, clathrins, ESCRT, and BAR **proteins can discriminate between degrees of curvature** (McMahon and Boucrot, 2015). Transmembrane proteins, depending on the shapes of their transmembrane domains, can have lower free energy in particular membrane conformations. Similarly, **membrane lipids can be divided** into three groups **depending on their curvature preference**: conical lipids (phosphatidylinositol), inverted conical lipids (phosphatidylethanolamine), and cylindrical lipids (phosphatidylcholine).

The local ratio of surface to volume could modulate membrane-based signaling pathways (Giese et al., 2018; Haupt and Minc, 2018). Cytoskeletal signaling activity is composed of membrane-based and some soluble effectors. Therefore, if some activity is confined to the membrane, there will be a signal gradient towards the cell's interior. In parts of the cell **where the surface to volume ratio is very high, as in membrane tubes or thin**

laminar sheets, the activity will be higher. This was reproduced in a synthetic system composed of a membrane-bound kinase and a soluble phosphatase (Meyers et al., 2006). Experiments in cells suggested that the transient increases of enzymatic products could be sustained by curvature or cytoskeletal organization, like changing cell shape (Rangamani et al., 2013; Schmick and Bastiaens, 2014). In *D. discoideum*, **the three-dimensional shape of cells changes the PIP_3 wave dynamics,** highlighting the importance of membrane topology in reaction-diffusion signaling. For these reasons, shape and signaling are likely to go hand by hand during morphogenetic processes. Signaling and shape can build positive feedback: Turing processes and a particular geometry enable robust morphogenesis *in vitro* lunch branching (Menshykau et al., 2014).

The cortex beneath the membrane imposes diffusion barriers to the lipids or proteins embedded in the bilayer. This fact has been well established in both in reconstituted systems (Heinemann et al., 2013) and in cells using FCS (Andrade et al., 2015). The **leading edge of keratocytes also constitutes a diffusion barrier** for lipids, that remain immobile in the distal region (Weisswange et al., 2005), and for actin nucleators (Mehidi et al., 2019). Akihiro Kusumi proposed in 2005 an updated model for membrane diffusion called "**hop diffusion**" or "pickets-and-fences diffusion" where lipids and membrane-embedded elements do not have a typical Brownian diffusion. Locally, they have Brownian dynamics, but they are confined to a small membrane domain. The possibility to "hop" to another domain is low and is defined by a certain k_{hop}. Cortical perturbations dramatically change the diffusive behavior of phospholipids and proteins. Less is known about the diffusion barriers that the cortex can impose on cytoplasmic elements. The **combination of membrane pinching and cortex can provide an effective diffusion barrier in blebs**. In confined A375 cells, Erk activity is concentrated in the bleb due to a diffusion barrier at the bleb neck (Logue et al., 2015).

Contribution of active mechanical processes to cell polarization

Actin polymerization alone cannot explain some cell- and tissue-scale active mechanical processes, often this depends on myosin motors. Mechanical or "**mechanochemical**" processes also participate in polarity (Howard et al., 2011). In 3T3 fibroblasts, mechanical stiffness mediates positive feedback through small GTPases, so that substrate contact sites such as **lamellipodia are sustained when they encounter strong mechanical**

feedback, a phenomenon called durotaxis (Lo et al., 2000). Local, periodic, and anisotropic external cues can direct cell motion in ways different from contact guidance, such as by coupling better the forces from retrograde flow to the substrate in a particular direction, due to topological ratchets. In cells migrating in 3D collagen networks, clathrin gives a concave topology to membranes to pinch collagen fibers. This creates transient attachment points to help cells exert forces on the fibers (Elkhatib et al., 2017), and a gradient of fiber density in the matrix or binding sites in the cell could mediate a response to a gradient. Interestingly, a recent study in leukocytes in microfabricated channels showed that T cells could transmit forces in the complete absence of transmembrane force coupling. Wavy channels and a textured surface can create retrograde shear forces that are sufficient to drive the cell forwards even in the absence of talins (Reversat et al., 2020).

When thinking about mechanical and physical processes in cell migration, our physical intuition built by everyday events can be misleading. **Inertia is negligible at the scale of cells compared to viscous forces, so cells need to produce continued forces to move** (Purcell, 1977). As a result, **laminar flows are frequent**, characterized by smooth, constant fluid motion. Another big conceptual difference between the human-scale and the cell-scale world is the importance of thermal energy. Brownian motion is the random motion of particles suspended in a fluid resulting from their collision with the fast-moving molecules in the fluid. The kinetic energy of the particles in a fluid can be defined as the fluid's thermal energy, which plays an important role at the scales of proteins and signaling responses inside the cell. We can use three dimensionless numbers to understand a living syetem: the **Péclet number** (relative importance of thermal diffusion and active transport, defined to be the ratio of the rate of advection by the flow to the rate of diffusion driven by a gradient: $Pe = \frac{diffusion\ timescale}{advection\ timescale} = \frac{L^2/D}{L/v}$), the **Reynolds number** (relative importance of inertial versus viscous forces in a fluid), and the $\boldsymbol{k_BT}$ **equivalence** (relative importance of the energy of a given bond or process compared to the thermal energy).

We can compare their respective length scales to understand how active forces produced by cytoskeletal motors can complement passive transport to create gradients. **the diffusion coefficient** of the molecules involved determines the typical **lengthscale of a reaction-diffusion process**. The Stokes-Einstein equation describes the diffusion of spherical particles through a liquid with low Reynolds number: $D = k_BT/6\pi\eta r$, where k_BT is the thermal energy, and $6\pi\eta r$ is the frictional coefficient. The diffusion coefficient

D $(\mu m^2/s)$ is inversely proportional to the radius of the particle r and the viscosity of the medium η $(Pa \cdot s)$. The average distance traveled by a particle diffusing in 3 dimensions is proportional to $\sqrt{6Dt}$, where D is the diffusion coefficient $(\mu m^2/s)$ and t, time (Berg, 1993). The intracellular diffusion coefficient of a small protein such as GFP is about 20 $\mu m^2/s$ (Gura Sadovsky et al., 2017). For a bacterial cell, which is about 1 μm in size, diffusion is an efficient process that can transport small and large molecules in seconds or milliseconds across the cell. However, for greater distances, for larger proteins, or in more viscous or crowded environments, the travel time becomes too large to be useful in signaling processes. The typical motor speed is 0.1-1$\mu m/s$ and cortical flows can reach speeds of 0.05-0.5$\mu m/s$, which surpasses the transport capacity of diffusion in distances more than a few micrometers. This reasoning explains why protein transport in bacteria occurs largely in the absence of motors but it is driven by motors in eukaryotes**. In large cells** such as neurons, continuous **active transport becomes essential**.

Bacterial cells are diffusion-dominated, with a small Péclet number. However, at the scale of mammalian cells, systems are often **dominated by a low Reynolds number** (dominated by viscous forces), a **high Péclet number** (dominated by active transport), and **binding energies or chemical potentials higher but of the same order of magnitude of $k_B T$**, thermal energy (Milo and Phillips, 2016). Since cell migration is a result of molecular processes, it is essential to take this into account while thinking about problems related to cell migration. Therefore, we find that many morphogenetic processes in mammalian tissues or even within single cells are driven by a mix of chemical and mechanical processes and depend on active transport. **Active transport mechanisms include transport by motors, endocytosis, or cortical flows**, which can result in different types of pattern formation (Howard et al., 2011) depending on the molecular mechanism:

- If cargoes are randomly hopping on and off in a random network, we will have active diffusion. The mathematical description is the same as for thermal diffusion (aka Brownian motion) changing the diffusion coefficient D by v, the advection velocity. The mean distance traveled by a particle in a 2-dimensional array of filament will be $x = \sqrt{4vt}$.
- If the motors are unidirectional and filaments organize so that the transport always occurs in the same direction, we will see an advection-diffusion pattern. There will be an exponential decay in the concentration of the cargo given by a length scale $\lambda = D / v$. This decay describes the localization of myosin IIA along stereocilia,

the localization of dynein motors in reconstituted microtubule asters, and the actomyosin gradient in polarized blebbing cells.

- The material properties of the cortex can also set the lengthscale for pattern formations. The actomyosin cortex is a viscoelastic material: in short time scales, it behaves as an elastic material, but in long timescales, it behaves as a viscous fluid. The viscosity and the friction coefficient define the material properties of the fluid. Motors will create active stresses that will lead to velocity gradients. The ratio between the two will set a particular timescale for the velocity gradient $\lambda = \eta / \gamma$. This mechanism is used by cortical flows to polarize the *C. elegans* embryo. They do so by bringing to one pole partitioning defective (PAR) proteins that regulate contraction. I will describe contractility-driven symmetry breaking in detail below

Role of contractility in polarity switches

The cell cortex can be thought of as an active gel layer beneath the membrane composed of actin filaments linked by crosslinkers and motors, generating active stresses (Jülicher et al., 2007). Cells modify their cortex's material properties in response to cell cycle, extracellular cues, confinement, spreading, or immune synapsis formation. For example, mitotic cells round up and increase cortical contractility, which can be due to increased motor activity or network connectivity (Belmonte et al., 2017; Bendix et al., 2008). **Notably, many cellular events are orchestrated by gradients in actomyosin contractility to generate and sustain large-scale cortical flows,** such as cytokinetic ring formation in mitosis. Likewise, cortical flows can break symmetry and establish polarity, participating in locomotion, embryogenesis, and signaling (Bray and White, 1988).

Actomyosin has an inherently unstable nature, which is evident by how myosin localizes in cells, often restricted to cortical foci. Theoretical work has proposed that these instabilities are inevitable at high contractility regimes (Bois et al., 2011). Early evidence showed the establishment of cortical periodic oscillatory activity in lymphoblasts in the absence of microtubules in cells treated with nocodazole (Bornens et al., 1989). It is well known that cells treated with nocodazole trigger contractility via the GEF-H1 RhoA pathway (Chang et al., 2008). There are detailed experimental descriptions of the pulsatile behavior of actomyosin (Maître et al., 2015; Munro et al., 2004; Rauzi et al., 2010) and that this **pulsatile behavior leads to actin patterning** (Hannezo et al., 2015).

The pulsatile behavior depends on additional elements such as actin turnover, cortex connectivity, and RhoA activation (Coravos et al., 2017; Yu et al., 2018). The shape of the actin pattern depends on cortex properties such as the active tension, hydrodynamic length, and Péclet number – if a regulator of contractility is introduced in the model (Bois et al., 2011; Nishikawa et al., 2017).

Early **symmetry breaking in the *C. elegans* embryo occurs due to actomyosin contractility,** which sets the plane of the first asymmetric division in its embryonic development. The asymmetry of myosin motors in the anterior and posterior sides produce anisotropic cortical stresses that produce advection flows (Mayer et al., 2010), carrying out polarity factors (PAR proteins) to one side and defining the anterior-posterior axis (Cowan and Hyman, 2007; Goehring et al., 2011; Munro et al., 2004; Munro and Bowerman, 2009; Salbreux et al., 2012). Therefore, passive advective transport in an active and flowing material is enough to produce gradients to polarize the cell and establish a gradient. The PAR polarity proteins constitute a reaction-diffusion system with multistable properties: in the absence of flows, the embryo remains unpolarized until advection triggers the PAR pattern formation. In this system, actomyosin and RhoA form a positive feedback loop: RhoA accumulates in regions with converging actomyosin flow, and myosin accumulation increases the velocity gradient. However, an **independent "pacemaker**" prevents total collapse. RhoA activity is not only controlled by the accumulation due to convergent flows but has another layer of activation, which is independent of myosin. The traveling waves of RhoA activity homogenize the unstable cortex to prevent its collapse (Nishikawa et al., 2017).

Conceptually, cytoskeleton polarity regulation can be described with **positive and negative feedback**, resulting in an **excitable system,** as described earlier (Figure 17). We can draw parallels between the regulation of chemical signaling networks and mechanical cytoskeletal networks, even if their nature is fundamentally different. Due to the organization of actin networks, any perturbation on the cytoskeleton can potentially create asymmetries (Cramer, 2010; Mullins, 2010). First, actomyosin shows cooperative effects in assembly or force generation. For example, **the WAVE complex assembles cooperatively** on the membrane (Pipathsouk et al., 2019), **myosin minifilaments have positive feedback** induced by force due in part to its **catch-bond behavior on actin**, and actin networks itself are mechanosensing since they adapt their behavior and force generation on the external load applied *in vivo* or *in vitro* (Bieling et al., 2016; Oakes et al., 2018). Secondly, the **actin architecture** is not homogeneous throughout the cell: it consists of branched dendritic networks on the sides and bundles on the ventral part,

which have a particular orientation. Dendritic branched networks are a poor substrate for myosin motors, which preferably bind on linear bundled networks. Myosin, in return, promotes bundling, closing a positive feedback loop. For this reason, even if a homogenous is applied onto the actin cytoskeleton, the consequences are not going to be the same for all parts of the cell. Bundles, for example, are intrinsically anisotropic because they will resist force in one direction. It has been proposed, for instance, that the reorientation of bundles in the ventral part of cells is a crucial step needed for break symmetry before migration (Cramer, 2010). Third, the actin cytoskeleton is a **viscoelastic material** whose properties can be changed by the state of the cell (e.g., adding crosslinkers to increase network connectivity or myosin motors to increase contractility). Due to the viscous part of the behavior, a deformation will not propagate homogenously in time and space. Any contractile force will have a more significant effect locally, stretching the network in a non-homogenous fashion and creating areas denser than others.

Models often describe transitions between cortical states as local minima in the free energy landscapes of the system. The energy to go from one state to another come from **stochastic fluctuations that are increased in amplitude with high contractility** (Kozlov and Mogilner, 2007). Depending on their properties, they will transition from a homogeneous to a polarized state and display different stability levels (Gucht and Sykes, 2009). Briefly, theoretical works attempt to describe the cortex with a set of nonlinear differential equations and then perform **linear stability analysis** to find particular stationary or quasistationary solutions. This approach was used to describe stochastic switches that drive cells from one state to another (e.g., from a non-polarized non-migratory state to a polarized migratory state). Perhaps counterintuitively, **stochasticity enhances gradient-dependent polarization of excitable systems**, resulting in a more robust behavior and a faster transition towards a new equilibrium (Lawson et al., 2013; Xu et al., 2019). For example, Cdc42 gradients in budding yeast arise from a positive feedback loop in which a stochastic increase in the local concentration of activated Cdc42 triggers a positive feedback loop between Cdc42 and actin polymerization (Wedlich-Soldner et al., 2003).

Steady-state solutions will depend on the molecular state of the cell. Interestingly, changing **parameters often yield bistable and non-monotonic responses (**e.g., contractility and connectivity). Whereas increased actomyosin contractility can provide the instabilities necessary to break the homogenous state and trigger cell polarity and locomotion (Tjhung et al., 2012; Yam et al., 2007), too high contractility can cause motors

to ‘sequester’ actin in contractile bundles and make calls so contractile that they will not be able to polarize (Lomakin et al., 2015). Asymmetrical cortical relaxation can also provide a cue to break symmetry (Gucht and Sykes, 2009). Similar conclusions arise from agent-based simulations where **middle-ground network connectivity and motor activity provide the highest network retraction** (Belmonte et al., 2017).

As in morphogenesis, **cell migration can rely on stochastic switches and contractility to break symmetry** (Bergert et al., 2015; Blaser et al., 2006; Callan-Jones and Voituriez, 2016; Graziano et al., 2019; Liu et al., 2015; Ruprecht et al., 2015; Yam et al., 2007). Referring to **symmetry breaking** in migrating cells **is practically equivalent to generating a cortical flow**. Active gel theory predicts that at low contractility, the stochastic perturbations are damped by the cortex, but they can be amplified at high contractility. These fluctuations in cortical density or myosin activity can be due to random events or inhomogeneities in the activators of myosin, cortical density, or ruptures in the cortex (blebs).

Under geometrical confinement, the **contractility increase transforms an initially homogeneous cortex into a polarized steady-state with a stable gradient of actomyosin and retrograde cortical flows**. The increase of contractility upon confinement and the switch to polarize blebbing migration has been identified in amoeba, choanoflagellates, developing tissues, immortalized cell lines, and primary cultures. The polarity is maintained thanks to positive feedback between myosin accumulation and convergent cortical flows. Cortical flows reinforce density gradients of molecules binding to the cortex, particularly myosin II, thereby strengthening the contractility gradients that drive these cortical flows (Figure 17, Figure 18). Contractility induced by LPA addition is sufficient to polarize PGCs, but confinement is needed to couple cortical flows to the substrate and migrate. Confinement itself also increases contractility due to **ROCK activation** by a cPLA2-mediated and Ca^{2+}-mediated signaling response (Lomakin et al., 2020; Venturini et al., 2020). Stable-bleb cell polarization is rapidly lost upon treatment with Latrunculin A (G-actin sequestering drug), Jasplakinolide (interferes with cortex turnover), or Blebbistatin (the myosin II inhibitor), indicating that **contractility and actin turnover are essential to maintain cell polarity** in this regime (Liu et al., 2015; Ruprecht et al., 2015). In contrast, inhibition of central cell polarity signaling molecules such as Cdc42 (ML-141 compound) or PI3Kinase (L-294002 compound) did not affect stable-bleb cell polarization in zebrafish PGCs (progenitor germ cells) (Ruprecht et al., 2015).

Interestingly, these cellular pathways triggered by confinement are similar to those involved in the chemotactic signal transduction network (**cPLA2, calcium**). cPLA2 and **PI3K/PTEN** pathways have been reported to act in parallel to mediate chemotaxis in amoeba and leukocytes (Chen et al., 2007). In *D. discoideum,* the loss of GPCR subunits or the inhibition of multiple signal transduction modes yields an attenuated response to mechanical stimuli in the form of sheer stress (Artemenko et al., 2016). Another study in *D. discoideum* reports that the response to a mechanical load is instead mediated by mechanosensitive **Piezo channels** (Srivastava et al., 2020). In both cases, a spike in the intracellular calcium levels was necessary, as in HeLa, but GPCRs and Piezo channels were not involved in HeLa cells' confinement response.

Contribution of cortical flows to the polarity of migratory cells

Cortical flows not only participate in the establishment of polarity but also maintain it. Besides, they provide a constant network treadmilling to exert forces on the substrate, also known as retrograde flow (Hawkins et al., 2011), can define shapes (Carvalho et al., 2013), and the areas of actin assembly and disassembly (Wilson et al., 2010). **Retrograde flows** appear as a broadly **conserved feature** in animal cell migration and are **shared between focal adhesion and friction-based migration**. However, in the first one, the flow is primarily driven by actomyosin polymerization and treadmilling, and in the latter, it is primarily driven by actomyosin network contraction on the rear (**Figure 18**). The migration of keratocytes, the best-studied model system for adhesion-based migration, requires Arp2/3 nucleators on the cell front and specific adhesive structures such as focal adhesions to transmit the forces to the substrate.

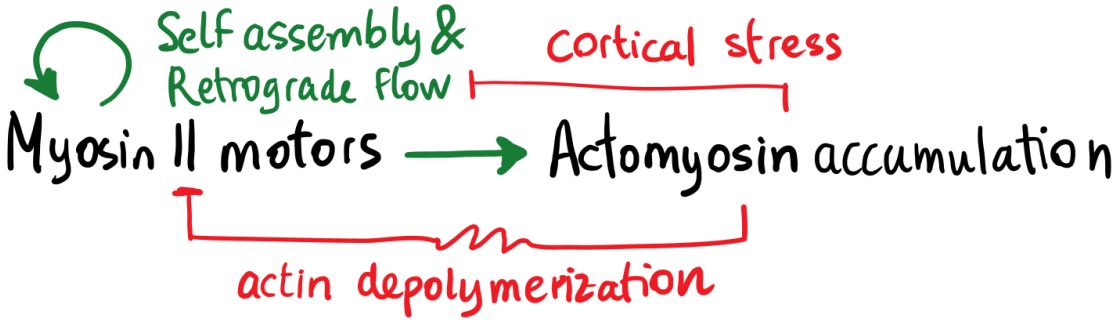

Figure 17: Conceptual model to explain some positive and negative feedback loops involved in actomyosin contraction. *Cell polarity can be maintained by a positive feedback loop between cortical contractility gradients and convergent cortical flows. Furthermore, myosin motors have an assembly process in minifilaments, which could be cooperative. Convergent cortical flows, in turn, accumulate actomyosin. However, areas with high accumulation disassemble actin due to network crushing. Myosin motors can stall at high stress areas.*

Friction-free or **amoeboid** migrating cells lack focal adhesions. Stable-bleb migrating cells have a **uropod** at the back, typical for cells like neutrophils, and a bleb at the front, driven by intracellular pressure. **A striking asymmetry in myosin localization**, accumulated at the rear, **causes a cell-scale retrograde flow**. The force transmission remains unclear but could be mediated by transient non-specific interaction between the cell membrane and the substrate. Despite differences in the shape and molecular mechanisms, they have in common the establishment of a rearward or retrograde flow that provides the force assymetry necessary for cell locomotion (Callan-Jones and Voituriez, 2016).

This model predicts that for any migratory cell in general, the faster the retrograde flow is, the steeper the gradient of cortex-bound molecules should be. Models describe cell trajectories as paths with a speed and a persistence length, which quantifies cells' ability to maintain their direction of motion as they move. If the propulsion force and the cell speed are proportional to the retrograde flow, and if the retrograde flow carries polarity cues such as myosin or ezrin, one could expect a link between persistence and speed. Experimental data showed that, indeed, that **persistence and speed are linked, and one cannot be tuned without the other**. To move faster, the cell will need to speed up the retrograde flow, which will create a steeper gradient of polarity cues, making it harder to depolarize. The '**universal coupling between cell speed and persistence' (UCSP) model** described the behavior of many cell types and most of the observed migration

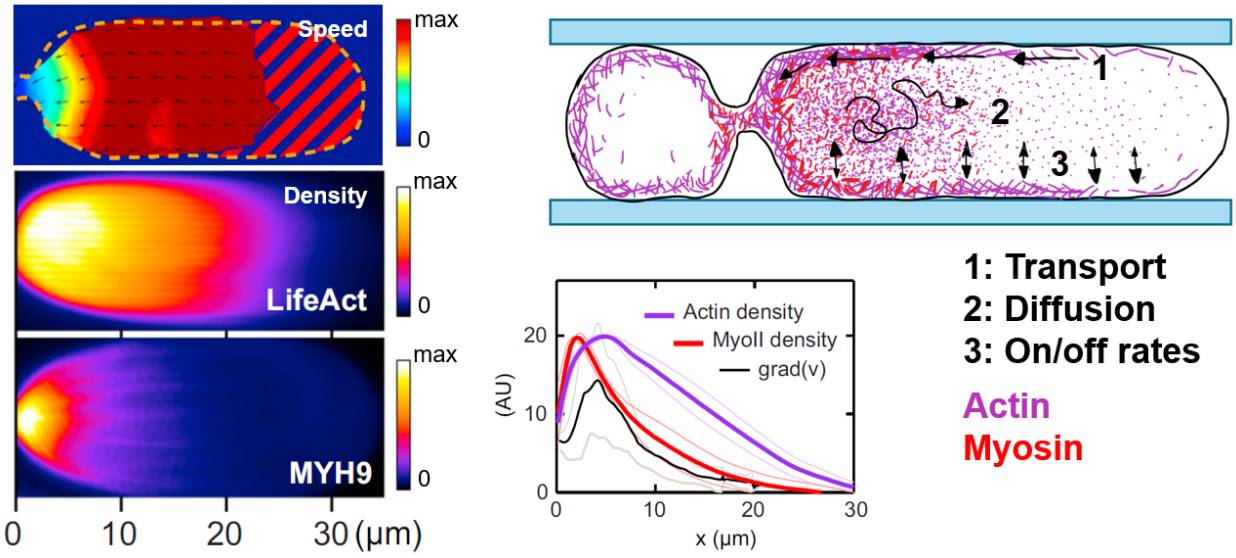

Figure 18. Advection-diffusion profiles in stable bleb cells. *Left: spatial average of cortical flow speed, and density profiles of actin (lifeact-mCherry) and non-muscle myosin II (MYH9-GFP) in stable bles. These values are plotted as a function of the bleb longitudinal axis with grad(v), the spatial change in flow velocity. We can observe exponential decay profile for myosin. Adapted from Liu et al. 2015. Top right: Schematic representation of the three events driving the steady-state density profile or cortex-bound molecules.*

behaviors in cells robustly, by changing the affinity of polarity cues to actin (Maiuri et al., 2015, 2012). This model is an elegant example of how molecular dynamics could influence a cell's behavior and predict the outcome of fundamentally stochastic processes. However, if there are universal molecular mechanisms mediating the relation between persistence and retrograde flow speed remains unknown.

Some results suggest that a **gradient of membrane-actin mediators could be the molecular mechanism linking speed and persistence** (Bisaria et al., 2020; Olguin-Olguin et al., 2021). Researchers have used probes to track the actin in close contact with the membrane and found that even in friction-based migrating cells such as HUVEC, HeLa, or RPE-1, the density of membrane-proximal F-actin is low in the front and high in the back. The **gradient of membrane-proximal actin is a common feature between mesenchymal and amoeboid cells, and can me established by cofilin activity**. Furthermore, spontaneous local membrane protrusions only form following local decreases in membrane-proximal F-actin density, and global Rac1 activation by membrane recruitment of TIAM1 produced protrusions only in segments of the membrane with low proximal F-actin. These results argue that actin-membrane interaction at the leading edge can be the determinant of persistent migration.

It is well established that local membrane-cortex detachment produces blebs, and recent studies show that it might also be the case for actin-rich protrusions. Actin-rich protrusions are believed to instead depend on a balance between actin protrusive forces and tethering, following the Brownian ratchet model (Peskin et al., 1993). Recent studies suggest that “mechanical” membrane-cortex detachment by intracellular pressure or “chemical” by PIP_3 signaling and FERM/ezrin disengagement could cooperate to maintain a persistent protrusive front in adhesion-based migration as well (Welf et al., 2020, 2019). By precisely monitoring ezrin, actin, and membrane dynamics in melanoma cells, they showed **that local depletion of membrane cortex links is an essential step in initiating both pressure-based (blebs) and actin-based protrusions (lamellipodia, filopodia)**. This highlights the importance of the molecular mechanisms at the leading edge in controlling cell migration. My Ph. D. thesis's primary focus is on the interaction of actin and membrane at the bleb front and how this interaction governs protrusion persistence. Over the next chapter, we will describe the properties of an assembling actin network and explain how molecular and physical mechanisms cooperate at the leading edge to produce protrusions.

Box 1: Estimation of protein gradients in stable blebs

We can make a simple estimation of the gradients produced by retrograde flow. In diffusion, the change in concentration of a molecule is a function of the diffusion coefficient (eq. 5), and in unidirectional transport, it will be a function of the velocity (eq. 6). Gradients of molecules in cells with a stable cortical flow can be described with simple advection-diffusion equations that combine these two like in eq. 7 (Berg, 1993).

$$(Eq.5)\quad Diffusion\colon \frac{\mathrm{d}C}{\mathrm{d}t} = D\frac{\mathrm{d}^2C}{\mathrm{d}x^2} \qquad (Eq.6)\quad Advection\colon \frac{\mathrm{d}C}{\mathrm{d}t} = -v_x\frac{\mathrm{d}C}{\mathrm{d}x}$$

$$(Eq.7)\quad Advection\text{-}diffusion\colon \frac{\mathrm{d}C}{\mathrm{d}t} = D\frac{\mathrm{d}^2C}{\mathrm{d}x^2} - v_x\frac{\mathrm{d}C}{\mathrm{d}x}$$

Let's consider a molecule that can bind or unbind the cortex with certain rates, $k_{on}(s^{-1})$ for binding and $k_{off}(s^{-1})$ for unbinding. If it is bound to the cortex, the molecule will be transported by advection with a certain velocity $v\ (\mu m/s)$ and if it is free in the cytosol it will move by thermal diffusion with a diffusion coefficient $D\ (\mu m^2/s)$. The change in the concentration of free and bound molecules can be described as follows:

$$(Eq.8)\quad \frac{\mathrm{d}C_{Free}}{\mathrm{d}t} = D\frac{\mathrm{d}^2C_{Free}}{\mathrm{d}x^2} + k_{Off}C_{Bound} - k_{On}C_{Free} \qquad (Eq.9)\quad \frac{\mathrm{d}C_{Bound}}{\mathrm{d}t} = v\frac{\mathrm{d}C_{Bound}}{\mathrm{d}x} - k_{Off}C_{Bound} + k_{On}C_{Free}$$

We assume steady-state and propose as possible solutions $C_{Free}(x) = C_{Free}(0)\,\mathrm{e}^{-\frac{x}{\lambda}}$ or analogously $C_{Bound}(x) = C_{Bound}(0)\mathrm{e}^{-\frac{x}{\lambda}}$. We then proceed to find out how the decay length $\lambda\ (\mu m)$ can be described in terms of $D,\ v,\ k_{on},\ k_{off}$. Substituting this in equation 8 and 9 yields the description of the steady-state, which follows an exponential decay. Advection-diffusion systems can be intuitively understood with parameters representing the relative importance of transport versus diffusion. We can consider a **"diffused length"** $l_d = \sqrt{\frac{D}{K_{On}}}$ and a **"transported length"** $l_t = \frac{v}{K_{Off}}$. These are the average distance traveled by a molecule while diffusing or while being transported by the cortical flow, respectively. We can then express lambda in terms of these lengths (eq. 12) and explore how the decay length changes with the relative importance of diffusion or transport. Similarly, we can define a Péclet-like number (dimensionless) for our system to determine if it is diffusion or transport-dominated (eq. 13).

$$(Eq.12)\quad \lambda = l_d\left(\frac{l_d}{2l_t} + \sqrt{1 + \left(\frac{l_d}{2l_t}\right)^2}\right) \qquad (Eq.13)\quad Pe = \frac{transported\ length}{diffused\ length} = \frac{l_t}{l_d} = \frac{v/k_{Off}}{\sqrt{D/k_{On}}}$$

We can refer to the literature to find values for motor binding rates $K_{On} = 0.2\ s^{-1}$ (Stam et al., 2015), motor unbinding rates $K_{On} = 1.71 - 0.03\ s^{-1}$ depending on the force load (Guo and Guilford, 2006; Stam et al., 2015), diffusion coefficients $D = 0.8\ s/\mu m^2$ (Uehara et al., 2010), and cortical flow speeds in **HeLa cells migrate with a stable bleb** (Liu et al., 2015).

This yields a system dominated by transport and bound myosin species at high force load ($Pe = \frac{transported\ length}{diffused\ length} \approx 25$), and small decay lengths ($\lambda \approx 2.5\ \mu m$). Taken reasonable values for the constants, this **simple model can predict that in the transition from a related to a tensed network** (increasing load), the system will transition from diffused to bound-dominated. Nevertheless, we are omitting some important features such as the fact that the cortical flow is not uniform throughout the cell and also follows a gradient, or that the myosin molecules or other cortex-bound molecules might have their assembly process carrying non-linear dynamics.

Chapter 5: Assembly and dynamics of actin networks

Conceptualization: continuum models versus agent-based simulations

onceptually, one can make theoretical models or approximations of the actomyosin cortex by **continuum equations**, where the cortex is modeled as a continuous mass, or by **agent-based simulations**. Initially, theoretical models related to cell motility focused on the molecular dynamics observed from bottom-up experiments such as actin polymerization, or on a purely mechanical point of view in tissues and cells. Nowadays, experimental methods have been able to link better the two aspects, and so have theoretical models done too.

Random walks are often used as the mathematical model describing the trajectories of **migrating cells** (persistent or correlated random walks) or diffusing **molecules** (isotropic random walks) (Berg, 1993; Codling et al., 2008). The theory of random walks was first developed by Thorvald N. Thiele (1880) and Louis Bachelier (1900). Albert Einstein (in one of his 1905 papers) and Marian Smoluchowski (1906) used statistical physics to write diffusion equations for Brownian particles and extract the **diffusion coefficient**. Random walks come from a microscopic theory where we consider only agents moving in a lattice, but we obtain the diffusion equation by taking the continuum limit. In isotropic random walks – like particles in solution – we consider that the molecules move in any direction with the same probability.

Perturbation theory is a mathematical tool widely used in physics and biophysical modeling while describing cortical contractility switches between steady states. We consider a steady-state, on the top of which we introduce small perturbations, which allows us to investigate if the steady-state is stable. If this is not the case, a minimal **perturbation** can **drive** the system **out of the steady-state**. This approach has been used, for example, to describe the tendency of cells to polarize at increasing contractility, in the context of stable bleb migration (Liu et al., 2015; Ruprecht et al., 2015). In such models, actomyosin is considered as an active viscoelastic fluid.

Another relevant concept for actomyosin network modeling is percolation. Percolation models represent lattices of different geometries where the nodes can be connected with the nearest neighbors with a given probability p. We define network properties as a

function of *p*: conductivity, mean cluster size, and percolation threshold, which is the probability that a path connects opposite boundaries of the system. For square 2D lattices, the percolation threshold is p_c = 0.5. Percolation-based models are the simplest models that can yield a **first-order phase transition**. As we vary the percolation probability p slowly, we find an abrupt increase in the probability of a **large cluster** with the size of the system. However, if $p \approx> p_c$ we find that the shortest path across our system will meander a lot and is much longer than the size of our system *L*. As p increases, the length of the shortest path will be approximately the same as *L*. This change in conductivity represents another **phase transition, of second-order, from a "flexible" to a "solid"** cluster (Alvarado et al., 2017; Stauffer et al., 1994).

Some actomyosin models are based on classical conductivity percolation theory and try to predict the observed regimes of actomyosin networks as a function of network connectivity and motor activity: **active solutions, stressed gels, or global and local contraction** events (**Figure 19**). However, the real picture is rather complex, as these two parameters are intertwined. Stresses due to myosin activity can unbind some crosslinkers with a slip-bond behavior, and myosins can sever actin filaments during contraction (Vogel et al., 2013). At the same time, myosins are also crosslinkers and can crosslink and align the network, affecting the percolation threshold. Some authors found that reconstituted networks *in vitro* display a robust near-critical behavior at large ranges of motor and crosslinker concentrations, which might be explained by the antagonistic effects of molecular motors on actin networks (Alvarado et al., 2013).

Moreover, the **ordering of the actin filaments can affect percolation** and force transduction. If there is a preferred orientation field, the conductivity will increase in the

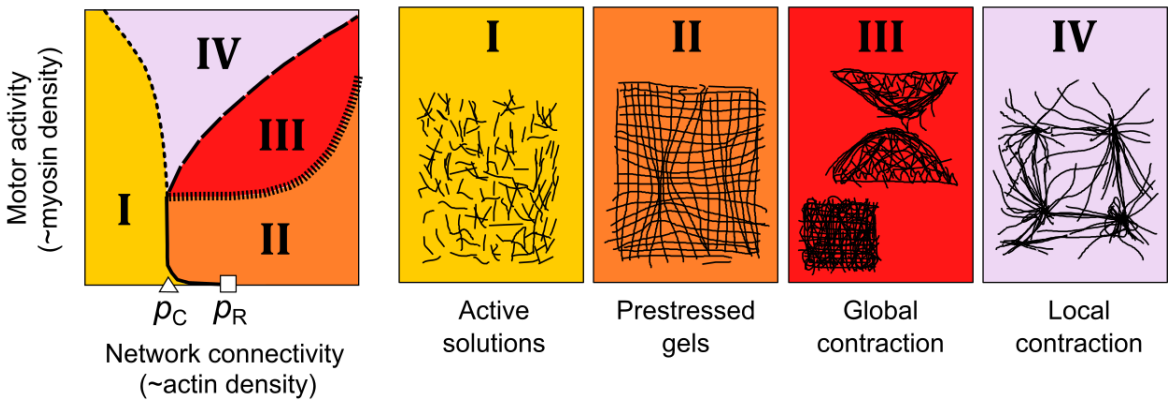

Figure 19: Active solutions (I) exhibit fluid-like motions. *Prestressed gels (II) maintain contractile stresses. In global contraction (III), motors pull the network on system length scales, resulting in compaction of unanchored gels, or breaking of anchored gels. In local contraction (IV), motors compact gels into smaller clusters. Adapted from Alvarado et al., 2017.*

alignment direction and decrease perpendicularly. This bias might be significant in cells adopting a specific membrane configuration or spatial constraint. In confined configurations, and in the presence of actin bundles, **filament length and stiffness will increase** (Claessens et al., 2006), biasing actin filaments to adopt the configurations with **lower curvature** (Koudehi et al., 2019). Force percolation of contractile gels is central to my Ph.D. work, but given the complexity and extension of this field, we will now focus on experimental methods rather than theory (Alvarado et al., 2017, 2013; Tan et al., 2018).

Lastly, some authors chose purely agent-based models to understand the behavior of the cytoskeleton. These are **computationally heavy simulations** that include **realistic force** interactions, **Brownian dynamics,** and **steric hindrance**. Accurate force values, network arrangement, and dynamic behavior can be extracted to predict cell behavior. For example, this approach has been successfully applied to the study of the effect of crosslinkers versus myosin motors in actin network (Belmonte et al., 2017; Ennomani et al., 2016) and the amplification of **actin polymerization forces under a load**, described by experiments and predicted by agent-based modeling (Bieling et al., 2016; Dmitrieff and Nédélec, 2016).

Recapitulating cortex dynamics in vitro

Researchers calculated binding affinities and kinetic parameters of actin-binding proteins from *in vitro* systems, observing the polymerization into filaments and filament dynamics. Assays with more molecules have replicated network properties to allow for force measurements and modeling, which usually go hand-in-hand. Initial *in vitro* work on actin dynamics focused on the biochemistry and discovered the basis of actin polymerization by measuring it in bulk assays, but with the advancement of microscopy and microfluidics, more sophisticated setups allowed to measure elongation rates and polymerization from TIRF (total internal reflection fluorescence) microscopy images (Amann and Pollard, 2001).

Studies have measured the **bending stiffness** of actin filaments as a function of the bundling protein concentration and concluded that the stiffness depends strongly on fascin but not plastin concentration (Claessens et al., 2006). On the molecular dynamics, *in vitro* work showed, for example, that the **localization of actin-binding proteins** depends on actin filament bending (Harris et al., 2020), and that actomyosin networks undergo active **polarity sorting** remodeling actin-myosin networks into asters (Wollrab

et al., 2019). These techniques have also shed light on the relationship of actin filament curvature and branching direction (Risca et al., 2012), detailed formin and Arp2/3 dynamics (Kovar and Pollard, 2004; Suarez et al., 2015), and, in combination with microfluidic techniques, the force sensitivity of Arp2/3-mediated actin filament branches (Pandit et al., 2020; Romet-Lemonne and Jégou, 2013).

For *in vitro* work, the number of purified elements increases the complexity of the experiments considerably. Nevertheless, assays have become more sophisticated, and some of them can reproduce the dynamic aspects of actomyosin networks. A simple but powerful reconstitution of actin and myosin can yield **contractile actomyosin bundles** between beads of cellular length and force scales (5–50 µm and 0.1–5 nN), contracting at 5-20 µm/min (Thoresen et al., 2011). In addition to myosin II, crosslinkers (filamin A) are necessary to recapitulate *in vitro* the **strain stiffening** behavior observed in cells. Moreover, there is a central **role of turnover in active stress** generation in a filament

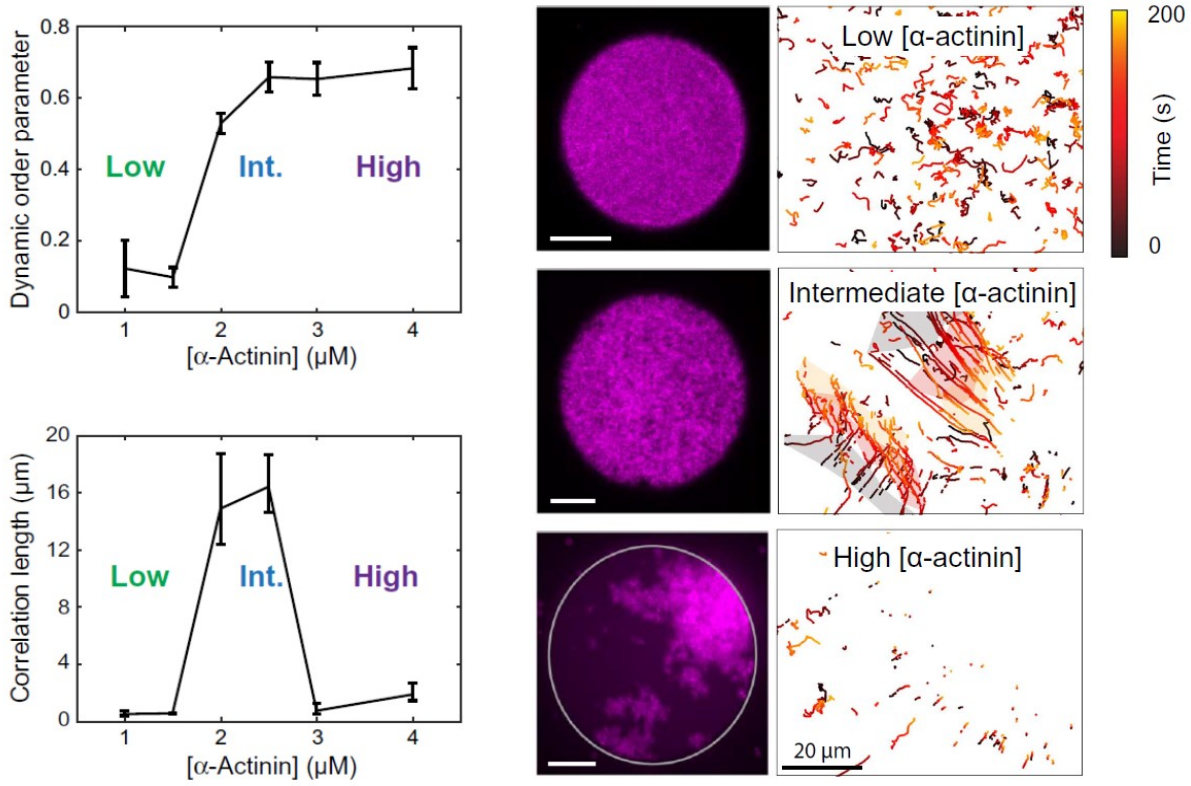

Figure 20: State transition of a reconstituted actin cortex at increasing alpha-actinin concentrations*. The* ***dynamic order parameter*** *quantifies persistence of local velocities, and is calculated as the angular correlation of velocities in coarse-grained boxes, averaged over 50s. The* ***correlation length*** *is the normalized velocity fluctuation correlation function in space, and quantifies the correlation between the velocity of a particle and the average velocity of a box of length r. We find an increase in order and persistence of trajectories from low to intermediate states. At high alpha-actinin, the fluctuations of the velocities are also small that correlations get buried in the noise. Right: Images of the fluorescent probes inserted in the actin network and trajectories over 200s. From Tan et al., 2018.*

network: maximum stress is reached for an optimum ratio of the filament and cross-linker turnover rate (Hiraiwa and Salbreux, 2016). The reconstitution of dynamic steady states from pure elements has been less successful. Contraction events have been reconstituted, which is useful to measure the effects of ATP concentration, ionic strength, or the concentration of specific proteins (Alvarado and Koenderink, 2015), but end up collapsing after a gelation-contraction transition (Bendix et al., 2008). The combination of VCA (short peptide promoting Arp2/3-mediated actin nucleation), Arp2/3 complexes, actin, myosin, and a supported lipid bilayer can provide turnover. This setup yields a minimal cortex with **continuous actin turnover**, in which myosin contraction facilitates **network disassembly** and the formation of **transient contraction foci**. This dynamic cortex undergoes coarsening and redistribution phases, but cannot reconstitute the large-scale flows found in migrating cells (Sonal et al., 2018).

The reconstitutions resembling the most to cellular events are ***Xenopus* egg extracts** in water-in-oil emulsion **droplets**. They contain a mixture of all cell components, to which ATP renewal and additional labeled or unlabeled proteins can be added (Abu Shah et al., 2015). These experiments have unveiled the relationship between molecular events and large scale force transduction events. **Contractile forces can pull and align actin bundles** that adhere to the interface, and in regions with low connectivity, the network keeps some flexibility so that bundles can fluctuate with each other (Bendix et al., 2008). The behavior of loose actin cortices has never been observed in live cells and constitutes one of the original elements in my Ph. D. work.

The *Xenopus* extracts can be polymerized in glass capillaries and molded into a long rod. These rods can exert contractile forces of ~1mN, corresponding to **few tens of pN per bundle**. Homogeneous contractile networks will have a gradient of flow velocity, being lower at the center. Remarkably, the flow and network density analysis allow for the measurement of critical physical parameters such as **compressibility and viscosity**. Mitotic *Xenopus* egg extract droplets confined between two slides exhibit periodic gelation-contraction waves of bulk actin, different from the actin polymerization waves found in migrating cells (Field et al., 2011). Cell cycle-dependent contraction-gelation is due to differences in polymerization but not myosin activity or concentration of crosslinkers. The model to explain the waves is based on percolation theory so that there is a minimal density at which the actin network can crosslink and transduce forces to be carried by the centripetal flow. When a portion of the network is taken to the center, it takes some time to nucleate actin and form another wave.

The transition to a percolated cortex could be reconstituted in *Xenopus* extract droplets covered on the inside with ActA, an actin-binding protein from *L. monocytogenes*. At increasing alpha-actinin concentrations, cortices display different dynamic steady states. At low connectivity, we find disordered flows, and trajectories are not persistent. At intermediate connectivity, we find strong ordered flows with a smaller correlation but similar to the system size. At high connectivity, most of the actin has collapsed into an immobile cap (**Figure 20**) (Tan et al., 2018). As network connectivity increases with low temperature, the symmetry breaking is a temperature-dependent switch. After decreasing from 30 to 20°C, cortices take 10-20 minutes to transition from a homogeneous to a polarized steady state with constant cortical flows. This switch requires myosin activity and sufficient network connectivity, but is microtubule-independent and does not depend on a pre-patterned localization of nucleators or local changes at the interface. Remarkably, the polarized cortices **recapitulate many of the shape and network characteristics of the cortical flows inside a stable bleb of a confined HeLa cell**, and cell-like behavior such as polar force generation and blebbing (Abu Shah and Keren, 2014) (**Figure 21**). Hydrodynamic friction (Darcy friction) can also position the center of the contraction wave in the middle of the droplet (Ierushalmi et al., 2020; Pinot et al., 2012). There is a competition between the hydrodynamic centering force and attractive interactions with the boundary in this system. An increase in size or contraction rate will favor the centering force, and interactions between actin and the boundary will promote symmetry breaking. This centering mechanism is analogous to ooplasm segregation in zebrafish eggs (Ierushalmi and Keren, 2019).

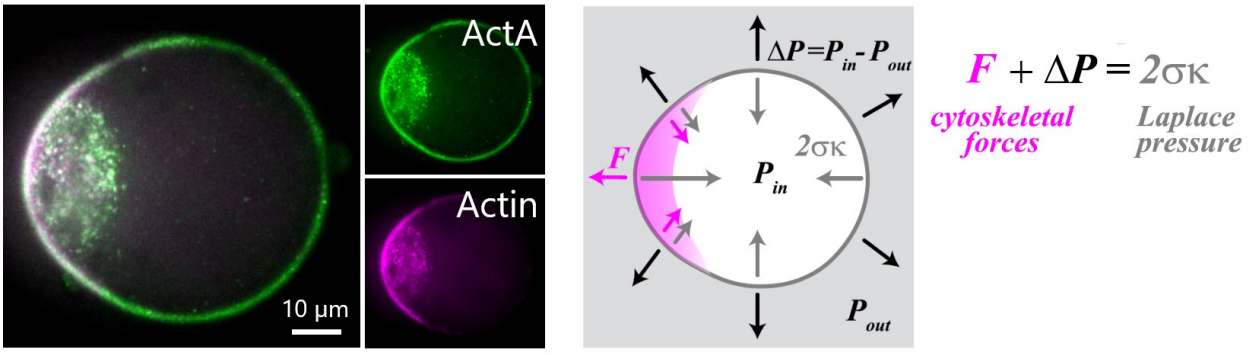

Figure 21: Cell-like behavior of reconstituted* Xenopus *cortices. *Left: localization of the rhodamine-labelled actin and ActA. ActA is conjugated with an amphiphilic bodipy, which targets ActA to the water–oil interface, leading to local activation of Arp2/3 and formation of a cortical actin network. Right: The cortices generate forces at the boundary, as shown by the differences in curvature. The cytoskeletal forces on the inside and the pressure difference are balanced by the surface tension and the local curvature. This shows that the cytoskeleton exerts a net protrusive at the middle of the cap. From Abu Shah and Keren, 2014.*

A more detailed study of flows in this system found that the contraction rate is roughly proportional to the network turnover rate for most conditions and that contraction is homogeneous throughout the system even at different network density. The addition of crosslinkers (alpha-actinin) or actin branches (ActA) leads to deviations in the ratio of contraction versus turnover (Malik-Garbi et al., 2019), and inhomogeneities in the network contraction. This result suggests that the turnover rate and network geometry regulate cortical actin flows.

Cell protrusions are the basis of migration.

The assembly of actin networks occurs at the leading edge of migrating cells, localized in specialized structures called protrusions. Cellular protrusions contain all the elements needed for migration, which suggest that the regulation of migration and the elements are already present in the cortex and do not need transcription and translation in the short term. Fragments of the front of keratocytes or blebbing cells reproduce the shape and dynamics of whole cells (Malawista, 1982; Verkhovsky et al., 1999) and can migrate for a few hours. There are different **cortical protrusions, such as blebs, filopodia, lamellipodia, invadopodia, lobopodia**. (Bodor et al., 2020). These protrusions are filled with actin (but not in the case of blebs) and originate at the cell cortex. In the cell, we also find other actin structures which are not protruding: stress fibers, embedded in a contractile cortical network (Vignaud et al., 2020), nuclear actin (Caridi et al., 2019), transmembrane actin-associated nuclear (TAN) lines (Luxton et al., 2011), and actin used in intracellular transport, or even by intracellular pathogens (Theriot et al., 1992; Welch and Way, 2013). I will compare how actin assembles at the best-studied actin-driven protrusion, the lamellipodium, with the bleb to put our research into context.

The lamellipodium: the quintessential actin-rich cell protrusion

The fish keratocyte is a rather extreme form of cell migration essentially driven by a large lamellipodium at the cell front. Its simplicity and accessibility made it a **classical and well-studied model for cell migration** and shed light on cortex assembly at the cell leading edge (Mogilner et al., 2020). The lamellipodium's front concentrates actin polymerization, where it generates forces pushing the membrane forward and driving lipid flows. The interactions between actin and membrane at the leading edge have been

conceptualized by the Brownian ratchet model (Peskin et al., 1993), and its generalization applied to the lamellipodium leading edge, the elastic Brownian ratchet (Mogilner and Oster, 2003, 1996), which accounts for an intermediate phase of actin-membrane attachment. The more recent **tethered Brownian ratchet** model (Welf et al., 2019) accounts for the role of membrane-actin mediators such as ezrin in allowing protrusion initiation.

The cumulative work of Svitkina T, Mogilner A, Theriot J, Danuser G, Pollard T, Waterman C, Mullins D, and many others have built a detailed model for the keratocyte, for which we know the actin polymerization spatial rates and the localization of motors, actin plus-ends, and bundlers. Michael Abercrombie coined the term “lamellipodium” in 1970. The lamellipodium is a **thin layer of actin covered with a membrane** of about 110–160 nm thick in a primary chick fibroblast (Small, 1981) or 140 - 200 nm in fish keratocytes (Laurent et al., 2005). As seen by electron microscopy, the orientation of actin filaments is parallel to the direction of protrusion, with their **barbed ends pointing towards the edge** (Svitkina et al., 1997). Typically, the retrograde flow velocity depends on the friction with the substrate, but it generally is ~5 μm/min, and the front edge velocity is about 2-10 μm/min. The projected shape of the keratocyte lamellipodium is approximately 20 μm by 5 μm width.

In comparison, the size of blebs will depend on the cellular conditions: melanoma cells can make blebs of 1-5 μm diameter while being unconfined, whereas confined “leader bleb” or “A2” cells will make a single large bleb at the front. The bleb can take almost all the cell volume and measure ~10 by 30 μm while being confined at 3 μm. Non-adhesive, confined blebbing cells produce retrograde flows of about 10-20 μm/min, and move at about a speed of 5-10 μm/min. Membrane tension and actin dynamics determine the shape of keratocytes and their lamellipodium (Barnhart et al., 2011), and so it has been described for the shape of blebs (Tinevez et al., 2009) and single-bleb migrating cells (Ruprecht et al., 2015) (**Figure 10**).

Molecular regulation of actin assembly at the lamellipodium

Helping actin filaments push on the membrane, we find a set of proteins to promote the actin network's growth and organization. These include the **Arp2/3 complex, profilin, capping protein, and ADF/cofilin**. Motion is initiated spontaneously or by receptors that converge through membrane signaling downstream into the **activation of Rac and**

acidic phospholipids and WAVE regulatory complex (WRC), which activates the actin nucleator Arp2/3 producing branches on existing filaments. Filaments in the lamellipodium are quickly capped, so the network at the tip is composed of highly branched short filaments. Actin filaments age by hydrolysis of their bound ATP and dissociation of the γ phosphate, after which they are sensitive to depolymerization by ADF/cofilin proteins. The **recycling of filaments** is ensured **by profilin**, which catalyzes ADP's exchange by ATP in actin monomers and stays bound to them until actin is recruited by a nucleator (Funk et al., 2019; Holz and Vavylonis, 2018; Pollard and Borisy, 2003). Actin sequestering proteins such as **thymosin beta-4** (in mammals), **adenylyl cyclase-associated protein 1** (yeast), and profilin can be present in the cell at high concentrations up to 0.5 mM and are major regulators of network assembly. Other proteins playing a role in actin protrusion are Ena/VASP proteins, which enhance actin filament elongation. The binding of Ena/VASP to WAVE stimulates Arp2/3 complex activity and actin assembly. Many of these effectors cooperate in clusters, yielding excitable-like behavior (Cheng and Mullins, 2020; Hansen and Mullins, 2015; Havrylenko et al., 2015) (**Figure 22**).

As mentioned before, there is a delicate force balance between adhesion, membrane tension, polymerization, and network disassembly, which is adjusted continuously. In practice, this converts the lamellipodium in a force sensor, being sensible to the load the membrane puts on the tip actin barbed ends. For example, *Xenopus* XTC cells will increase actin polymerization at the lamellipodial tip after stretching, in a way proportional to the magnitude of the stretch (Koseki et al., 2019). Despite this body of work, there are still some open questions, such as how the lamellipodium gets ATP-actin at the front since a significant amount of monomers need to cross a thin (150 nm) layer of membrane packed with branched actin networks. The current view is that the **membrane actively accumulates monomers to feed nucleators** at the surface. In CAD cells, the actin network at the leading edge is sourced from two different G-actin pools: the formins at the very tip take actin from the cytosolic pool (bound to thymosin), and the Arp2/3 complexes, more distributed, take G-actin coming from lamellipodium disassembly (Mullins et al., 2018; Skruber et al., 2018).

Similarly to *Xenopus* egg extract droplet experiments, actin turnover profiles in migrating cells demonstrate the **interdependence between contraction and network turnover**. NMII assembles at the base of the lamella of fibroblasts, as in keratocytes, to remodel the network into bundles (Verkhovsky et al., 1995). They create contraction centers that disassemble actin at the back of the cell, allowing for network treadmilling (Wilson et al.,

2010). Similarly, retrograde flow in neural growth cones depends to a similar extent on both NMII contractility and actin-network treadmilling (Medeiros et al., 2006). Recently, research done on *Drosophila* macrophages *in* vivo showed that convergent points of the retrograde flow field strongly correlate with cell directionality and are stable over large timescales (Yolland et al., 2019). The convergent points are sites of **network disassembly** by cofilin and NMII contraction and are better **predictors of cell direction** than leading-edge fluctuations. This result highlights the role of network disassembly in the organization of active stresses and flows in the cell.

However, this does not mean that a monomer incorporated at the front of the lamellipodium will travel until the cell's back to then disassemble by network crushing. The average distance traveled by an actin monomer in the cortex is about 1µm. Thus, the cortex undergoes ~10 cycles of turnover in a keratocyte while traveling from front to back. FCS results also suggest that two-thirds of the actin in the cell is in solution, and that about a quarter of the actin in solution are not G-actin monomers, but oligomers of ~13 actin subunits (Raz-Ben Aroush et al., 2017). This reveals the importance of severing and debranching in network disassembly, which can also be deduced from flow analysis

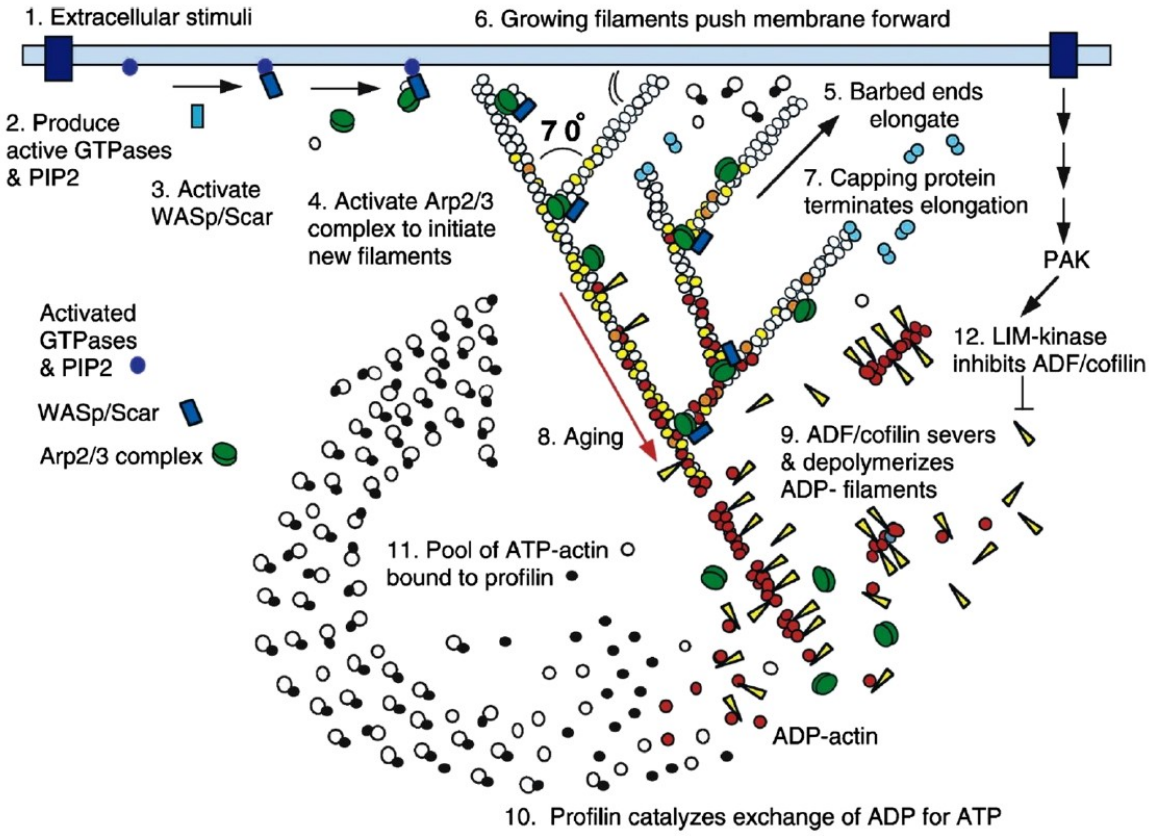

Figure 22: The steps leading to actin polymerization at the leading edge of a lamellipodium. *Taken from (Pollard and Borisy, 2003).*

(Miyoshi and Watanabe, 2013), and poses a question if these oligomers can be directly assembled into a network.

The life and times of a bleb

Blebs are blister-like membrane protrusions formed during cellular processes such as cell migration, apoptosis, mitosis, cell spreading, or virus uptake. Blebs have been traditionally described as transient protrusions and retract after formation when the cortex's links reform or when the hydrostatic pressure is equilibrated. These transient bleb protrusion-retraction cycles can also lead to persistent cell translocation if directed (Maugis et al., 2010; Welf et al., 2020). The typical cycle for a retracting bleb involves 1) **bleb nucleation**, due to local detachment of the cortex from the plasma membrane or by local rupture or weakening of the cortex; 2) **bleb growth**, where the bleb membrane inflates driven by hydrostatic pressure and 3) **bleb retraction**, where a new contractile cortex is formed under the membrane and eventually retracts to the initial position (Charras, 2008; Charras et al., 2008).

1 - Bleb nucleation

The plasma membrane is linked to the contractile actomyosin network beneath, which maintains hydrostatic pressure. The bleb formation will happen at sites of membrane-cytoskeleton strain resulting in membrane delamination or cortex rupture. Local perturbation with perfusion of myosin-II-inhibiting drugs inhibits **blebbing locally**, which suggests that the pressure does not equilibrates throughout the cell at the time scale of cell motility, and that blebbing is due to local pressure (Charras et al., 2005).

2 - Bleb growth

The expansion of a transient bleb usually lasts less than a minute and involves growth in both volume and surface area. Generally, factors that will increase bleb nucleation such as contractility and membrane-cortex attachment (FERM proteins) will also increase bleb size, and consequently balance the cell migration strategy towards blebbing (Bergert et al., 2015; Diz-Muñoz et al., 2010; Liu et al., 2015; Ruprecht et al., 2015; Srivastava et al., 2020; Tinevez et al., 2009; Yoshida and Soldati, 2006). Early studies found a **correlation between expansion rate and final bleb volume**, which suggests a **fixed time (~4s) for cortex buildup,** after which bleb growth could be stopped (Cunningham, 1995). Growing blebs are generally devoid of actin cortex: the limitation for bleb growth is likely cortex

reassembly and membrane tension and not an equilibration of forces between the bare bleb membrane and the cell.

Early work on migration proposed that **cytoplasm flows** in blebs following a "**fountain flow**" pattern (Taylor et al., 1973), which was supported by model computational tools to model hydrodynamic flows in blebbing cells (Goudarzi et al., 2019). This flow pattern might have a consequence for the cortical localization of elements whose transport by diffusion is limited. Recent work done on zebrafish primordial germ cells (PGCs) has

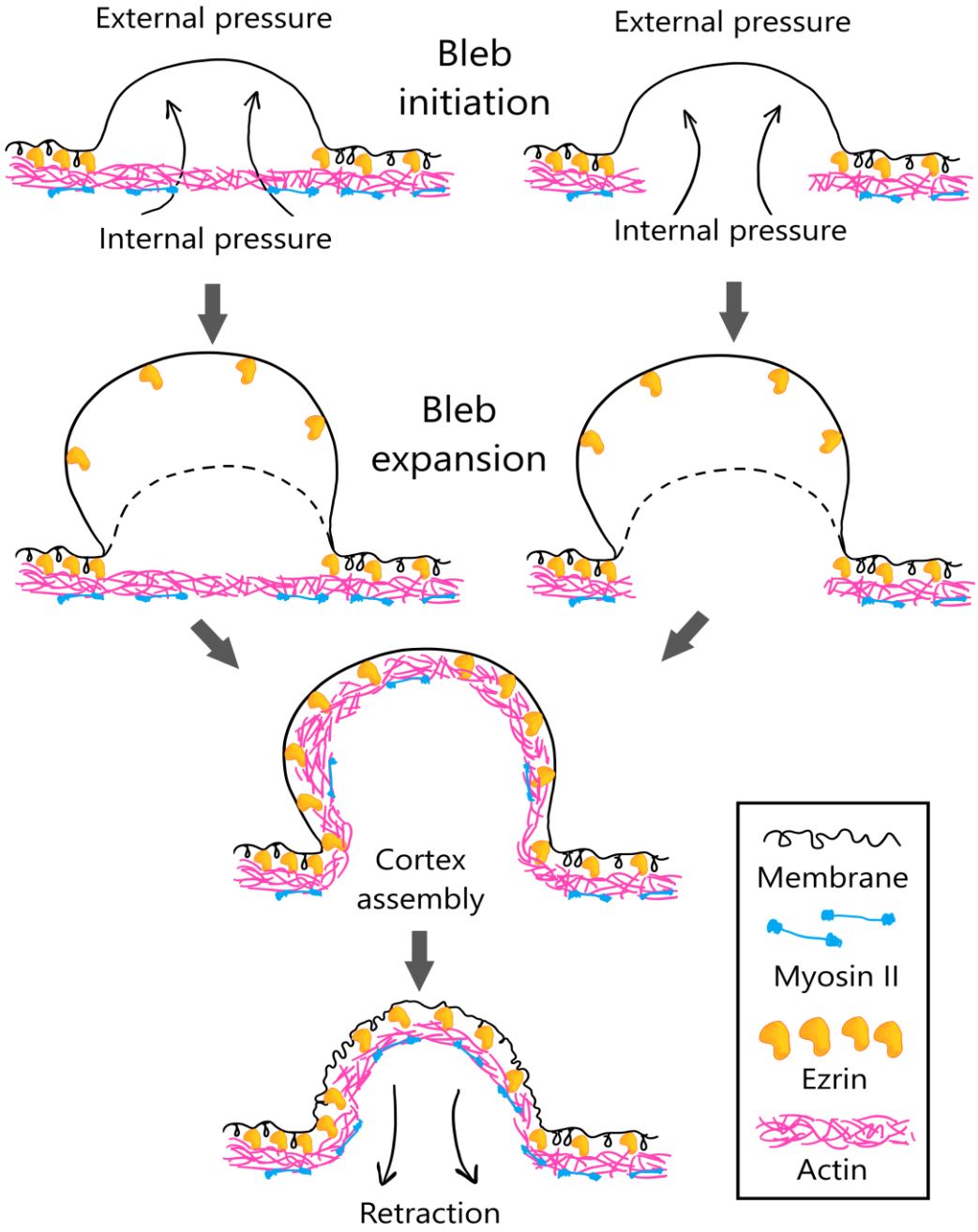

Figure 23: Model for bleb formation. *Adapted from (Charras and Paluch, 2008).*

debated over the importance of membrane permeability by aquaporins to drive bleb formation, finding contradictory results over the effect of aquaporin knockdown, the correlation of changes in cell volume and blebbing, and even the magnitude of these volume fluctuations (Goudarzi et al., 2019; Taloni et al., 2015). The regulation of cell volume during confinement and migration is a current subject of research (Cadart et al., 2019), and more detailed work on volume and blebbing will have to be performed with methods allowing more spatiotemporal resolution (Cadart et al., 2017).

Lipid bilayers can stretch only ~2% (Hallett et al., 1993), but the membrane contains multiple invaginations that store up to **~3.4 times the apparent surface** of HeLa cells (Venkova, 2019). Surface and **membrane flow towards blebs** have been identified on walker cells, and *Fundulus* (Fedier et al., 1999; Tickle and Trinkaus, 1977), but more recent research on PGCs found that bleb expansion depends on a **supply of membrane from local** cell surface **invaginations** (Goudarzi et al., 2017; Lavi et al., 2019). This might then depend on the biological system or the experimental conditions. PGCs can polarize and form a single large bleb immediately after stimulation, but Hela cells would take several hours to form a single large bleb. This might suggest that HeLa cells need to unfold their membrane progressively to allow enough membrane supply to the large bleb. Blebs can grow by **membrane tearing,** also called circus movement (Fujinami and Kageyama, 1975)**, or by inflation,** and it is not yet clear how this is regulated or what favors one of these two mechanisms (Charras et al., 2008; Graziano et al., 2019). Identifying the different types of membrane dynamics at the bleb front constitutes one of this Ph. D. thesis's focus.

Bleb **growth stalls when a new pressure equilibrium is reached**, for example, by an increase of cortical tension in the bleb coming from the reassembly of the cortex or depletion of membrane reservoirs near the bleb – both increase apparent membrane tension. In cells maintaining a stable bleb, there is a continuous bleb growth and cortex assembling, but this process is sequential in retracting blebs.

3 - Cortex reassembly at the bleb

Cortex reassembly has been well documented in blebs due to its accessibility. The cortex of a growing bleb seems to be composed of only erythroid “cortical” cytoskeleton (**protein 4.1, ankyrin B).** EM replicas show that growing blebs are mostly devoid of actin. **Cortex components accumulate sequentially**: first, ERM (5 s before actin); second, actin; third, alpha-actinin, coronin, and tropomyosin (few s after actin); and then fimbrin and

myosin (5-10 s after actin) in M2 cells (Charras et al., 2006). In DLD-1 adenocarcinoma cells, myosin has a longer delay (~15s) relative to actin (Aoki et al., 2016). Retracting blebs have a significantly thinner cortex than the cell (~10–20-nm thick), which thickens as it retracts (Charras et al., 2006; Chikina et al., 2019).

There is an intense buildup of actin networks in the new bare membrane, which significantly changes actin dynamics in retracting blebs compared to a resting cortex. FRAP measurements show a 10x higher turnover of actin in retracting blebs than in a mature cortex (Fritzsche et al., 2013). Blebs contain components of the **arp2/3** and **WAVE complexes**, **formin mDia1**, and **cortactin**. Both Arp2/3 and mDia1 were found to contribute to equal amounts of F-actin in blebs of M2 melanoma cells (Bovellan et al., 2014). **RhoA** and **KIAA0861**, a RhoGEF closely related to dbl, are present at the membrane during all phases of blebbing (Charras et al., 2006). There is at least one active signaling process downstream of Rho to control cortex reassembly. RhoA/ROCK activity in contracting blebs was found to be temporally regulated by a **GEF-GAP cycle involving MYOGEF and p190BRhoGAP**. p190BRhoGAP and Rnd3 localize by an unknown mechanism in the membrane of expanding blebs, inhibiting RhoA. p190BRhoGAP dilution as membrane continues expanding allows a positive feedback cycle mediated by MYOGEF-RhoA-ROCK-Ezrin, which recruits actin, myosin-II, and other proteins (Aoki et al., 2016; Bovellan et al., 2014; Ikenouchi and Aoki, 2017). It is

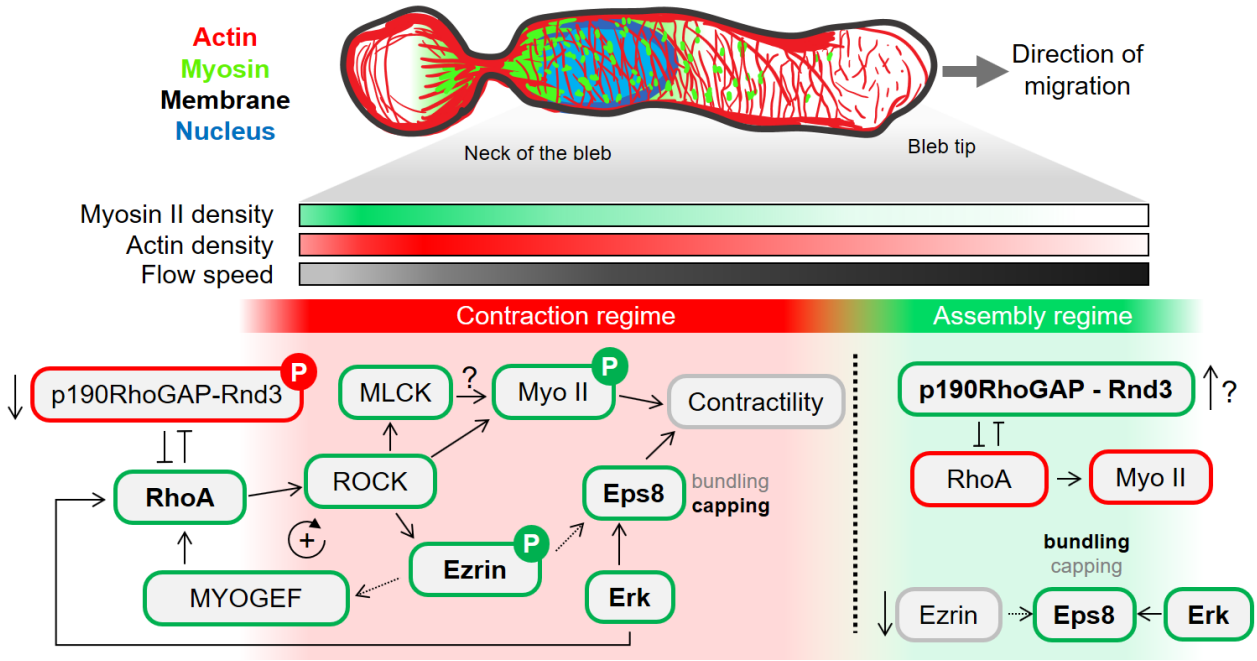

Figure 24: Signaling pathways involved in the protrusion cycle of transient blebs and its possible distribution along a single bleb migrating cell.

not clear how this or other GEF-GAPs signaling plays a role in single-bleb migration, and how they are spatially regulated along the bleb.

Stable blebs

A few independent studies have reported blebs that are large and stable in cells under non-adhesive geometrical confinement in recent years. In a single cancer cell under non-adhesive confinement, multiple blebs are formed and retracted until a single large bleb drives the migration. These **large blebs of the cell scale create a continuous actomyosin flow that propels the entire cell** (Bergert et al., 2015; Liu et al., 2015; Ruprecht et al., 2015). **Unlike previous blebs described, they can overcome retraction**. Therefore, stable blebs are a new type of cellular structures that amoeboid cells can use to migrate, analogous to filopodia, or lamellipodia for mesenchymal cells.

The cycle of bleb formation, cortex buildup, and retraction (Figure 23) has been very well described, but we lack an understanding of the actin dynamics during the formation of stable blebs, which is one of the focus of the current work. It has been suggested that actin bundling at the bleb front and actin network anisotropy between the front and the back are essential to maintain cell shape and polarity during single bleb migration (Logue et al., 2015). Still, the mechanisms by which this contributes to bleb stabilization is not known. It is maybe possible that there is a gradient of chemical activities between the front and the back of the stable bleb to ensure back retraction and front protrusion (Figure 24).

The dynamics of cell protrusions **determine the migration** of a cell. Recent studies suggest that membrane-actin interaction can be an important regulator of protrusions. In neutrophils, membrane tension can inhibit WAVE complex and actin polymerization, perturbing cell polarity and migration (Diz-Muñoz et al., 2016; Houk et al., 2012). In other cell types such as HUVEC or epithelial cells, membrane-proximal actin has been proposed as the general organizer of cell polarity. In these cells, protrusions have been reported to be restricted to the sites where actin is not in close contact with the membrane, with higher cofilin actility (Bisaria et al., 2020). In melanoma cells, ezrin (membrane-actin crosslinker) is depleted before protrusion formation, and this is a crucial step to allow actin polymerization to protrude (Welf et al., 2019). The molecular mechanisms that dictate whether a protrusion retracts or stabilizes are better understood for actin-rich protrusions, but they remain unclear for stable blebs.

Chapter 6: Project objectives

My Ph. D.'s primary goal is to understand **molecular and physical mechanisms that can make a bleb stable and maintain a steady retrograde flow to propel the cell.** In other words, **how the dynamic organization of actin and myosin contribute to the emergence of retrograde flow**. The objectives to understand this mechanism are:

1. Describe the initial steps of bleb formation under confinement and transition from transient to stable blebs, and **which conditions or events lead to retrograde flow**. In particular, describe how the **spatial organization of actin and myosin** contributes to establishing retrograde flows.

2. Explore the **effect of confinement geometry and topography** in the actin cortex structure and assembly.

3. Study the effect of actomyosin cortical gradients in **protrusion persistence during motility**.

4. Propose a **model for bleb shape** and stabilization, taking into account the substrate (adhesiveness, geometry), the subcellular localization of cytoskeletal components (e.g., actin, myosin II, ezrin), and the characteristics of the cortex.

Part III: Main results

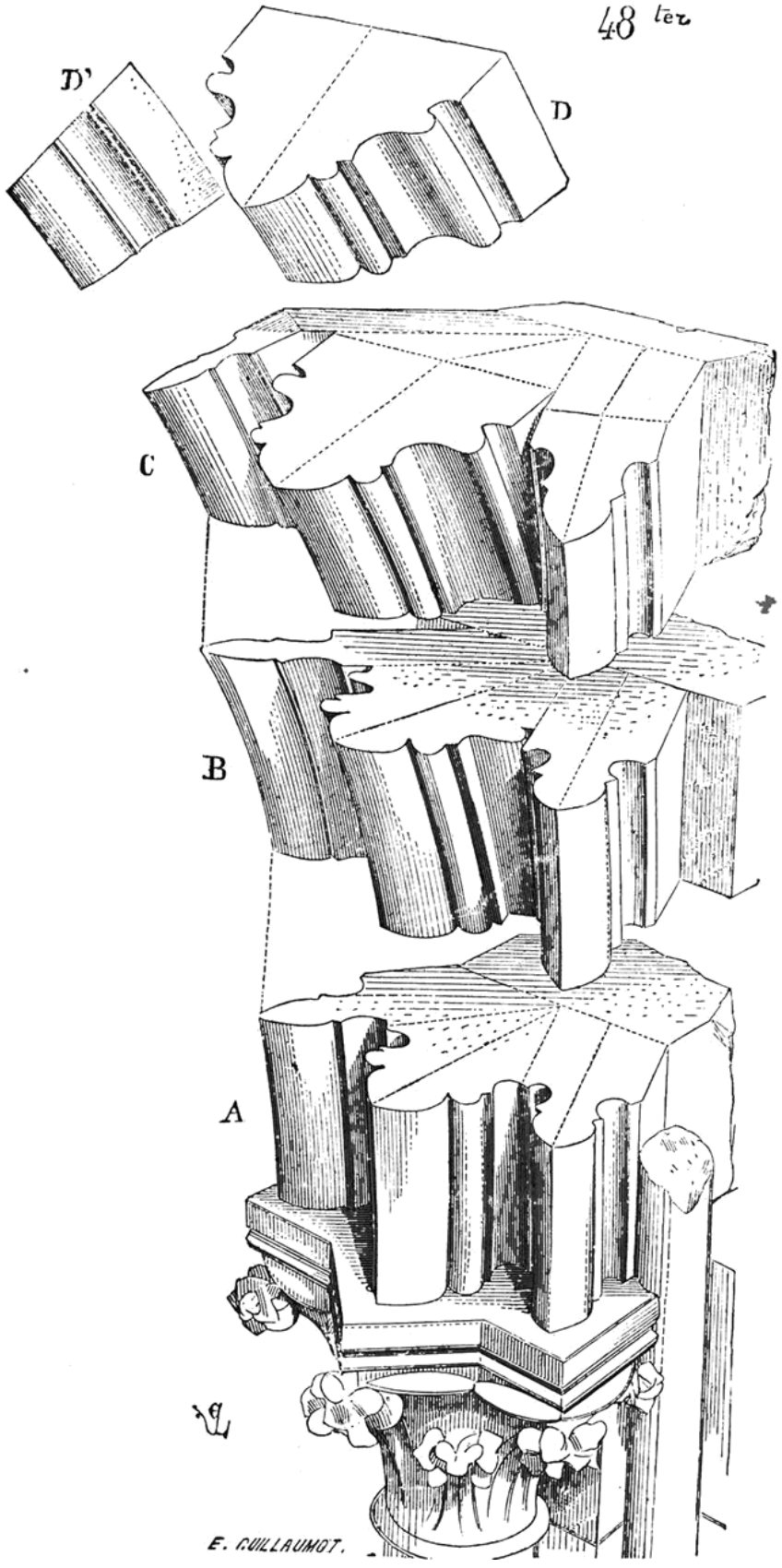

Chapter 7: Experimental methods.

Cell culture

Human cervical adenocarcinoma cells HeLa-Kyoto stably expressing myosin IIA (Myh9)-GFP and LifeAct-mCherry or Myh9-GFP, or Lifeact-mCherry and the plasma membrane-targeting CAAX box fused to GFP, or TALEN-edited ActB fused with GFP (Cellectis, Paris, France), or with no stable marker were maintained in DMEM/F12 supplemented with 10% FBS (Invitrogen) at 37°C and 5% CO2. All cell lines were tested for mycoplasma contamination using MycoScope PCR Mycoplasma Detection Kit (Genlantis), and treated once a year with Plasmocin profilactic Mycoplasma Elimination Reagent (InvivoGen).

DNA transfections

Cells were transfected with plasmid DNA using Lipofectamine 3000 reagent (Thermofisher) transiently or stably, according to manufacturer's protocol, and imaged from 24 to 72 hours after transfection. The following expression vectors were used for plasmid DNA transfections:

Plasmid name	Description / Targeted molecule	Source
pLVX-CIBN-GFP-CAAX	CIBN-CAAX (optogenetic partner on membrane)	Courtesy of Mathieu Coppey's lab (Institut Curie)
pHR- ArhGEF11-CRY2-mCherry	ArhGEF11-CRY2 (optogenetic activator of RhoA)	
pHR- TIAM1-CRY2-mCherry	TIAM1-CRY2 (optogenetic activator of Rac1)	
pHR- ITSN-CRY2-mCherry	ITSN -CRY2 (optogenetic activator of Cdc42)	
pCMV-mCherry-MHC-IIA	Myosin-IIA heavy chain	pCMV-mCherry-MHC-IIA was a gift from Venkaiah Betapudi (Addgene plasmid # 35687 ; http://n2t.net/addgene:35687 ; RRID:Addgene_35687)
pCMV- mEmerald-FilaminA-N-9	FilaminA	mEmerald-FilaminA-N-9 was a gift from Michael Davidson (Addgene plasmid # 54098 ; http://n2t.net/addgene:54098 ; RRID:Addgene_54098)

pCMV- mCherry-FilaminA-N-9	FilaminA	mCherry-FilaminA-N-9 was a gift from Michael Davidson (Addgene plasmid # 55047 ; http://n2t.net/addgene:55047 ; RRID:Addgene_55047)
pCMV- mEmerald-Alpha-Actinin-19	Alpha-actinin 19	mEmerald-Alpha-Actinin-19 was a gift from Michael Davidson (Addgene plasmid # 53989 ; http://n2t.net/addgene:53989 ; RRID:Addgene_53989)
pCMV- mCherry- Alpha-Actinin-19	Alpha-actinin 19	mCherry-Alpha-Actinin-19 was a gift from Michael Davidson (Addgene plasmid # 54975 ; http://n2t.net/addgene:54975 ; RRID:Addgene_54975)
pCMV-mApple-MyosinIIA-N-18	Myosin II A	mApple-MyosinIIA-N-18 was a gift from Michael Davidson (Addgene plasmid # 54930 ; http://n2t.net/addgene:54930 ; RRID:Addgene_54930)
pLenti Lifeact-iRFP670 BlastR	Lifeact	pLenti Lifeact-iRFP670 BlastR was a gift from Ghassan Mouneimne (Addgene plasmid # 84385 ; http://n2t.net/addgene:84385 ; RRID:Addgene_84385)
pEGFP Ezrin T/A	Ezrin T567A (constitutively inactive)	Gift from Monique Arpin (UMR7216 CNRS)
pEGFP Ezrin T/D	Ezrin T567D (constitutively inactive)	
pEGFP internal GFP Ezrin	*wt* Ezrin	Courtesy of Florence Niedergang (Institut Cochin)

Drug assays

The following pharmacological inhibitors and chemical compounds were used: 10 µM ezrin inhibitor **NSC668394** (EMD Millipore), 10 µM ROCK-mediated contractility inhibitor **Y-27632** (Y27) (ED Millipore), 20 µM Ca2+-sensitive myosin light chain kinase/MLCK inhibitor **ML-7** (Sigma-Aldrich), 2 mM extracellular Ca2+ chelator **BAPTA** (Sigma-

Aldrich), 10 µM intracellular Ca2+ chelator **BAPTA-AM** (Sigma-Aldrich), 2 or 20 µg/ml of Rho GTPase inhibitor **C3Tfase** (Sigma-Aldrich), 30 µM of Cdc42 GTPase inhibitor **ML141** (Sigma-Aldrich), 20 µM **AACOCF3** (AA) inhibiting the nuclear envelope stretch-sensitive enzyme cPLA2 (Tocris Bioscience), 50µM of apoptotic caspase inhibitor **zVAD** (Sigma-Aldrich), 100 µM **2APB** blocking stretch-activated inositol triphosphate receptors (InsP3Rs) on the ER/nuclear membranes (Tocris Bioscience). Growth medium was supplemented with 1% DMSO (vol/vol) (Sigma-Aldrich) in control experiments when DMSO was used as a solvent. Cells were imaged 10 to 30 minutes after treatment. The PDMS devices in contact with cells during imaging were incubated in medium supplemented with the final concentration of drug during at least 1h before the experiment.

Microfabrication

Cell confiner

We used a device developed in our lab for cell confinement, which combines confinement precision and high imaging quality (Le Berre et al., 2014). The confinement device (Figure 1 A) is composed of three parts: a standard glass-bottom petri dish (a fluorodish of 35 mm diameter from WPI Inc.), a home-made confinement coverslip (made with RTV PDMS 1:10), and a home-made PDMS compression device. The confinement coverslip consists of a standard 10 mm-diameter glass coverslip with a PDMS layer microfabricated on a SU8 mold made by photolithography. This PDMS layer contains pillars of a precise height, which will create a chamber composed of glass at the bottom and PDMS at the top. The pillar height determines the minimum confinement that can be applied to the cells before collapsing the structure. The coverslip is mounted on the compression device, which is connected to a vacuum generator. When the vacuum is turned on, the roof of the confinement device will be depressed, and the coverslip will be pushed against the glass-bottom petri dish. The device allows total control of the coating of the top and bottom sides of the chamber, consisting of a non-adhesive coating of 0.5 mg/ml of PLL-*g*-PEG (SuSoS, Dübendorf, Switzerland). The confinement device allows for live imaging of the cells as they are being compressed, but bears two main disadvantages: the compression will change the focus plane and deform the coverslip, which can be problematic with TIRF imaging the height of the confinement is only precise after full compression.

Nanogrooves

First, recordable CDs (*CD-R*) were cut on the sides and scotch-taped to remove the protective iridescent layer. CDs were then submerged in isopropanol for about 15 seconds to remove the organic dye from the grooves, and then washed with clean isopropanol and dried with an air gun. In parallel, 25 mm. glass coverslips were plasma treated for 5 minutes to create bonds in the glass surface. Fresh, degassed PDMS 1:10 was then prepared and poured in the CDs' surface, and the plasma-treated coverslips were applied on top of it. The PDMS was cured overnight in an over at 60°C, and coverslips were removed with a scalpel.

This fabrication process creates a very thin layer of nanogrooved PDMS on top of the glass coverslips, allowing for decent imaging. The regularity and size of the grooves were measured by Sergii Rudiuk in the lab of Damien Baigl (ENS Paris) using an AFM Agilent Technologies 5100 Scanning Probe Microscope in tapping mode in air. Raw AFM images were baseline corrected and rendered using Gwyddion.

PDMS confinement

Trypsinized cells were resuspended in phenol red-free DMEM/F-12 medium supplemented with 10% FBS (Invitrogen) and plated on PLL-g-PEG coated glass-bottomed 35-mm dishes (WPI, Sarasota, FL, USA) just before confinement. In the case of high NA TIRF imaging, the setup does not have CO2 regulation, so cells were resuspended instead on CO2-independent medium. The surface of the confining side was treated with a solution of 0.5g/l of PLL-*g*-PEG in PBS (SuSoS, Dübendorf, Switzerland) or with 0.5 g/l of PLL solution in PBS (diluted from Poly-L-lysine solution 0.1 % (w/v) Sigma ref. P8920) following passivation at a plasma cleaner.

AFM confinement

Dishes with cells were mounted in a dish heater (JPK Instruments) and kept at 37 °C under an inverted light microscope (Axio Observer.Z1; Zeiss) equipped with a confocal microscope unit (LSM 700; Zeiss) and the atomic force microscope (AFM) head (CellHesion 200; JPK Instruments). Focused ion beam (FIB)-sculpted, flat silicon microcantilevers were processed and calibrated as described in (Cattin et al., 2015). The microcantilevers were fixed on a standard JPK glass block and mounted in the AFM head. The cantilever was lowered on the cell to a preset height with a constant speed of 0.5 µm·s-1, and the resulting varying force and cantilever height were recorded over time.

At the same time, differential interference contrast (DIC) and fluorescence images at the confined cell's midplane were recorded every 5 seconds using a 63× water immersion objective. All microscopy equipment was placed, and experiments were carried out in a custom-made isolation box at 37 °C (The Cube; Life Imaging Services).

Micropatterning

Micropatterns were created using deep UV illumination on polylysine grafted polyethyleneglycol (PLL-g-PEG) treated coverslips, and then coated with fibronectin 50µg/ml using standard microfabrication techniques (Azioune et al., 2010).

Nanofiber electrospinning

10 wt% gelatin powder from porcine skin was dissolved in the mixed solution of acetic acid, ethyl acetate, and DI water at the volume ratio of 21:14:10 before electrospinning. The gelatin solution was electrospun from a syringe needle to the lower plate on 25 mm diameter glass coverslips, placed on an aluminum foil at 10 cm distance from the needle tip. The solution was injected at 0.2 mL/h by syringe pump, while the voltage between the needle and the foil was kept at 11 kV (Huang et al., 2020). Coverslips were then sticked with PDMS on the bottom of perforated 35 mm plastic dish (Mattek Life Sciences). To observe the behavior of adherent cells in aligned collagen, cells were seeded at least 3 hours prior to the experiments

Fixation and staining of cells under agarose confinement

Cells were confined under 5% (w/v) low melting point agarose (UltraPure Low Melting Point Agarose, Invitrogen) pads, 5mm thickness, dissolved in culture medium DMEM FBS 10%. To preserve the actin structure and membrane shape, we used a protocol courtesy of Larisa Venkova (Institut Curie) to preserve the osmolarity of cells during fixation, thus preventing the formation of blebs by osmotic pressure. This protocol involves a 3-minute prefixation step (75-80% 2xPHEM + 20-25% MilliQ + 0.25% glutaraldehyde) and a 10-minute fixation step (4% PFA + 1xPHEM + 0.25% glutaraldehyde). 2xPHEM buffer contains PIPES 120mM, HEPES 0. 50mM, EGTA 20mM, $Mg(CH_3COO)_2$ 8mM in MilliQ water. The pH is corrected to 6.9 using a 6M KOH solution, and a 0.2µm filter passes the solution before storage. After fixation, we removed the agarose confiner and washed gently with PBS three times, incubated for 15 min incubation in freshly prepared on PBS + $NaBH_4$ 1mg/ml, and washed again with PBS. For actin visualization, cells were stained with 0.16µM solutions of Alexa Fluor 488

Phalloidin (Thermofisher) for a few hours and then washed with PBS. For STORM imaging, cells were placed in Abbelight (Paris, France) commercial buffer appropriate for STORM imaging, and then an air-tight chamber was created on top using resin and a coverslip.

Preparation of cytoplasts

The day before the experiment cells were seeded on polysterene plastic slides (Evergreen Scientific, Ca, USA) coated by fibronectin (50µg/ml, Fibronectin from bovine plasma, Sigma). Slides were coated following UV treatment (5 minutes), incubation with the fibronectin solution (45 minutes), and washing with PBS.

We 3D-printed plastic holders with biocompatible resin (Formlabs) to hold vertically slides on 50 milliliter tubes (Eppendorf). Two slides were placed per tube, back to back. Cells were incubated in the tube with enucleation medium 25 minutes prior to centrifugation. The enucleation medium consists of standard DMEM+10%FBS supplemented with 2mg/ml of Cytochalasin D (Sigma). Centrifugation was performed on a pre-heated rotor and centrifuge (Fiberlite F15-8x50cy in a centrifuge X1 from Thermofisher) at 16750g for 55 minutes at 37°C. Slides were washed gently on PBS several times and recovered for at least two hours in culture medium before trypsinization and confinement.

High NA TIRF microscopy

The high NA TIRF consisted of a home-made TIRF setup with standard settings, equipped with a 473nm laser 500mW (Laserquantum), an objective TIRF NA=1.49 (Olympus), and a camera Andor Zyla 4.2. For two-color TIRF, a 561nm laser 500mW (Laserquantum) was used, and the acquisition was performed sequentially. A custom-made made FPGA trigger was used for the lasers, synchronized with the camera. A single notch filter was used in the emission light path to block the laser lines 405/473/561/640 (Chroma). Acquisition was controlled by the Andor SOLIS software.

Polarization-resolved fluorescence microscopy

The optical set-up, described in detail in (Kress et al., 2013; Mavrakis et al., 2014; Wang et al., 2013), is based on a confocal spinning disk unit (CSU-X1-M1; Yokogawa, Tokyo, Japan) connected to the side port of an inverted microscope (Eclipse Ti-U; Nikon, Tokyo, Japan). A polarized 488-nm continuous laser with power control provided continuous excitation (Sapphire 488–20; Coherent, Santa Clara, CA). The laser beam passes by an

electro-optic modulator (EOM) (Pockels cell, No 28-NP; Quantum Technology, Lake Mary, FL) followed by a quarter-wave plate (WPQ05M-488; Thorlabs, Newton, NJ) to produce a linear rotating polarization. A polarization distortion compensator was used to compensate for ellipticity and diattenuation produced by the optics in the microscope objective's excitation path. The beam was expanded using a 10× telescope (BE10; Thorlabs) and sent directly to the microlens array of the CSU by reflection in its dichroic mirror (Di01-T488-13×15×0.5; Semrock, Rochester, NY). An objective lens (Nikon Plan Apo VC 60×, N.A. = 1.2, water immersion) is used for excitation and light collection. The detection was filtered (bandpass 525/45) and imaged onto a camera (iXon 897 EMCCD, 512×512 pixels; Andor, Belfast, United Kingdom). The microlens and pinhole array of the CSU disks rotated synchronously at a fast speed. The EMCCD and EOM were also synchronized fast stack recording for 18 different incident polarization angles (0-170°) per Z-plane.

Optogenetic experiments

HeLa cells were transformed with lentivirus particles derived from the GEF-CRY2/CAAX-CIBN plasmids. Positive clones were FACS-sorted at intermediate fluorescent levels and a multiclonal population was used in the experiments. The optogenetic experiments were performed using a variation of TIRF, called azimuthal TIRF on a x63 or x100 oil objectives. This setup spins the laser and generates homogeneous illumination, avoiding fringe interferences and imaging artefacts. The microscope was coupled with a DMD (digital micromirror device) controlled by a Matlab software. This software is allowed to draw a region and illuminate it with blue light (420nm) provided by a LED light source. In our experiments, we have used a DMD device with dimensions of 640 x 480 able to generate 8-bit grayscale patterns with a blue LED source (SPECTRA LightEngine (Lumencor, Beaverton, OR). Cells were illuminated every 3 seconds during the activation periods, and images were sequentially recorded on the other channels.

Chapter 8: Image and data analysis.

Blebbing dynamics

Bleb morphogenesis

Cells were radially resliced using Fiji. Time of bleb nucleation was recorded relative to the beginning of compression, and its angular position, maximal bleb length, maximal bleb width was measured with the help of a kymograph using a semi-automatic home-made Fiji macro. From the kymograph, we manually measured the total lifetime (until the bleb was retracted) and the maximum retraction speed. Aspect ratio was defined as maximal bleb length divided by maximal bleb width.

Actomyosin dynamics

Fluorescence images taken by spinning disk confocal microscopy were background subtracted and bleach corrected using Fiji (https://imagej.net/Bleach_Correction). The cytoplasmic/cortical ratio was calculated using a cytoplasmic region not containing the nucleus, and a 500 nm-wide cortical region, manually selected at every time point.

For analyses measuring the cortical accumulation of actomyosin in proximal and/or distal sides, the images were subtracted the minimum background in the cytoplasmic regions, and then a 500nm-wide region was manually selected at the bleb front or the bleb side, immediately next to the cell body. In time analysis, these regions were manually selected at every time point.

To measure cortical gradients, the images were subtracted the minimum background in the cytoplasmic regions, and a 500 nm-wide line was manually traced at the onset on maximal bleb area. To compare cortical gradients between round and elongated blebs, the length was normalized by dividing it to the total, and mean intensities were calculated as a function of bleb position divided in 10 bins: (0,0.1], (0.1,0.2], … (0.9,1.0], taking 0 for the bleb base and 1 for th bleb front

Projected bleb area and neck width dynamics were manually segmented using Fiji and a screen graphic tablet.

To calculate the CV (coefficient of variation) of the myosin signal, blebs were segmented manually at each time point, and background subtracted. The background was defined as the minimum cytoplasmic signal in the cell at any time point.

To calculate the actin polymerization dynamics in the cortex, we first subtracted the background inside the cell, outside of the actin shell. Then, we manually selected 2 by 0.5 μm windows on the cortex as they moved backward with the retrograde flow and calculated the intensity at each frame. The curves were divided by their mean value on the plateau reached after 10-20 seconds. The slopes were then calculated, doing a linear fitting on the range (0.25-0.9).

Membrane dynamics

The Blebbing angle was measured manually using Fiji. The main bleb angle was defined as the angle of the bleb body during the entire duration of the time series. The bleb angle was defined as the direction of the blebbing at the bleb front and was measured relative to the main bleb angle.

Classification of blebbing dynamics: blebs or cell fragments were manually classified according to membrane dynamics and the middle plane on the actin channel. Persistent blebs were defined as bleb with no actin scars and persistent tip, without significant perturbations in the blebbing angle. Winding blebs were defined as blebs with alternating actin scars on the middle plane in the actin channel, and with a winding membrane tearing at the bleb front. Unstable blebs were defined as blebs that keep a constant blebbing at the cell front while transiently rebuilding a cortex all along the cell contour.

To calculate the fraction of blebs in a given condition, we recorded time-lapse movies on the actin and bright field channels. The stable blebs (not retracting, not round) present in each field of view were classified every minute based on the characteristics of the actin cortex and membrane dynamics, and the data pooled together. To classify the blebbing phenotype of cell fragments, movies were divided in 25-second intervals and blebs were manually assigned a dominant behavior in these time windows.

Orientation of blebs on nanogrooves

To calculate the polarization of blebs as a function of their orientation to grooves, images were first rotated so that the grooves are horizontal. Then, blebs were manually segmented in Fiji and their area and Ferret’s angle calculated and plotted.

To calculate the orientation of only the bleb tip or bleb front, we measure the direction of protrusion, as opposed to the Ferrets angle of the entire bleb.

Accumulation of ArhGEF11 in optogenetic experiments

To calculate the time accumulation of ArhGEF11, we subtracted the background of the image outside the cell. The intensity was normalized, applying a 1pixel median filter and dividing by the maximum at each frame.

Contours of bleb fragments

Bleb fragments were segmented using Fiji, and then exported into inkscape, were the contours was transformed into a svg vector file and manually aligned.

AFM force curves and images

The raw AFM force data contains height, force and time. We made a Python script which identifies the times where the cell is unconfined and calibrates the minimal force by their median value; then identifies the beginning of confinement, defined as the first time point at which the target height is reached (in this case 3µm); and lastly aligns the force curves by the time of the beginning of confinement. The script also identifies the time of active force onset. To do so, force curves are first applied a rolling mean over 5 seconds. Then, the force onset time point is defined as the first time point where $\mathrm{d}F(t)/\mathrm{d}t = 0$, where $F(t)$ is the AFM force.

The CV of NMIIA signal was calculated by a home-made Fiji script, subtracting the mean fluorescence background outside the cell, and then calculating the mean and standard deviation on the cell. The mean edge retraction speed was calculated on the segmented actin channel using the Fiji plugin ADAPT “Automated Detection and Analysis of ProTrusions (Barry et al., 2015).

The number of blebs per cell was calculated defining four random regions in the cell and measuring the time of appearance, length, and width of all blebs in these regions during 300 seconds following confinement.

Cortical flows

Measurement of cortical flow speed

Two methods were used to calculate cortical flows: manually measured kymographs or automated PIV analysis. When named “flow speed”, and not “PIV speed”, speeds were instead measured from kymographs on the myosin or actin channels taken at the top of

bottom plane of cells or blebs. The instantaneous speed at time t was defined as the mean slope of the flow in the kymograph around time t. The slopes were manually measured.

Automated PIV analysis was performed in Fiji using the “iterative PIV” plugin (https://sites.google.com/site/qingzongtseng/piv) initially developed for force traction microscopy, removing in the parameters any vector interpolation bias (Tseng, 2011; Tseng et al., 2012). This plugin was primarily based on JPIV, an open-source PIV software, which used standard algorithms to calculate the displacement vectors (available at https://eguvep.github.io/jpiv/). The interrogation window was estimated to be large enough from the images' feature size, and the search window was estimated to be large enough to capture the maximal displacement observed in the images, such as search window size = interrogation window size + 2 × maximal displacement. The x, y, ux, uy components were imported into a home-made python script to allow for processing and data analysis. The median PIV Y speed was calculated as the median of all the non-zero uy components, to exclude regions outside the bleb.

Network divergence and turnover

We developed a Python script to calculate the mean density in each PIV window for every time point. Knowing the density and the cortical flow, one can calculate the flow divergence and the actin turnover rate. The divergence of the velocity field is a good indication of the relaxation or contraction of the cortex. The divergence was calculated as $\boldsymbol{\nabla} \cdot \boldsymbol{v} = \frac{\partial v_x}{\partial x} + \frac{\partial v_y}{\partial y}$.

The spatial distribution of network turnover in 2D can be calculated from the mass conservation equation $S(t,x,y) = \frac{\partial \rho}{\partial t} + \left(\boldsymbol{\rho}(\boldsymbol{\nabla} \cdot v)\right) + \left(\boldsymbol{v} \cdot (\boldsymbol{\nabla}\rho)\right)$, where ρ is the fluorescence intensity and S the network turnover (Yolland et al., 2019). We will consider steady states, so $\frac{\partial \rho}{\partial t} = 0$, so we drop the t dependence in S. This implies that $S(x,y) = \left(\rho(\boldsymbol{\nabla} \cdot \boldsymbol{v})\right) + \left(\boldsymbol{v} \cdot (\boldsymbol{\nabla}\rho)\right) = \boldsymbol{\nabla} \cdot (\rho \boldsymbol{v})$, where the last equality is a mathematical identity. Therefore, knowing $\boldsymbol{v}(x,y)$ and $\rho(x,y)$ one can calculate the local network turnover.

Correlation length and local order parameter

We are interested in finding, from the velocity field, the average distance at which velocities are correlated. The velocity spatial correlation function is defined as:

$$C(\vec{r},t) = \frac{\langle u^*(\vec{r}'+\vec{r},t) \times u^*(\vec{r}',t)\rangle_{\vec{r}'}}{\sqrt{\langle u^*(\vec{r}',t)^2\rangle\langle u^*(\vec{r}'+\vec{r},t)^2\rangle}}$$

where $\vec{r}$ is the correlation distance and u^* is the normalized velocity such as $u^* = u - \langle u\rangle$ (Petitjean et al., 2010). This function averages across many pairs of points at distance $\vec{r}$ at a specific time. Using u^* instead of u gives the good normalization, such as $I(\vec{0},t) = 1$ for all times and $\lim_{\vec{r}\to\infty}(\vec{r},t) = 0$. We take an averaged correlation over all directions, so $C(r) = C(\|\vec{r}\|)$, define the center cell as $(x,y) = (0,0)$ with an autocorrelation value $C(0) = 1$, and define $u^*(0)$ as the velocity of the cell in the center, our reference to calculate the correlation. The correlation at distance r from the center $u^*(0)$ will be: $C(r) = \frac{\langle u*(0)\times u^*(r)\rangle}{u^*(0)\sqrt{\langle u^*(r)^2\rangle}}$, which simplifies to $C(r) = \frac{(u*(r))}{\sqrt{(u^*(r)^2)}} \times \mathrm{sgn}(u^*(0))$. This satisfies the condition $C(0) = 1$, as $C(0) = \frac{u^*(0)}{\sqrt{\langle u^*(0)^2\rangle}} = \frac{u^*(0)}{|u^*(0)|} = \mathrm{sgn}(u^*(0))$. For our purposes, we defined the correlation distance $C(r)$ at the closest distance at which $C(r) < 0.5$. To simplify the analysis, we took only the Y component of the velocity vector, as the X component does not represent a significant part of the velocity. This algorithm was implemented in a home-made Python script and the averaged $C(r)$ over time was calculated for each window position.

To determine the local alignment $\langle\cos\theta\rangle_{\mathrm{local}}(x,y)$ of actin flows, the cosine similarity between all velocity vectors and their 8 nearest neighbors was computed using $\cos\theta = v_1 \cdot v_2/|v_1||v_2|$ (Yolland et al., 2019). For simplicity, we selected only the y component of the velocity vectors. This algorithm was implemented in a home-made Python script and the averaged $C(r)$ over time was calculated for each window position.

As an output, we obtain a correlation length and local order for each PIV window at each time point. To plot the relationship between these two parameters and the actin density, we binned all PIV windows by their median density, excluding the windows close to the background signal. We then plotted the distribution of correlation lengths and local order per density bin.

Cell outline tracking and cross-correlation analysis

Middle plane movies of actin-GFP bleb fragments taken on a confocal spinning disk were manually segmented for a few frames. These manually segmented frames were input into a pixel classification routine on Ilastik (Berg et al., 2019), that was used to segment the rest of the movie.

The segmented images and the actin-GFP channel were processed using the Fiji plugin ADAPT (Automated Detection and Analysis of ProTrusions) (Barry et al., 2015). The parameters used were as follows: smoothing filter radius: 1, erosion iterations: 2, spatial filter radius (µm): 0.5, temporal filter radius (s): 1, cortex depth (µm): 0.5, Visualization line thickness: 2. The output of ADAPT is an edge velocity and actin density map (summed over the 0.5µm-wide cortical region).

As described in (Machacek et al., 2009; Maeda et al., 2008), the normalized cross-correlation matrices were calculated from edge velocity and actin density signal maps. The cross-correlation value $c_{(x,y)}$ at a coordinate (x, y) within the cross-correlation map, c, of two images I_1 and I_2, is calculated as follows: $C_{(x,y)} = \frac{1}{mn\sigma_1\sigma_2} \times \sum_{i,j}^{I_1,I_2} (I_1(i+t,j+s)-\mu_1)(I_2(i+t,j+s)-\mu_2)$, where $m \times n$ are the dimensions of the images I_1 and I_2, σ_1 and σ_2 are the standard deviations of I_1 and I_2, μ_1 and μ_2 are the means of I_1 and I_2, and $t = x - m/2$ and $s = y - n/2$. For the calculation of the autocorrelation, I_1 = I_2. This algorithm was implemented in a home-made Python script. To calculate only the temporal or the spatial cross-correlation coefficient, only a vector of the cross-correlation matrix $C(s,t)$ was taken into account: $C(0,t)$ for the temporal cross-correlation or $C(s,0)$ for the spatial cross-correlation. To extract the decay length, a linear fit were performed in log space for the correlation range = (0.95-0.25).

Persistence width and time of protrusions

To calculate the persistence times and width of bleb fragments, we performed autocorrelation of the edge velocity map, $C_{vel\,vel}(s,t)$. By definition, after normalization, $C_{vel\,vel}(0,0) = 1$. We fitted an exponential $p_{norm}(t) = e^{-\lambda t}$ to the autocorrelation matrix at no space lag $C_{vel\,vel}(0,t)$. The mean protrusion lifetime or persistence time was defined as $\tau = \frac{1}{\lambda}$, where is λ is the decay constant of the fitted exponential. This is similar to the persistence time defined in the study of cell trajectories defined as persistent Brownian motion (Selmeczi et al., 2005). If we take instead a lag time = 0, we will find the probability to have the form of $p_{norm}(x) = e^{-\lambda x}$, and the persistence width of the protrusion $\sigma = \frac{1}{\lambda}$.

Shape of bleb fragments

The principal component analysis of shapes of bleb fragments was calculated using the Python-based open source software Celltool (Pincus and Theriot, 2007). Briefly, the software is provided with the segmented shapes from Ilastik, from all fragments,

timepoints, and conditions. Then, the polygonal contours are extracted from the binary masks and scaled into microns for further analysis. The contours are then mutually aligned by Celltool so that corresponding parts of each contour's shape are aligned as best as possible. Once the shapes are aligned, Celltool proceeds to the principal components analysis (PCA) of population shape variability. After alignment, the remaining variation in their shape represents the "intrinsic" spread of shapes. To summarize this variability, Celltool performs the PCA to decompose the variability space into a basis set of orthogonal "shape modes", ranked by their order of importance, meaning the contribution to the total variability. These shape modes constitute the shape model and are easy to plot and understand intuitively. Moreover, such modes can be used as a quantitative measure of shape: a given contour's position along several shape modes is a numerical descriptor that can be of great statistical use, as to calculate average widths or lengths. To calculate a score in each mode for a given fragment, we calculate the average of the score at all timepoints.

Polarized microscopy

Molecular order and aperture angles

The molecular order and aperture angles (ρ, ψ) were deduced from the measurement of the intensity modulation $I(\alpha)$ using a Matlab-based software developed by Cristel Chandre (CNRS) Manos Mavrakis (CNRS) at Institut Fresnel, implementing the algorithm described in (Loison et al., 2018). The signal processing is described in detail in (Kress et al., 2013; Loison et al., 2018). Physically, ψ determines the degree of angular variations present within the focal spot at a given pixel position. This angle, denoted “molecular order”, encompasses the orientation variations among probes (related to the static organization of actin filaments) as well as their time angular fluctuations (related to the degrees of freedom relative to their binding site). ρ, on the other hand, determines the preferential orientation of the probes. ρ and ψ thus permit us to quantify the full information on molecular organization at each image's pixel.

Polarimetry data processing

The distribution of angles ρ and ψ were calculated with a polarimetry software developed and maintained by the Cell Morphogenesis lab at Institut Fresnel (https://sites.google.com/view/cell-morphogenesis-lab/polarimetry). The software reads the 18 rotating fluorescent images, thresholds the images, and outputs the distribution of

ρ and *ψ.* The software is calibrated to take into account the molecular properties of the fluorophore, in our case Alexa 488. We selected 4 regions of interest in each of the 10 representative bleb examples, one at the front, two on the sides, and one in the middle of the bleb, between the side regions. From each ROI, the software outputs a mean and standard deviation of *ρ* and *ψ*. We calculated the combined standard deviation of *ρ* and *ψ* via ANOVA as square root of the grand variance, and the mean of the means. These analyses were weighted by N, the total number of orientation vectors.

Actin network segmentation and skeleton analysis

Fragment versus network filaments

In figure 37F, the actin segmentation was done manually, and filaments classified as “fragments” if not connected to the main network or “network” if connected to the min network.

Molecular dynamics of actin filaments

To calculate the growth speed and angle from filament branching events, we first selected events that were clearly identifiable, growing for at least a few tens of time points, and observable from the start. The branching angle was manually measured from a time projection. The branch length was calculated at each timepoint and the instantaneous growth speeds were calculated from these values.

When comparing the accumulation of actin and alpha-actinin in bundles, the background outside the cell was subtracted from each image, and then divided by its mean value.

Actin structure at the front of fixed blebs

To measure the orientation of actin filament at the front of blebs, we selected a representative number of blebs (5 for each) of 4 different groups: large blebs (from cells polarized cells, displaying only one bleb) with an actin-free front (we cannot appreciate a clear bleb contour), retracting large blebs (we appreciate clearly a contour), small blebs (from non-polarized cells, displaying multiple small blebs) with actin-free front, and retracting small blebs. We used Fiji to select square regions at the front of blebs and drew segments representing actin filaments' orientation. We measured the relative orientation respective to the main bleb axis and the length of these segments. We then plotted a histogram of angles weighted by the segment length.

To calculate the actin bundle thickness from STORM images, the super-resolution data was processed using Abbelight proprietary software and then imported into Fiji as density data with a pixel size of 15 nanometers. This allowed for signal processing analogously to standard light microscopy data. We calculated the bundle thickness from manually selected line scans, as the full width at half maximum of the Gaussian.

Actin structure at the front of blebs on nanogrooves

Due to the thickness of the PDMS layer, imaging conditions deteriorate and the identification of single bundles is not apparent in most blebs. We selected two examples that contained less background and in which the actin structure was clearer., and manually segmented in Fiji the actin network at the front, on the plane of the grooves and on the top plane. Since we were interested only in the distribution close to y=0, the statistical test was one-tailed instead of two-tailed.

Actin filament segmentation and skeleton

To segment the actin filaments in the TIRF movies, we manually segmented a few frames and inputted this manual segmentation into Ilastik. We manually cropped each frame to remove other blebs, cells, and background present in the image. This binary image was processed in Fiji with the “Analyze particles” function. The biggest cluster was colored in blue, and all other clusters were colored in red. We then performed a resliced along the bleb length to construct a kymograph and show the relationship between connection to the biggest cluster and velocity.

Calculation of the critical network density

The binary image was processed using the Fiji plugin skeletonize, which outputs 1 pixel-wide skeleton from the binary image. Similarly, clusters were colored according to their size. To analyze the progression of percolation, we cropped a horizontal window in the skeletonized network at a time window where we did not observe the retrograde flow. We used Fiji to analyze the number of clusters and their size. We defined the cluster size as the width of a given cluster divided by the width of the interrogation window. The cluster size distribution and size were analyzed and plotted using a Python script.

Statistical analysis of the data

Unless stated otherwise, statistical significance was determined by two-tailed unpaired or paired Student's/Welch’s t-test after confirming that the data met appropriate

assumptions (normality, homogenous variance, and independent sampling). Statistical data are presented as average ± SD. Sample size (n) and p-value are specified in the text or figure legends. In most cases, the sample size was defined as the number of cells counted/examined within multiple different fields of view on the same dish/slide, representing data from a single sample within a single experiment. When data from a single sample are shown, they are representative of at least three additional samples from independent experiments.

Chapter 9: Main results

Previously associated with apoptosis, blebs have arisen in the past decade as **important structures for amoeboid cell migration**, particularly cancer cells (Charras and Paluch, 2008). A few independent studies have reported large and stable blebs in cells under non-adhesive confinement in recent years. This universal switch to bleb-based migration happens in amoeba (Srivastava et al., 2020), choanoflagellates (Brunet et al., 2020), immortalized cell lines, and primary human and murine cultures (Liu et al., 2015; Ruprecht et al., 2015). Unlike the typical blebs described in the literature (Charras et al., 2008), stable blebs **overcome retraction and establish a constant actin flow**. Stable blebs are a new type of cellular structures that amoeboid cells can use to migrate, analogous to filopodia or lamellipodia for mesenchymal cells. In a single cell, multiple blebs form and compete against each other, so that eventually, a single bleb drives the migration (Liu et al., 2015; Ruprecht et al., 2015). Previous studies showed how Myosin II activity produce a stable steady-state in large single migrating blebs by driving a large scale actin retrograde flow (Liu et al., 2015; Lomakin et al., 2019).

Nevertheless, the initial steps of stable bleb formation following confinement, their 'life and times' (Charras et al., 2008), have not yet been described in a systematic, quantitative manner. More generally, the simplicity and accessibility of the stable bleb as a model system for cortical flows can provide a quantitative understanding of the emergence of polarity in actomyosin systems, which constitute the basis of migration (Callan-Jones and Voituriez, 2016). Indeed, stable blebs are solely driven by actomyosin and constitute an almost pure membrane-actomyosin reconstituted system, but harbor features such as motility that is not yet possible to reproduce with *in vitro* systems (Ierushalmi et al., 2020; Vogel et al., 2020).

This project aims to understand the mechanisms for bleb stabilization and the emergence of retrograde flows. We will do so by providing a detailed and quantitative description of bleb morphogenesis and bleb stabilization in confined cells, using microfluidics to control the confinement height, coating, and topography combined with live-cell imaging, focusing on the first few minutes after confinement.

Most of this study is based on quantitative analysis of timelapse movies. I would like to encourage the reader to watch the supplementary movies accompanying each figure when marked "**video available**." The title of the videos corresponds to the figure panels they complement. In many cases, although the still images and the quantifications

capture the essential aspects, the movies are extremely informative and convey some additional information which has not yet been fully quantified at that stage but make qualitative points which are important for the reasoning and the demonstration of the central finding of the study. Supplementary Videos are archived on https://doi.org/10.6084/m9.figshare.14053964.v1

1. Stable and transient blebs formed immediately after confinement contain different actomyosin profiles

Many organisms and model systems switch to bleb-based amoeboid motility upon confinement (Brunet et al., 2020; Liu et al., 2015; Ruprecht et al., 2015; Srivastava et al., 2020). Here, we chose to work with HeLa cells due to the robustness of the blebbing phenotype and the availability of already-made cell lines and reagents. To study the blebbing phenomenon, we detach HeLa cells and place them in the confiner device with a non-adhesive coating (**Figure 25** A) (Le Berre et al., 2014). Within a few minutes following confinement at 3µm, non-adherent HeLa cells display large blebs that protrude outwards from the cell body (**Figure 25** B). Qualitatively, the typical response to confinement consists of a **first phase** during which the cells form only round blebs, and a **second phase** where these first blebs have retracted and new blebs that can be more elongated appear (**Figure 25** C). To gather a quantitative description, we followed the dynamics of bleb formation using fast phase-contrast imaging during the first 5 minutes after confinement. We manually measured bleb height, width, and time of appearance. This detailed analysis showed that during the first phase of about 15 seconds, the mean aspect ratio of forming blebs is close to 1, corresponding to the round blebs of the first phase. The average aspect ratio then increased rapidly because new forming blebs in this second phase were narrower (**Figure 25** D top and right graphs). In this second phase, a fraction (about 20%) of very elongated blebs (AR>3) also appeared (**Figure 25** D lower graph).

The typical lifetimes, retraction speeds, and cytoskeletal organization of transient round blebs are well-known (Charras et al., 2008). We were then interested in comparing the dynamics of round and elongated blebs. Compared to round blebs, we found that elongated blebs have a longer lifetime. Nevertheless, when they retracted, their retraction speed was similar to the retraction speed of round blebs. Their longer lifetime was instead

due to the appearance of a stable phase between the extension and retraction phases (**Figure 25** E).

This analysis shows that atypical elongated blebs form with a delay after confinement is applied. These blebs have two main characteristics: they are more elongated than the previous blebs (mostly because they are narrower), and they display a stable phase before retraction. The delay in their appearance means that they are not a direct mechanical consequence of confinement, contrary to the initial round blebs. While the round shape of the initial blebs results from a pressurized and detached pure plasma membrane (Tinevez et al., 2009), initially without a cytoskeleton, the elongated shape of the second phase blebs suggests the formation of an inner structure (Callan-Jones et al., 2016; Callan-Jones and Voituriez, 2013), which could also explain the stable phase.

To investigate this further, we conducted live-cell imaging of the actomyosin cytoskeleton. We used a cell line containing a copy of the MYH9 gene fused with GFP (**non-muscle myosin II A**, NMIIA) and the actin-binding probe lifeact combined with mCherry. In both round and elongated blebs, NMIIA changes its localization from mostly cytoplasmic to mostly cortical during the first 30 seconds following bleb formation. As previously described (Charras et al., 2008), a dense and homogeneous actomyosin cortex formed a rim all along with the membrane of round blebs (**Figure 25** F, G, **video available**). On the contrary, in most elongated blebs, we observed the formation of an internal gradient of both actin and myosin II (**Figure 25** F, H, **video available**).

How do these actomyosin patterns emerge after bleb appearance? As previously described (Charras et al., 2008), round blebs inflate to their final area within 5-10 seconds,and then accumulate actomyosin at the edge and retract within a minute (**Figure 25** G, bleb area quantified in **Figure 25** I, black line). On the contrary, elongated blebs keep expanding during the first minute and stay at an equilibrium area for several minutes (**Figure 25** H; bleb area quantified in **Figure 25** I, black line). Round blebs first accumulate actin, then NMIIA with a few seconds delay. Actin and NMIIA have a more visible accumulation on the distal membrane, correlating with the retraction phase. When they first appear, elongated blebs are also spherical, meaning that they most likely correspond to pure membrane detachment, like round blebs. They also initially present a similar and low actomyosin density in the proximal and distal membrane. As the bleb grows towards its equilibrium maximal projected area, the bleb's proximal side gets enriched in both actin and myosin, while, contrary to round blebs, the distal side gets depleted (**Figure 25** I). Measuring the cortical actomyosin profiles at the time of bleb maximal projected area

confirmed that round blebs displayed a homogeneous cortex, while elongated blebs acquired a gradient of actomyosin density (**Figure 25** K). Altogether, these results indicate a role of the cytoskeleton in the different dynamics of round and elongated blebs formed following confinement. Round blebs showed the same lifetime (~60 seconds) and cytoskeletal organization as transient blebs described in the literature (Charras et al., 2008). Although smaller at these early time points following confinement, elongated blebs were reminiscent of the previously described large stable blebs driving cell migration under confinement (Liu et al., 2015).

From these observations, we conclude that three key parameters discriminate between the two types of blebs formed after confinement: their lifetime, shape, and internal organization of actomyosin. We studied these three parameters at the population level to determine if they constitute two distinct categories or display a phenotypic continuum. We defined a polarity index to describe the polarization of the cytoskeleton in the bleb ($Polarity\ index = (\rho_{proximal} - \rho_{distal})/(\rho_{proximal} + \rho_{distal})$, where ρ is the actin or NMIIA cortical density). When the cytoskeleton is mostly at the proximal membrane, $Polarity\ index \cong 1$, and when the cytoskeleton is homogeneous, $Polarity\ index \cong 0$. We plotted, for every single bleb, its aspect ratio versus its polarity index and color-coded its lifetime. This plot shows two well-defined groups of blebs: **round, homogeneous, short-lived blebs** versus **elongated, polarized, and long-lived blebs** (**Figure 25** L). The lack of intermediate phenotypes, which is even more evident on the NMIIA polarity graph, suggests that, while all blebs are initially round free membrane devoid of actomyosin, their evolution in time diverges into two groups, one which forms a distal cortex and retracts, and one which forms a gradient of actomyosin and remains stable. We thus choose to call them transient and stable blebs. Importantly, transient blebs can appear from time zero and at all later time points, while the first stable blebs appear at least 15 seconds after confinement. This delay suggests that stable blebs require an additional mechanism that drives the formation of an actomyosin gradient instead of a distal cortex. Recent work from our lab showed that confinement induces, within a few tens of seconds, the activation of NMIIA due to a signal coming from nuclear deformation (Lomakin et al., 2019). We thus quantified the cortical enrichment of NMIIA following confinement in our experiments and found that it correlated in time with the appearance of elongated and stable blebs (**Figure 25** G).

We thus hypothesized that the phenotypic bifurcation leading to either stability or retraction depends on NMIIA activation.

2. Activation of NMIIA by cPLA2 and Ca2+ is required to trigger cortical contractility and formation of stable blebs

To further test this hypothesis, we characterized the contractile response to confinement, a functional readout of myosin II activation, and its relation to elongated blebs' appearance. To do so, we used an AFM device equipped with a FIB-sculpted flat cantilever coupled with a confocal system (***Figure 26*** A). This setup allows for simultaneous live-cell imaging and force recording (Fotiadis et al., 2002; Lomakin et al., 2019). For this part, we analyzed unpublished raw data provided from a set of experiments performed by A. Lomakin and C. Cattin in the lab of D. Müller.

As reported before (Lomakin et al., 2020), the response of NMIIA to confinement by the AFM cantilever involves a rapid change in the localization, from cytoplasmic (globular monomers) to cortical (minifilaments), as seen with the PDMS confiner (***Figure 26*** B, ***Figure 26*** C). To quantify this transition, we used the coefficient of variation of the NMIIA signal in the whole cell (CV = σ/μ). To calculate it, we subtract the background outside the cell and calculate the mean signal and its standard deviation on a mask covering the entire cell area. The CV increases steadily from 10 to 90 seconds after confinement to reach a plateau. We define this plateau as the “maximum myosin clustering” time, at which myosin has reached a new equilibrium in the confined state.

The force response followed an initial increase followed by a fast decay typical of elastic response. Despite the significant cell-to-cell variability, the relaxation phase was perturbed by an active force response at ~15 seconds, which we labeled “active force onset” (figure 2 B, right). This “bump” was particularly evident when the time was normalized by this force peak (***Figure 26*** B, center). The active response amplitude can be estimated in comparison with the force curve in the absence of myosin activity (Y27632 treatment, ***Figure 26*** B). Following the active force onset in control conditions, the force response slightly increased for another 10 seconds to slowly decay again. The timing of active force onset coincided with the beginning of cortical NMIIA clustering (***Figure 26*** B, C, and D). These results show that the onset of myosin clustering and the active force response corresponds to a delay of about 15 seconds, similar to the delay before the long blebs' appearance.

We first performed a detailed analysis of bleb formation together with force response and myosin clustering on two representative cells, which displayed different timing in the onset of the force response. This analysis allowed us to define the sequence of events

following confinement: i) appearance of round blebs concomitant with the fast elastic relaxation; ii) onset of NMIIA clustering and active force response onset, concomitant with retraction of the first set of round blebs formed during the confinement; iii) appearance of elongated blebs and slow decrease of the active force; iv) maximum NMIIA clustering and persistant appearance of both round and long blebs. These two cells show different timing of these events, but the same order and the same correlation of events (***Figure 26*** E, **video available**) and are representative of the entire set in which these quantifications have been performed (n=32 cells). These observations show that long blebs appear only after the onset of the active force response, suggesting a role for NMIIA activation.

To verify NMIIA activation's role in the formation of elongated blebs, we analyzed the results from a small drug screening performed upon 3 µm confinement with the AFM (***Figure 26*** F). $cPLA_2$ and Ca^{2+} are the key molecular players in the confinement response of HeLa cells (Lomakin et al., 2019). This response involves the translocation and insertion from the cytoplasm to the inner nuclear membrane of the Ca^{2+}-dependent enzyme $cPLA_2$, promoting the conversion of phospholipids into arachidonic acid. Arachidonic acid is a signaling molecule that activates myosin (Garcia et al., 2009; Gong et al., 1992) and the precursor for the synthesis of other signaling molecules termed eicosanoids, mediating paracrine signaling and inflammation. The release of Ca^{2+} after confinement has a double effect activating $cPLA_2$ and non-muscle myosin (Scholey et al., 1980; Somlyo and Somlyo, 2003). We used two pharmacological treatments targeting specifically the $cPLA_2$ pathway by AACOCF3 (20µM) and the intracellular calcium channels by 2-APB (100µM), which specifically inhibit myosin II activation upon confinement without affecting its basal activity before confinement. We then analyzed the bleb phenotypes immediately after confinement (round blebs, labeled as “early response”) or after the onset of the active response in control cells (after 15 seconds, elongated blebs, labeled as “late response”). As a control, non-specific chelation of intracellular Ca^{2+} (BAPTA-AM) and ROCK inhibition (Y-27632) disrupted both the early and late blebs' behavior (***Figure 26*** F).

Conversely, we found that the inhibition of the $cPLA_2$ pathway by AACOCF3 or the Ca^{2+} release from intracellular compartments by 2-APB did not alter the early response (formation of round blebs) but inhibited the late response (appearance of elongated blebs). Instead, we observed only round blebs at all time points following confinement. Other treatments, such as the inhibition of apoptotic caspases, Rac1 or Cdc42 inhibitors, or extracellular Ca^{2+} chelation did not yield any significant differences in early or late

response or any differences in bleb formation. This result qualitatively shows that elongated bleb appearance depends on the same pathway as confinement-induced NMIIA activation.

To understand the relationship between contractility onset and blebbing, we focused on the two conditions that showed differences in the later response but not in the immediate response (2-APB and AACOCF3). We compared them to their respective controls (labeled “control”, “control without FBS”, respectively), and a condition inhibiting myosin activation (Y-27632). AACOCF3 and 2-APB-treated cells showed an intermediate phenotype between the positive and the negative controls, showing limited cortical accumulation of NMIIA and blebbing (***Figure 26*** G, **video available**). We then measured the coefficient of variation of the NMIIA signal (a measurement for clustering), the force exerted against the cantilever, and the mean retraction speed in the first 5 minutes after compression. These parameters confirmed that 2-APB and AACOCF3-treated cells show an intermediate phenotype in all three parameters, indicating a milder activation of NMIIA compared to control (figures 5 H and 5 I), but not a full inhibition, as expected from previous work. 2-APB and AACOCF3-treated cells formed fewer blebs per cell (figure 5 J) and mostly round transient blebs (***Figure 26*** K). Importantly, 2-APB and AACOCF3-treated cells produce dynamic transient blebs, confirming that basal myosin II activity was preserved. This suggests that basal myosin II contractility is enough to trigger the formation of round blebs and their retraction but not to trigger elongated/stable blebs.

Initial confinement produces very high pressure, as assessed by the force curve right after confinement, without producing any elongated, but only round blebs, while myosin activation following confinement, which produces only a mild increase in pressure, seems required for long/stable bleb formation. We thus hypothesize that a higher threshold in myosin activation, and not general contractility/internal cell pressure, is required to produce elongated stable blebs. This interpretation can explain the delay in the formation of stable/elongated blebs after confinement.

3. Depletion of actin from the bleb front is required to establish a retrograde flow during bleb formation and avoid retraction

A fundamental difference between round and elongated blebs is that most elongated blebs display a stable phase or even never retract (defined as reaching a plateau in their

projected area). We then asked what governs this stable phase. We noticed that a small number of blebs retract despite being elongated. We thus focused on comparing transient elongated blebs versus stable elongated blebs. We imaged actin and NMIIA in confined cells simultaneously and performed PIV on the NMIIA channel to visualize the extent and amplitude of cortical flows. We first focused on two representative blebs, one stable (***Figure 27*** A, B, **video available**) and one transient (***Figure 27*** C, D, **video available**). The evolution of the stable bleb morphology shows an increase in the projected area followed by a plateau while the proximal side pinches (***Figure 27*** A, quantified in ***Figure 27*** B bottom graph, **video available**). The transient bleb shows an increase in the projected area, followed by a decrease corresponding to the retraction and a narrowing of the proximal side resembling that of the stable bleb. The main difference between the two blebs is that the transient bleb area stops growing before the onset of an actomyosin retrograde flow. The arrest in the area growth corresponds to the time at which the actin cortex fully covers the transient bleb's distal tip. Stable blebs do not accumulate actin in the bleb front at any point, and the flow onset does not lead to a reduction of the projected surface area (***Figure 27*** B). Transient blebs also delay bleb formation and flow onset, but the flow onset appears after forming a complete actin cortex, including the distal tip, and corresponds to bleb retraction (***Figure 27*** D). Imaging confined cells with both membrane and actin markers showed that long blebs were generally devoid of actin at their distal tips (***Figure 27*** E). We hypothesize that the blebs' stable versus transient behavior depends on the presence or absence of actin at their distal tip at the time of myosin II activation and onset of retrograde flow.

To quantitatively analyze the temporal patterns across many stable and transient blebs, we aligned and averaged projected area dynamics, distal actin density, and coefficient of variation of the NMIIA signal relative to flow onset (assessed visually). Stable blebs start myosin clustering ~20 seconds before flow onset and reach a maximal projected area ~15 seconds after flow onset. Transient blebs start myosin clustering ~10 seconds before flow onset and get a maximal projected area a few seconds before the time of flow onset (***Figure 27*** F). Stable blebs persistently keep the front free of actin, whereas transient blebs start building a front cortex ~15 seconds before flow onset (***Figure 27*** G). These observations confirm that transient blebs display distal actin accumulation before the onset of retrograde flow, while stable blebs never accumulate distal actin.

Going back to the two representative blebs shown in panels A and C of ***Figure 27***, we analyzed the temporal evolution of the cortical actin distribution along the length of the bleb (***Figure 27*** H). Interestingly, both blebs displayed a similar flat distribution at early

times, but they progressively drifted apart. The cortical gradient increased over time in stable blebs, with an accumulation of actin at the bleb neck and depletion at the distal tip, following the onset of the retrograde flow. On the other hand, the transient bleb cortex became more homogeneous with time (***Figure 27*** H). These results suggest a mechanism for actin depletion at the tip of stable blebs, potentially due to cortical flows, and the assembly of a complete cortex in retracting blebs before the establishment of a flow, drifting these two states apart.

Altogether, these results led us to propose a conceptual model for bleb stabilization during bleb growth (***Figure 27*** I). We considered two parallel processes occurring during bleb formation: actin cortex assembly by polymerization, and NMIIA activation. Actin cortex formation stalls membrane outgrowth, whereas NMIIA activation triggers contractility and the onset of retrograde flow. Each process occurs with a typical timescale, which can vary in each bleb. The timing of the retrograde flow onset corresponds to NMIIA reaching enough contractile strength to pull the actin network (Callan-Jones et al., 2016; Callan-Jones and Voituriez, 2013). The difference between the timing of actin cortex assembly and NMIIA activity thus determines whether the retrograde flow onset occurs before or after the actin cortex has populated the entire bleb membrane. If the actin cortex fully reforms before flow onset, the onset of the cortical flow will retract the bleb membrane, and the actin cortex will restrain the membrane from expanding upon the increase in pressure generated by the contraction. On the other hand, if the flow onset occurs before complete cortex formation, the contractile action of NMIIA on the actin network will deplete the bleb front of actin, and thus stabilize a cortical actomyosin gradient as proposed in previous models for the steady-state of large motile blebs (Callan-Jones et al., 2016; Liu et al., 2015; Ruprecht et al., 2015). This depletion of actin from the bleb tip will also enable membrane protrusion upon increased pressure generated by the actomyosin contraction.

To test this model's first prediction, we replotted the graph from ***Figure 25*** K to consider bleb stabilization. We found that the actin polarity is a better predictor for the occurrence of a stable phase than the NMIIA polarity. Stable blebs all display an actin polarity index $\gtrapprox 0.8$, and transient blebs all display an actin polarity index below this threshold value. On the other hand, NMIIA polarity is a good predictor for bleb shape (round versus long), while actin polarity is not (***Figure 27*** J, K), which can be explained from previous physical models (Callan-Jones et al., 2016). Comparing actin and myosin polarity indexes for stable and transient blebs shows that myosin can get polarized in a subset of transient blebs where actin is not polarized (***Figure 27*** L). Our working model predicts that the

relative time of maximal membrane maximal extension (membrane stalling) and flow onset after bleb initiation should predict the stability or retraction of elongated blebs. Plotting these two times against each other and color-coding bleb stability showed a clear separation between stable and transient blebs, confirming our model predictions. The time of flow onset in transient blebs was always longer than the time of membrane stalling, and the opposite was true for stable blebs (***Figure 27*** M).

4. Myosin activation promotes bleb retraction or stabilization depending on the blebbing state

(NOTE: this part is shown because it contains interesting preliminary results and helps the reasoning, but further data and quantification will support it before publication)

To more directly test this prediction of the model, we developed optogenetic HeLa cell lines to control the activity of RhoA, Rac1, and Cdc42 in the bleb after it formed. We imaged the confined cells in a TIRF microscope equipped with a DMD (digital micromirror device), allowing spatial control of the illumination at a micron level (see methods on Optogenetic experiments, page 78). The optogenetic system consists of the CIBN/CRY2 *A. thaliana*-derived proteins, which dimerize when exposed to blue light (***Figure 28*** A). In the dark, the two proteins slowly lose their interaction. CIBN is bound to the membrane by a CAAX motif, and CRY2 fused with an exchange factor for the small GTPase targeted. We first used ArhGEF11, a guanine nucleotide exchange factor (GEF) for RhoA, which promotes the conversion of GDP by GTP, leading to the active state of RhoA, an upstream regulator of Myosin II, often used in optogenetic studies to modulate contractility (Valon et al., 2017). Blue light controls the spatiotemporal recruitment of ArhGEF11 to the plasma membrane. The cell line HeLa GFP-CIBN-CAAX mCherry-CRY2-ArhGEF11 lifeact-iRFP670 allows for imaging of the CIBN partner on the membrane (GFP), the RhoA activator (mCherry), and the actin (iRFP670, deep red). As expected, we observed the recruitment of the GEF to the illuminated membrane within a minute of exposure (***Figure 28*** B, **video available**). ArgGEF11 recruitment promoted global contractility (higher blebbing area), but locally (at the site of illumination) inhibited blebbing and caused edge retraction (***Figure 28*** B, C).

We chose cells with a large stable bleb and localized blue illumination at the protrusion front to study RhoA activity's effect on the protrusion (to avoid illuminating the entire cell

and activating global contractility of the cell). When activation ocurred at the tip of a bleb in the stable state (***Figure 28*** D, **video available**), ArhGEF11 accumulated mostly at the bleb's neck, probably due to the actomyosin retrograde flow (***Figure 28*** E, F, G). Conversely, when activation occurred at the tip of a bleb that already initiated the retraction phase (***Figure 28*** H, **video available**), ArhGEF11 concentrated mostly at the site of activation (the distal tip, ***Figure 28*** I, J, K). For the three blebs in the stable phase assayed (***Figure 28*** L), the bleb remained stable, with an apparent change of morphology of the tip which became more smooth and regular (phase-contrast images on ***Figure 28*** F and J), suggesting a further depletion of actin from the bleb tip. Conversely, activation on the four blebs that had initiated retraction accelerated the retraction (***Figure 28*** K, L), as predicted by our working model. Using validated constructs for activation of other small GTPases (TIAM1, T-*lymphoma invasion and metastasis*, for Rac1; and *intersectin*, ITSN, for Cdc42) (de Beco et al., 2018), we did not observe any effect following activation, neither on blebs in the stable phase or blebs in the retraction phase. This observation served as a control for the specificity of contractility activation and showed that modulation of actin polymerization (Rac1) or polarity determinants (Cdc 42) did not affect the bleb behavior.

Overall, these results confirm the differential role of myosin activity in stable and transient blebs and our working model. Myosin II activity upregulation leads to either bleb stabilization or retraction depending on the actin cortex's state at the time of activation. Note that on the current results, the quality of the imaging of the actin probe did not allow to make a clear conclusion on the state of actin at the bleb tip at the time of illumination, and we inferred it from the state of the bleb and the blebbing dynamics from the phase-contrast (stable phase versus retractile phase).

5. Retracting blebs can be switched back to a stable state by increasing external compression.

(NOTE: this second series of perturbation experiments is also at the preliminary results phase and will be expanded before publication)

So far, our results suggest that NMIIA activity stabilizes blebs by depleting actin from the front tip and promotes retraction of blebs with a fully polymerized actin cortex. Another consequence of an increase in NMIIA activity is to increase the tension of the cell surface

and, thus, its internal pressure (Petrie et al., 2012; Sorce et al., 2015). The increase of internal pressure triggers blebbing when the pressure becomes high enough to lead to membrane detachment from the actin cortex (Cattin et al., 2015; Charras et al., 2005). We thus asked whether the increase in pressure driven by the activation of myosin II upon confinement could also contribute to the switch between transient and stable blebs. To test that independently of NMIIA activity, we varied the pressure in the confinement device after the blebs had already formed. We thus first confined cells, inducing blebbing, with the variety of bleb types described earlier in the study. We then applied further compression after a few minutes (***Figure 29*** A, **video available**). As expected, this led to the general expansion of most already formed blebs, but, contrary to the very initial blebs formed upon the initial compression, the vast majority of the expanded blebs formed upon the second compression were immediately stable, with internal retrograde flow and a tip devoided of actin. This observation suggests that internal pressure can also stabilize already formed blebs.

To gain further insights into a potential difference between transient and stable blebs when pressure increases, we used the fine control of pressure allowed by our digital pressure controller to apply either a slight additional pressure or a larger amount. Upon a small increase in pressure, which corresponds to a small roof height decrease (***Figure 29*** B, **video available**), some blebs expand, as in the previous case, but some do not. A closer examination, using Lifeact-mCherry to visualize the state of actin in the blebs, showed that only blebs devoid of actin at their distal tip expanded. In contrast, the blebs with a fully formed actin cortex resisted the pressure increase and even kept retracting (***Figure 29*** B, **video available**, quantification of the new projected area, and zoomed regions in ***Figure 29*** C). We concluded that in this case, the increase of intracellular pressure we generated was enough to expand the blebs in the stable phase (devoid of actin at their distal tip) but did not perturb the blebs in their retraction phase (with actin at their distal tip). This observation suggests that the actin at the distal tip can hold the membrane under a pressure that would otherwise expand a free membrane bleb. It also suggests that the increase of pressure generated by the activation of myosin II could expand and thus contribute to stabilizing the blebs in their stable phase (by moving the membrane at their tip further away from the actin cytoskeleton, thus delaying the retraction phase). Together it explains how both types of blebs can co-exist in the same cell. It also suggests how NMIIA activation contributes to maintaining a distal tip free of actin, thus contributing to bleb stability: by generating a retrograde flow and producing an increase in pressure that pushes the membrane forward.

We then produced a more considerable increase in pressure and then observed that all blebs expanded, whether in a stable or retractile phase before the second compression. ***Figure 29*** D, E, and F show representative examples of blebs switching to stable behavior. ***Figure 29*** D shows a retracting bleb (full actin cortex, images on the left before the second compression), switching to a winding behavior with a partially free tip (middle images) and a fully developed persistent bleb with a distal tip free of actin and elongated shape (images on the right). ***Figure 29*** E and F show two more examples: membrane detachment led to the fusion of adjacent blebs into a single stable bleb, with a full internal actin reorganization and polarization within a few seconds.

We can conclude from these observations that retracting blebs can be switched to stable blebs following a large enough increase in pressure, leading to the detachment of the membrane from the actin at their distal tip (a bleb-on-a-bleb). This event is followed by a reorganization of the actin into a polarized and flowing network, dense at the neck and loose at the tip, which represents a stable configuration as described before (**Figure 25**) (Liu et al., 2015; Ruprecht et al., 2015). Overall, these experiments suggest that depletion of actin from the distal tip of a bleb is necessary and sufficient to induce a switch to a stable state, even starting from a retracting state.

6. Stable blebs can spontaneously switch between blebbing modes, displaying persistent, unstable/winding, or transient retraction phases.

To better understand the role of actin depletion in protrusion stability, we followed the dynamics of already formed stable blebs. For that, we focused on large stable blebs that have a lifetime of several hours. Even hours after bleb formation, we observed temporary retraction events associated with an actin enrichment at the bleb tip (***Figure 30*** A, B). These retraction vents caused blebs to decrease their length and decrease the retrograde flow speed (***Figure 30*** A). Notably, at the onset of each retraction phase, the actin flow concentrated towards the proximal side of the bleb (the neck) and slowed down during retraction (***Figure 30*** B, C, **available video**). Because the retrograde flow is instrumental in depleting the actin from the distal tip, this suggests that the initiation of a retraction phase could self-reinforce as the increase in the actin at the distal tip correlates with a decrease in the flow speed, potentially due to a direct mechanical coupling from front to back of the bleb, thus favoring actin assembly at the tip.

We focused on the dynamics of the membrane at the bleb front, and we observed that stable blebs displayed different front dynamics, which we classified into three types: "**persistent**," "**winding**," and "**unstable**" (***Figure 30*** D and E, all with **available videos**). Persistent blebs do not significantly change shape over time, winding blebs have waves of membrane tearing from one side to the other, and unstable blebs grow by serial blebbing events on the front side. There are numerous reports in the literature describing persistent blebs (Liu et al., 2015; Ruprecht et al., 2015), the so-called "circus blebbing," driven by membrane tearing (Charras et al., 2008; Fujinami and Kageyama, 1975; Graziano et al., 2019), and unstable blebbing, common in *D.* discoideum (Srivastava et al., 2020). However, no study has systematically determined the differences between these blebbing modes, which we found can all co-exist on the same cell.

We imaged actomyosin dynamics to find out how the cytoskeleton was contributing to these differences. We did not observe any apparent differences between the NMIIA localization or structure between the three types (**Figure 30** E, **available videos**). However, imaging the actin cytoskeleton revealed a simple picture consistent with our working model: stable blebs has a distal tip entirely devoid of actin, while winding bleb displayed repeated events of membrane detachment from the distal tip, with a region free of actin moving alternatively from one side to the other of the tip of the bleb while the actin reformed along the detaching membrane, always leaving just a part of the distal tip free of actin. These dynamics produced actin structures in the form of successive arcs that vanished as they moved towards the cell with the retrograde flow (visible as bumps on the linescans shown in **Figure 30** E on the right **available video**). Unstable blebs corresponded to repeated blebs-on-blebs, forming actin arcs moving backward and vanishing, but with distal tips fully closed by an actin cortex between each blebbing event. In comparison, retracting blebs did not display internal actin arcs but just a fully formed and retracting cortex (***Figure 30*** E, line scan shows no bumps, as persistent blebs). These differences in the cortex organization emphasize the role of front actin in the dynamics of the bleb tip and highlight the main modes we observed.

In addition to displaying various modes at their distal tips, stable blebs can also spontaneously switch between these modes within a few minutes. The transitions themselves displayed characteristic patterns. The winding and unstable protrusion dynamics were often transient states lasting only a few minutes, during transitions between a retracting and a persistent bleb protrusion or vice versa. ***Figure 30*** F shows examples of representative cases of transitions with intermediate patterns (**available videos**).

Winding blebs displayed a broad front and an irregular contour, whereas persistent blebs were more elongated and regular (***Figure 30*** G, **video available**). During the transition, the blebbing angle went from a stereotypical swinging movement to a persistent blebbing angle of around 0° (in the axis of the main bleb body, ***Figure 30*** G, right graph), and from leaving cortex scars at the front to have a hollow shell (see also additional results ***Figure 38***). As the bleb elongated in the transition to a persistent state, the actin gradient approached the distal tip (***Figure 30*** G kymograph and ***Figure 30*** H right graph). Normalizing by the length, the actin gradient remained unchanged (***Figure 30*** H left graph). The data suggests that even though actin seems responsible for the front dynamics, the overall actin gradient does not change significantly during the transition, pointing to the actin at the distal tip as the main element responsible for the bleb tip dynamics and the transitions from retracting to persistent and vice versa. The transitions correspond to states in which the retrograde flow and the pressure produced by NMIIA are enough to produce new membrane detachments in a bleb in which actin has reached the front tip. The observed trends are potentially due to the reinforcing feedback described earlier, which converges either to a persistent or a transient bleb.

As a working model, we proposed that the motor activity of NMIIA in blebs has two different roles in bleb stabilization: to create cortical flows that remove actin from the front and increase intracellular pressure to advance the front membrane. At the distal tip, actin can bind to the membrane and hold it against the internal pressure, eventually bringing it backward with the retrograde flow. The retraction of the front membrane will depend on the force balance between i) the number of actin filaments bound to the membrane, ii) the binding force of each filament to the membrane, and iii) the membrane tension, a function of the intracellular pressure. If the membrane tension is higher than the actin-membrane binding force, the front membrane will not retract. Nevertheless, if the intracellular pressure decreases, just a few filaments will be able to pull enough to retract the front membrane, producing winding or unstable blebbing. When made more quantitative, these observations will serve as a basis for a physical model explaining the dynamic behavior of the stable bleb protrusions.

Substrate friction or drugs perturbing actin turnover can modify the steady-state actin gradients in stable blebs (Liu et al., 2015; Ruprecht et al., 2015). Following our model, we hypothesized that conditions that deplete actin from the front or perturb actin-membrane attachment should promote persistent blebs. Conversely, conditions that bring the actin gradient forward and increase actin density at the front should increase the fraction of winding or unstable blebs. We analyzed the fraction of persistent, winding,

or unstable blebs in cells every minute under different experimental conditions based on membrane and cortex dynamics. We chose two conditions known to change the steady-state gradient: polylysine coating (increased substrate friction, increasing steady-state actin concentration at the front) (Ruprecht et al., 2015) and jasplakinolide (promotes filament stabilization, decreases steady-state actin concentration at the front) (Liu et al., 2015). We also treated cells with NSC668394 compound, a cell-permeable quinoline that directly binds to ezrin and inhibits PKCι-mediated ezrin phosphorylation at Thr567, ezrin being a primary actin- membrane attachment. Consistently, polylysine coating increases the fraction of winding and unstable blebs, and jasplakinolide and ezrin inhibition increase the fraction of persistent blebs (***Figure 30*** I).

7. Cortical actin controls protrusion dynamics in motile bleb fragments

The blebs we have considered so far were forming from the cell body and remained attached to it, which has consequences for several parameters. First, the bleb and cell body membrane are continuous, so a significant **membrane reservoir** is available. The bleb's total surface area could thus change as it expands or retracts (we have not estimated to which extent the bleb's total membrane is changing in the previous experiments). Second, the pressure inside the bleb can have two sources: the flowing and contractile bleb actomyosin cortex and the **cell contraction** (we have not estimated to which extent the bleb volume changes during the experiment, which would give an estimate of the fluid flows between the main cell body and the bleb). Third, the friction produced by membrane-cortex attachment on the bleb neck and cell body restricts forward membrane flow. This friction restrains the capacity of the forces acting on the bleb membrane to produce an effective protrusion and holds the bleb in place. In previous works considering late very large blebs, the stable bleb reached a size comparable or larger than the cell body, and the actomyosin flow in the bleb was able to drive the motion of the entire cell (Liu et al., 2015; Ruprecht et al., 2015).

To assess the importance of these aspects in the dynamics of blebs, we turned to a subfraction of the blebs fully detached from the main cell body. These motile fragments initiated spontaneous and autonomous migration. We frequently observed such events when cells were confined on a PLL-coated surface, likely because the enhanced friction provided enough engagement between the retrograde actomyosin flow and the surface to generate propulsion forces to detach the bleb. These motile fragments initially formed

similarly to other blebs in the stable state, and as they expanded and moved away from the main cell body, the membrane neck at their base eventually ruptured. The rupture event did not affect their motile behavior nor their general shape, and they eventually looked very similar to regular stable blebs, with an elongated shape and a gradient of actomyosin from front to back (***Figure 31*** A). Contrary to stable blebs, these fragments, once detached from the main cell body, displayed persistent and fast motility for hours, at speeds of 5 to 15 µm/min.

Similarly to stable blebs, cortical actin inhibited membrane protrusion in motile fragments. The membrane only protruded in zones free of cortical actin. Cortical actin accumulated at the membrane a few seconds before the protrusion stalled (***Figure 31*** B, kymographs, **video available**). The overall similarity in shapes and front dynamics between blebs and motile fragments suggested that most of what we described before is independent of the main cell body (flows of membrane or fluid from the cell body): a bleb-autonomous behavior. The difference with the attached blebs is that actomyosin forces induce motion instead of being counterbalanced by resisting forces from the cell body. We thus analyzed the relation between actin dynamics and membrane protrusion in these fragments, which represent a simpler version of a motile cell.

We developed an image analysis pipeline to study the correlation between actin and edge velocity. First, we acquired a middle-plane actin-GFP image on a confocal spinning disk. We manually segmented a few frames and fed into the machine-learning software Ilastik, which then segments the full movie (Berg et al., 2019). With the mask and the actin signal, we use the Fiji-based plugin ADAPT (Barry et al., 2015) to extract a map of edge velocities and intensities. We studied the relation between the edge velocity and the intensity using a home-made cross-correlation Python script to normalize, average, and plot the results (***Figure 31*** C).

We could then link the edge velocity and the actin intensity at each point of the contour and time point. A simple analysis plotting the distribution of edge velocities against the binned densities (***Figure 31*** D) at all time points showed the same conclusion suggested by the kymographs in ***Figure 31*** B: actin density stalls protrusion above a threshold density. At contour points with low actin densities, edge velocity is positive. We observe a sharp threshold density at which protrusion is not favored anymore. Intermediate actin density, the edge velocity is zero, and at increasing density, edge velocity gradually becomes more negative (retracting edges).

To understand the spatiotemporal relation of actin density and edge velocity, we performed a cross-correlation analysis. We classified the motile fragments according to the three states of front dynamics we already observed in stable blebs: **persistent**, **winding**, and **unstable** (***Figure 31*** E, **video available**).), and plotted the cross-correlation analysis for each blebbing state: edge velocity autocorrelation, actin vs. edge velocity cross-correlation, and $d\mathrm{actin}/d\mathrm{t}$ vs. edge velocity cross-correlation. ***Figure 31*** F shows the cross-correlation matrices for representative examples of **persistent**, **winding**, and **unstable** states. ***Figure 31*** G shows the same fragments again but plotting the value of the correlation coefficient along either the line of zero time lag, $\Delta t = 0$, for various spatial shifts, which gives the length scale of the correlation; or for zero spatial shift, $\Delta s = 0$, which gives the temporal correlation fo events occurring at the same place. ***Figure 31*** H shows the same curves averaged over all fragments (n=17).

This analysis gives a detailed description of the relation between the actin density and edge velocity in the three cases. Here we point to the main features and their meaning. As expected from the behavior observed in the movies, the edge velocity and actin intensity have a pronounced negative correlation at zero time lag. The zero-lag means that the maximum edge velocity occurs at the time and places of lowest actin density, and vice versa: the highest retraction speed occurs at the time and places of highest actin density. There is an interesting pattern emerging when we compare the change in time of the actin density ($\mathrm{d}actin/\mathrm{dt}$) and the edge velocity: we find a negative correlation peak at -1.5 seconds and a positive correlation peak at +8.5 seconds. Taking together our observations of the movies and the analysis of the kymographs, we interpreted that the increase in actin signal starts 1.5 seconds before the decrease in edge velocity. Similarly, for the positive correlation peak, there is an increase of actin signal 8.5 seconds after high edge speed. Overall, the analysis indicates that the rise in cortical actin precedes the membrane stalling and is thus likely causing it, while membrane detachment and protrusion (high edge speed) is followed after a delay of about 8 seconds by repopulation of the membrane with actin, consistent with what is known for regular blebs. The difference is that here this applies to a motile fragment and regulates its motile behavior, with the unconventional aspect that actin assembly at the front is negatively correlated with the front protrusion, which is the opposite of the classical picture from lamellipodial protrusions but is consistent with recent findings resulting from a detailed analysis of cell protrusion behavior (Welf et al., 2019).

While actin inhibits protrusion in all the three types of motile fragments, others aspects differ between them. We compared the cross-correlation matrices (abbreviated as ★) for single fragment examples of each of the protrusion states (***Figure 31*** E and F). The edge velocity ★ edge velocity matrix can serve to calculate the mean "persistence" or "typical" time and width of protrusions by fitting an exponential. These parameters are analogous to the ones used to study cell migration trajectories as persistent random motion (Selmeczi et al., 2005). If taken with a lag space = 0, the normalized autocorrelation coefficient has the form of $p_{norm}(t) = e^{-\lambda t}$ where λ is the decay constant. We can extract the mean protrusion lifetime or persistence time: $\tau = \frac{1}{\lambda}$. If we take instead a lag time = 0, we will find the probability to have the form of $p_{norm}(x) = e^{-\lambda x}$ where we can extract the persistence width of the protrusion $\sigma = \frac{1}{\lambda}$. As expected, persistent fragments have the highest persistence time and width, and winding blebs have an intermediate persistence time and width (indicated on the top for each example in ***Figure 31*** F, G, and plotted against each other for all fragments in ***Figure 31*** I).

Remarkably, the actin ★ edge velocity and edge velocity autocorrelation matrices of winding blebs are tilted due to the traveling membrane tearing wave. The actin ★ edge velocity matrices show that the edge velocity and actin density are less anticorrelated in unstable blebs. We plotted the actin ★ edge velocity around $\Delta(s,t) = (0,0)$ – in other words, the correlation coefficient of actin and edge velocity – against the persistence times and persistence widths. This showed a negative trend, supporting this result. The $d\mathrm{actin}/d\mathrm{t}$ ★ edge velocity matrix loses the correlation pattern in persistent blebs, is tilted in winding blebs, and is pronounced in unstable blebs. In unstable blebs, the maximum correlation peak occurs typically at 4s earlier than the average curve, suggesting a more rapid cortex formation at protrusion sites. In conclusion, by providing a more quantitative description of the edge dynamics, this protrusion analysis depicts distinct patterns for each of the three states and confirms the classification we proposed for blebs. It also further comforts our working model for bleb dynamics and the role of actin at the bleb tip.

8. Reduction of the membrane-actin attachment promotes persistent blebbing in motile fragments

Following our working model, decreasing actin-membrane attachment should increase protrusion persistence. To verify this, we used the ezrin inhibitor drug NSC66839 (Bulut et al., 2012; Ghaffari et al., 2019). We observed that NSC668394-treated fragments could

still moved efficiently (5-15µm/min) but had different morphological features: ezrin-inhibited fragments displayed wider fronts, more significant projected area, and less unstable blebbing events. NSC668394-treated fragments also displayed faster cortical flows and slower front membrane velocity, suggesting less friction with the substrate. NSC668394-treated fragments had less frequently a uropod (representative images of control and treated motile fragments in ***Figure 32*** A, **video available**).). We manually classified the behavior of individual fragments every 25 frames (12.5 seconds), for the entire duration of the recording of their motion, into the persistent, unstable, winding, or retracting modes (***Figure 32*** B), depending on the actin and membrane dynamics at the front. This classification showed that NSC668394-treated fragments display persistent protrusion dynamics more often than control (averaged over all fragments on the top in ***Figure 32*** B) and individual fragments below).

We then performed an analysis of cortical actin density. Density at the front tip was lower in NSC668394-treated fragments but not in the rest of the cortex (***Figure 32*** D left graph, zoom on the front tip on the middle graph, the statistical significance of the difference on the right graph, showing that the difference is statistically different only for a few microns at the very front tip). We then looked at the cortex build up speed from a sparse cortex to a steady-state cortex (***Figure 32*** E). To do so, we followed in time cortical windows of 500 nm-depth as they flowed from the front to the back of the fragment. We defined the cortical buildup speed as the 1/t, where t is the time taken from cortex density=0.1 to 0.9, normalized by the intensity plateau. We found that the slope does not differ significantly between NSC668394-treated fragments and control, suggesting that ezrin inhibition does not change the nucleation rate of actin in the cortex. These results suggest that, ezrin either delays cortex formation initiation or perturbs the force balance between membrane tension and actin at the front, thus leading to less actin binding at the front or more detachment due to the retrograde flow. These findings are consistent with previous results on ezrin's role in bleb cortex formation (Charras et al., 2006).

Because tip dynamics dictate overall bleb shape, we also analyzed the differences in shapes between NSC668394-treated fragments and controls. Visually, treated fragments displayed more straight shapes than the control, and larger projected areas (***Figure 32*** C). We studied the shape of blebs more quantitatively by performing a principal component analysis (***Figure 32*** F). We identified six shape modes accounting for 95% of the variance. The primary shape mode (76.7% of the variance) consists of size variability. The second and third modes (7.2 and 6% of the variance) describe the transition between straight and curved shapes, and the other minor shape modes describe undulations of

the bleb contour (2.3, 2.2, and 1.1% of the variance). Overall, we confirm that the ezrin inhibition promotes blebs with a broader front than the control condition.

Lastly, we performed the same cross-correlation analysis as for control fragments to see any differences in edge velocity and actin dynamics in NSC668394-treated fragments (***Figure 32*** G). This analysis confirmed the increased persistence phenotype and the broader front of the ezrin-inhibited fragments, with larger persistence time and width. We found a more negative actin density ★ edge velocity correlation at $\Delta(s,t) = (0,0)$ (***Figure 32*** G), and a forward shift in the cross-correlation of change of actin density ★ edge velocity (***Figure 32*** H). This result is consistent with a more persistent migration and a delayed cortex formation after protrusion, also seen in the cortex density analysis (***Figure 32*** D).

These analyses suggest that despite a very subtle change in the front actin density, the depletion of ezrin has a strong phenotype on the shape and blebbing dynamics. These observations suggest that the negative effect of front actin density on protrusion dynamics is mediated by its degree of attachment to the front tip membrane. This further strengthens our working model's relevance, stating that the action of front actin is mediated by its pulling action on the front, inducing switches from protrusive to retracting behaviors. A prediction is that ezrin inhibition would hinder actin's ability to hold the front membrane against the inner pressure, thus displaying increased events of snapping of the membrane from the underlying actin. These events are illustrated in ***Figure 32*** I, and will be completed in the next part (**video available**)

In summary, the above results suggest i) the existence of a threshold in cortical actin density to allow for membrane protrusion, and ii) that dynamic interaction between actin filaments and membrane determine bleb shape.

This first part of the results allowed us to propose a general working model for the dynamic transitions between stable and transient blebs, from their initial appearance upon confinement to their steady-state dynamics. The classical mocel for a retractile bleb describes that the cortex assembly on the free membrane is followed by myosin recruitment and retraction of the bleb. Here, we propose that another bleb state can emerge when myosin activity is high enough during bleb morphogenesis. High myosin actility contract from the bleb base an incomplete bleb cortex and depletes of actin from the bleb front. This state is stable (Liu et al., 2015; Ruprecht et al., 2015) because the actomyosin retrograde flow as two actions: 1) it prevents front cortex formation and that

retractile forces pull on the front bleb membrane, 2) it generates an internal pressure which pushes the free membrane and tenses it. The internal pressure and membrane tension facilitates the detachment and removal of the nascent actin cortex from at the front and generates free membrane regions. We then showed that these stable blebs could display several blebbing modes depending on whether the bleb front is devoid of actin or displays transient actin assembly. Finally, we demonstrate that these blebbing modes are independent of the cell body, as these blebs can detach and form motile fragments that display the same phenotypes.

Because detaching stable blebs always display a motile behavior, we can conclude that stable blebs are simple autonomous motile structures. Because they have only a few elements and simple geometry and internal actin organization, we propose that they could serve as model systems to understand a simplified cellular motile engine in its most minute details. In order to do so, we turned towards more resolved microscopy methods and, in the second part of the results below, we show how the various dynamic aspects of stable bleb protrusion described above can be explained down to the behavior of single actin filaments, their nucleation, elongation, and bundling, by their association to myosin motors and their binding to the membrane. This produces, to our knowledge, the first report of the functioning of a motile cellular structure at this level of detail and understanding. We also propose that most of the complex dynamics of these motile objects are well captured by the percolation theory, which was already used to explain actin networks assembled in vitro, but not extended so far to cellular structures.

9. Actomyosin network assembly in stable blebs

The conditions necessary to see single filaments, at least in the least dense region of the bleb, at the proximal tip, were achieved in a custom-made set up by a high numerical aperture TIRF (objective Olympus NA=1.49, camera Andor Zyla 4.2) combined with microfluidics, which furthers reduces illumination background. Usually, the cortex consists of a dense meshwork, and even super-resolution techniques have a hard time resolving single filaments. We played with the advantage of the existence of a gradient of actin density in stable blebs. The gradient creates areas at the bleb front sparse enough to observe the organization and dynamics of actin bundles or single filaments. We used for most of these experiments a HeLa ActB-eGFP (named actin-GFP from now on) created using TALEN gene editing, named commercially as VizuCELL and

developed by Cellectis (Paris, France). This cell line provided better resolution without any apparent alteration in the shape or dynamics of blebs. We also used Lifeact-mCherry combined with MYH9-GFP (stable BAC cell line), which proved to be enough to visualize actin structures but with much less resolution than the actin-GFP cell line.

We first examined the actin network's general features in a stable bleb observed by high NA TIRF (***Figure 33*** A, **videos available**, see more examples in the supplementary information of ***Figure 33***). Visual examination reveals three regions with very distinct actin organization and dynamics, (the following describes a representative movie of a stable bleb):

1) at the proximal end of the bleb, actin is extremely dense and cannot be resolved but flows robustly towards the neck;

2) in the middle of the bleb, actin filaments are more sparse and could correspond to single filaments or bundles; this region, described in more details later, flows continuously and shows a purely translational motion, filaments keeping the same relative position from one image to the next;

3) the front region, with areas devoid of filaments or with short filaments and bundles not connected into a network, sometimes reaching to the very front of the bleb. In this region, filaments can display diffusive motion (‘jiggling’), suggesting they are not firmly bound and do not show persistent retrograde flow. The actin density in this region can change drastically in time: phases devoid of actin can be followed by actin enrichment, leading to more connected filaments, until it gets connected to the flowing region. Then, the flow removes the entire ensemble of new connected filaments in a bloc.

To gain more quantitative insight, we performed a PIV analysis on a 2-minute movie (***Figure 33*** A right image shows analysis on a representative bleb). The three regions were also appeared clearly in the PIV analysis, with a region without consistent flow (region **I**), a region of consistent parallel flow (region **II**), and a region of convergent flows at the proximal end (region **III**) (see more examples in the supplementary information of ***Figure 33***). Plotting characteristics of the actin meshwork and velocity field can further show these three regions from the distal to the proximal end (***Figure 33*** B), averaged over the bleb's width. As previously reported (Liu et al., 2015; Ruprecht et al., 2015), the actin density increases steadily towards the proximal end (***Figure 33*** B, top graph). The flow speed (same graph) first increases from the leading edge to reach a steady velocity

in what corresponds to region **II** and diminish towards the bleb base, reaching zero at the neck (which suggests that actin does not flow out of the bleb to the main cell body, as the analysis of the motile fragments already revealed). Plotting together the divergence of the flow field, its local order, and its correlation length also clearly established the existence of three distinct regions with the characteristic features observed before in a qualitative manner. Overall, the region **I** shows a low actin density and an inconsistent flow with a very low correlation length; region **II** shows a persistent fast parallel flow with high local order and correlation length, while the region **III** shows a high actin density with a persistent low-speed convergent flow, a high local order and an intermediate correlation length. Together, these results give a first image of the actin meshwork in the stable bleb with a 'gas-like' disordered distal front (region **I**), a flowing 'solid-like' intermediate region (region **II**), and a flowing contractile rear (region **III**).

We first focused on region **III** and imaged together actin (Lifeact-mCherry) and NMIIA (MYH9-eGFP). Most of the NMIIA signal concentrated in this region, with only very few individual myosin II clusters visible in region **I** and a few sparse small clusters in region **II** (***Figure 33*** C for a representative bleb, **video available**). PIV on the NMIIA channel confirmed the contractile regime of region **III** (***Figure 33*** C right image).

Stable blebs constituted simple and accessible living systems useful to study actomyosin dynamics. Like other biological molecules, NMMIA has inherent polymerization dynamics: NMIIA monomers assemble intro cortical minifilaments of ~30 molecules and ~300nm long. In the field, the classical model for the assembly of myosin clusters consists of i) myosin monomers turn into an open configuration and arrive at the actin cortex, ii) recruitment of monomers until the formation of a stable bipolar minifilament, iii) polarity sorting and network remodeling, iv) coalescence or coarsening of minifilament into contraction sites, at the center of asters. However, recent works have argued some aspects of this model, describing additional mechanisms for the establishment, coarsening, and propagation of myosin minifilaments in the 2D cortical network (Das et al., 2020; Fenix et al., 2016; Mosby et al., 2020; Wollrab et al., 2019). Complementary to the network contraction model, the network expansion model proposes that existing minifilaments serve as a template for new ones. Following this model, minifilaments can spit to "colonize" neighboring regions and eventually concatenate into ordered 2D networks. The **network contraction** model is dominant in the myosin clusters found at the lamellipodium base, but **network expansion** is dominant in the contractile actomyosin ring in dividing U2OS cells. In-depth analysis of the NMIIA clustering

dynamics provided in these images is likely to provide novel insights in the assembly of the contractile actomyosin meshwork at the proximal end of the bleb but was left aside because it has been treated in other studies and relatively well understood (Fenix et al., 2016; Fenix and Burnette, 2018; Jiu et al., 2019; Laporte et al., 2012; Taneja and Burnette, 2019; Wilson et al., 2010).

Nevertheless, we provide a few interesting observations showing the colocalization of NMIIA clusters with actin filament asters (***Figure 33*** D), merging myosin foci into larger aggregates (***Figure 33*** E-G, **videos available**). Note that it is possible that quantitative analysis of the intensity in the myosin dots, especially in the less dense region, could allow us to count single motors, but this analysis has not been performed. We observed minifilament dynamics supporting both expansion and contraction models in stable blebs. We observed that some myosin minifilaments could coarsen gradually, increasing the myosin intensity and slowing invading the neighboring cortex (***Figure 33*** E). Other clusters combine coarsening with network expansion, showing splitting events, in which a new minifilament emerges from an existing cluster to make a step of ~1µm to the side, and then establish there and coarsen (***Figure 33*** F). These events appear to be more common at medium actin densities. Overall, we conclude that the proximal end of the bleb concentrates most of the contractile activity of the network, generating the retrograde flow of the entre bleb.

10. Actin network assembly in stable blebs: *a connected and not contractile network forms between the front, free of actin, and the contractile base.*

The actin cortex in the middle region (region **II**) seemed visually more passive, with pure translational motion, suggesting a highly cross-linked network without contractile activity, moved backward by region III's contractility. The high correlation length (above 6 µm) in this region confirms the solid-like behavior (representative bleb in ***Figure 34*** A) and the parallel nature of the flow (***Figure 34*** B, **video available**). The least dense region of the bleb front (also the region with smoother contour) displays a group of filaments/bundles not connected to the network (***Figure 34*** C, **video available**). The least dense region localizes in the direction of bleb protrusion: in the front of persistent blebs and on one side of winding blebs (***Figure 34*** C). These unconnected filaments did not flow rearward (***Figure 34*** D, arrow) until they connected to the flowing network, leading to a depletion

of the very front. As a result, the PIV analysis, which shows a persistent flow of the connected region (red line, bottom right graph ***Figure 34*** D, **video available**), revealed transient retrograde flows in the distal tip region, corresponding to events of loose actin bundles or network fragments connecting to the main flowing network. This detailed analysis of representative examples reveals an unexpected stochastic aspect of the flow dynamics at the bleb front, as the assembling network reticulates and connects to the rearward flowing network.

11. Actin network assembly in stable blebs: from single actin filaments at the distal tip to a connected network

We last focused on the network assembly at the distal tip of stable blebs. This region does not display any consistent flow, contrary to the rest of the actin network in the bleb (***Figure 35*** A). We could observe typical actin molecular dynamics similar to the ones observed in *in vitro* reconstitutions such as what appears to be single filaments of various sizes displaying diffusive movement (***Figure 35*** B, C, **available movie**), branching (***Figure 35*** D, **available movie**), linear elongation (***Figure 35*** E, **available movie**), and crosslinking (***Figure 35*** F-H, **available movies**). The diffusive behavior ('jiggling') and the branching angle and polymerization speed values (***Figure 35*** D bottom graphs) suggest that we can detect single actin filaments on the membrane of blebs. We observed many small fragments that stitch together in bigger linear or branched bundles (***Figure 35*** F top images and **available movie**). Consistently with the role of crosslinking in stable bleb migration described in earlier works (Logue et al., 2015), we find that crosslinking is prominent at the bleb front and is a major mechanism for network formation from multiple seeds or fragments, as opposed to solely nucleation of pre-existent cortex emanating from the base. Nevertheless, we interpreted that there is also a presence of nucleators, in particular Arp2/3, as the branching angles and polymerization speeds coincide with its in vitro description by TIRF methods (Amann and Pollard, 2001).

To observe the localization and dynamics of the main actin bundlers present in HeLa (information from Gregory Adams in C. Waterman's lab at NIH), we transfected fluorescently-labeled alpha-actinin and filaminA alone or in combination with actin-GFP. When transfected alone, we noticed a characteristic banded pattern, similar to what we find on the actin channel (***Figure 35*** F bottom left images and arrows). When transfected

on the actin-GFP line, we observe a clear co-localization of the two markers. Strikingly, alpha-actinin can bind to actin filaments up to the front of the bleb, decorating even small bundles. As expected, bundlers decorate in particular overlapping regions between actin filaments (***Figure 35*** F, bottom right images, black arrows). Bundlers are absent from small filaments, which we interpret as one more sign of the ability of this technique to detect single filaments. To confirm that, we analyzed the density of signal along an actin bundle showing spots of alpha-actinin and found that regions dense in alpha-actinin (red, ***Figure 35*** G) also corresponded to regions of increased signal in the actin-GFP channel (blue, ***Figure 35*** G). We followed filaments meeting to form bundled networks and found that crosslinkers quickly (<1 second) decorate filaments when they encounter (***Figure 35*** H and **available movie**). This observation suggests that crosslinkers are both abundant and very dynamic at the bleb front and induce rapid bundling of the single actin filaments, generating the connected network found in region **II**.

12. Actin network assembly in stable blebs: *force transmission from the proximal contractile end to the distal tip through the connected network. Signs of force percolation.*

As shown for less resolved images, in stable blebs, NMIIA motors usually concentrate in the base of the bleb, while actin filaments can reach further towards the bleb front. As mentioned earlier, some parts of the membrane can have such low actin concentration that filaments or groups of filament appear not to connect to the flowing network. To verify this hypothesis, we followed actin filament dynamics in sparse regions. We found that filaments remain static or with Brownian-like motion if not linked to the flowing network. This remark confirms that the actin cytoskeleton is practically an empty shell close to the membrane and that the TIRF images are sufficient to explain the molecular behavior of the actin filaments. In sparse regions, we found an irregular pulsatile behavior. The actin network's connection to the retrograde flow below results in a complete and fast depletion of actin. Actin depletion, in turn, prevents mechanical connections between the bleb front and the bleb base, creating a network of static filaments that do not flow until new links form. This behavior suggests that dtress percolation through the network controls actin dynamics. We observed a **region of sparse filaments at the front** of persistent blebs, allowing for a persistent membrane protrusion.When the stress percolated to the front membrane produces more complex dynamics, such as winding and unstable blebbing.

In winding blebs, the region populated with sparse filaments localizes on the side, but always on the protrusion direction.

Based on these observations, we propose that the actin network is responsible for propagating contractile forces at long ranges from the bleb proximal end up to the distal front. This long-range force transmission can describe the stable, contractile, and intermediate regimes, which were not described by previous models (Callan-Jones et al., 2016; Ruprecht et al., 2015). The existence of intermediate regimes implies that single bundles or single filaments must exert forces on the membrane and other filaments. The addition of molecular percolation events then creates a gradual transition from a steady persistent to a tortuous winding protrusion, then to a retracting bleb.

We selected a few examples of molecular events that exemplify force percolation events between actin filaments and from actin filaments to the membrane. Filaments align when subjected to stress, and crosslinking bonds are flexible enough to allow alignment and flattening of network connections (***Figure 36*** A). When subjected to higher stress, bundles can break, resulting in fast relaxation events in the form of network recoil, showing that the contractile stress produced at the base is enough to break the network at the front (***Figure 36*** B).

We also observed events of bundles or single filaments that can transmit forces to the membrane. For example, bundles can slide and reorient while keeping their connection to the membrane, using the membrane as "rails." This shows that not only networks but also single filaments or bundles and can keep a strong membrane adhesion while moving tangentially (***Figure 36*** C). We also observed cases of membrane-filament snapping, reminiscent of the events observed at lower resolution in ***Figure 32*** I: a single bundle can hold the membrane front, indenting it, until it detaches, followed by a rapid recoil (***Figure 36*** D). Lastly, membrane-filament interaction can also result in membrane retraction (***Figure 36*** E).

13. Phase transitions in cortical actin in blebs. *Actin network percolation could explain the dynamics of actin networks in stable blebs.*

(Note: we show here the first steps towards providing evidence and quantification which will later serve to build a physical model of the network dynamics, based on percolation theory – an ongoing collaboration with Raphael Voituriez)

The theory describing force percolation in contractile gels is well developed and could predict the contractile behavior of *in vitro* actin networks (Alvarado et al., 2017, 2013; Tan et al., 2018). To test whether the actin flows and force transmission in stable blebs could be described with similar elements, we performed a more detailed analysis in a representative example of a stable bleb. We used a homemade image analysis pipeline combining Ilastik, Fiji, and custom-made Python codes, to compute actin density $\langle \rho_{act} \rangle$, network skeleton density, and the cortical velocity field $u(x,y)$ (***Figure 37*** A) For these parameters, we average over the entire movie to provide average values per region. First, from the velocity field we can calculate the divergence $\langle \nabla \cdot u(x,y) \rangle$ to identify regions where the cortical network is relaxing (div>0) or contracting (div<0). Assuming steady-state density, we can calculate the average network turnover $\langle \nabla \cdot (\rho \cdot u(x,y)) \rangle$, to see where actin is being polymerized or disassembled. In contractile actomyosin networks with increasing link density, the correlation length $\langle C(r,0) \rangle$ and a local order parameter $S = \langle \cos\theta \rangle_{local}$ are expected to capture the first transition from a gas to a solid phase and the second transition from a solid to a contracting network. Consistently with the literature, we find that with increasing density, the local order parameter is monotonic, whereas the correlation length has a peak in the solid phase towards the base of the central region (region **II**, ***Figure 37*** A).

If the gas-to-solid transition is due to the molecular interaction of filaments in the plane of the membrane, the transition from a gas to solid phase should be reflected in a 2D network analysis (***Figure 37*** B). To do so, we converted the actin network into a binary skeleton (***Figure 37*** B, left images). When plotting the skeleton density against the actin density, we observed a first phase when both parameters are linearly proportional, and a second phase when the actin density increases at a constant skeleton density (figure 13 B right graph). The first phase corresponds to increasing 2D network density. The second phase starts after actin has fully covered the layer close to the membrane: the increase in fluorescence density does not correspond to increasing network density, probably due to the filament stacking. The percolation should happen before the end of the first phase when the 2D network is critically connected. To verify this condition, we binned individual interrogation windows by density and plotted their correlation length (***Figure 37*** C) and local order parameter (***Figure 37*** D). Consistently, we find that the phase transition occurs at a network density <1µm/µm^2, even though the maximal network density is ~2µm/µm^2.

We focused on the binarized and network skeleton to check more predictions from the percolation theory. We identified the biggest cluster C_1, attached to the base, and all the

other clusters C_2, C_3, …, C_n ordered by size (ξ) such as $\xi_2 > \xi_3 > \ldots > \xi_n$. We should see that C_1 is the sole cluster moving downwards and that smaller clusters incorporate to the retrograde flow only after connecting to C_1. Indeed, we verified this condition and noticed a delay between cluster networking and flow, suggesting a causal relationship (***Figure 37*** E). Percolation theory also predicts that at increasing percolation probabilities, ξ_1 (the size of C_1) should increase monotonically, but ξ_2 (the size of C_2) should have a peak around the critical percolation density ρ_C. We identified the biggest and second-biggest cluster size in the skeleton analysis (***Figure 37*** F). Since the bleb contains a wide range of density along its length, we focused on smaller windows that have network densities in the linear regime (<2μm/μm^2) (***Figure 37*** H). Consistently, we find a monotonic increase in size of C_1 and a peak in the size of C_2 at $\rho_C \approx 0.9$ (***Figure 37*** I), which is approximately the same network density at which we see the phase transitions in figure ***Figure 37*** C and ***Figure 37*** D. We conclude from this analysis (which needs to be conducted on more blebs) that the network percolation theory developed for in vitro actin networks has a great potential to fully capture the main features of the actin network dynamics in a stable bleb, and explain how the force transmission from the contractile proximal end to the distal assembling end generates the complex dynamics and the shape of stable blebs and, by extension, of motile fragments.

14. Additional evidence on the 3D actin structure in the bleb and its importance to control bleb shape

Actin network structure in fixed blebs

Previous studies proposed that the orientation and organization of actin filaments give rise to stress anisotropies in the actin cortex and control the elongated shape of blebs (Ruprecht et al., 2015). We asked if the orientation of actin filaments at the front could give some insight into the formation of long shapes observed in blebs. Fixed samples allow for a detailed analysis of the actin filament microstructure, orientation, either with light microscopy techniques or with electron microscopy. We developed a method that allows the fixation of confined cells. It consists of a plastic holder placed with a 1% low melting point agarose block on a PLL-*g*-PEG-coated glass, pushing down a soft agarose block against the coverslip seeded with cells. The fixative is applied onto the agarose, which is later removed, and the sample is processed accordingly (***Figure 38*** A). Cells

maintain dynamic blebbing under agarose (***Figure 38*** B). However, the system cannot control the confinement height, which can be under 1.5 micrometers at the blebs' front.

We stained HeLa cells with phalloidin-alexa488 to visualize the F-actin network. We observed that the cortical network at the front of blebs comprises a well-ordered collection of bundles perpendicular to the main bleb axis (***Figure 38*** C). Actin bundle formation at the front seems to be more predominant in fixed samples than in live cells, possibly by the change in geometry (***Figure 38*** C). We observe that the bulk of the bleb contains cortex “scars,” suggesting sequential blebbing events and transient cortex formation. The perpendicular orientation of actin bundles is specific to blebs that display actin-free front (stable blebs) and is lost in blebs that have rebuilt a cortex all around the bleb contour (***Figure 38*** C, right). The biased bundle orientation visually decays in the middle of the bleb, regardless of the state of the front cortex, but it is hard to quantify orientation in dense actin networks with standard microscopy. This suggested that actin turnover could perform fast remodeling and ‘randomize’ the structure.

To quantify the cortex's orientation in the denser bleb regions, we performed polarized confocal microcopy on fixed samples. This technique consists on projecting polarized light on the sample and turn it to capture the entire angular spectrum, and it is particularly useful to see general orientation in biological polymers (Mavrakis et al., 2014). Using the correct actin dyes and fluorescent markers with a restructured molecular vibration, one can quantify the orientation and degree of alignment of a dense network. The analysis outputs two angles: ρ, the mean angular orientation, and ψ, the angular aperture. The first will measure the filament's general direction and the latter will measure if the filaments are well aligned (***Figure 38*** D). ψ is limited by the choice of dyes and fluorescent probes because they will have intrinsic variability. For actin-phalloidin-Alexa488, the minimum measured aperture angle is ~120°. Consistently with previous results, we observed that the front cortex comprises highly aligned bundles that follow the bleb contour. Compared to the middle of the bleb, the mean angular aperture $\langle\psi\rangle$ at the front is reduced, and the distribution of normalized mean orientation $\rho - \langle\rho\rangle$ is narrowed (***Figure 38*** D J bottom).

Other results point to the effect of membrane topology in the structure of the cortex. In winding blebs, the order of actin filaments aligns with the positions where there was a membrane, creating cortical topological defects (***Figure 38*** E, zone 2). At the middle and the back of the bleb, actin gradually becomes more disordered, and some asters are formed, probably by the effect of cortical motors (***Figure 38*** E, ρ field of entire bleb). The

ordered configuration following bleb contour is lost, on average 10-20 microns after the bleb front (***Figure 38*** E, ρ field of entire bleb). The 'decay length' could be explained by network turnover, assuming retrograde flow speeds in the order of 10μm/min (Liu et al., 2015) and actin turnover in the order of min^{-1} (Bovellan et al., 2014). Strikingly, the ordered and aligned configuration is not lost at the bleb sides, where the curvature is higher than the middle of the bleb. We measured the mean angular aperture $\langle\psi\rangle$ and the distribution of normalized mean orientation $\rho - \langle\rho\rangle$ at regions at the bleb front, middle, and sides, and verified that the sides and the front present similar molecular order, but that this order was lost in the bleb middle (***Figure 38*** F). This consistently suggests that curvature and turnover play a role in determining the molecular orientation of actin filaments in the confined experimental conditions we are working on. The effect of confinement and high crosslinking in producing bundles parallel to the contour was predicted by previous work based in simulations and *in vitro* work (Koudehi et al., 2019).

The fixation allows for high-resolution techniques based on single molecules, such a STORM, which provides a single-molecule resolution of the organization of actin at the bleb front. We used STORM to verify this network organization and calculate the average bundle thickness found at the bleb fronts (***Figure 38*** G). Reliably with the other techniques, we found that actin organizes in bundles at the bleb front, preferentially perpendicular to the main bleb axis (***Figure 38*** H) and that bundle thickness ranges from 20 to 250 nm, with a typical size of 77nm (***Figure 38*** I). This value is consistent with the measured bundle thickness in vitro in actin/alpha-actinin/fascin networks, in which bundle thickness is typically 50-100 nm, corresponding to 20-100 filaments approximately (Claessens et al., 2006).

Inverted contact guidance of blebs on nanogrooves

We hypothesized that the biased bundle formation at the bleb front constrains the membrane to grow forward and produces the elongated bleb shape. To study the blebbing direction of long blebs, we had to find a condition that biased and aligned the migration of the cells. For this purpose, we modified the confiner device and introduced nanogrooves on the bottom of the chamber. Nanogrooves are well known to bias the migration of cells, in a phenomenon described for adhesive fibroblasts in the early 1920s termed "contact guidance" (Harrison, 1914; Weiss, 1934). To make the nanogrooves, we molded PDMS on unmounted CD-ROMs, consisting of a regular and large nanogrooved

surface. We then stick a thin layer of molded PDMS to a glass coverslip. The coverslips with the molded PDMS are used as the “floor” of our confinement chamber and retain a regular groove pattern shown by an AFM profiler (***Figure 39*** A).

Astonishingly, stable blebs displayed *inverted* contact guidance on the nanogrooves. Contrary to the parallel alignment of adhesive cells, or *D. discoideum* (Driscoll et al., 2014), blebs polarize perpendicularly to nanogrooves (***Figure 39*** B, **video available**). This bias is increased in larger blebs (>100μm^2) (***Figure 39*** C), and increases with time as cells polarize (***Figure 39*** D). However, grooves do not significantly change the overall polarization dynamics (***Figure 39*** E). As mentioned before, smaller blebs do not bias perpendicularly to grooves; however, we found that the front of small blebs is biased (***Figure 39*** F, **video available**). We hypothesized that the grooves could stabilize protrusions by i) slowing down the retrograde flow and preventing retraction, ii) perturbing the membrane dynamics, or iii) biasing front actin bundle formation. We found that the front membrane advances smoothly when protruding parallel to grooves, but with brief pauses when advancing perpendicular to grooves, suggesting that the perpendicular protrusion finds some resistance and that this effect cannot promote perpendicular bias in the protrusion (***Figure 39*** G, **video available**). We then measured the cortical flow speeds on the bottom plane, parallel and perpendicular to grooves. While we found a significant difference in the flows measured inside the cell on the margins, blebs did not display a significant difference in the flow speed as a function of the orientation (***Figure 39*** H, **video available**). These results suggest that the groove effect on bleb retrograde flow or retraction cannot explain the perpendicular bias.

We imaged the actin dynamics at the front of blebs on grooves and found that filaments are sensitive to the membrane's topology below, aligning to it. Accordingly, filaments forming on a flat surface present random orientation but filaments on a grooved surface tend to orient along the grooves (***Figure 39*** I). This effect is evident in regions that depleted of actin. When filaments are transiently disconnected from the flow and are free to polymerize to bundles, they appear parallel to grooves on membrane valleys (***Figure 39*** J, **video available**). We observed that the actin shell structure formed at the bleb front is stable and does not change its shape as it flows back (***Figure 39*** K, **video available**). We take this into account to propose a working model for bleb inverted contact guidance. The membrane topology at the bottom of the chamber biases the orientation of actin bundles, promoting bundles parallel to the grooves. This results in the alignment of ring-like structures at the bleb (already present without the grooves) and the projection of membrane protrusions perpendicular to the grooves. Altogether, our data support the

hypothesis that actin structure in blebs is biased by the membrane topology and that the confined cell geometry enhances the elongated shape produced by the bundled organization at the bleb front.

Figure 25: Stable and retractile blebs formed immediately after confinement contain different actomyosin profiles

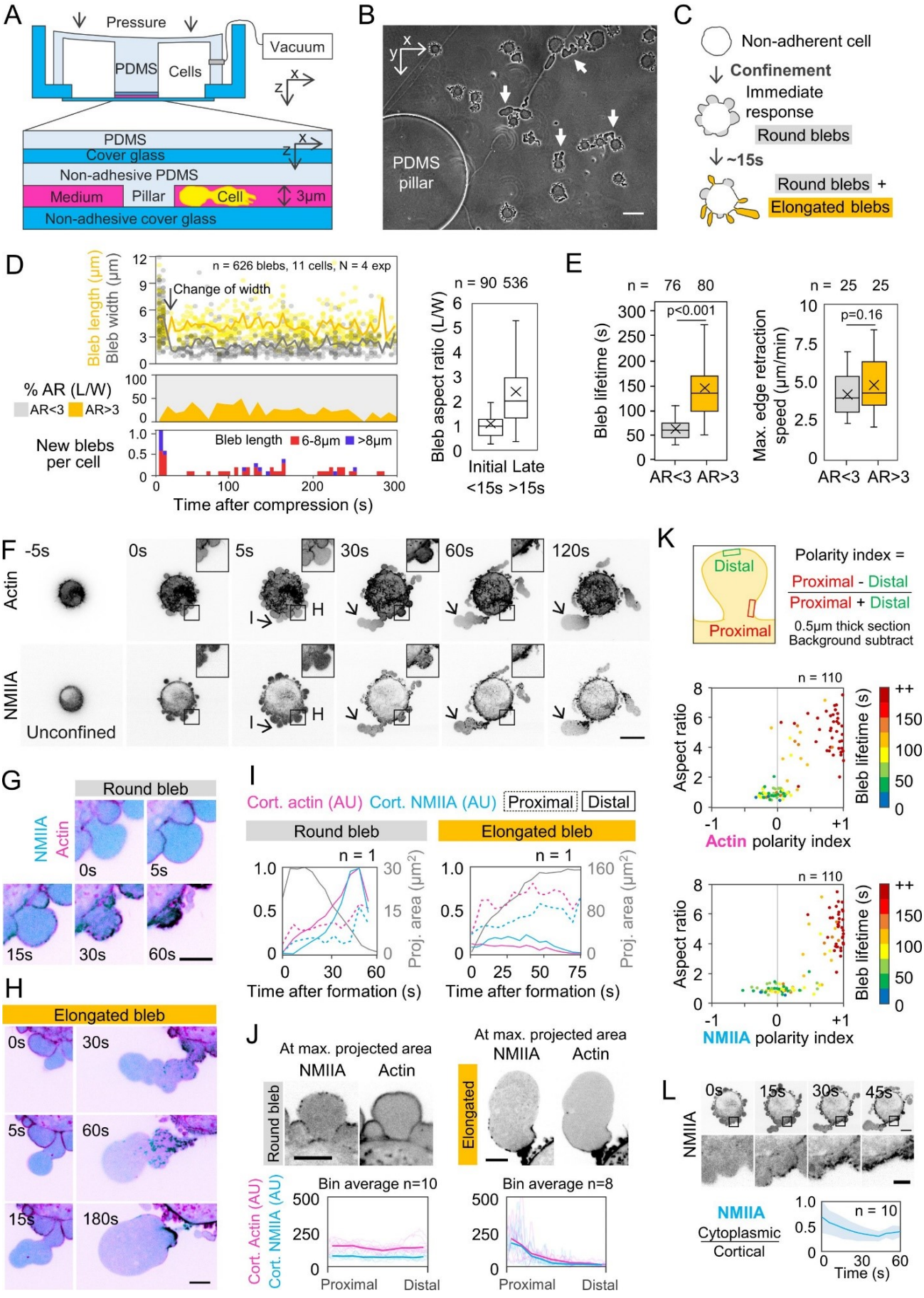

Figure 25: Stable and transient blebs formed immediately after confinement contain different actomyosin profiles

A: Schematic representation of a confinement device. Cells are confined between a microfabricated PDMS surface containing pillars of 3µm and a standard single-well glass-bottom culture dish coated with non-adhesive polymers, either PLL-*g*-PEG at 0.1mg/ml or PAcrAm-g-(PMOXA, NH2, Si) at 0.1mg/ml.

B: 20x phase image of a typical confinement experiment of Hela MYH9-eGFP. White arrows point at big blebs that cells form upon confinement and can contribute to cell migration. Imaged 15 minutes after confinement, on PDMS coated with 500µg/ml PLL-g-PEG. Scale bar: 50µm. Experiment ID: 20180213.

C: Schematic representation of the morphological features of blebs formed upon confinement. The immediate response of non-adherent cells to confinement is the formation of round, transient blebs. Within a minute, more elongated and stable blebs are formed along with round blebs.

D (top): Manual measurement of individual bleb width and bleb length (grey and yellow dots) and mean (lines) of Hela MYH9-eGFP Lifeact-mCherry cells under flat-cantilever AFM compression. We observe a rapid decay of bleb width in the first time points but not of bleb length, which is pointed by the grey arrow. **D (bottom):** relative frequency of blebs shorter than (gray) or longer than 3µm (orange). Histogram of absolute frequencies of new blebs per cell longer than 8µm (dark orange) or between 6 and 8µm (light orange). **D (right):** Quartile intervals and mean (cross) of the aspect ratio (length/width) for all blebs in the first few time points (15s) versus all blebs after the first time points. We observe that blebs are round (AR = 1) for the first timepoints to then become elongated. For clarity, the boxplot excludes the outliers.

E: Manual measurement of individual bleb lifetime (the difference between the time of formation and time when the bleb is completely retracted) and maximal retraction speed (measured manually from kymographs on MYH9-GFP signal). We observe a significant difference in bleb lifetime (Welch's $p<0.001$) but not on retraction speed (Welch's $p=0.16$). The difference the lifetime could be due in part to the time needed to retract a longer projection. HeLa MYH9-eGFP Lifeact-mCherry cells under flat-cantilever AFM compression.

F: Representative images on a spinning disk 100x+1.6x of a 3µm confinement experiment of Hela MYH9-eGFP, Lifeact-mCherry on a PDMS coated with 100µg/ml PAcrAm-g-(PMOXA, NH2, Si). Cells produce initially round blebs that swiftly retract within 60 seconds (black square, H), and then produce longer blebs that stabilize (black arrow, I). Frame frequency: 1.15s. Scale bar: 10µm. Experiment ID: 20191002_25.

G, H: Representative examples of round transient bleb and elongated stable bleb. Same images as in 1F. Merge of Lifeact-mCherry (labeled as "Actin") and MYH9-eGFP (labeled as "NMIIA"). Scale bar: 5µm.

I: Manual measurement of distal (solid line) and proximal (dashed line) actin (magenta) and NMIIA (cyan) cortical accumulation during bleb lifetime in two representative examples of a transient round bleb (gray, as in figure 1IH) and an elongated stable bleb (orange, as in figure 1I). We observe that the round bleb accumulates both distal and proximal actin and NMIIA, but the elongated bleb depletes its distal actomyosin. Intensity density is calculated as Raw Integrated Intensity divided by the area. Densities are normalized by dividing by the maximum density.

J: Round and elongated blebs establish distinct NMIIA (cyan) and actin (magenta) density gradients along the bleb length. The actomyosin 500nm-wide profiles are taken at the time point immediately after the maximal projected area is reached, when the cortex forms. Intensity density

is calculated as Raw Integrated Intensity divided by the area, subtracting the cytoplasmic background. A binned mean is represented in bold line for 10 representative examples of round blebs and 8 elongated blebs from 3 different cells, by diving the total length of the bleb in 10 parts and calculating their average. Scale bar: 5μm.

K: Classification of blebs by aspect ratio (length over width), NMIIA or actin polarity, and lifetime. We defined a polarity index ranging from -1 to 1 as a measurement of the asymmetry in cortical actomyosin accumulation and the direction of its gradient. Blebs accumulating actomyosin only in the back will have a polarity index close to +1. Conversely, blebs accumulating actomyosin homogeneously will have a polarity index of 0. The actomyosin profiles are taken at the time point immediately after the maximal projected area is reached, when the cortex forms. Due to the short duration of the movies, we cannot measure precisely the duration of blebs over three minutes. Data is measured from 110 blebs from 9 different cells each in individual confinement experiments.

L (top): Zoom of the region marked with a black square in the top, where we can appreciate the accumulation of myosin in the cortical regions and its depletion from the bulk of the cell. Scale bar: 10μm (top) and 2.5μm (bottom). **L (bottom):** Ratio of signal densities between a cytoplasmic region not occupied by the nucleus (where the signal is excluded) and a 500nm cortical region in 10 representative cells.

Figure 26: Activation of NMIIA by cPLA2 and Ca^{2+} is required to trigger cortical contractility and the formation of stable blebs

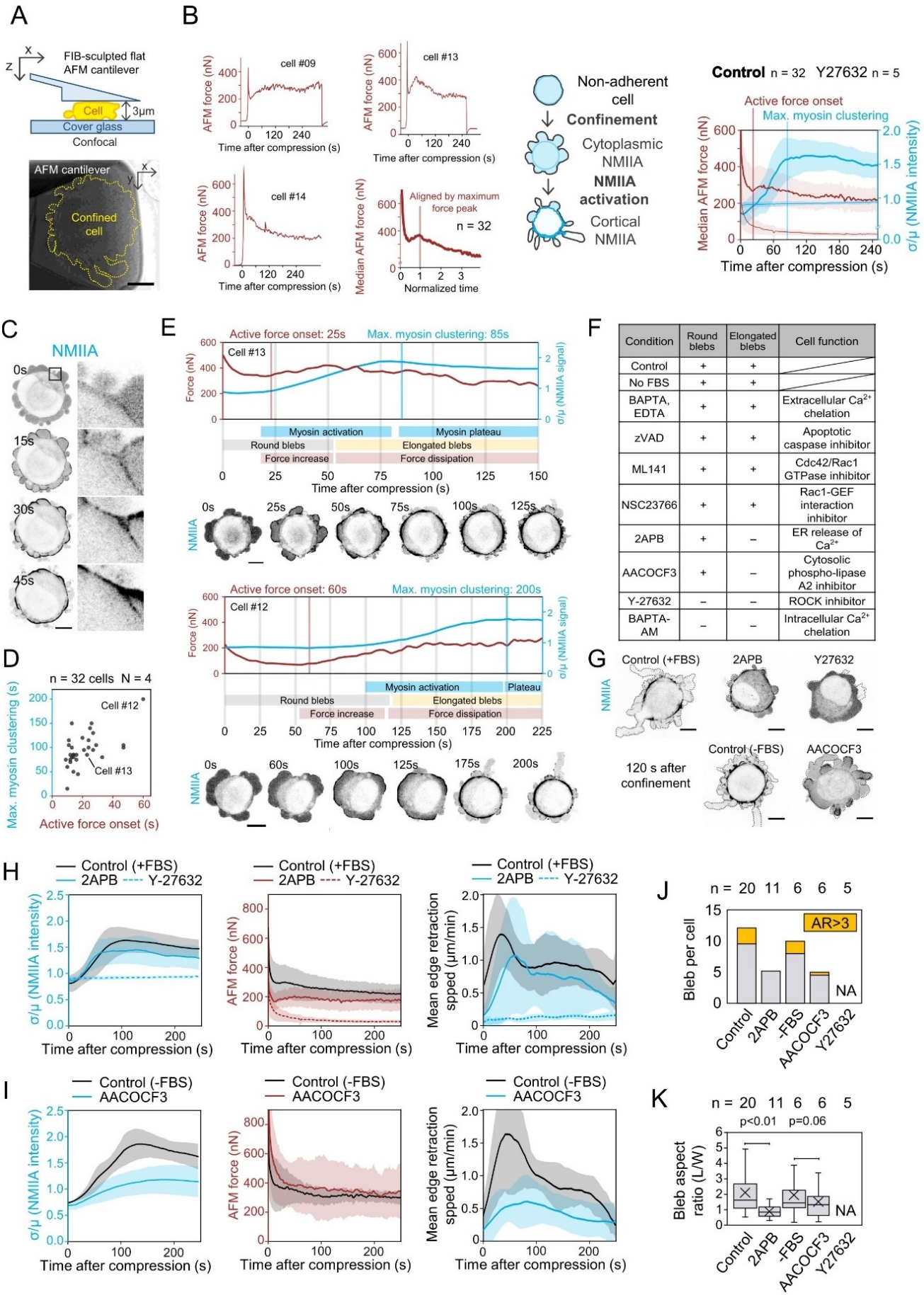

Figure 26: Activation of NMIIA by cPLA2 and Ca2+ is required to trigger cortical contractility and formation of stable blebs

A (top): Schematic representation of a cell confined to 3µm under a FIB-sculpted flat AFM cantilever. The measurements of the force exerted by cells on the cantilever and the confocal images are recorded simultaneously. **A (bottom):** 63x phase image of a confined Hela cell MYH9-eGFP Lifeact-mCherry. Scale bar: 10µm. Experiment ID: 20160202_03.

B (left): Examples of force curves following compression in three cells, showing the variability of behaviors observed. B (bottom right): Cells aligned by the maximum force peak, with normalized time ($\times 1 / t_{\text{maximum force peak}}$).

B (center): Non-muscle myosin IIA (NMIIA) is mostly cytoplasmic in non-adherent Hela cell MYH9-eGFP Lifeact-mCherry cells. Data shown for control cells (bold line) and Y-27632-treated cells (light line). Confinement promotes a transition from cytoplasmic globular NMIIA to cortical phosphorylated minifilaments. This signal clustering can be captured by the standard deviation (σ) divided by the mean (µ) of the NMIIA intensity (coefficient of variation) after subtracting the background outside the cell, depicted on B (right).

B (right): Average (solid line) and standard deviation (shade) of the coefficient of variation of the NMIIA signal (cyan) and the AFM force exerted against the cantilever (dark red). We observe a steady increase in NMIIA clustering from 10s to 90s after confinement, followed by a plateau (marked with a vertical cyan line). The force follows an initial decay curve typical of an elastic response, followed by a change of trend labeled as “active force onset” caused by the retraction of round blebs, and a subsequent decay produced by the release of pressure and volume by elongated blebs. Data computed for 60 frames (300 s total) for 32 cells from 4 independent experiments.

C: Full cell and zoom (black square) on a cortical region of an AFM-confined MYH9-eGFP HeLa cell. Scale bar: 5µm.

D: Time of active force onset (change of trend in the AFM force curve) plotted against the time of maximum myosin clustering time (start of the plateau of the coefficient of variation of the myosin signal) as detected by a custom made python script. Data from 32 control cells from 4 independent experiments. Two cells, named cell #12 and cell #13 are marked and plotted in detail in figure 2E.

E: Temporal description of a cell’s response to confinement. We show in parallel AFM force measurement and myosin clustering (top graphs), a summary of the cell behavior (labels describing myosin accumulation, bleb shape, force response), and images on the NMIIA channel. We observe two representative examples for a cell triggering NMIIA clustering rapidly upon confinement (#13 at the top) and another with a significant lag time (cell #12 at the bottom). Scale bar: 10 µm.

F: Summary of a small drug screening on Hela Kyoto MYH9-GFP Lifeact-mRFP aiming at identifying the mechanisms for the formation of round blebs formed immediately after confinement versus the more elongated blebs formed upon activation of contractility.

n cells	Condition	Description
20	Control	
6	Control-no serum	Control for AACOCF3 cPLA2 inhibitor, which needs to be dissolved in DMEM without serum.
11	2APB	Inhibits Ca^{2+} going out of the ER mechanically (100µM). Activator of the Orai3 (ORAI calcium release-activated calcium modulator 3) protein. Inhibits Ca^{2+} influx through transient receptor potential

		2 channels in rat dorsal root ganglion neurons. Membrane-permeable SOCE (store-operated Ca^{2+} entry) inhibitor.
5	BAPTA	Chelates Ca^{2+} outside the cell (2mM)
6	BAPTA-AM	Cell cell-permeant chelator, highly selective for Ca^{2+} (100μM).
6	EDTA	Chelates Ca^{2+} outside and disrupts integrin-mediated focal adhesions (5mM)
7	C3Tfase	Inhibits Rho GTPase. Concentrations at 2 (n = 7) and 20 μg/ml (n = 10).
6	ML141	Inhibits Cdc42 GTPase (30 μM)
5	NSC23766	Inhibits Rac1 GTPase (50μM)
5	Y27632	Inhibits ROK, Rho kinase (10μM)
6	cPLA2	AACOCF3 cPLA2 inhibitor (no FBS, 20 μM). cPLA2 produces Arachidonic acid.
5	zVAD	Inhibits apoptotic caspases (50 μM)

G: Representative confocal 63x images of HeLa MYH9-eGFP Lifeact-mCherry taken 120 seconds after confinement with an AFM cantilever under different conditions: control + FBS, 2-APB 100μM, Y-27632 10μM, control - FBS, and AACOCF3 20μM. Scale bar: 10 μm.

H: Description of cell response to confinement in control + FBS (n = 20), 2-APB 100μM (n = 11), and Y-27632 10μM (n = 5) conditions. Solid lines represent averages and shades represent standard deviations. **H (left):** Standard deviation (σ) divided by mean (μ) of NMIIA intensity (coefficient of variation) as a function of time. **H (middle):** AFM force measurements. **H (right):** Average retraction speed of the cell edges (μm/min) as a function of time, measured by the Fiji plugin ADAPT (Automated Detection and Analysis of ProTrusions).

I: Description of cell response to confinement in control - FBS (n = 6), and AACOCF3 20μM (n = 6) conditions. Solid lines represent averages and shades represent standard deviations. **I (left)**: Standard deviation (σ) divided by mean (μ) of NMIIA intensity (coefficient of variation) as a function of time. **I (middle):** AFM force measurements. **I (right):** Average retraction speed of the cell edges (μm/min) as a function of time, measured by the Fiji plugin ADAPT (Automated Detection and Analysis of ProTrusions).

J: Comparison of bleb frequencies in control cells (gray) versus drug treatments (white). Blebs were manually counted in 4 cell regions during 300s. Absolute total frequency of blebs and frequency of blebs with an aspect ratio greater than 3 is plotted for control + FBS (n = 20), 2-APB 100μM (n = 11), Y-27632 10μM (n = 5), control - FBS (n = 6), and AACOCF3 20μM (n = 6) conditions.

K: Quartile distribution and mean (cross) of the blebs in **panel J** in control cells (gray) versus drug treatments (white). Outliers are not plotted. Welch's t-test.

Figure 27: Depletion of actin from the bleb front is required to establish a retrograde flow during bleb formation and avoid retraction

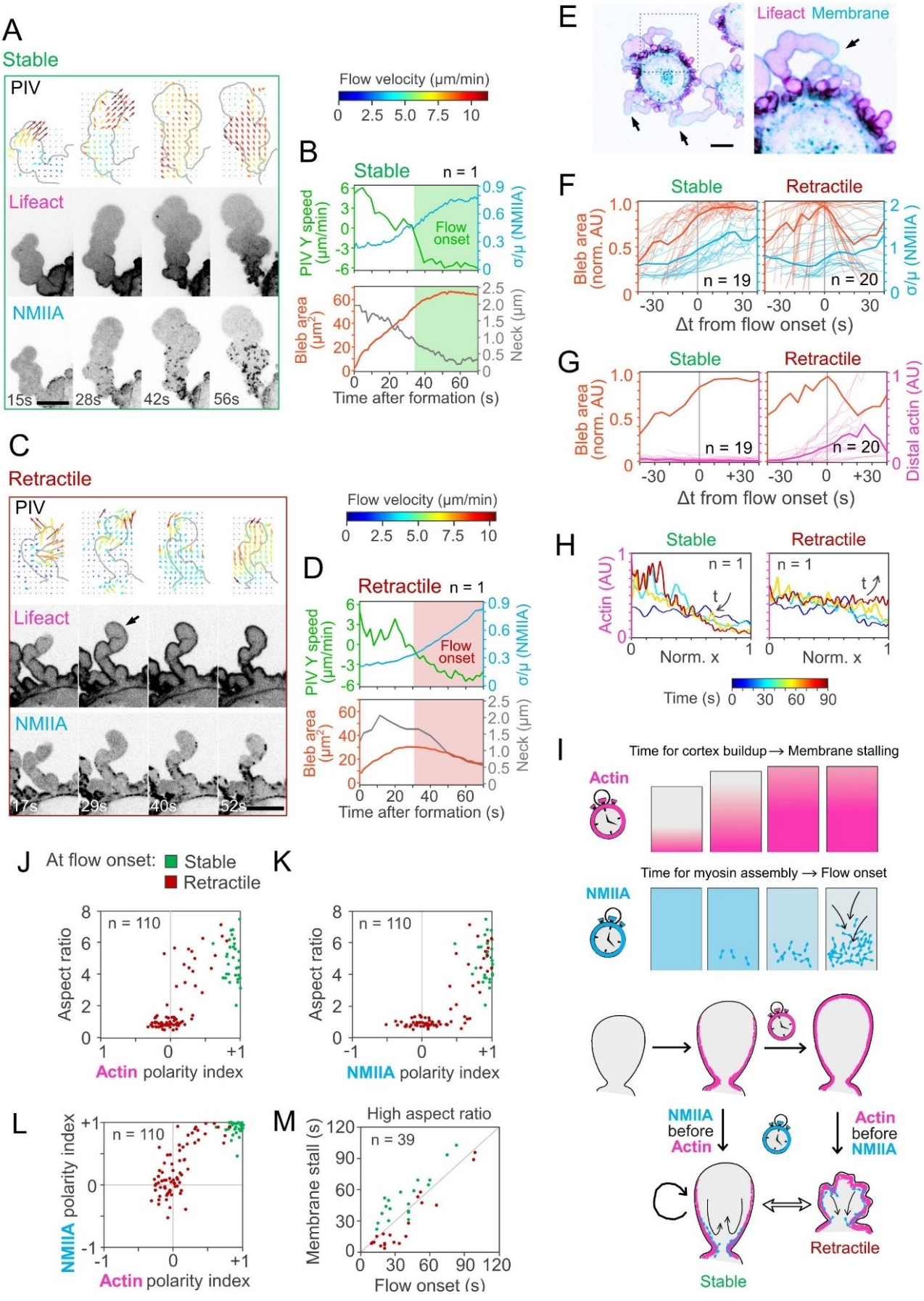

Figure 27: Depletion of actin from the bleb front is required to establish a retrograde flow during bleb formation and avoid retraction

A: Representative example of the formation of a stable bleb in confined HeLa MYH9-eGFP Lifeact-mCherry. **A (top)**: sequences of PIV (particle image velocimetry) applied at the binarized NMIIA channel. We appreciate an initial phase where the PIV detects membrane forward expansion while keeping immobile NMIIA clusters at the base of the bleb. Gradually, membrane stalls and the cluster begin a retrograde cortical flow which is captured by the PIV. **A (middle)**: bottom plane on the actin channel, where we observe a gradient of cortical accumulation of actin. **A (bottom):** bottom plane on the NMIIA channel, where we observe a progressive depletion of the cytoplasmic background and enrichment of the NMIIA cortical clusters. Scale bar: 10μm.

B: Quantification of the average PIV speed on the Y-axis, the coefficient of variation of the NMIIA signal, the bleb area, and the bleb neck width of the stable bleb shown in **panel A** as a function of time. The green shade represents the area where the average PIV speed on the Y-axis goes below 0, representing the onset of retrograde flow, labeled “flow onset”.

C: Representative example of a transient bleb in confined HeLa MYH9-eGFP Lifeact-mCherry. **C (top):** sequences of PIV (particle image velocimetry) applied at the binarized NMIIA channel. **C (middle)**: However, as appreciated in the lifeact channel, this onset occurs after the cortex forms all along the bleb contour, as marked by the black arrow. Scale bar: 10μm.

D: Quantification of the average PIV speed on the Y-axis, the coefficient of variation of the NMIIA signal, the bleb area, and the bleb neck width of the transient bleb shown in **panel C** as a function of time. The red area represents the flow onset, which in this case leads to retraction and a decrease in the bleb projected area.

E: HeLa cells with lifeact-mCherry stained with cell mask Alexa-647 (membrane dye) confined at 3μm at a 100x spinning disk confocal. Scale bar: 10μm. We appreciate the tip free of actin of growing blebs (black arrows).

F: Average normalized bleb area and coefficient of variation of the NMIIA signal aligned by flow onset for stable (**E left**) and transient blebs (**E right**). Bleb area is normalized by the maximum area reached by each bleb. Individual curves are represented as shaded lines. Data corresponding to 39 blebs from 11 individual confinement experiments (12 cells) and 2 different dates.

G: Distal cortical actin density in blebs aligned by flow onset for stable (**F left**) and transient blebs (**F right**), with the average normalized bleb area as a reference.

H: Time evolution of the actin cortical gradients of the blebs in panels A and C, color-coded as a function of time.

I: Model for the formation of a stable bleb protrusion. i) We define a kinetic parameter for the formation of a cortex, which leads to membrane stalling. This time depends on the presence of nucleators and the geometry and extension of the bleb. ii) We define another kinetic parameter for the onset of contractility, which depends on the presence of mature NMIIA minifilaments, cortex architecture, and signaling. The onset of contractility produces a flow. iii) If the onset of contractility occurs before the formation of a cortex completes, the actin will be removed from the front of the bleb continuously, creating a stable gradient and a persistent retrograde flow. iv) If the onset of contractility occurs only after the cortex has completely reformed, NMIIA motor activity will retract the bleb.

J, K: Classification of blebs by aspect ratio (length over width), NMIIA polarity, and actin polarity (defined as in figure 1L) and colored by bleb stability. We observe that actin polarity can be a

predictor for bleb stability (I) but not NMIIA polarity (J). Conversely, actin polarity cannot predict bleb shape, but NMIIA can. Data is measured from 110 blebs from 9 different cells each in individual confinement experiments.

L: Classification of blebs by NMIIA and actin polarity. We observe that actin and NMIIA polarity are proportional, but that stabilization is observed only at high actin polarity. Data is measured from 110 blebs from 9 different cells each in individual confinement experiments.

M: Classification of blebs by time of membrane stalling (defined as the second frame at which the area stalls or decreases), and time flow onset (defined as the second frame at which a centripetal myosin flow is observed). Data corresponding to 39 blebs from 11 individual confinement experiments (12 cells) and 2 different dates.

Figure 28: Myosin activation promotes bleb retraction or stabilization depending on the blebbing state

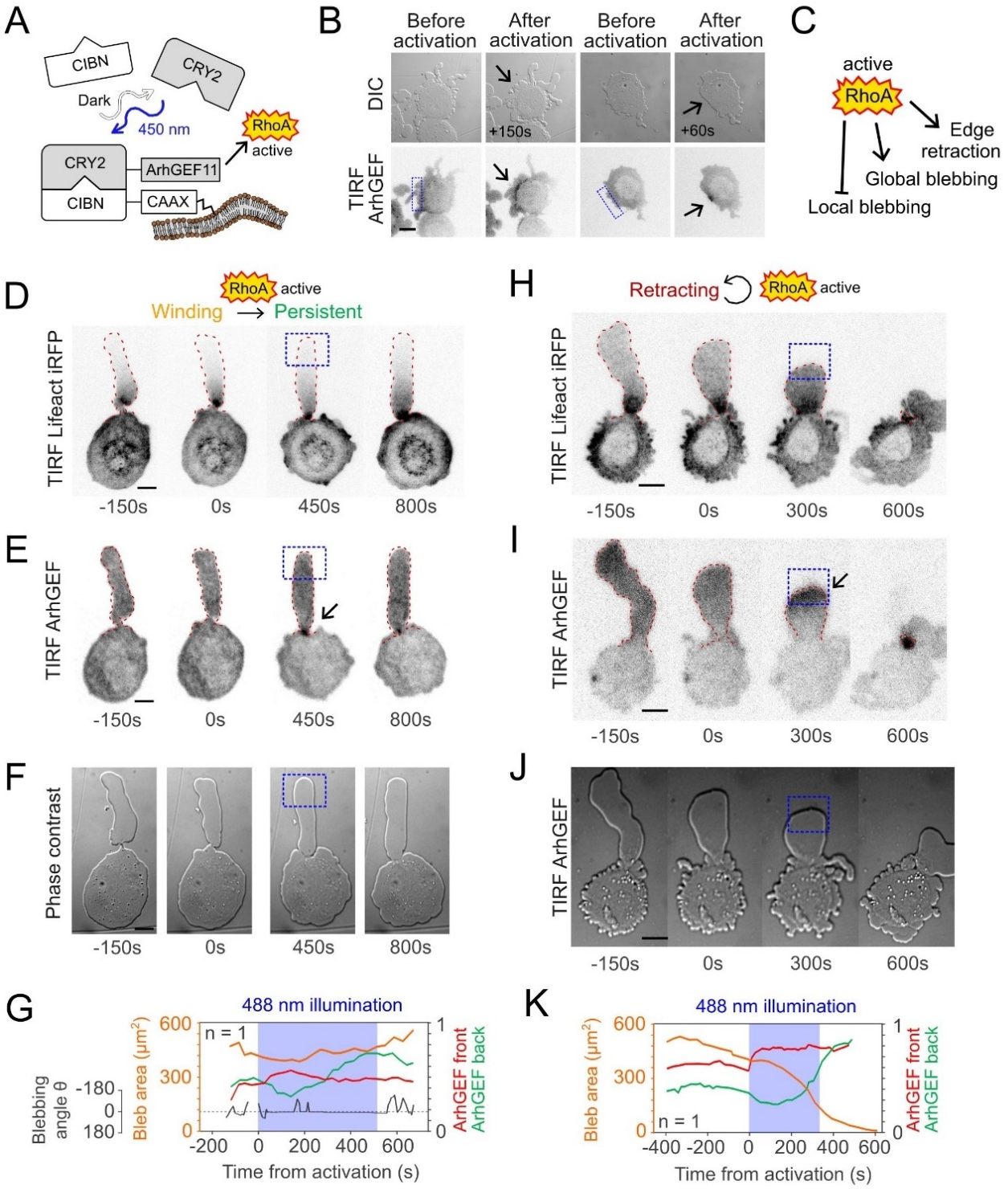

L

Construct	Active GTPase	Effect on retracting blebs (n)	Effect on stable blebs (n)
CIBN-ArhGEF11	RhoA	Promotes retraction (4/4)	Promotes stabilization (3/3)
CIBN-TIAM1	Rac1	No effect	No effect
CIBN-ITSN	Cdc42	No effect	No effect

Figure 28: Myosin activation promotes bleb retraction or stabilization depending on the blebbing state

A: Schematic illustration of the optogenetic system used to induce local activation of contractility. The CIBN/CRY proteins dimerize under blue light, recruiting ArhGEF11 to the membrane, which activates RhoA locally.

B: Effect of local blue illumination on HeLa GFP-CIBN-CAAX mCherry-CRY2-ArhGEF11 lifeact-iRFP670 cells. DIC (top row) and ArhGEF-mCherry 60x TIRF images of 3µm-confined before and after activation. Blue square shows the area where the illumination pattern is projected, at a frequency of 3 seconds. The black arrows point at the sites of recruitment of ArhGEF11. Scale bar: 10µm.

C: Summary of the observed effects of illumination on HeLa GFP-CIBN-CAAX mCherry-CRY2-ArhGEF11 lifeact-iRFP670 cells.

D: Effect of illumination at the front of a stable bleb. HeLa GFP-CIBN-CAAX mCherry-CRY2-ArhGEF11 lifeact-iRFP670 cells are illuminated at the area marked with the blue dashed square every 3 seconds. The time labels refer to the time of the start of illumination. Scale bar: 10µm.

E: Same as panel D, TIRF images of the ArhGEF11-mCherry channel.

F: Same as panel D, phase-contrast image sequence.

G: Measurement of bleb area, blebbing angle (defined as in figure 4 G), and ArhGEF11 density at the front and neck of the bleb as a function of time from the start of illumination, for the stable blebbing cell in figures 5 D and E. The illumination period is marked with the blue shaded area.

H: Effect of illumination at the front of a retracting bleb. HeLa GFP-CIBN-CAAX mCherry-CRY2-ArhGEF11 lifeact-iRFP670 cells are illuminated at the area marked with the blue dashed square every 3 seconds. The time labels refer to the time of the start of illumination. Scale bar: 10µm.

I: Same as panel H, TIRF images of the ArhGEF11-mCherry channel.

J: Same as panel H, phase-contrast image sequence.

K: Measurement of bleb area and ArhGEF11 density at the front and neck of the bleb as a function of time from the start of illumination, for the retracting blebbing cell in figures 5 G and H. The illumination period is marked with the blue shaded area.

L: Summary of the results of the optogenetic experiments conducted with ArhGEF11, TIAM1, and ITSN small GTPase activators.

Figure 29: Retractile blebs can be switched to stable states by increasing external compression

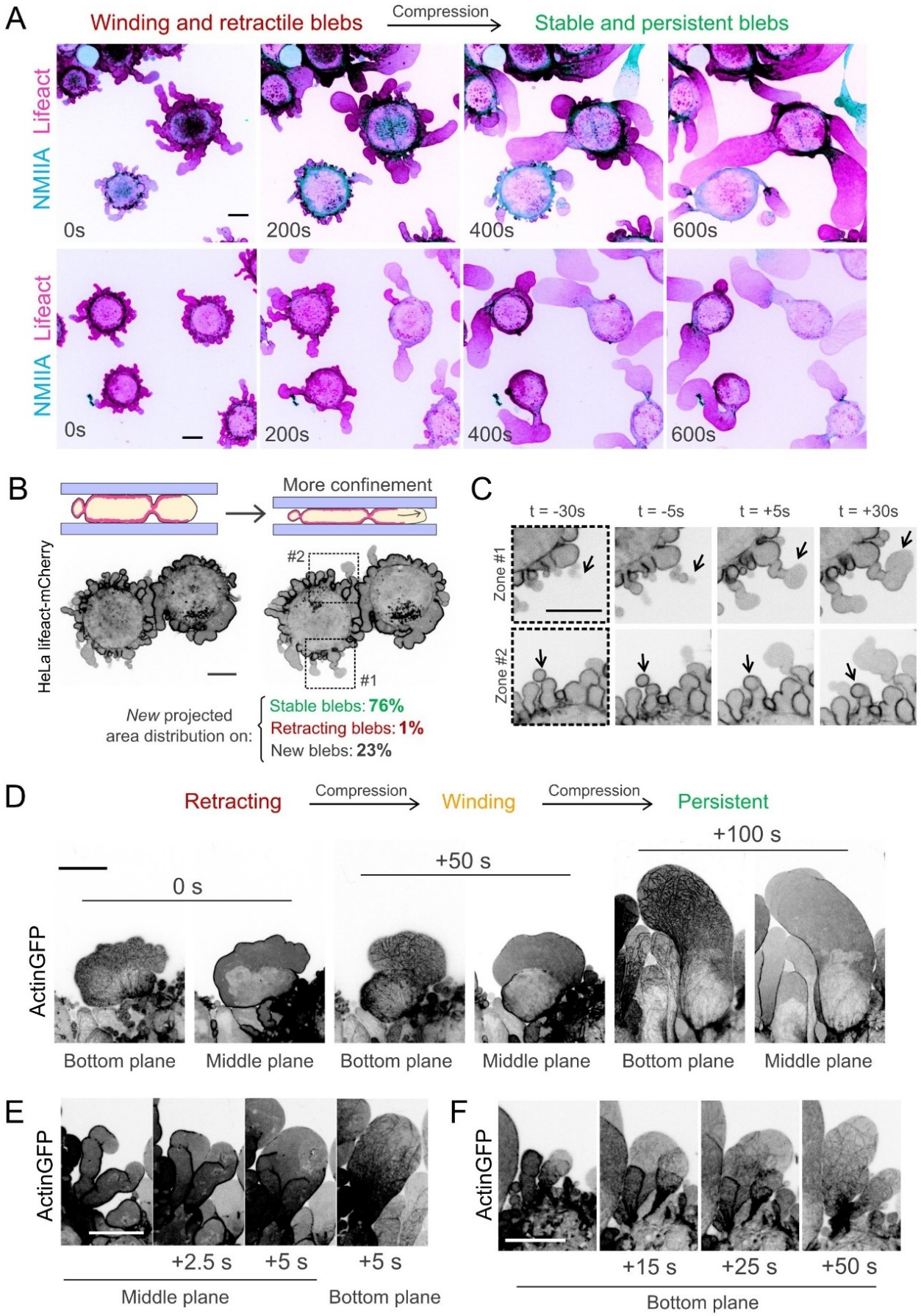

Figure 29: Retracting blebs can be switched back to a stable state by increasing external compression

A: Blebs in confined HeLa cells can rapidly polarize and stabilize upon confinement increase. Image sequence of HeLa cells MYH9-eGFP lifeact-mCherry under increasing confinement. Scale bar: 10µm.

B: Increase of confinement in blebbing cells leads to an increase in cell projected area, which is preferentially protruding from new blebs and already-formed stable blebs (with a front low in actin), but not on retracting blebs. Images of the middle plane of actin-GFP confined HeLa cells at ~4 versus ~3 µm. Scale bar: 10 µm.

C: Time sequence and zoom of the two regions depicted with dashed black squares in panel 5B.

D: Blebs can stabilize upon increased confinement. A retracting bleb (t=0s) swiftly transitions first to a winding state (t=+50s) and then to a persistent state (t=+100s) upon confinement. On the right, we see an example of two smaller winding blebs that fuse under increase confinement and immediately switch to a persistent blebbing state. Images of Hela Actin-GFP cells on a 100x confocal spinning disk. Scale bar: 10 µm.

E, F: Image sequence at bottom or middle planes of blebs in HeLa actin-GFP cells after increased confinement. Scale bars: 10 µm.

Figure 30: Stable blebs can spontaneously switch between blebbing modes, displaying persistent, unstable/winding, or transient retraction phases

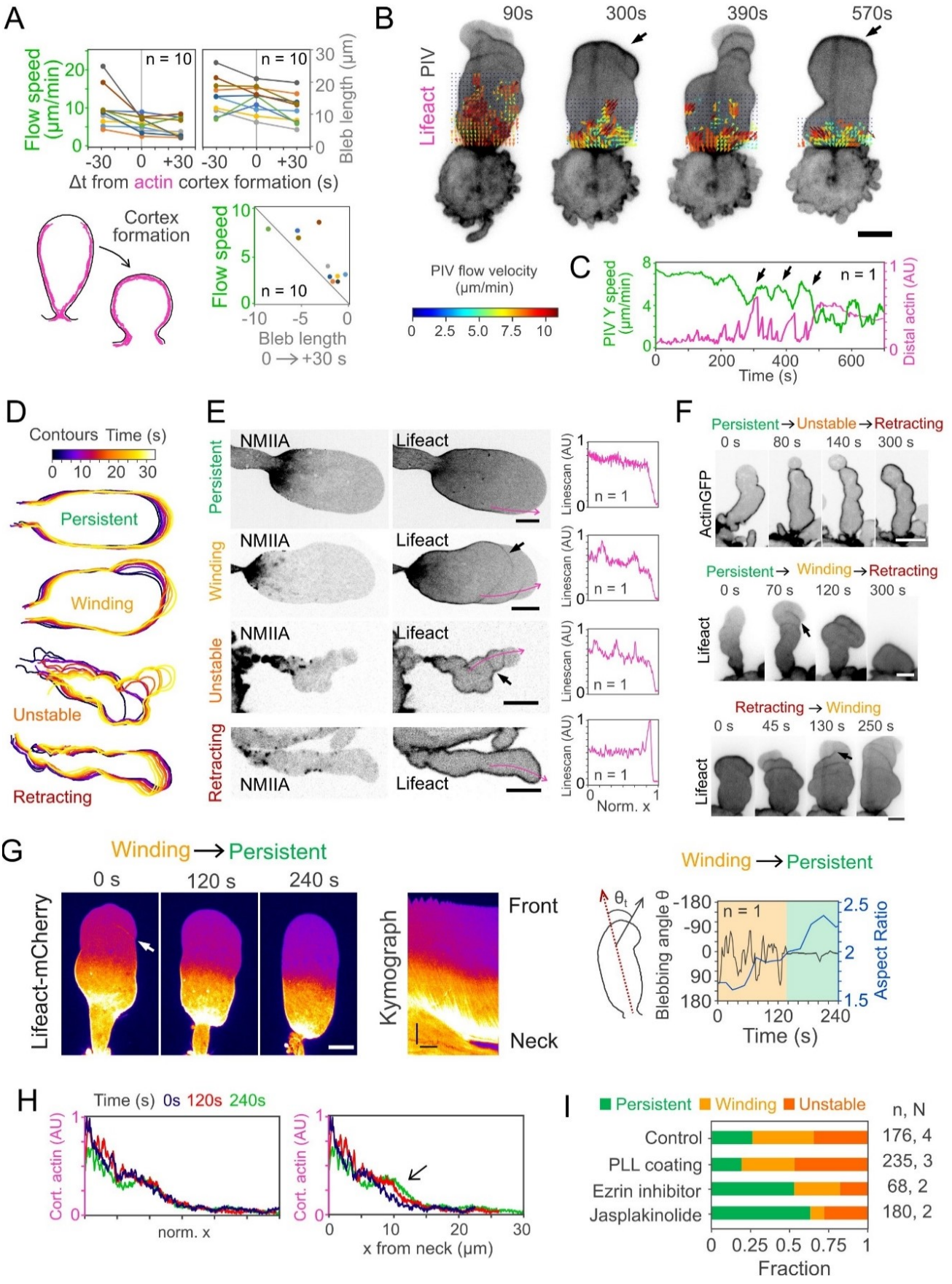

Figure 30: Stable blebs can spontaneously switch between blebbing modes, displaying persistent, unstable/winding, or transient retraction phases

A (top): Evolution of flow speed and bleb shape in stable blebs that collapse. Flow speed (measured manually on NMIIA kymographs) and bleb length as a function of the time from actin cortex reformation at the bleb front. **A (bottom)**: Relation between flow speed (30 seconds after cortex formation) and change in bleb length (change from 0 to 30 seconds after cortex formation).

B: Lifeact-mCherry images and PIV (based on the NMIIA channel) of a confined HeLa cell MYH9-eGFP Lifeact-mCherry over 10 minutes. We observe transient retraction events at which the cortex covers the entire contour of the cell (as indicated by the black arrows). Scale bar: 10 μm.

C: Average PIV speed on the Y-axis and distal cortical actin density of the cell represented in figure 4A. We observe sudden increases of actin density, which correlates in time with a decrease in flow speed as indicated by the black arrows.

D: Evolution of bleb contours over 30 seconds of representative examples of a persistent, winding, unstable, and retracting bleb.

E (left): Representative NMIIA and lifeact images on the middle-plane of representative examples of persistent, winding, unstable, and retracting blebs. In winding and unstable blebs, we can observe scars of the cell cortex flowing back inside the cell, as pointed by the black arrow. **E (right)**: normalized, background-subtracted actin line scans on the pink arrows indicated on the images. Scale bars: 10 μm.

F: Actin-GFP (top) or lifeact-mCherry (middle and bottom) middle-plane examples of transitions towards retraction or towards stability. The data suggest that winding and unstable behavior are transitions between the persistent blebbing and a retracting bleb. Scale bars: 10 μm.

G: Spontaneous transition from a winding to a persistent blebbing. **G (left)**: Lifeact-mCherry bottom plane images of the transition in false color. Scale bar: 10 μm. Kymograph of actin density along the longer bleb axis. Dotted red lines represent the positions of the bleb front and bleb neck. Scale bars: 5 μm and 60s. **G (right)**: Bleb protruding angle (respective to the bleb main axis) and aspect ratio over time. We appreciate the sudden stabilization of the protruding angle around 130s. The green and yellow shaded regions represent the times of winding or persistent blebbing behavior.

H: cortical actin gradients along the bleb contour, as a function of distance from the bleb neck or normalized x. We observed that the normalized gradients fall under the same line, suggesting a dynamic reconfiguration of the actin density gradient.

I: Fraction of blebs in persistent, winding or unstable modes under different conditions: control (PLL-*g*-PEG coating), jasplakinolide at 100 nM (actin stabilizer, known to increase the actin gradient), PLL coating (increased friction, known to decrease the actin gradient), and cells treated with the ezrin inhibitor NSC668994 at 10μM.

Figure 31: Cortical actin controls protrusion dynamics in motile bleb fragments

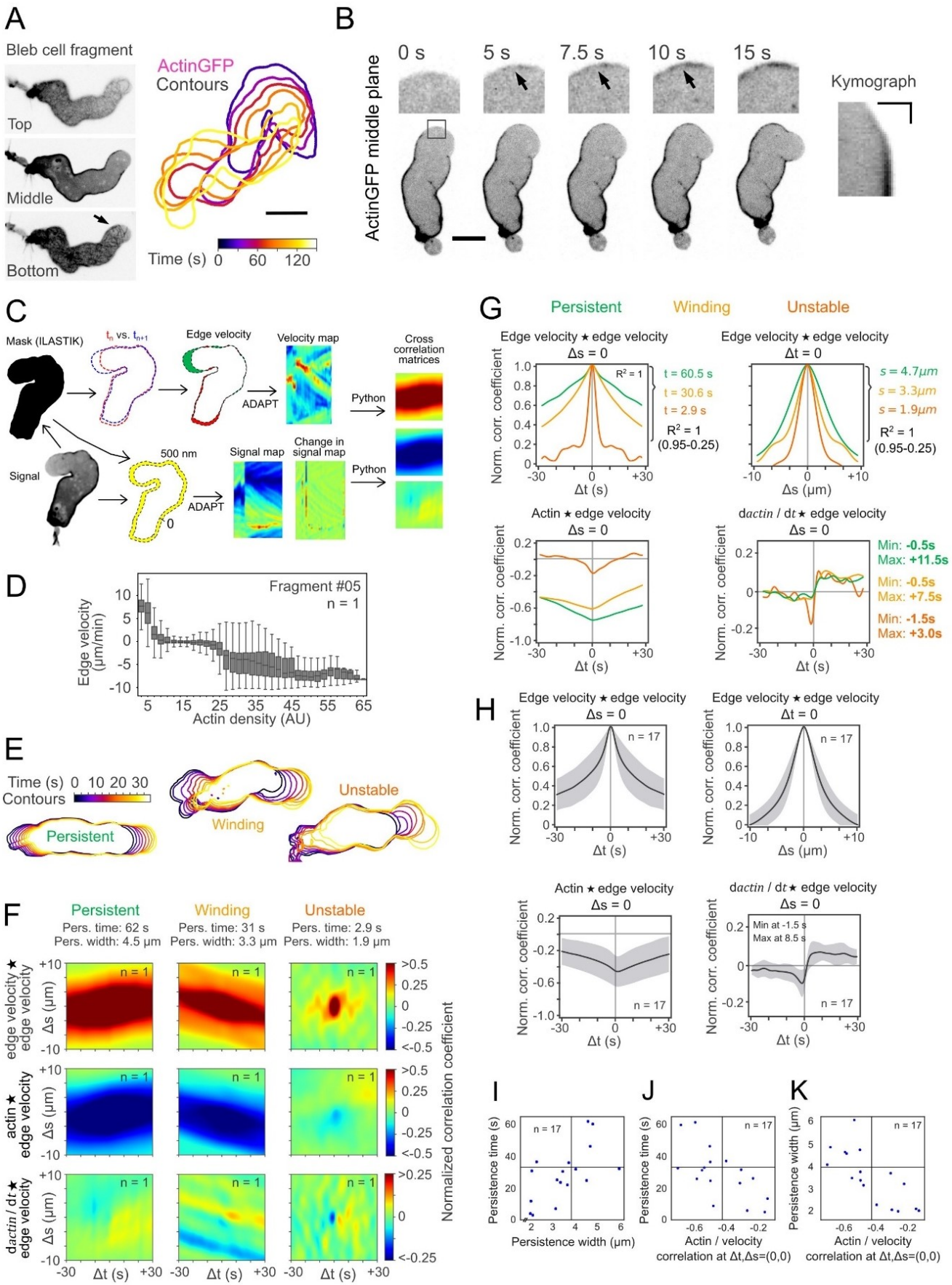

Figure 31: Cortical actin controls protrusion dynamics in motile bleb fragments

A: Top, middle, and bottom planes of an actin-GFP bleb fragment, and contours over 2 minutes. We observe the sparse and bundled actin cortex present at the bleb front, as indicated by a black arrow. Scale bar: 5μm.

B: Image sequence of a Hela actin-GFP bleb fragment changing direction and zoom in on the front cortical region marked with a back square (top). Scale bar: 5 μm. We observe that actin accumulation at the front precedes to membrane stalling with a small delay, as shown by the kymograph on the right.

C: Pipeline for protrusion and actin cross-correlation analysis of bleb fragments. First, the signal is acquired on actin-GFP. The high background of the actin-GFP signal allows for a good segmentation, which is performed manually for a few time points and then fed into Ilastik to segment the rest of the movie. The Fiji plugin ADAPT (Automated Detection and Analysis of ProTrusions) allows for the analysis of protrusion edge and image segmentation. The actin cortical density is calculated on a 300 nm area beneath the cell contour, on background-subtracted actin-GFP movies. The cross-correlation analysis, normalization, and plotting is performed using a homemade Python algorithm. The output of the pipeline is three cross-correlation matrices: edge velocity ★ edge velocity, actin ★ edge velocity, and d*actin*/d*t* ★ edge velocity.

D: Distribution of edge velocities per binned actin density at each contour segment for a single fragment at 300 time points (0.5s/frame).

E: Contours of cell fragments over 30 seconds on persistent, winding, and unstable blebbing.

F: Cross-correlation (sliding dot product) matrices of edge velocity ★ edge velocity, actin ★ edge velocity, and d*actin*/d*t* ★ edge velocity for representative examples of persistent, winding, and unstable blebbing states.

G: Cross-correlation coefficients at for three representative examples of persistent, winding, and unstable blebbing. The X-axis represents the lag imposed to the second function, and the Y-axis represents the normalized cross-correlation coefficient, which yields a time-dependent Pearson correlation coefficient between the two functions. **F (top left)**: Edge velocity autocorrelation at $\Delta s = 0$. The tipical time t is extracted from a linear regression of $t = \log(correlation\ coefficient)$. **F (top right)**: Edge velocity autocorrelation at $\Delta t = 0$. The tipical width s is extracted from a linear regression of $s = \log(correlation\ coefficient)$. **F (bottom left)**: Cross-correlation coefficient of actin ★ edge velocity at $\Delta s = 0$. **F (bottom right)**: Cross-correlation coefficient of $d actin/dt$ ★ edge velocity at $\Delta s = 0$. Detected minima and maxima around t=0 are marked on the right.

H: Averages (solid line) and standard deviations (shade) of different cross-correlation coefficients for all control fragments. **G (top left)**: Edge velocity autocorrelation at $\Delta s = 0$. **G (top right)**: Edge velocity autocorrelation at $\Delta t = 0$. **G (bottom left)**: Cross-correlation coefficient of actin ★ edge velocity at $\Delta s = 0$. In average, we observe a minimum peak at zero lag, which indicates that that the highest edge velocity occurs at the lowest actin density and that the lowest edge velocity (negative) occurs at the sites with high actin signal. **G (bottom right)**: Cross-correlation coefficient of $d actin/dt$ ★ edge velocity at $\Delta s = 0$. In average, we observe a minimum peak at -1.5 second lag (-3 time points), which suggest that the maximum increase of actin signal happens 1.5 seconds before the maximum decrease of velocity, or that the decrease of actin signal happens 1.5 seconds before the increase of velocity. We also observe a positive correlation peak at +8.5 s (+17 time points), suggesting a delay of +8.5 seconds between the maximum increase in velocity and the maximum increase of actin, meaning that 8.5 seconds after a protrusion we will have an increase in the actin signal

I: Persistence time and bleb width computed from the edge velocity autocorrelation matrix, computed for each motile fragment.

J: Persistence time plotted against actin ★ edge velocity at $\Delta(s,t)=(0,0)$, computed for each motile fragment.

K: Persistence width plotted against actin ★ edge velocity at $\Delta(s,t)=(0,0)$, computed for each motile fragment.

Figure 32: Reduction of the membrane-actin attachment promotes persistent blebbing in motile fragments

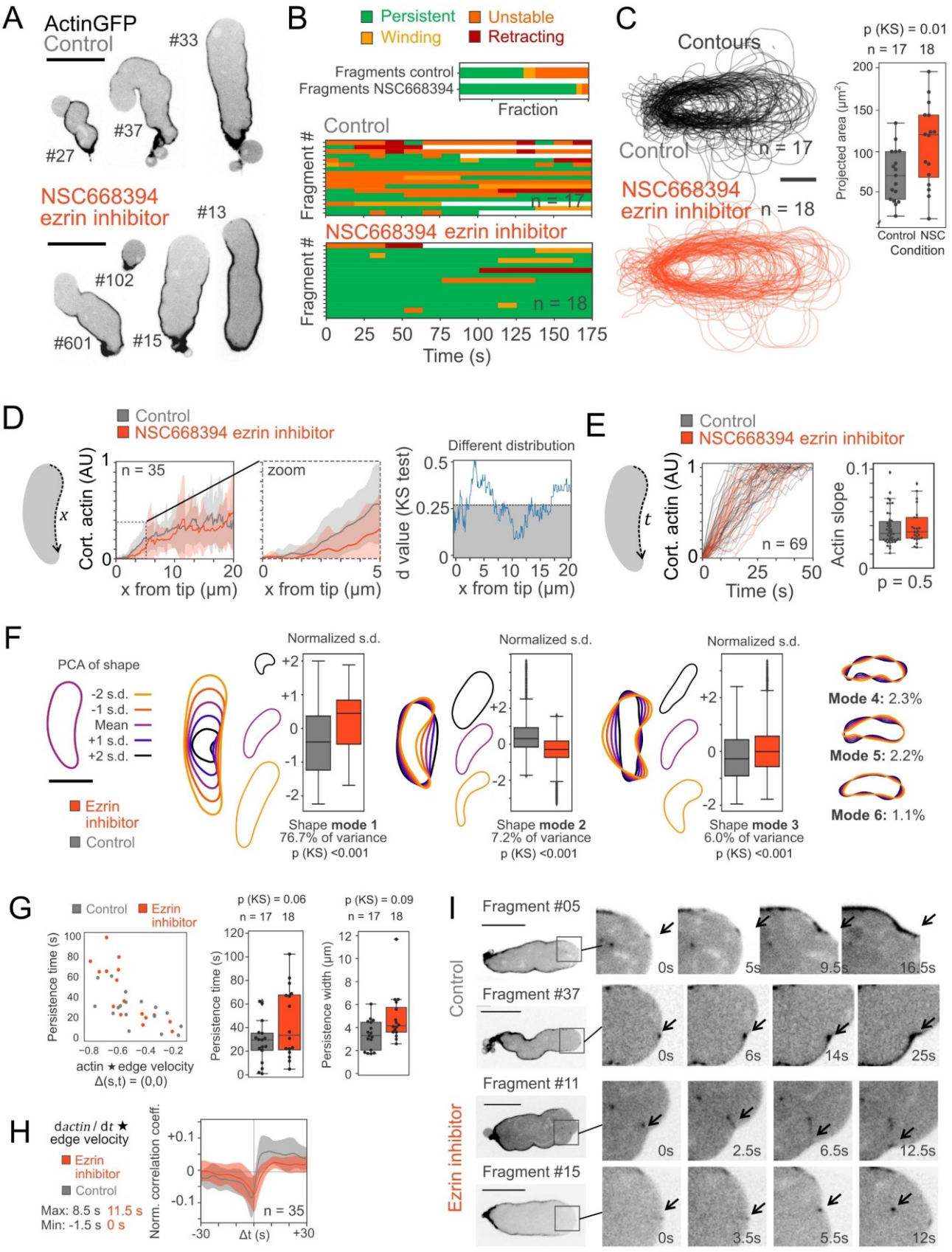

Figure 32: Reduction of the membrane-actin attachment promotes persistent blebbing in motile fragments

A: Examples of bleb fragments of control cells (top) and cells treated with ezrin inhibitor NSC668994 at 10µM (bottom).

B: Representation of the migration phenotypes of bleb fragments of control cells (top) and cells treated with ezrin inhibitor NSC668994 at 10µM (bottom) over 3 minutes, manually classified.

C: Superposed and aligned contour of all control and ezrin inhibitor fragment every 30 s. **C (right):** Distribution of projected areas in control and ezrin-inihibited motile fragments. Scale bar: 10 µm.

D (left): Actin cortical gradient of control versus ezrin inhibitor-treated fragments as a function of distance from the bleb tip. **D (right):** d-value (from Kolmogorov–Smirnov test) resulting from a comparison between the ezrin inhibitor and control densities at every point. White area represents the sections at which the two distributions can be considered different, with d-values at which alpha<0.05 is significant, equivalent to a p value < 0.05.

E: Cortical actin density in cortical regions flowing from the front to the rear, as a function of time (time=0 is bleb front). Curves are normalized by their plateau. Slope of the curves from normalized density=0.2 to 0.8. Welch's p value.

F: Principal component analysis of bleb shapes (taking together control and ezrin inhibitor conditions). This analysis of shape identifies the main variations contributing to the overall shape variance. We identified 6 principal shape modes, accounting for 95% of the variance. **K (left):** Average shape calculated from the PCS of shape**. K (center):** Histograms of shape modes 1, 2, and 3 in control and ezrin inhibitor conditions. The first mode represents the variety in sizes, accounting for about 76.7% of the variance, and the second and third modes account for changes in bleb shape. The rest of the mode represents minor edge undulations. **K (right):** representation of other minor shape modes.

G (left): Persistence width plotted against actin ★ edge velocity at $\Delta(s,t)=(0,0)$, computed for each motile fragment in control and ezrin inhibition conditions. **G (right):** Computed persistence time and bleb width from the edge velocity autocorrelation matrix. P-value computed from a Kolmogorov–Smirnov test.

H: Cross-correlation matrix of d*actin*/d*t* ★ edge velocity for control and NSC668994 conditions.

I: Representative examples of control and ezrin inhibitor-treated fragments, and their membrane-actin dynamics at the tip. Scale bar: 10µm. **I (right)**: Time sequence and zoom at the fragment front. Black arrows point at actin and membrane interactions.

Figure 33: Actomyosin network assembly in stable blebs

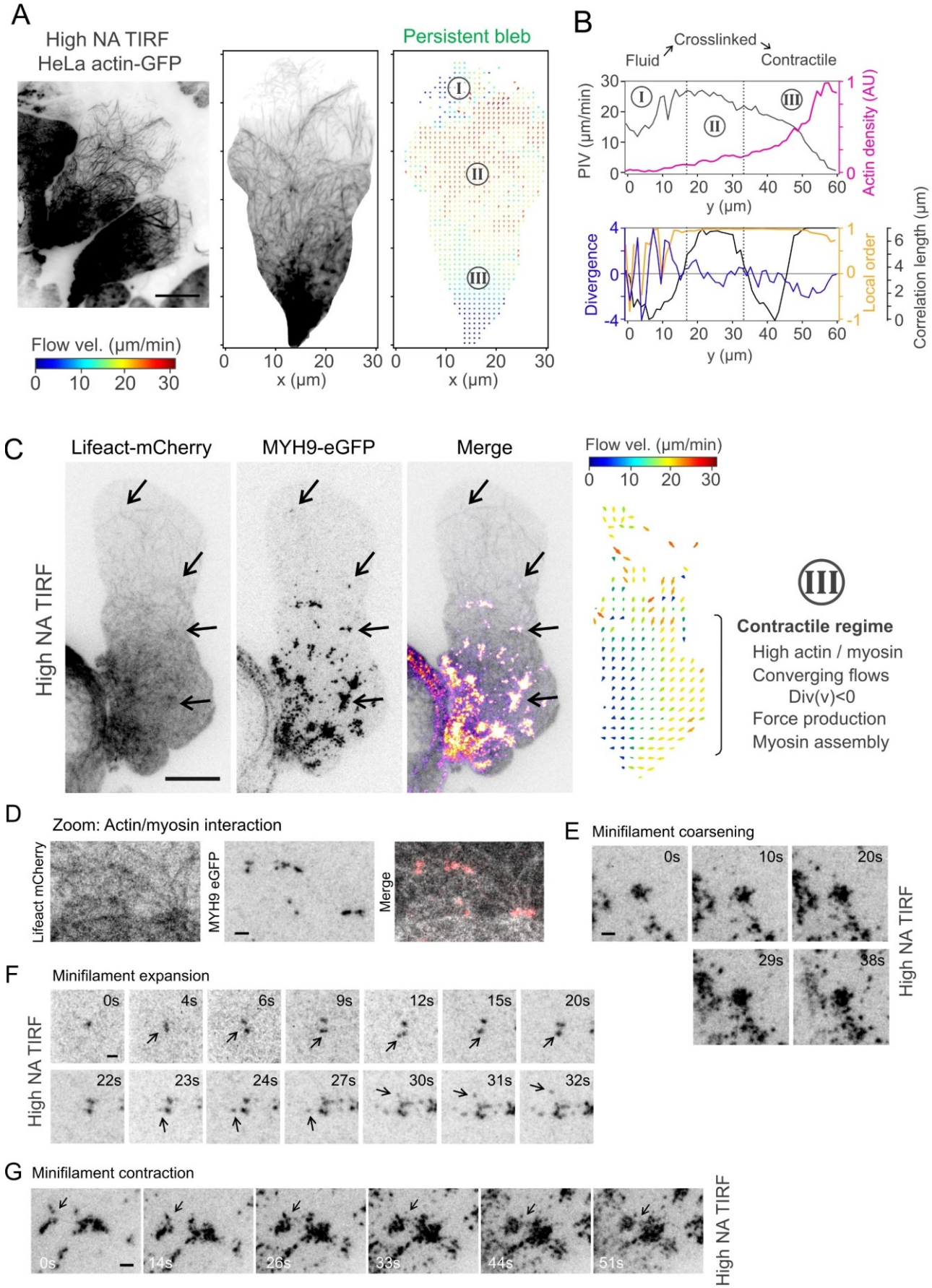

Figure 33 supplementary: Example images of ActinGFP HeLa confined cells on high NA TIRF

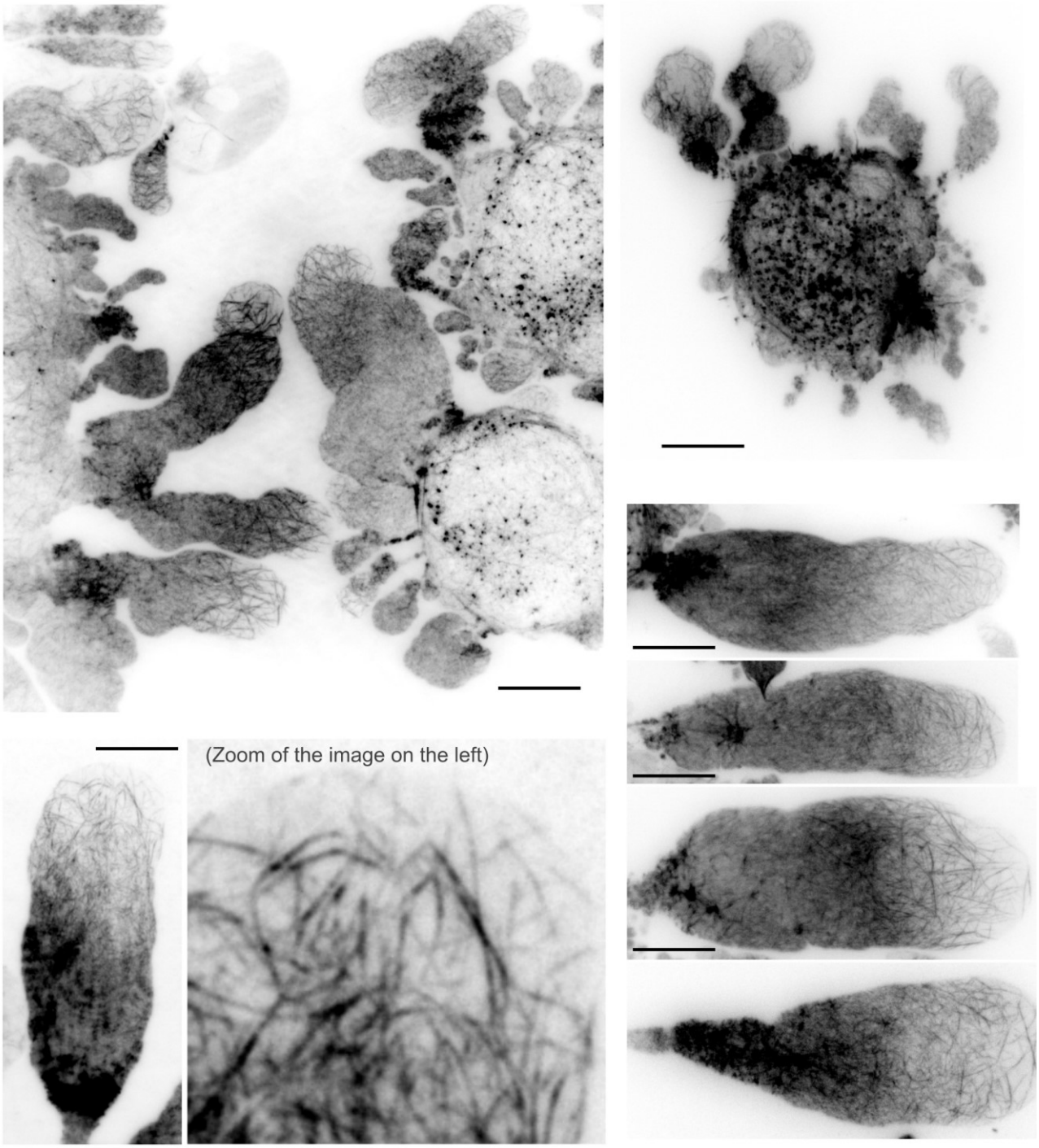

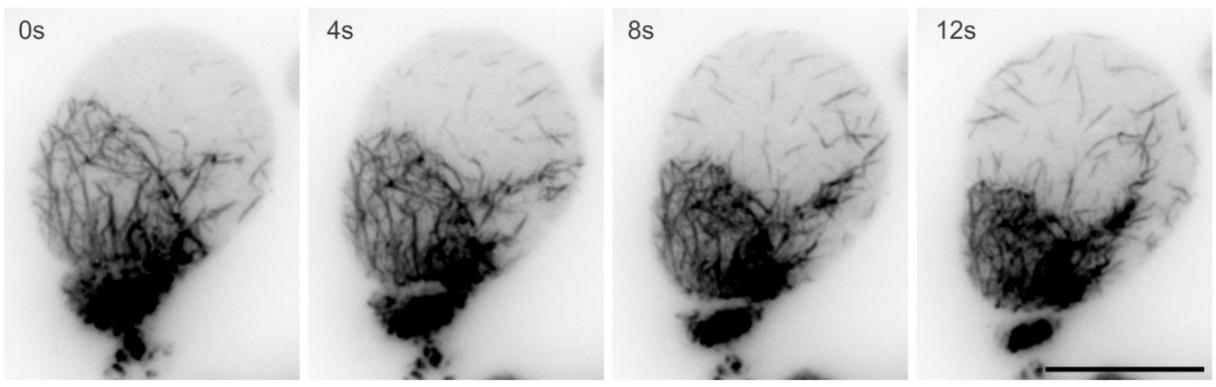

Figure 33: Actomyosin network assembly in stable blebs.

A (left): High NA TIRF image of a stable bleb. Scale bar: 10 µm. **A (right):** PIV flow analysis of a persistent bleb. Numbers point at the three identified cortical regions in panel 2B. **A (bottom):** Scale bar of PIV flow velocities.

B: PIV speed (grey line, top), actin density (pink line, top), correlation length of the velocities (gray line, bottom), local order (orange line, bottom) and PIV divergence (blue line, bottom). Values averaged on the X axis in window between 10 and 20µm and plotted as a function of Y position. Dashed lines represent the approximate limits of the regions 1 (fluid cortex), 2 (crosslinked cortex), and 3 (contracting cortex).

C: High NA TIRF images of a bleb in a HeLa lifeact-mCherry MYH9-eGFP cell, and PIV analysis on the myosin channel. Scale bar = 10µm.

D: Zoom of a region from panel C. Scale bar: 1µm.

E-G: Time sequences of HeLa MYH9-eGFP cell on high NA TIRF. Scale bars: 1µm. **E**: Event of filament coarsening (myosin minifilamtn nucleation without apparent network contraction). **F:** event of minifilament expansion (splitting of myosin minifilaments to colonize the neighboring cortex). **G:** Event of minifilament contraction (coarsening of minifilament my contraction of the surrounding network).

Supplementary data: High NA TIRF image of a stable bleb. Scale bars: 10 µm.

Figure 34: **Actin network assembly in stable blebs**. A connected and not contractile network forms between the front, free of actin, and the contractile base.

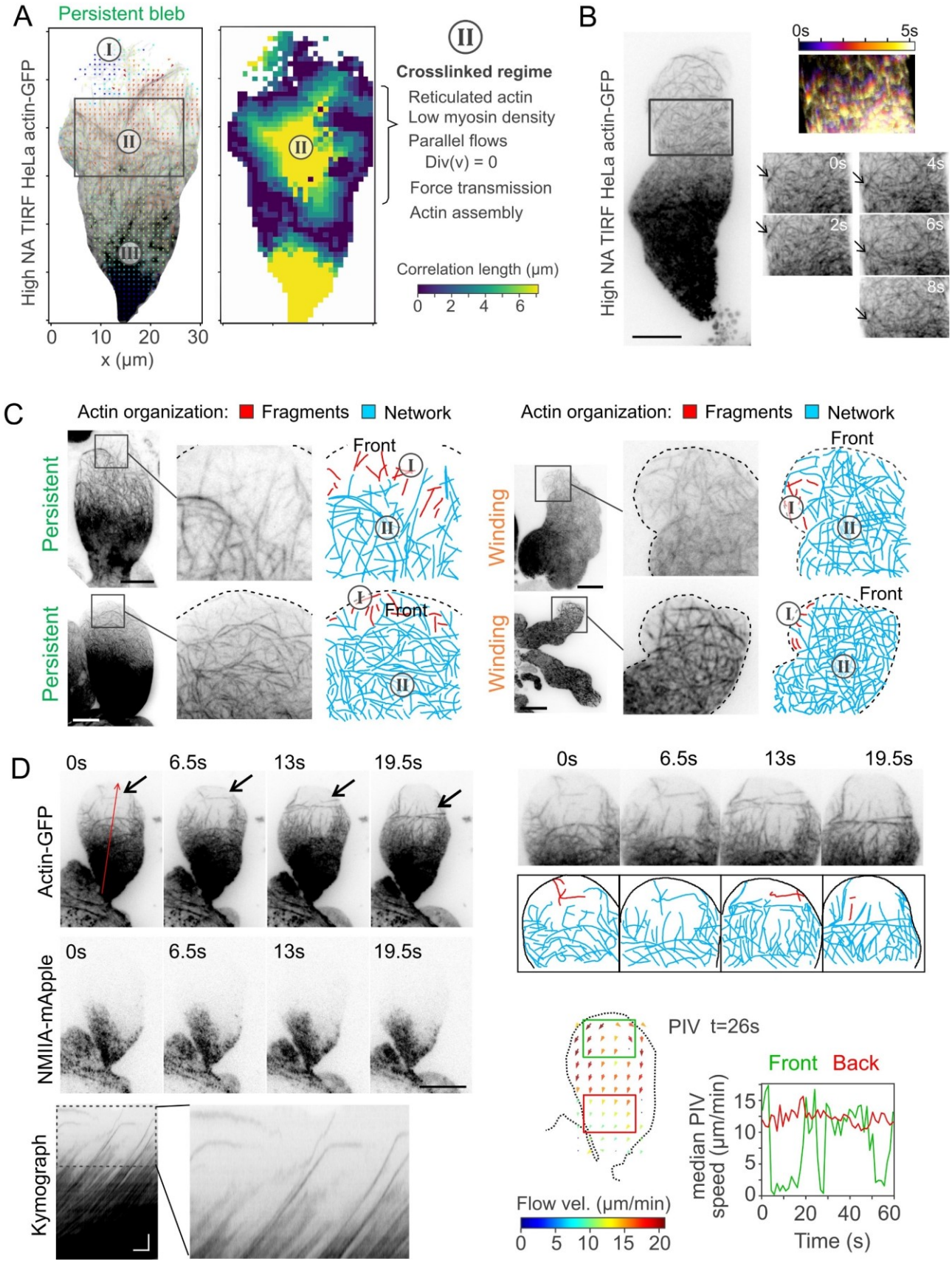

Figure 34: **Actin network assembly in stable blebs.** A connected and not contractile network forms between the front, free of actin, and the contractile base.

A: Left: Example of PIV flow analysis of a persistent bleb shown in figure 9A, highlighting the crosslinked cortex regime. **Right:** Spatial plot of the correlation length of the cortical flows, defined as the length at which the average correlation is above 0.7.

B: High NA TIRF image of an actin-GFP confined bleb, the black square marks the cross-linked region. Scale bar: 10μm. **B (right):** time sequence of the cortex on the region, and color-coded time projection.

C: Representative example of actin network structure at the front of persistent (left) or winding blebs (right). Red lines mark actin filaments not linked to the main network, which is marked in blue. Scale bar: 10μm.

D: Top left: Time sequence of a persistent bleb on high NA TIRF, on the actin-GFP channel (top), and on the myosin (NMIIA-N-18-mApple) channel (bottom). Scale bar: 10μm. Red arrow shows the site used to plot the kymograph below. Black arrow points at a moving actin bundle carried by the flow. **Bottom left**: Kymograph of the flow pointed with the red line on top. Black arrows point at events were the bundles are transiently not flowing. Scale bar: 20s/1μm. **Top right**: Zoom on the front region on the actin-GFP channel. Red lines mark actin filaments not linked to the main network, which is marked in blue. **Bottom right**: representative flow profile on a “continuous flow phase” of the bleb, at t=26s. PIV are colored by the velocity vector magnitude, in μm/min, showed below. We selected two windows at the front (green box, green line on the velocity plot on the right) and the back of the bleb (red box, green line on the velocity plot on the right), and calculated the median magnitude at each time point (velocity plot of the right).

Figure 35: **Actin network assembly in stable blebs**. Single actin filaments assemble into a connected network at the bleb front

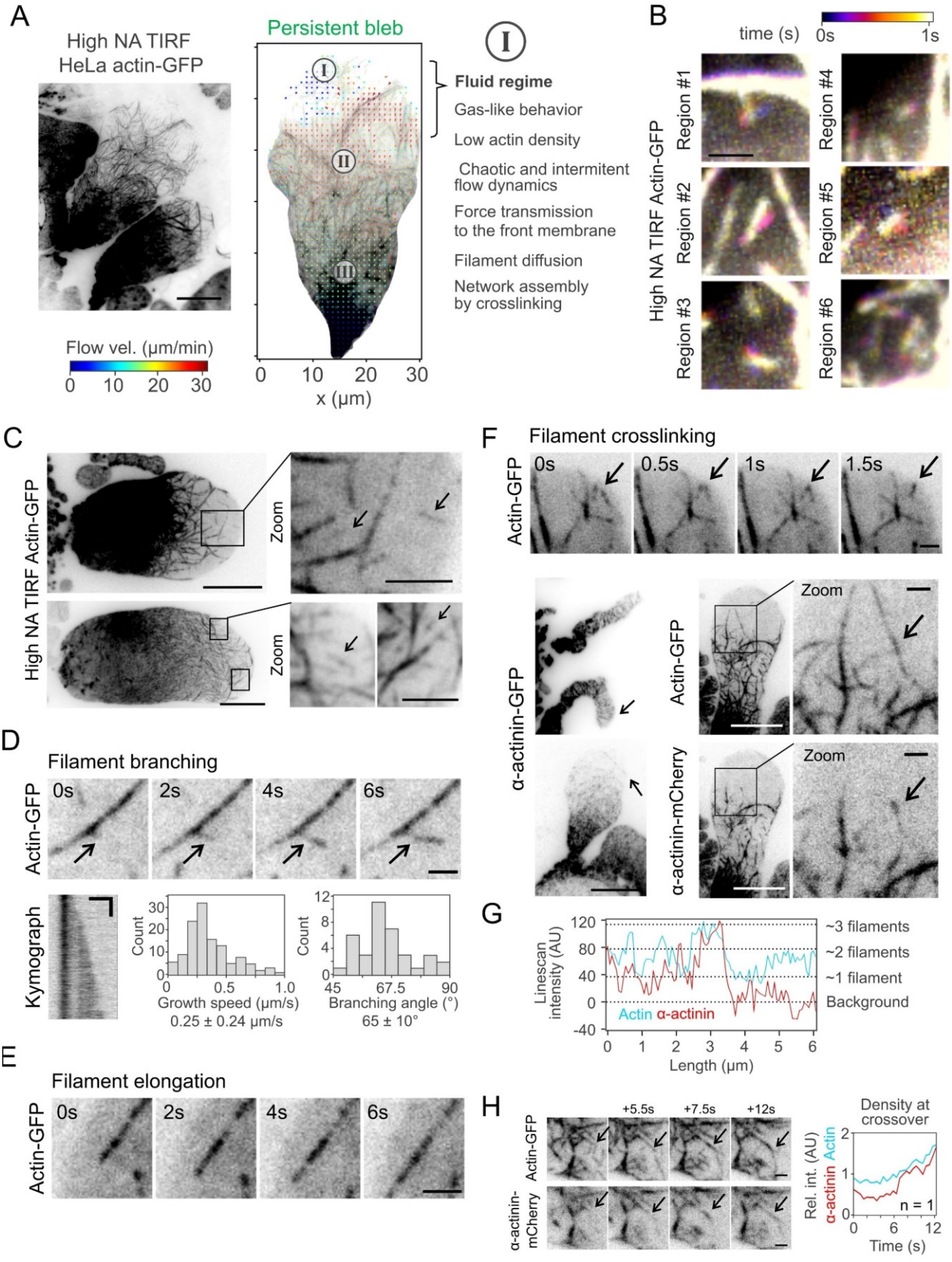

Figure 35: **Actin network assembly in stable blebs.** From single actin filaments at the distal tip to a connected network.

A: Example of PIV flow analysis of a persistent bleb shown in figure 9A, highlighting the fluid cortex regime.

B: Color-coded time projection of the diffusive behavior of actin filament in the sparse region of the front. Scale bar: 1µm.

C: Time sequence of a representative filament branching event. Black arrow points at the branch. Scale bar: 1µm. Bottom: kymograph along the filament length. Scale bars: 1s/1µm. On the right, histograms of filament growth speeds (µm/min) and branching angle (°), and mean value ± standard deviation.

D: Time sequence of a representative filament elongation event. Scale bar: 1µm.

E: Top: time sequence of a representative filament crosslinking event, marked with black arrows. Scale bar: 1µm. Middle right: snapshots of blebs transfected with alpha-actinin-GFP. Black arrows point at sites were we observe stipe patterns. Scale bar: 10µm. Middle left: representative image of a bleb transfected with alpha-actinin-mCherry on HeLa actin-GFP cell line. Image is zoomed from the black square. Black arrows point at sites of filament overlapping and sites of accumulation of crosslinker. Scale bar: 10µm.

F: Linescan on the filament pointed in figure 11E on the actin and alpha-actinin channels after background subtraction.

G: time sequence of a cortical network with alpha-actinin-mCherry on HeLa actin-GFP cell line. Black arrow marks the sites of filament overlapping. On the right, normalized intensity quantification over time on the sites of filament overlapping marked with the black arrow. Scale bar: 1µm.

Figure 36: **Actin network assembly in stable blebs.** Force transmission from the proximal contractile end to the distal tip through the connected network. Signs of force percolation.

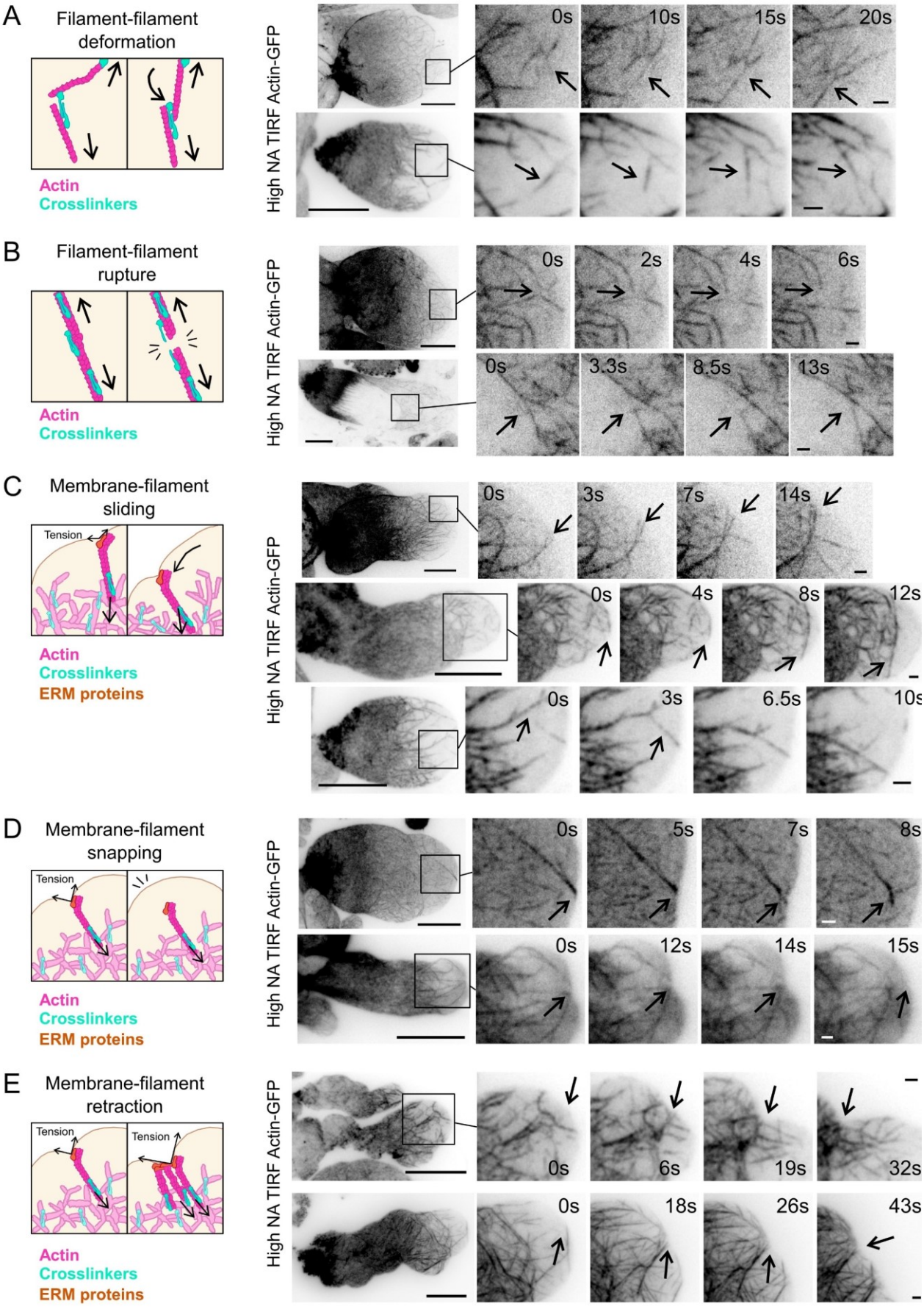

Figure 36: Actin network assembly in stable bleb. Force transmission from the proximal contractile end to the distal tip through the connected network, signs of force percolation.

A: Time sequence of two representative events of filament-filament deformation by retrograde flow at the front of actin-GFP blebs from HeLa cells on high NA TIRF. Scale bar: 10µm (left) and 1µm (right).

B: Time sequence of two representative events of filament-filament rupture at the front of actin-GFP blebs from HeLa cells on high NA TIRF. Scale bar: 10µm (left) and 1µm (right).

C: Time sequence of three representative events of filament-membrane deformation and sliding at the front of actin-GFP blebs from HeLa cells on high NA TIRF. Scale bar: 10µm (left) and 1µm (right).

D: Time sequence of two representative events of filament-membrane deformation and snapping (detachment) at the front of actin-GFP blebs from HeLa cells on high NA TIRF. Scale bar: 10µm (left) and 1µm (right).

E: Time sequence of two representative events of filament-membrane deformation and subsequent retraction at the front of actin-GFP blebs from HeLa cells on high NA TIRF. Scale bar: 10µm (left) and 1µm (right).

Figure 37: **Phase transitions in cortical actin in blebs.** Actin network percolation could explain the dynamics of actin networks in stable blebs.

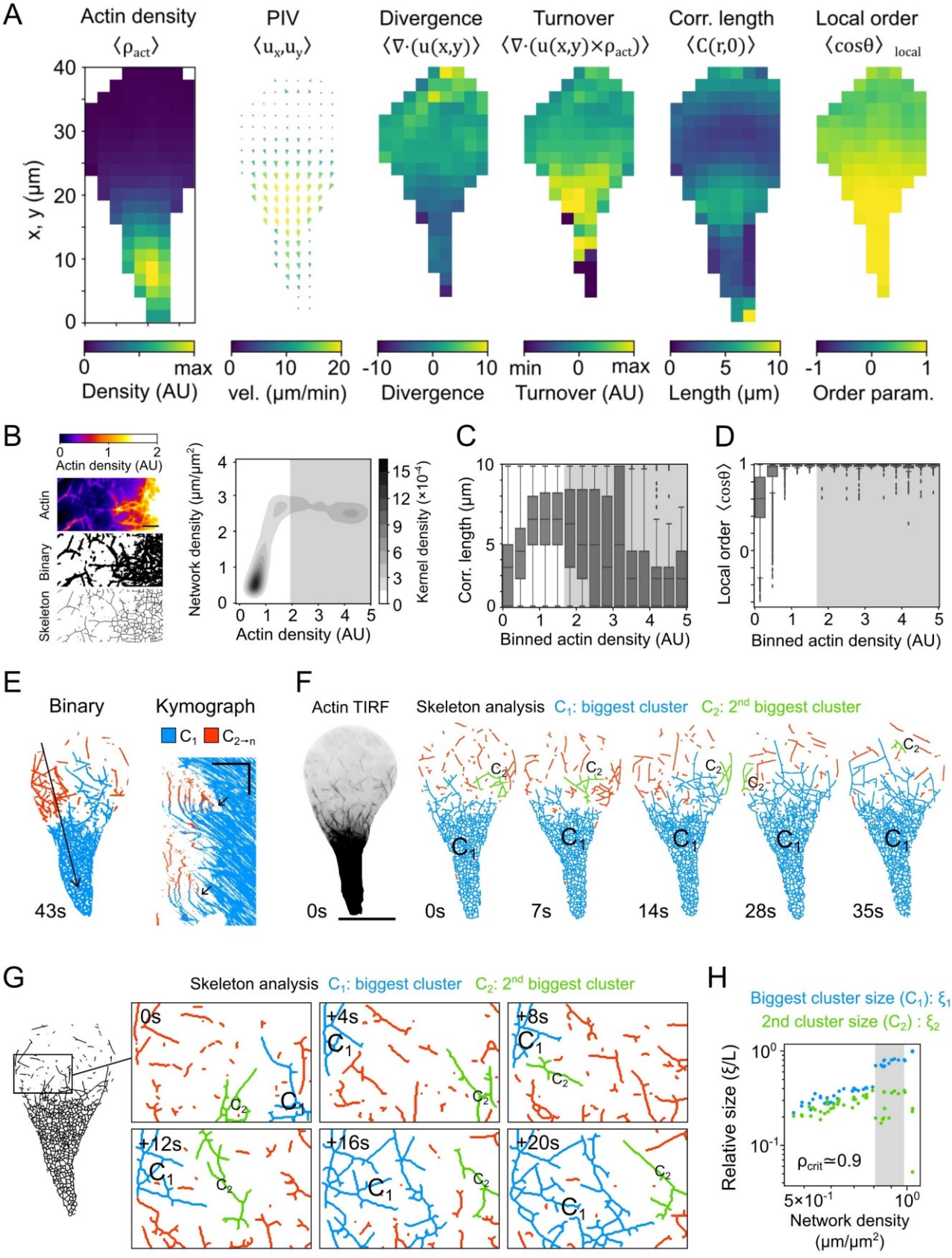

Figure 37: **Phase transitions in cortical actin in blebs.** Actin network percolation could explain the dynamics of actin networks in stable blebs.

A: Time averaged (314 time points) actin density, PIV vectors, divergence, turnover, correlation length, and local order parameter of a representative bleb with low actin density at the front.

B (left): Example network analysis of a bleb region, from the actin fluorescence channel (top), to the binarized image (middle), and the extracted skeleton. Scale bar: 1μm. **B (right):** network density (defined as the fraction of skeleton pixels in a given area / pixel calibration) plotted against the binned actin density for all time points. Shaded in grey, range of actin density at which network density does not increase.

C: Quartile distribution of correlation length plotted against binned actin density. Shaded in grey, range of actin density at which network density does not increase.

D: Quartile distribution of local order plotted against binned actin density. Shaded in grey, range of actin density at which network density does not increase.

E: Snapshot of a binarized actin network in a bleb. The largest cluster is colored in blue, and all secondary clusters are colored in red. The black arrow indicated the site to produce the kymograph on the right. Black arrows indicate time points of stress percolation ("red clusters" become part of the main "blue cluster") and subsequent flow. Kymograph scale bar: 30s/10μm

F: Cluster analysis of the skeletonized actin network in the bleb at different time points. The main cluster is colored in blue, the second biggest cluster is colored in green, and the rest of clusters are colored in red. At time 0, the unprocessed actin-GFP channel is shown. Scale bar: 10μm.

G: Time sequence on a small region of the skeletonized region. The main cluster is colored in blue, the second biggest cluster is colored in green, and the rest of clusters are colored in red.

H: Log-log plot of relative sized (normalized by the system size) of the biggest cluster and the second biggest cluster, as a function of the network density. The critical concentration is expected to be the ones at which the two sizes diverge, which is approximately 0.9.

Figure 38: Actin network structure in fixed blebs

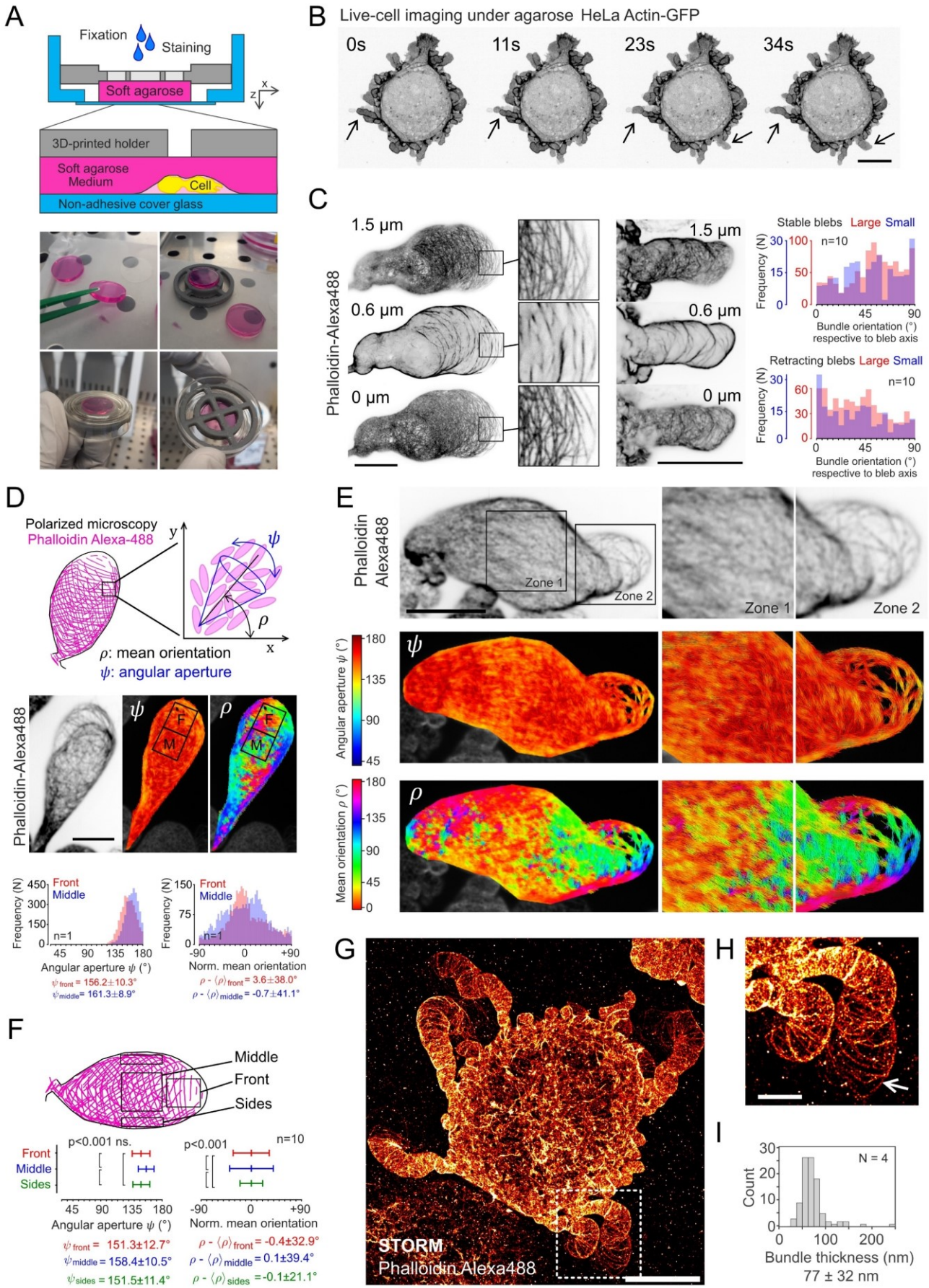

Figure 38: Actin network structure in fixed blebs

A: Schematic representation of the agarose confinement device (top), and pictures of the device (bottom).

B: Live-cell imaging of HeLa actin-GFP cells under agarose confinement. Black arrows point at events of dynamic blebbing. Scale bar: 10µm.

C: Top, middle, and bottom planes of a bleb fixed under agarose confinement, displaying an actin-free front, stained with phalloidin-Alexa488. Regions marked with a black square are pictured on the right side. Middle: Top, middle, and bottom planes of a bleb fi fixed under agarose confinement, displaying a front with a clear cortex, stained with phalloidin-Alexa488. Scale bar: 10µm. Right: histogram of filament orientation at the front of blebs relative to the main bleb axis, weighted by the segment length. Right top: histogram of filament orientation of large (red) small (blue) blebs with an actin free tip. Right bottom: histogram of filament orientation of large (red) small (blue) blebs with aa full actin front.

D: Top: schematic representation of the molecular order and aperture angles (ρ, ψ). Middle: representative example of a bleb with an actin-free front, confined under agarose and stained with phalloidin-Alexa488. Scale bar: 10µm. On the right, calculated molecular order and aperture angles (ρ, ψ) fields. The angular color code is shown in figure 7K. We marked two regions: front ("F") and middle ("M"). Bottom: histogram of molecular order and aperture angles (ρ, ψ) from the front ("F") and middle ("M") regions. The values at the bottom of the histograms for ψ_{front}, ψ_{middle}, ρ_{front} and ρ_{middle} represent mean ± standard deviation.

E: Top: bottom plane of a bleb fixed under agarose confinement, displaying a winding phenotype, stained with phalloidin-Alexa488. On the right, zoom of the zone 1 (middle of the bleb) and zone 2 (front of the bleb). Scale bar: 10µm. Middle, bottom: calculated molecular order and aperture angles (ρ, ψ) fields. The angular color code is shown on the left.

F: Mean ± standard deviation of the molecular order and aperture angles (ρ, ψ) fields in the front, middle, or side regions of 10 selected blebs as representative examples. The plot and values represent the combined standard deviation of ρ and ψ via ANOVA as square root of grand variance, and the mean of the means for the selected regions in the 10 blebs. Statistical comparison of front and middle regions yielded non-significant difference in the angular aperture ($p=0.09$), but significant difference between the front and middle or sides and middle regions ($p<0.001$). We compared the variances in the angular orientation using F-test for variances, which yielded significant differences in all three pairs of tests ($p<0.001$).

G: Render of the STORM image of agarose-confined phalloidin-Alexa488 cells using Abbelight software. Pixel size = 15 nm, scale bar: 10µm.

H: Zoom of the region marked with a dotted white square. Scale bar: 2.5µm. White arrow marks the actin bundles observed at the bleb tip.

I: Quantification of the mean ± standard deviation of bundle thickness observed at the front of blebs. Bundle thickness was computer as the full width at half maximum of the bundle Gaussian from manually traced linescan profiles.

Figure 39: Inverted contact guidance of blebs on nanogrooves

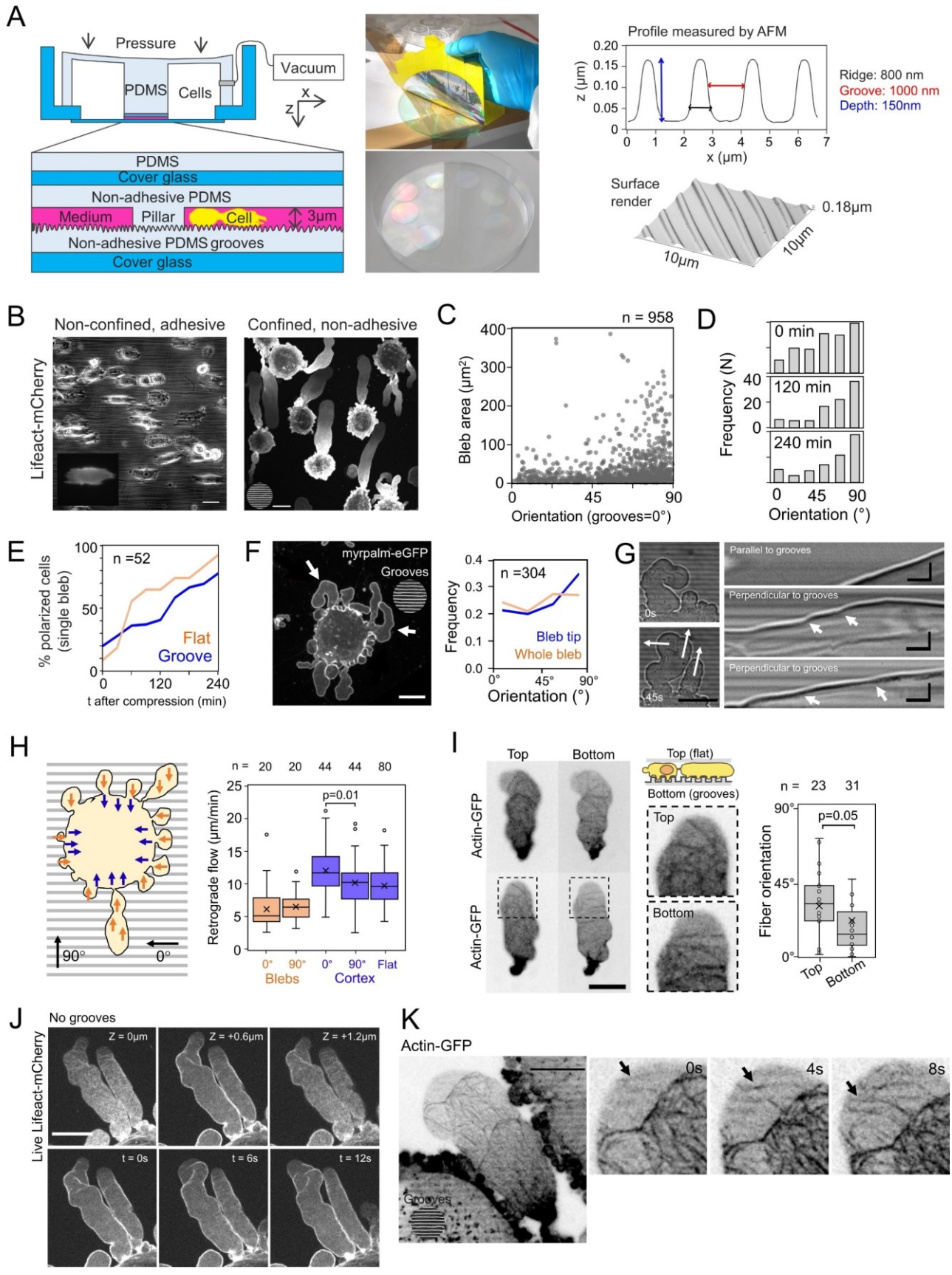

Figure 39: inverted contact guidance of blebs on nanogrooves

A: **Left**: Schematic representation of the confiner device combined with nanogrooves. Middle: Pictures of the fabrication process of the PDMS nanogrooves, on top the process of removing the protective iridescent layer on CD-ROMs and on the bottom the finished coverslips with grooves, showing the diffraction of light caused by the surface topography. **Right**: AFM measurement of the profile of the grooves, and their dimensions. Right bottom: rendering and dimensions of the surface.

B: **Left**: Representative phase contrast image of adherent HeLa cells seeded on aligned collagen electrospun fibers. Inset shows lifeact-mCherry cells. **Right**: Representative fluorescent image of lifeact-mCherry HeLa cells confined over PEG-*g*-PLL coated nanogrooves. Scale bar: 20μm. Image was rotated to orient the grooves horizontally.

C: Bleb area and orientation (Ferret's angle of the bleb relative to groove angle) of blebs during the first four hours following confinement, pooled from snapshots every 10 minutes. **D**: Histogram of bleb orientation (Ferret's angle of the bleb relative to groove angle) at 0 minutes, 120 minutes and 240 minutes after confinement.

E: Percentage of polarized cells, defined as bearing a single bleb, for HeLa cells confined on PEG-*g*-PLL coated flat or nanogrooved PDMS, measured from snapshots every 30 minutes.

F: Left: Representative image of a myrpalm-GFP HeLa cell (membrane marker) confined on PEG-*g*-PLL coated PDMS nanogrooves. The white arrow points at events where the tip is oriented perpendicularly to nanogrooves while the rest of the bleb is not. Scale bar: 10μm. Right: histogram of relative frequencies of the orientation of whole blebs from non-polarized cells and the orientation of the bleb tips (defined as the direction of protrusion, respective to the grooves). Image was rotated to orient the grooves horizontally.

G: Fast recording on phase contrast of a representative example of a protruding bleb on nanogrooves. **Left**: snapshots at 0 and 45 seconds. White arrows indicate the linescans used to construct the kymographs on the right. Scale bar: 5μm. **Right**: kymographs of the membrane position advancing perpendicular or parallel to nanogrooves. White arrows indicate times at which the membrane advancement is perturbed by the grooves. Scale bars: 5s/2.5μm. Image was rotated to orient the grooves horizontally.

H: Cortical flows at the bottom plane of confined HeLa MYH9-eGFP cells (plane with the nanogrooved surface), measured with kymographs at either 0° or 90° respective to grooves. Left: schematic of the position of kymographs: quartile distributions (cross: mean value) of the retrograde flow speed perpendicular or parallel to grooves, in blebs or cortical regions, in flat or grooved PDMS.

I: **Left**: top and bottom planes of an actin-GFP bleb fragment confined on nanogrooves. Scale bar: 10μm. Middle: schematic of the experiment, with grooves in the bottom planes and a flat surface on top, and zoom in of the tip region. **Right**: Quantification of fiber orientation at bleb tip, Boxes and bars represent quartile distributions, crosses represent mean values, and p value represents one-tailed Welch t-test. Image was rotated to orient the grooves horizontally.

J: Z-stack (top) and time sequence of a bleb from HeLa lifeact-mCherry cells confined on PLL-*g*-PEG coated glass. Scale bar: 10μm.

K: **Left**: Snapshot of a bleb from HeLa actin-GFP confined over PLL-*g*-PEG coated nanogrooves. Scale bar: 10μm. **Right**: Zoom and time sequence of an actin-free region at the front. Black arrows point at the fibers forming at the front of the bleb. Image was rotated to orient the grooves horizontally.

Part IV: Discussion and perspectives

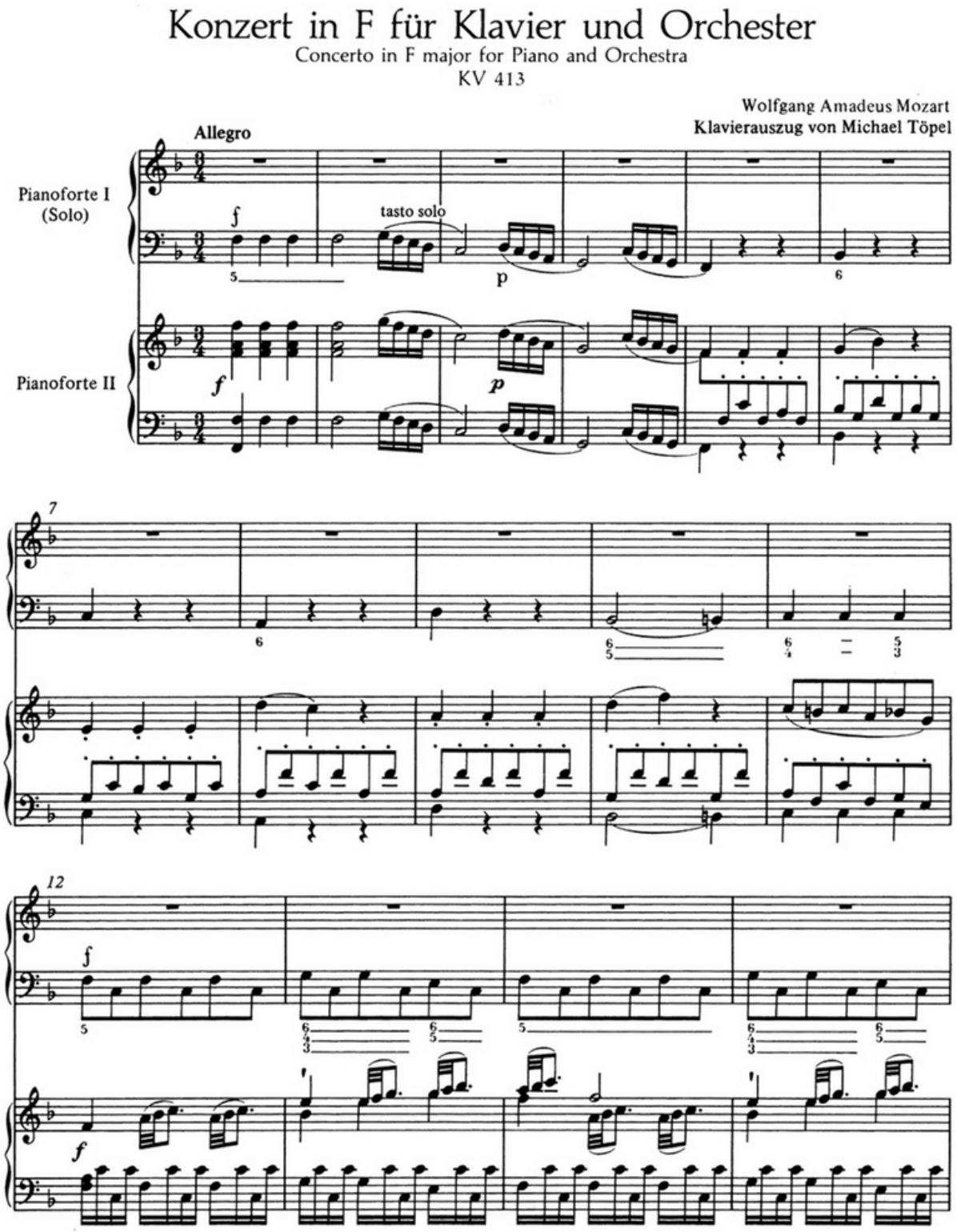

Chapter 10: Discussion of main results

Summary of the work

The first part of my work described bleb morphogenesis immediately after confinement. Based on the shape, actomyosin organization, and lifetime of individual blebs, we classified blebs into two groups: **round** and **elongated** blebs. Round blebs start to form immediately after confinement, but elongated blebs start to form only after a delay (~15s). Round blebs recapitulate actomyosin dynamics and lifetime previously described for transient blebs (Bovellan et al., 2014; Charras et al., 2008; Cunningham, 1995; Tinevez et al., 2009). Conversely, we found that elongated blebs gradually deplete actomyosin from the front to achieve a steady-state gradient during formation. Remarkably, small elongated blebs recapitulate the actomyosin gradient and dynamics of much larger stable blebs formed in polarized confined cells (Callan-Jones and Voituriez, 2013). These large blebs, described in recent works from our lab and others, **form actomyosin gradients due to a sustained retrograde flow** that concentrates actomyosin and cortex-bound proteins to the back of the cell (Bergert et al., 2015; Liu et al., 2015; Logue et al., 2015; Ruprecht et al., 2015).

We propose a working model for bleb morphogenesis in which the final phenotype (transient or stable bleb) is due to the **relative timing of cortex formation versus myosin contraction**. We observed that blebs, regardless of their shape, only avoided retraction if they had their front free of actin at the onset of contraction. On the other hand, blebs that retract accumulate actin at the front before the onset of retraction. In other words, if the cortex forms completely before contraction, then the bleb will retract. However, if the contraction happens before the cortex has completely formed, the bleb will go into a steady-state and form an actomyosin gradient. Consistently, we found that optogenetic activation of myosin activity in stable blebs promotes stabilization, but it increases retraction speed in retracting blebs.

Stable blebs **can transition between different dynamic steady-states (persistent, winding, unstable)**, characterized by different actin-membrane dynamics front. Persistent blebs keep a constant and smooth shape, and winding blebs protrude by sequential cycles of bleb and cortex formation. These three stable steady-states plus the retracting state are present in blebs attached to cells and detached motile bleb fragments, indicating a bleb-autonomous behavior. Different conditions that weakened the links between actin filaments and membrane or conditions that depleted actin from the bleb

front increased the fraction of persistent blebs and persistent motile fragments. Moreover, the time cross-correlation analysis of edge velocity and actin density suggested cortical actin prevents membrane protrusion over a threshold density. Our interpretation is that the **physical interactions between actin and membrane at the bleb front mediate the switches between the dynamic steady-states** and that in persistent blebbing, there has to be a complete **mechanical uncoupling** between the actin filaments and the membrane at the front.

We performed confinement experiments with a high NA TIRF setup, which allowed us to see the actin cortex dynamics in the bleb in greater detail, from the nucleation and network assembly at the front to the contraction and network disassembly at the back. We identified three cortical regimes in blebs: I) a **contractile cortex** at the base of the bleb, enriched in NMIIA, with convergent flows and concentrating the actin network disassembly; II) a **crosslinked cortex**, in the middle region, that transduces the forces from the base to the bleb front but does not contract; and III) a **fluid cortex** at the bleb front, composed of single filaments poorly attached to the membrane or small actin clusters forming a loose network. Our results present a negative role of actin-membrane attachment in protrusion persistence and contribute to the recent findings in the field pointing in the same direction (Bisaria et al., 2020; Welf et al., 2019). They also introduce an additional role for NMIIA contractility, which is essential for maintaining intracellular pressure and depleting actin from the cell front. Our results also explain crosslinkers' function in network assembly, previously identified as essential for stable bleb migration (Logue et al., 2015). Crosslinkers create the intermediate non-contracting reticulated network, which is responsible for the long shape of blebs.

These observations are reminiscent of the **force percolation** dynamics of *in vitro* reconstituted **contractile actin networks** but have not yet been directly observed in a living system (Abu Shah and Keren, 2014; Alvarado et al., 2013; Bendix et al., 2008; Ierushalmi et al., 2020; Malik-Garbi et al., 2019; Tan et al., 2018). Even *in vitro* experiments have not yet been able to link percolation regimes to the density of filaments at the molecular level. The theory predicts that depending on connectivity or motor activity, active contractile gels can acquire different regimes: active solutions, prestressed gels, local contraction, or global contraction. Depending on actin and myosin densities, the cortex of blebs can recapitulate these regimes: the contractile cortex at the base corresponds to a global contraction regime, the crosslinked cortex corresponds to a prestressed gel regime, and the loose fluid cortex at the bleb front corresponds to the active solution regime. The conductivity density threshold determines the steady-state

shape of persistent blebs and can explain the intermediate states between persistent and retracting that were not accounted for by previous bleb-based migration models. The description of a cellular process explained by percolation theory at a molecular level constitutes a novel contribution to the cell biophysics and cytoskeleton field.

I will now discuss some parts of my work, put it in perspective with the state-of-the-art scientific literature, analyze the novelty of the work and the strength of the claims from the experimental proofs, and introduce some preliminary data that was not included in the results section. I will also propose possible future directions for the work and improvement in the experiments or data analysis.

Bleb shape

Blebs in mammalian cells have been the subject of studies in the field of cell biophysics in the last two decades (Bovellan et al., 2014; Charras et al., 2008; Cunningham, 1995; Tinevez et al., 2009). In the context of cell migration, studies have proposed that subsequent polarized blebbing can contribute to cell migration in the absence of cellular adhesions to the matrix (Charras and Paluch, 2008). Researchers have recently discovered that large blebs bearing a persistent flow can contribute to cell migration (Bergert et al., 2015; Liu et al., 2015; Logue et al., 2015; Ruprecht et al., 2015). However, so far only the final, steady-state picture has been described, and it is unclear how the cell transitions from a non-polarized state to a polarized state with only elongated large blebs. It is also unclear what are, if any, the fundamental differences between the transient blebs described in the literature and the stable blebs that sustain a retrograde flow.

The first part of my work contributes to understanding the immediate response to confinement. We classified blebs into two groups based on three parameters: cytoskeleton organization, shape, and lifetime. While round blebs start to appear immediately from confinement, elongated blebs start to appear only after a delay, which suggested that they are not a direct consequence of the confinement. Blebs form when the membrane detaches from the cortex, so they should have a round shape at formation. We showed that, during expansion, elongated blebs form an actomyosin cytoskeleton at the base, pinching the bleb and giving it a long shape.

Actin and myosin are the main cortex components and are often conceptualized as a single composite active material: “actomyosin.” However, actin and myosin gradients in large stable migratory blebs do not follow the same pattern: myosin is more polarized towards the bleb base than actin (Liu et al., 2015). Similarly, elongated blebs always show polarized myosin localization, but do not necessarily polarize actin. The differences in the stoichiometry of actin and myosin give rise to the different cortical regimes found in the base and the front of blebs.

Mechanisms to form a long shape

Our analysis of the role of actin and myosin focused on the emergence of retrograde flow in elongated blebs. While we described the role of cytoskeletal organization in the emergence of retrograde flow and bleb stability, we did not investigate what causes a nascent bleb to acquire an elongated shape. Here I will discuss what could be the mechanism to form a long bleb. At birth, both round and elongated blebs have the same shape (**Figure 25** G, H), but elongated blebs keep growing outwards. Since elongated blebs acquire their long shape before the onset of contraction, myosin contraction of the neck cannot explain their long shape at the beginning of bleb formation. However, we showed that in conditions with reduced myosin activation, cells produce dynamic round blebs but not elongated blebs, suggesting that the role of myosin activity in the initial bleb shape might be due to the increase in intracellular pressure rather than its motor activity at the bleb neck. We observed fragments that transiently lose polarization and motility and then regained them, suggesting that the initial polarization can be fully autonomous (driven by bleb contractility) and does not require pressure from the cell (**Figure 40**).

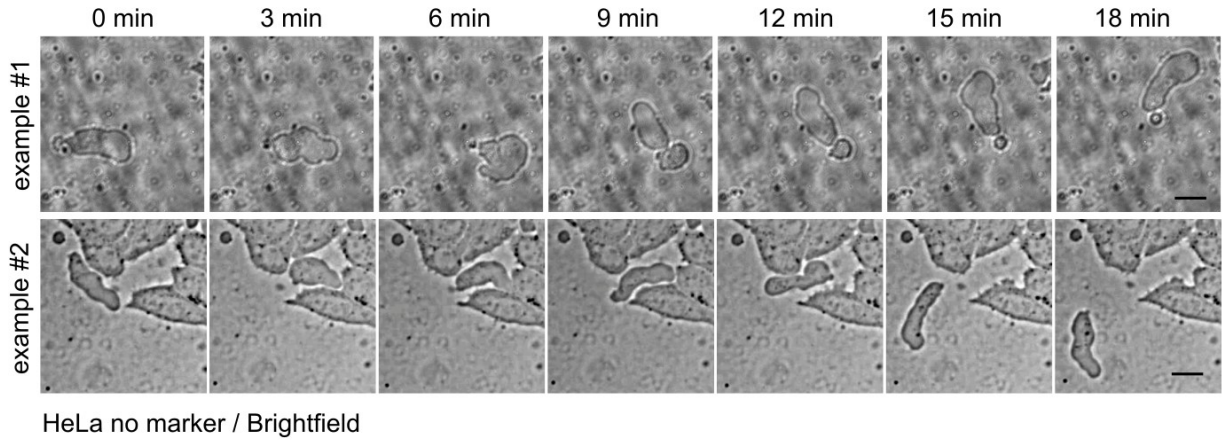

***Figure 40**: Bleb fragments losing and regaining polarity spontaneously or after falling into an impasse. Scale bars: 10µm.*

We consider different scenarios to explain the differences between elongated and round blebs immediately after bleb nucleation when myosin activity has not achieved contraction yet. To form a round shape, either membrane tension must achieve equilibrium before the membrane starts filling with actin or actin must populate the bleb membrane homogeneously. While actin polymerization precedes membrane stalling in elongated blebs or bleb fragments, we have not verified this in round blebs. After membrane growth stops by either mechanism, the bleb can retract. If a second bleb forms on the retracting bleb, this will create a polarized structure leading to a steady-state with a contracting cortex at the base and an actin-free membrane at the front (**Figure 41** A, **Figure 42** B), constituting a first mechanism to produce a long shape.

We can consider other mechanisms to create elongated blebs by differences in membrane expansion. Bleb membrane expansion in zebrafish PGCs in vivo relies on the local flattening of inwards-pointing tubular invaginations of the plasma membrane, mediated by N-BAR proteins (Goudarzi et al., 2017). A recent model (Lavi et al., 2019) studying the stress-strain (or tension-expansion) relationship during bleb expansion proposed that the new apparent area (surface area) under constant true area (number of lipids) could be provided by the flattening of the membrane tubes (at constant membrane tension) or at the expense of the thermal fluctuations (increasing membrane tension). Assuming different energy ranges for the disassembly of membrane tubes or increase in membrane tension and that there are no lipid flows, the authors proposed that at increasing bleb volumes, the membrane could transition from a phase of stretch (at the expenses of thermal fluctuations and increasing membrane tension) to a phase of membrane tube flattening. Importantly, tube flattening in PGCs only occurs in the actin-free region of the expanding bleb (i.e., tubes in the proximal part of the bleb membrane did not disassemble), which could be due to a stabilization of membrane tubes through their interaction with cytoskeletal components (Goudarzi et al., 2017). Supposing that the cortex formation in the bleb follows a gradient, membrane expansion by tube unfolding can happen only at the front, free of actin. The unfolding could create a long shape in a single bleb event, without needing subsequent blebbing. If the base of the bleb builds a contractile cortex before the actin has reached the front, the neck's closure could stabilize the steady-state (**Figure 41** B).

Goudarzi et al. did not find large-scale membrane flow towards bleb protrusions, but they did not consider the large blebs formed under confinement. Older research found surface and membrane flow towards blebs on walker cells, and *Fundulus* (Fedier et al., 1999; Tickle and Trinkaus, 1977). We also know that membrane-to-cortex attachment is a key

factor regulating cell migration and that the cortex perturbs the molecular diffusion and flow of phospholipids (Andrade et al., 2015; Diz-Muñoz et al., 2010; Shi et al., 2018). The front bleb membrane could unfold all the membrane tubes, passing to a regime where expansion occurs at the expense of the thermal fluctuations, increasing membrane tension. If we consider membrane flows, the differences in membrane tension between the front and the neck can trigger the membrane to flow towards the front. We could test if the neck's formation defines the steady-state projected area by increasing membrane-to-cortex attachment and restricting membrane flows (**Figure 41** C). We estimate that the maximal projected bleb area in large blebs corresponds to approximately 3 to 4 times the initial bleb area (immediately after formation), within the maximal membrane stretch measure by hypotonic shocks (Venkova, 2019).

Neck formation

Preliminary observations suggest that neck formation is a necessary condition for establishing a retrograde flow and a stable steady-state. When round blebs trigger a flow without retraction, we observed a tangential cortical flow (as opposed to “retrograde

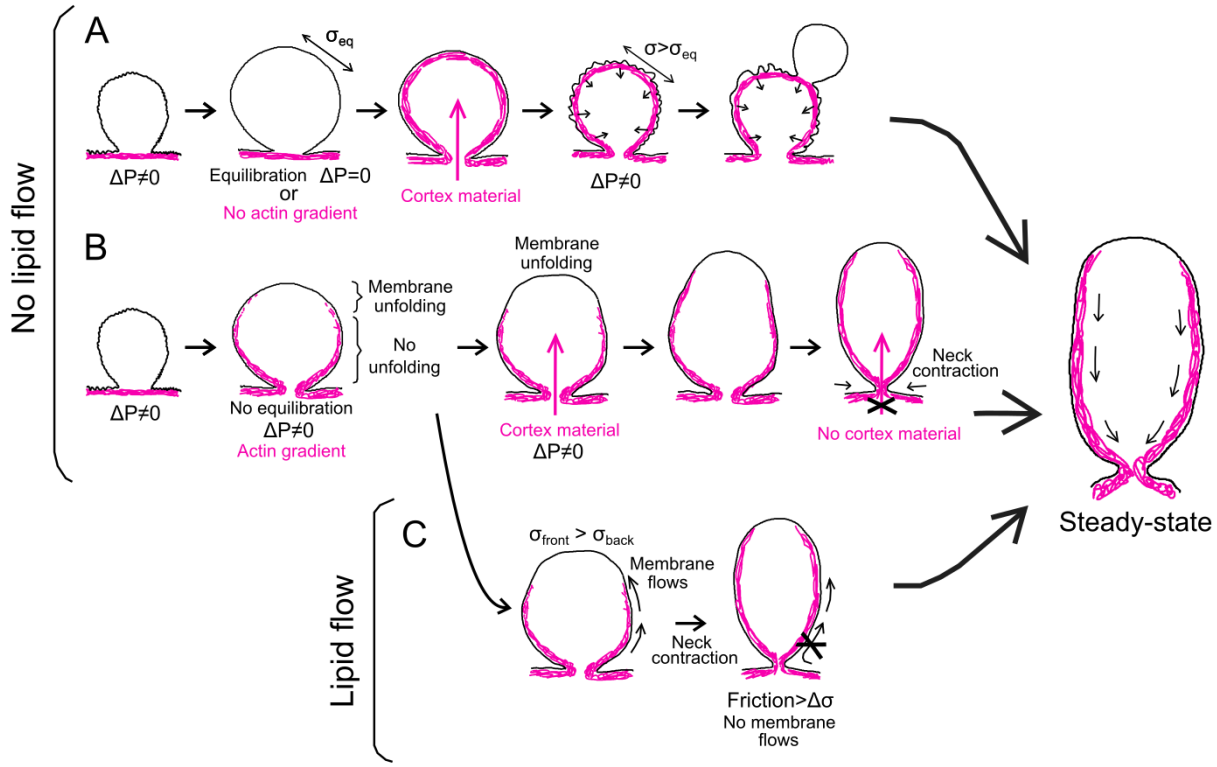

Figure 41: Possible mechanisms for the morphogenesis of an elongated bleb *with a polarized actomyosin cytoskeleton.* ***A:*** *Subsequent blebbing.* ***B:*** *Role of actin cortex formation: inhibition of membrane expansion at the bleb base by an actin gradient, and restriction of cortex material from the cell by neck closure.* ***C:*** *Possible role of cortical flows in the establishment of an elongated phase.*

flow"), and bleb movement sideways (similar to circus blebbing) until the bleb was completely retracted (**Figure 42 A, B, for more details see videos available**). The neck was necessary to produce retrograde flow, but the neck could only form in elongated shapes. The neck can contribute to actin disassembly by creating a permanent zone of convergent cortical flows, a central feature in cell migration. Zones of convergent flow are sites of actin cortex disassembly and are the best predictors for cell migration directionality and persistence (Yolland et al., 2019). Confining the convergence zone to the neck ensures persistent retrograde flows. The neck could also constitute a barrier for actin nucleators and signaling from the cell, preventing excess cortical material, which could be detrimental to achieving a constant flow. The neck constitutes a significant barrier, stopping the diffusion of proteins or chemical species. Consequently, blebs can keep different levels of Erk activity or calcium (Logue et al., 2015; Lomakin et al., 2019).

Preliminary observations suggest a potential role for the nucleus in local bleb growth. Blebs blocked in their neck by the nucleus, which can break in some blebs, were larger

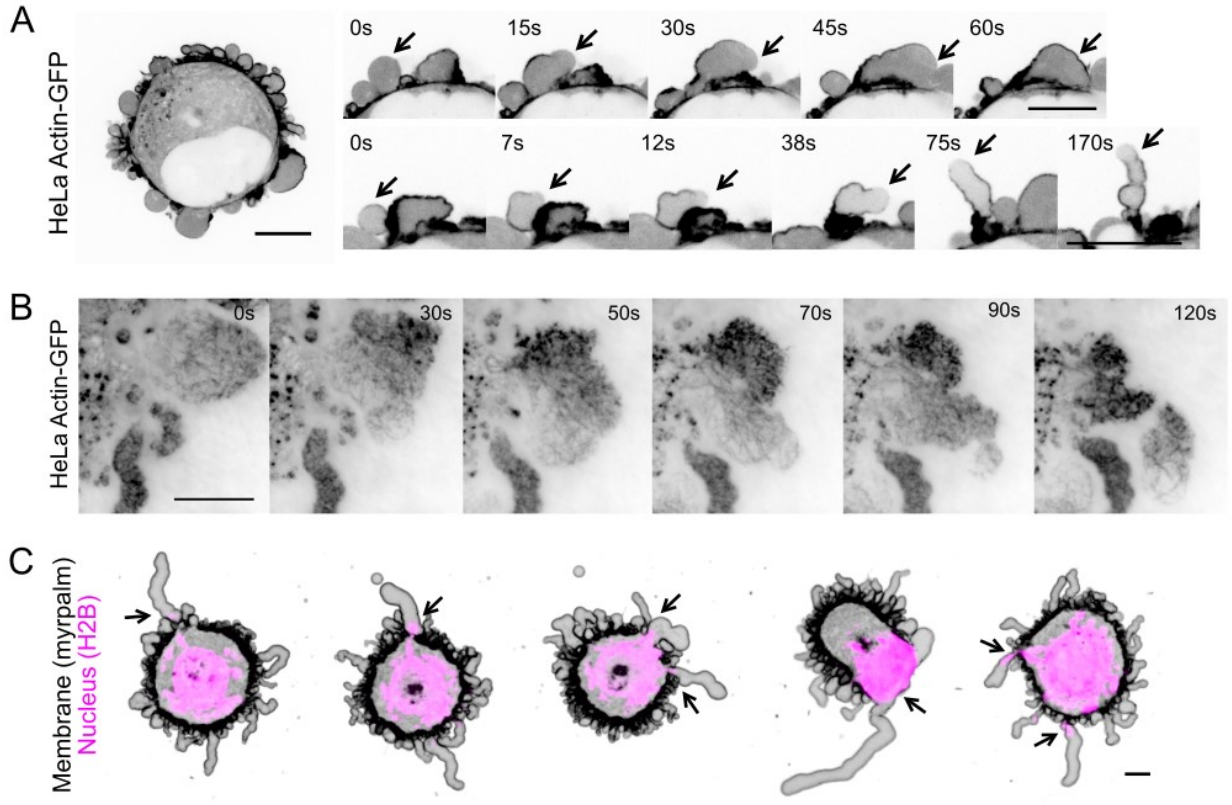

***Figure 42**: A: HeLa actin-GFP cells confined under ~4µm, displaying mainly transient blebs. On the right, time sequence of blebbing events leading to the formation of a neck (bottom) or not (top). Scale bars: 10µm. B: Time sequence of a bleb forming a neck. High NA TIRF of HeLa cells confined under 3µm. Scale bar: 10µm. C: 2 representative cells at 3 and 2 different time points. Black arrows show blebs which are "blocked" by a part of the nucleus, and display bigger volume. HeLa myrpalm-GFP H2B-mCherry Scale bar: 10µm.*

(**Figure 42 C**). Nevertheless, other factors related to the nucleus could be involved. At 3µm confinement, the nuclear envelope can break, and it could expose some chromatin-associated factors (i.e.: Ect2) that induce cortical contractility (Ramkumar and Baum, 2016). Lomakin et al. observed the release of vesicles from the nucleus which induced blebbing when reaching the cortex, suggesting that that nucleus provides signaling molecules to increase myosin activity locally.

The role of the nucleus in bleb formation

More globally, recent work by our lab and others (Lomakin et al., 2019; Venturini et al., 2019) showed that contractility is activated upon confinement by a mechanoresponse pathway mediated by the release of calcium and the activation of the enzyme cPLA2 (Enyedi et al., 2016). These works proposed that the contractility activation happens under 5µm compression due to nuclear stretching and that the stretch depended on the cell cycle stage or the state of the nuclear lamina. We explained the observed delay in NMIIA activation and elongated blebs formation by the activation delay in the pathway. Compared to the previous work, we linked bleb shape with the level of contractility in the cell. We analyzed AFM data at 3µm confinement to describe the contractility response under confinement and concluded that the onset of contractility was consistent with the appearance of longer blebs and that it was cPLA2-dependent (**Figure 26**).

However, we observed that bleb fragments sustain migration and polarity, showing that the nucleus is not a necessary condition to sustain blebbing. An alternative explanation is that motile fragments could be carrying some factors from the cell produced by the nucleus upon membrane stretch. Other results, shown in Lomakin et al. 2019 nuance the nucleus's role in blebbing migration and bleb formation: enucleated cells can trigger stable blebbing and migrate at low confinement height. We find similar results (***Figure 43*** A B). At heights greater than 3µm, only cells triggered blebbing (due to nuclear stretch), but under 3µm or lower, both cells and cytoplasts formed large stable blebs. However, upon cPLA2 inhibition, the activation of blebbing happened at the same height in cells and cytoplasts (***Figure 43*** C D). These results suggest that other factors complement the nucleus-mediated cPLA2 pathway to activate contractility at high confinement. It also suggests that blebbing and contractility-induced polarity is a **cytoplasm-autonomous behavior** that can be established without the concert of the other organelles.

Intracellular pressure under confinement and bleb formation

We did not explore the evolution of intracellular pressure under the different pharmacological inhibitors. We can relate the flat AFM confinement force and the cell's pressure by a **shell-liquid core model** of cell shape (Fischer-Friedrich et al., 2014). This model has been used to calculate intracellular pressure and surface tension of cells going through mitosis and estimated that cells increase pressure and surface tension from ≈ 40 Pa and 0.2 m·Nm^{-1} during interphase to ≈ 400 Pa and 1.6 m·Nm^{-1} during metaphase. At decreasing confinement height, or increasing AFM force, mitotic cells build-up intracellular pressure and trigger persistent blebbing, decreasing intracellular pressure (Cattin et al., 2015). Contractility included by confinement is a “double-sword: confinement initially increases actomyosin-dependent surface tension and intracellular pressure, but upon reaching a yield point, defects in the cortex caused blebbing and a

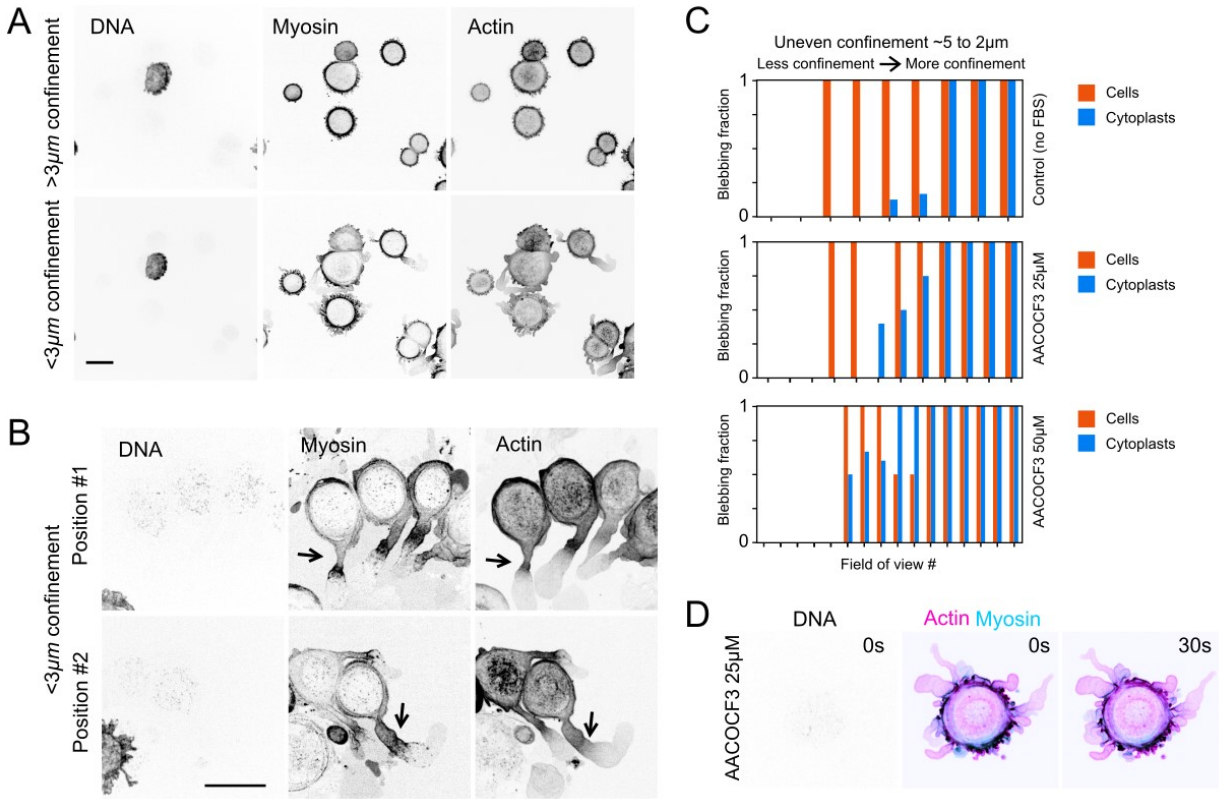

Figure 43: A: Confinement of cytoplasts and cells HeLa MYH9-eGFP lifeact-mCherry. DNA live staining: Hoescht NucBlue. Height is controlled only with valve pressure and is therefore not precise. Scale bar: 10µm. B: Two represented positions of cytoplasts confined under 3µm. At very low height, nucleated cells tend to burst (bottom row). Black arrows point at cytoplasts showing stable blebs. Scale bar: 10µm. C: Fraction of blebbing cells and cytoplasts at increasing confinement height in experiments with uneven confinement. Fields of view are ordered by percentage of blebbing cytoplasts, then blebbing cells. Top: control experiment. Middle: AACOCF3 25µM (cPLA2 inhibitor). Bottom: AACOCF3 50µM (cPLA2 inhibitor). D: Time sequence of a cytoplast displaying dynamic blebbing, confined under 3µm in the presence of AACOCF3 25µM (cPLA2 inhibitor). First column: Hoescht NucBlue; second and third columns: MYH9-eGFP lifeact-mCherry channels.

decrease in the pressure, as in a herniation event. Increased myosin activity amplifies fluctuations in the cortex (Laplaud et al., 2020), which then cooperates with blebbing to define cell polarity (Liu et al., 2015; Ruprecht et al., 2015). We described that the drop in AFM force corresponds to the formation of elongated blebs, not transient. It could be interesting for the future to relate the onset of elongated blebs with the AFM force and with the calculated intracellular pressure (derived from geometrical parameters and the AFM force), to show if elongated blebs form after a pressure threshold. Consistent with the observations from Cattin et al., the sustained force at 3µm confinement does not change significantly upon cPLA2 inhibition. We speculate that cPLA2-inhibited cells can sustain a more significant force against the cantilever due to the lack of force dissipation by elongated, stable blebs (**Figure 44** A).

Lastly, our results suggested a positive relationship between the initial volume and the sustained force (**Figure 44** C), as predicted by the shell-liquid core model (Cattin et al., 2015). Our data did not suggest a relationship between the timing of the response and the initial volume (**Figure 44** B), or between the timing of the force or myosin responses and the sustained force (data not shown), suggesting that the timing of the response is not linked to its amplitude. Importantly, the shell-liquid core model assumes constant cell volume, but this is not clear from the scientific literature. Some works suggest that cells lose a significant amount of volume (~10%) upon strong deformations (Venkova, 2019), and others that aquaporin mediates volume loss during bleb retraction (A. Ponuwei and R. Dash, 2019). Other works suggest that expansion is at constant volume (Goudarzi et al., 2019) or even increasing cell volume (Taloni et al., 2015).

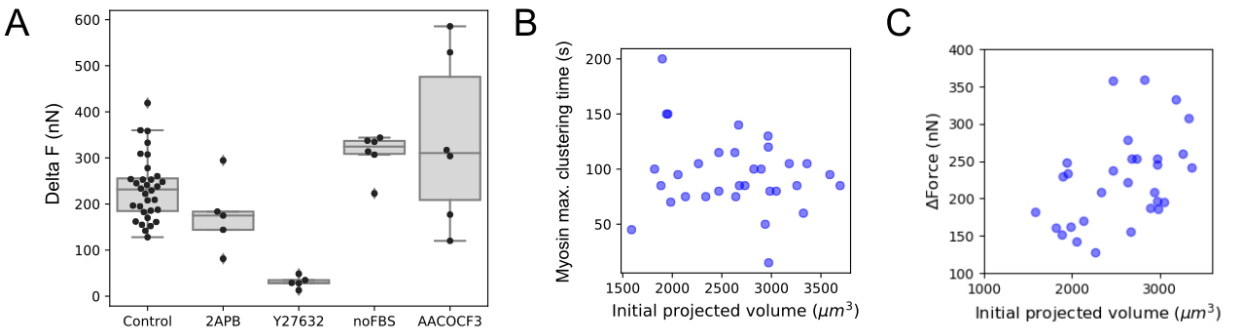

***Figure 44**: A: Quartile distributions of sustained force (delta F, nN) for different conditions. B: Plot of time of maximum myosin clustering plotted the initial projected cell volume (before confinement). C: Sustained force (delta F, nN) against the initial projected cell volume. N=32 control cells.*

Establishment of retrograde flow and bleb stabilization

The second part of our work described the emergence of retrograde flow and bleb steady-state. We observed that blebs, regardless of their shape, only avoided retraction if their front was free of actin at the onset of contraction. On the other hand, blebs that retract accumulate actin at the front before the onset of retraction. A study of the emergence of retrograde flow at a population level revealed that it depends on the relative timing of two events: the formation of the actin cortex all along the bleb contour and the activation of contractility. If the actin cortex forms all around the bleb before contraction starts, then the bleb will retract. If contraction happens before the cortex has completely formed, the bleb will transition to a steady-state and form a stable actomyosin gradient. Figures ***Figure 27*** L and ***Figure 27*** M summarize the main findings related to bleb morphogenesis and retrograde flow emergence: only blebs that polarize both actin and myosin achieve a stable flow and avoid retraction. Consistently, the relative timing of contraction onset and the timing at which the membrane stops growing can predict the bleb's stability. A future direction could include perturbing membrane-actin attachment, myosin activity, or actin nucleation during bleb nucleation. Perhaps counterintuitively, our working model predicts that decreasing myosin activity and delaying the onset of contraction during bleb formation should promote bleb retraction. Likewise, promoting the activity of nucleators during bleb growth should induce retraction.

This work contributes to understanding the steps leading to the steady-state but could be completed with perturbation experiments to support some of its claims. For example, to support the claim that elongated blebs are produced by an over activation of myosin after confinement, we could treat blebbing cells that have been confined for a few minutes with different concentrations of myosin II inhibitor. A low concentration of inhibitor should perturb the formation of elongated blebs, equivalent to reverting the cell to the initial phase immediately after confinement, but higher concentrations should prevent the formation of both elongated and round blebs. Also, we could increase contractility pharmacologically in cPLA2-inhibited cells to trigger the formation of elongated bleb well later than the 15-second timing observed in control cells.

The time scale of the bleb formation (seconds) and the PDMS confiner setup makes it challenging to perturb blebs as they form. Compared with the AFM, the PDMS confiner is not accessible by micropipette or drug perfusion systems once the cells are confined inside. The bleb morphology and dynamics in the AFM experiments could not be compared with the PDMS confiner's data because of significant differences in actin and

flow dynamics. Blebs produced under AFM confinement, either elongated or round, always accumulated actin at the front, which leads to retraction. Therefore we did not analyze bleb actomyosin dynamics in this dataset. To work around these technical challenges, we used optogenetic cell lines, or pretreated cells with different drugs, and studied the bleb dynamic steady-states rather than the steps leading to bleb formation.

Optogenetic experiments

In ordered to test some predictions of the model, we collaborated with Kotryna Vaidžiulytė and Matthieu Coppey (Institut Curie) to build optogenetic cell lines to achieve spatiotemporal control of small GTPases activity. We selectively illuminated regions of the bleb or the cell to see the effect of small GTPase activation on protrusions' stability. Consistent with the working model, we found that activating RhoA (myosin activity) in retracting blebs enhances bleb retraction speed, but in stable blebs, it enhances bleb stabilization by promoting neck closure, smoother contours, and more persistent blebbing.

Initially, we hypothesized that activating RhoA activity at the front of stable bleb should promote its retraction, and activating RhoA at the base should promote bleb stabilization. The spatial localization and signaling in elongated stable blebs have not yet been described, but we had some clues from the regulation of retraction of round blebs. RhoA regulators are present in the bleb membrane such as KIAA0861, MYOGEF, and p190BRhoGAP (Aoki et al., 2016; Charras et al., 2006; Ikenouchi and Aoki, 2017). The small GTPase Rnd3/Rho8/RhoE, a RhoA antagonist, localizes at the membrane of expanding blebs. Previous work proposed that the dilution of p190BRhoGAP purely due to membrane expansion allows initiating a positive feedback cycle mediated by MYOGEF-RhoA-ROCK-Ezrin, which recruits actin and myosin-II to promote bleb retraction (Aoki et al., 2016; Bovellan et al., 2014; Ikenouchi and Aoki, 2017). Therefore, we hypothesized that Rnd3 could be inhibiting RhoA in the bleb front and RhoA activity could be present in the bleb base and that by activating RhoA at the front, we could break t promote bleb retraction. It was recently described that stable blebs maintain a gradient of Erk activity which regulates actin bundling through Eps8, being higher at the bleb base than at the front, so it could be plausible that other chemical gradients exist (Logue et al., 2015). We discovered, however that illumination resulted in accumulation of membrane bound GEFs at the neck of stable blebs, regardless of the site of activation. This is

probably due to the strong retrograde flows, which concentrate cortical proteins. We used this as an advantage to determine, together with the membrane contour in the phase channel, if the bleb that was being illuminated was stable (presented strong cortical flows) or was transient (did not present cortical flows).

A limitation of our optogenetic experiments is the poor quality of the actin and myosin images, which prevented us from concluding more clearly on the role of actin gradient changing bleb dynamics in this dataset. The CRY2/CIBN system was occupying the blue and green fluorescent channels, and the blue channel was additionally used to activate the optogenetic partner. Therefore, only the far-red channel was available to visualize actin or myosin. We used lifeact-iRFP670 and MRLC1-iRFP670 (ex: 643 em: 670), which represented a loss in image quality and resolution compared to the GFP channel.

Recent studies showed that, when confined, WAVE-null HL-60 cells migrate through winding blebbing upon chemoattractant stimulation. The blebbing restricted to a well-defined membrane zone with high Rac activity (Graziano et al., 2019). We performed a series of experiments to test if these GTPases could have a similar role in our cells, but we did not find an effect of Cdc42 or Rac1 activation in the front of blebs. We could see the efficient recruitment of Cdc42 and Rac1 GEFs, but this did not significantly change blebbing dynamics. Inhibiting Cdc42 and Rac1 in the AFM experiments did not show any significant difference in the formation of round or elongated blebs (***Figure 26*** F). Therefore, we could not conclude on a role for Cdc42 or Rac1 in blebs.

We could include a new series of optogenetic experiments to trigger small GTPases' inactivation by targeting CIBN to the mitochondria (CIBN-mito) instead of the membrane (CIBN-CAAX), although we do not know if mitochondria are in the bleb. Another technical improvement to control more precisely the localization of the active GEFs could be using a new generation of probes with very different binding affinities such as iLID, improved light-induced dimer (Guntas et al., 2015).

Dynamic steady-states and bleb motility

In the literature, several regimes or modes of blebbing have been described: persistent blebs (Liu et al., 2015; Ruprecht et al., 2015), the so-called “circus blebbing”, driven by membrane tearing (Charras et al., 2008; Fujinami and Kageyama, 1975; Graziano et al., 2019), and unstable blebbing, common in *D. discoideum* and other cells (Fackler and

Grosse, 2008; Srivastava et al., 2020; Zatulovskiy et al., 2014). However, no study has systematically determined if there are any fundamental differences between the blebbing modes and if transitions between these dynamic states are possible. With all the different perturbations we tested in blebs: optogenetics (to increase RhoA, Cdc42, or Rac1 activity), pharmacological, or physical, we studied what controls bleb stabilization and the relative prevalence of these blebbing modes. Our conceptual contribution is that **blebs can transition between the different dynamic steady-states (persistent, winding, unstable)** depending on the interaction between the contracting base of the bleb and the front membrane through the actin network.

Ruprecht et al., 2015 showed that PLL coating induces steady-states with more actin at the front and that jasplakinolide treatment concentrates actin at the bleb base. We used different perturbations in cells (jasplakinolide, PLL coating, ezrin inhibitor) and cell fragments (ezrin inhibitor) and showed that conditions restricting actin concentration at the front generally promote persistent blebbing. While we established that actin controls membrane protrusion for motile fragments, we did not study this in blebs still attached to cells: attachment to the cell hinders bleb locomotion.

The velocity ★ actin intensity cross-correlation and the comparison between actin density and edge protrusion showed that cortical actin must be below a threshold to allow protrusion, suggesting a similar mechanism to Welf et al., 2019. This model, called the elastic Brownian ratchet, proposes that actin needs a local sub-threshold ezrin concentration at the cell front to push the membrane. Moreover, recent data suggested that membrane-proximal actin (MPA), and not total actin density (i.e., f-tractin intensity), controls cell persistence (Bisaria et al., 2020). Other studies suggested that the coupled dynamics of actin flow and diffusing polarity cues mediate cell persistence. This coupling links cell persistence (~robustness of the polarity cue gradient) and velocity (~speed of cortical flows) (Maiuri et al., 2015).

Ezrin localization and function in blebs

We hypothesized that mechanical interactions at the bleb front mediate the switches between dynamic steady-states. Therefore, there must be an uncoupling between the actin filaments and the membrane at the front in persistent blebbing. Charras et al., 2006 found that microinjection of recombinant FERM domain of ezrin-mRFP (~ezrin inhibition) caused actin-membrane tearing when retraction initiated, resulting in an inward flow of

actin but a complete or partial failure of membrane retraction. While ezrin does not have a role in actin nucleation, it mediates the mechanical coupling necessary to drive membrane retraction (Charras et al., 2006). Therefore, in the absence of the mechanical coupling, they found an **inward flow without membrane retraction**, which we observe in stable blebs.

If actin alone plays the role of the governing polarity cue in persistence, then actin-membrane linkers must be abundant, active, and dynamic at the bleb front. Cellular ezrin pools are dominated by inactive, actin-unbound species, ready to be activated by PIP_2 or other signals (Braunger et al., 2014; Fritzsche et al., 2014). PIP_2 is a key regulator of ezrin activity and blebbing. Ezrin mutation T567D (constitutively active form) slows down cortical turnover ($t_{1/2}\ wt\ ezrin \approx 16\ s$ versus $t_{1/2}\ T567D \approx 34\ s$) (Fritzsche et al., 2014). After association with PIP_2 at the membrane and phosphorylation, ezrin binds to the F-actin cortex through an interaction that is highly labile compared to its membrane binding, with an unbinding rate $k_{off} \approx 1.3s^{-1}$, very short when compared to other non-covalent bonds in the cell (Braunger et al., 2014). Because ezrin is very abundant, this provides a mechanically stable but dynamic link, even if the membrane domains to which ezrin binds are less mobile. This ensures strong membrane-cortex adhesion energy but low friction between the membrane and the cortex (Fritzsche et al., 2014). Consistent with this behavior, we find in our work that actin filaments can diffuse while being tightly linked to the membrane (they remain for a long time on the TIRF plane), and that membrane retraction mainly depends on the geometrical configuration. That is, the membrane-actin link can sustain strong normal forces but move freely in the tangential direction.

We visualized ezrin localization by the internally-tagged pEGFP-Ezrin construct (Lamb et al., 1997; Marion et al., 2011). Ezrin tagging often leads to activation, but this is reduced with the internal GFP tagging. Our preliminary data suggest that wild-type ezrin-GFP similarly localizes in the bleb as actin, creating bands, and gradually accumulating in the cortex (**Figure 45**). In the winding blebbing (i.e., circus blebbing restricted to the bleb front), we found discontinuities in the gradient related to the membrane dynamics, as typically observed for actin. We did not yet perform colocalization analysis between ezrin and actin in the bleb tip, but the data suggest that ezrin can decorate single bundles or filaments, judging by its filamentous localization at the bleb front (**Figure 45**). Other experiments with transient transfection of ezrin-T567A-GFP versus ezrin-T567D-GFP (not internally tagged GFP) yielded results hard to interpret, and that will need to be repeated after the defense. Both constitutively active (T567D) and inactive (T567A) ezrin-

GFP are excluded from blebs, and constitutively active ezrin is even more excluded than constitutively-inactive ezrin. These ezrin proteins were not internally tagged, so exclusion from the bleb could be due to over-activation.

Molecular regulation of actin-membrane attachment at the bleb front

As discussed earlier, the main players in the biochemical regulation of round bleb retraction are Eps8, RhoA, RhoE, ezrin, and GAP/GEFs of RhoA and RhoE. The actin-bundling and actin-capping activities of Eps8 are essential to generate continuous blebbing (Aoki et al., 2016) and form stable migratory blebs (Logue et al., 2015). Eps8 and actin localization in the bleb require activation of ezrin, activated after the bleb stops expanding. This regulation is achieved by RhoE/Rnd3 and the p190 RhoGAP, predominant at expanding membrane blebs, and RhoA and ROCK activation at the membrane of retracting blebs. Even if ezrin-KO cells severely retarded bleb retraction and failed to localize Eps8, they eventually managed to localize actin at the bleb edge, so there might be an additional mechanism to localize actin at the bleb membrane independent of both ezrin and Eps8. The mechanism by which RhoE localizes to the cortex-free membrane in expanding blebs is still unknown. The authors speculated effects related to the membrane tension or membrane unfolding during bleb expansion

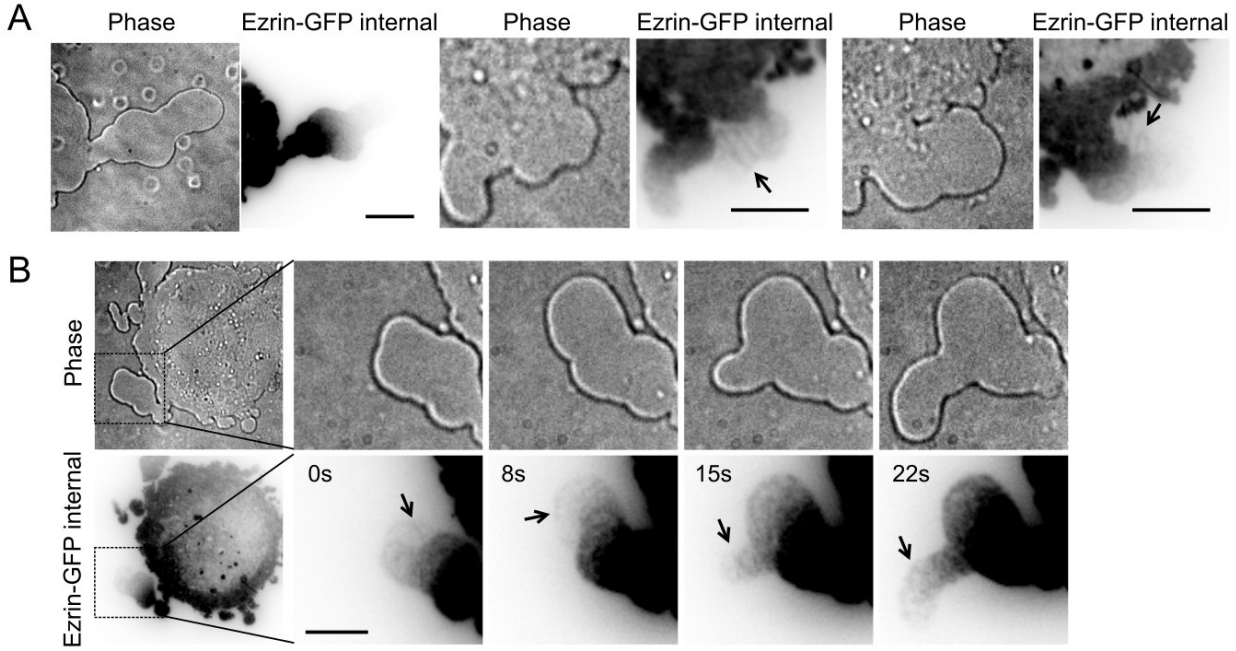

***Figure 45**: A: Representative examples of blebs from HeLa cells confined at 3µm (PLL-g-PEG coating). Black arrows point at sites where ezrin localization appears filamentous, reminiscent of the actin localization at the front. B: Time sequence of a protruding bleb. Scale bars: 10µm*

(Aoki et al., 2016). PIP2 activity is essential for the activation of the F-actin binding properties of ezrin and its biological function in cell migration (Bosk et al., 2011; Fritzsche et al., 2014; Hao et al., 2009). In agreement with this, blebs accumulate PIP2 at the membrane after expansion in a similar manner to myosin II, as indicated by GFP-PTEN (G129E), an indicator of PIP2 without phosphatase activity (Sugiyama et al., 2015).

Future work should focus on **cortex assembly regulation** in stable blebs to decipher whether there is different signaling between front and back. Our already established image analysis pipeline can describe the spatiotemporal order of molecular events at the bleb contour from fluorescence images. We could apply our analysis to cells or bleb fragments with different PIP2/PIP3 sensors or fluorescently-tagged small GTPase sensors, and modify their activity by the multiple optogenetic constructs, knockdowns, and pharmacological treatments available.

Our data did not suggest a mechanism disengaging actin and membrane at the front to promote persistent blebbing, which could support the presence of a gradient of signaling or membrane markers such as PIP3. We speculate that the biochemical 'identity' of the entire membrane is the one of a retracting bleb: enriched in PIP2 and active ezrin. If the limiting factor for bleb retraction is cortical actin, its stabilization could arise from the geometrical configuration and the actomyosin dynamics rather than specific signaling.

Another interesting point to check would be the localization of membrane-proximal actin (MPA). Recent work has shown that there is a gradient of MPA in cells and that the absence of MPA at the cell front allows for actin-rich protrusions (Bisaria et al., 2020). If PIP2 and ezrin are activated in the elongated blebs, we could see an inversion of the MPA polarity: the few actin filaments at the front of the bleb should be also positive for MPA and the membrane there should be rich for PIP2, as opposed for filopodia or lamellipodia driven migration.

Physical interactions at the bleb front

Our experimental system constitutes an excellent setup to study actin network assembly at the single filament level and interactions between actin filaments and the plasma membrane. We tried to transfect on several occasions actin nucleators (formin mDia1 or subunits of the Arp2/3 complex), but we have not yet been able to follow their localization with the high NA TIRF. Nevertheless, we have an extensive dataset on actin, myosin,

and membrane interaction at the bleb front that we have not completely exploited. I will discuss three points for possible future work: the lateral diffusion of actin oligomers tethered to the membrane, the normal forces exerted by filaments on the membrane, and the interaction between actin filaments.

The diffusion of a single monomer in the cytoplasm should be given by the Stokes-Einstein relation $D = k_B T \,/\, 6\pi\eta a$, where η is the dynamic friction coefficient and a the radius of the particle. The diffusion coefficient of molecules embedded on a lipid bilayer or membrane fluid domains is given by the more complex Saffman–Delbrück model, $D_{sd} = \frac{k_B T}{4\pi\eta_m h}[\ln(2L_{sd} \,/\, a) - \gamma]$, where a is the particle radius, h is the membrane thickness, η_m the membrane viscosity, η_f the viscosity of the surrounding bulk fluid, $L_{sd} = \frac{h\eta_m}{2\eta_f}$, and $\gamma \approx 0.577$ the Euler–Mascheroni constant (Quemeneur et al., 2014). We could assume an equivalent formula for the diffusion of membrane-attached bonds on the plane of the membrane.

If actin-membrane linkers are evenly distributed, the diffusion of actin filaments tethered to a 2D flat membrane should be dependent on their length (Howard, 2001). There are three different diffusion coefficients to consider: the lateral diffusion coefficient $D_{\parallel}$, proportional to $1/L$; the longitudinal diffusion coefficient $D_{\perp}$, proportional to $1/2L$; and the rotational diffusion coefficient D_R, proportional to $1/L^3$, L being the length of the filament in monomers (Heyes, 2019; Howard, 2001). In our experiments, we could observe the diffusion of actin oligomers for tens of seconds, with a framerate of ~20 frames per second. Making some assumptions, one could estimate the viscous drag of the membrane on the actin filaments. If the scaling of $D_{\parallel}$, $D_{\perp}$ and D_R does not match the prediction, one could assume a tether sampling effect (too few tethered bonds per filament) or alternative hypotheses. We observed that, even in the absence of focal adhesions in the blebs, the interaction of actin filaments with

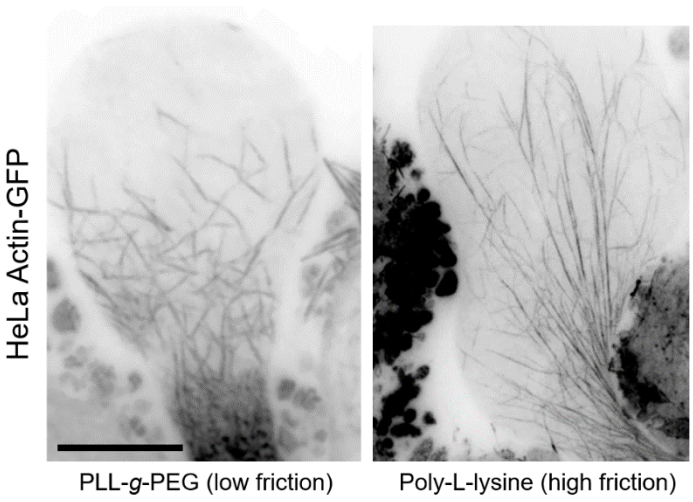

***Figure 46**: Actin flow at the front of blebs confined on PLL-g-PEG (low friction) or PLL substrate (high friction). **Video available**. Scale bar: 10µm.*

the membrane is biased by the external coating. Preliminary observations showed that blebs confined on PLL substrate (high friction due to the interaction of transmembrane proteins with the PLL, but no specific ligands and thus no engagement of integrins so no formation of focal adhesions) displayed high alignment of actin fibers in the axis of the bleb, as they get pulled backward with the retrograde flow. On non-adhesive PLL-*g*-PEG coating, this alignment was not present (**Figure 46**, **video avilable**). The nature of the actin-substrate molecular coupling in friction-based migration remains one of the unanswered questions in the field.

We could also provide some quantitative estimation of actin filaments' binding to the membrane from the events of membrane retraction or snapping. Calculating the angle at which the membrane detaches from the filament we can measure the adhesion energy $f = 2T_m(1 - \cos(\alpha)) > J$, assuming membrane tension values typical for a bleb $T_m \approx 8 \cdot 10^{-7} - 6 \cdot 10^{-6} N \cdot m^{-1}$ (Charras et al., 2008; Dai and Sheetz, 1999). The adhesion of membrane and cortex in tearing blebs was previously estimated as $J \approx 1.3 - 9.8 \cdot 10^{-6} J \cdot m^{-2}$ (Charras et al., 2008). We should also take into consideration the geometry of the confined bleb while doing the estimations.

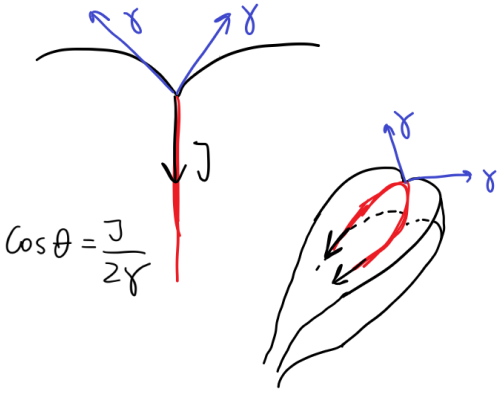

From this simple model, we obtain that at increasing membrane tension or at decreasing actin-membrane adhesion energies, the maximal angle that filaments exert on the membrane decreases. This is consistent with the results of the ezrin inhibition experiments, which have fewer geometrical perturbations of the membrane at the front. The binding energy of single ezrin molecules to f-actin is on the order of 50pN, which is much lower than its adhesion to the membrane (Bosk et al., 2011). One could estimate the density of ezrin links per filament or per bundle from the adhesion energy values after proper geometrical considerations. Comparing control with the ezrin inhibiting drug, we could then estimate the percentage of molecules of ezrin inhibited after treatment. We will work on these estimations after thesis submission and compare control versus ezrin inhibition conditions.

Lastly, we can also provide some estimates for the tension inside the actin network. We see some spontaneous events of network rupture. Knowing the angle between filaments before and after the rupture and the recoil velocity, we can estimate roughly the ratios between tensions assuming an elastic response on a short time scale. Experiments in *C.*

elegans have estimated the ratio between longitudinal and lateral tension and predict the cortical flows (Mayer et al., 2010; Nishikawa et al., 2017). We have tried to make laser ablation experiments in blebs, but it was not successful so far, as the blebs would tend to burst very easily, probably because the membrane was too close to the glass, but maybe due to the particularities in the bleb membrane.

Cortical regimes described by percolation theory

Percolation models describe connectivity and motor activity's contribution to the mechanical response to internal driving from motor activity. Percolation models represent random networks by lattice points called nodes, in different dimensions and structures (i.e., triangular, square). Percolation models can be based on lattice sides or sites, and have been used to model behavior in many systems (i.e., electrical conductivity, fire propagation in a forest, liquid flow through porous materials). We can define p as the probability of lattices to be occupied by a bond. As $p \to 0$, the system is composed of small clusters or individual isolated bonds. As $p \to 1$, the system is likely to be occupied by a large cluster, which will connect the system boundaries. Around $p \approx p_C$, the conductivity percolation threshold, the size of the largest cluster will rapidly increase, analogously to a phase transition. In systems around the critical probability $p \approx p_C$, the size distribution of clusters sizes (normalized by system size) obeys a power law $P(s) \sim s^{-\tau}$ irrespective of the lattice type, with $\tau \approx 2.05$, the Fisher exponent. The cluster size distribution is used to describe the behavior of percolation systems, and the extent of the critically connected state (Alvarado et al., 2013).

Networks above the conductivity threshold have non-zero conductivity Σ . Conductivity relates around $p \approx p_C$ to network density by the relation $\Sigma = \Sigma_0 (p - p_c)^{f_C}$, where f_C is the conductivity exponent ($f_C \approx 1.3$ in 2D irrespective of the lattice), and Σ_0 is the conductivity of one element lattice. Giving the mean adhesion energy J_0 applied by a single bundle, we could relate the total actin density with the total tension applied at the front membrane with a similar relation, $T = J_0 (p - p_c)^{f_C}$. If bonds are represented as mechanical springs, percolation can also describe mechanical transitions. In this case, a relevant threshold is the rigidity threshold p_R, which separates mechanical instability ($G = 0$, floppy state, G being the elastic shear modulus) from mechanical stability ($G > 0$). G increases as a power low in the distance of p from p_R, similarly to the conductivity threshold but with a different exponent (Alvarado et al., 2017; Stauffer et al., 1994).

Theoretical and experimental studies have used percolation models to describe actomyosin networks and have identified four non-equilibrium regimes: active solution (I), pre-stressed gel (II), global contraction (III), and local contraction (IV). The first three regimes are also found in passive systems, and the fourth is unique to active systems (**Figure 47**) (Alvarado et al., 2017). We observe these four regimes in the cortex of stable blebs, at different actin densities and motor activities. Our main contribution to the active soft matter field is to describe at the single filament level the existence of these four regimes in a living system and to propose a practical function for the different percolation transitions, which is to control protrusion persistence and bleb shape. This constitutes a **novel application of percolation theory** and will require some development to integrate actomyosin gradient and retrograde flow.

We speculate that bleb shape can be explained from these four regimes. In persistent blebs we observe a round membrane cap, which correlates with the presence of a fluid cortex (**Figure 48** A), corresponding to the active solution state. At the conductivity percolation threshold, which we determined $p_C \approx 1\,\mu m/\mu m^2$, actin filaments are able to transmit, holding opposite sides of the membrane. This defines the maximal bleb width and the extent of the (confined) hemispherical cap. Actin density form a gradient, and increasing density results in increasing bleb rigidity. If the myosin gradient is restricted to

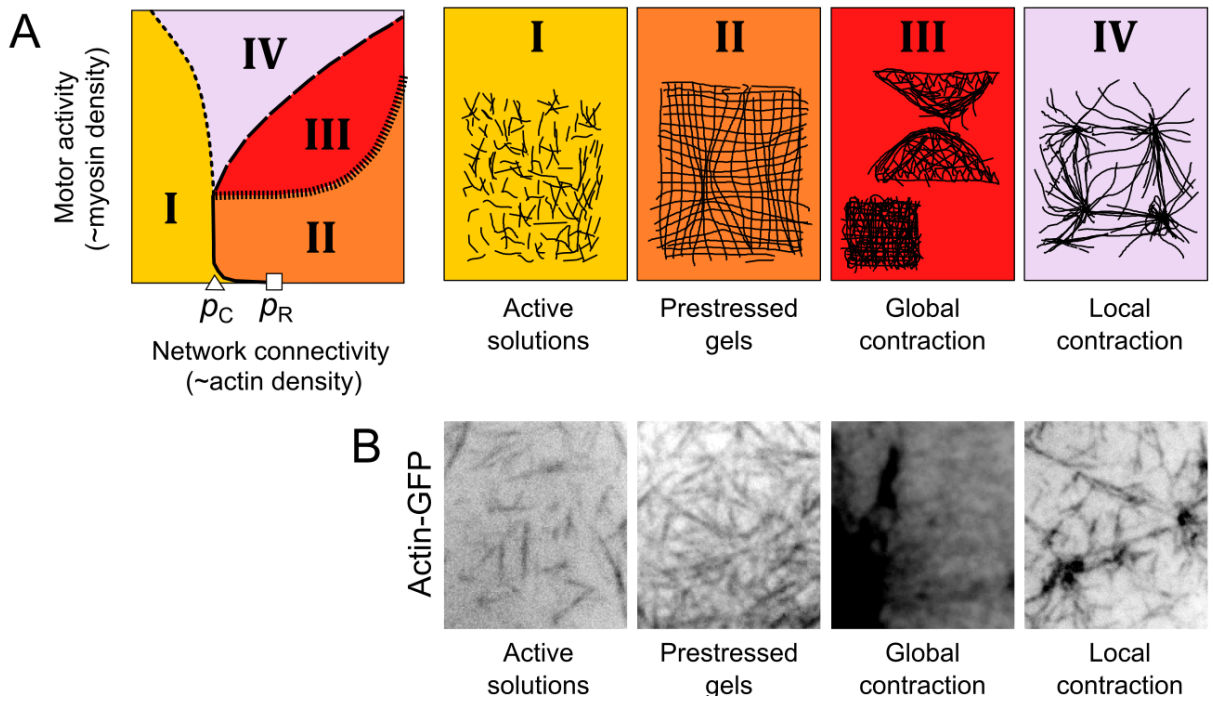

***Figure 47: A**: **Non-equilibrium regimes in active systems**: active solution (I), pre-stressed gels (II), global contraction (III), and local contraction (IV). Diagram adapted from Alvarado et al., 2017. **B:** Representative examples of Actin-GFP cortical networks in each of the four regimes.*

the base, there will be a portion of the bleb with a high correlation length and a cylindrical shape, without contraction. At high network density, motor contraction results in failure of percolation, and global network contraction. As the cortex is very rigid and dense, myosin motors will contract the network slower.

Usually, the local contraction regime (regime IV in **Figure 47**) is not found in blebs. However, perturbing actin polymerization by Arp2/3 or formin inhibitors can reveal this regime. Formin inhibitor SMIFH2 or Arp2/3 inhibitor CK666 do not seem to have an immediate effect on bleb dynamics, but we started to observe after approximately one-

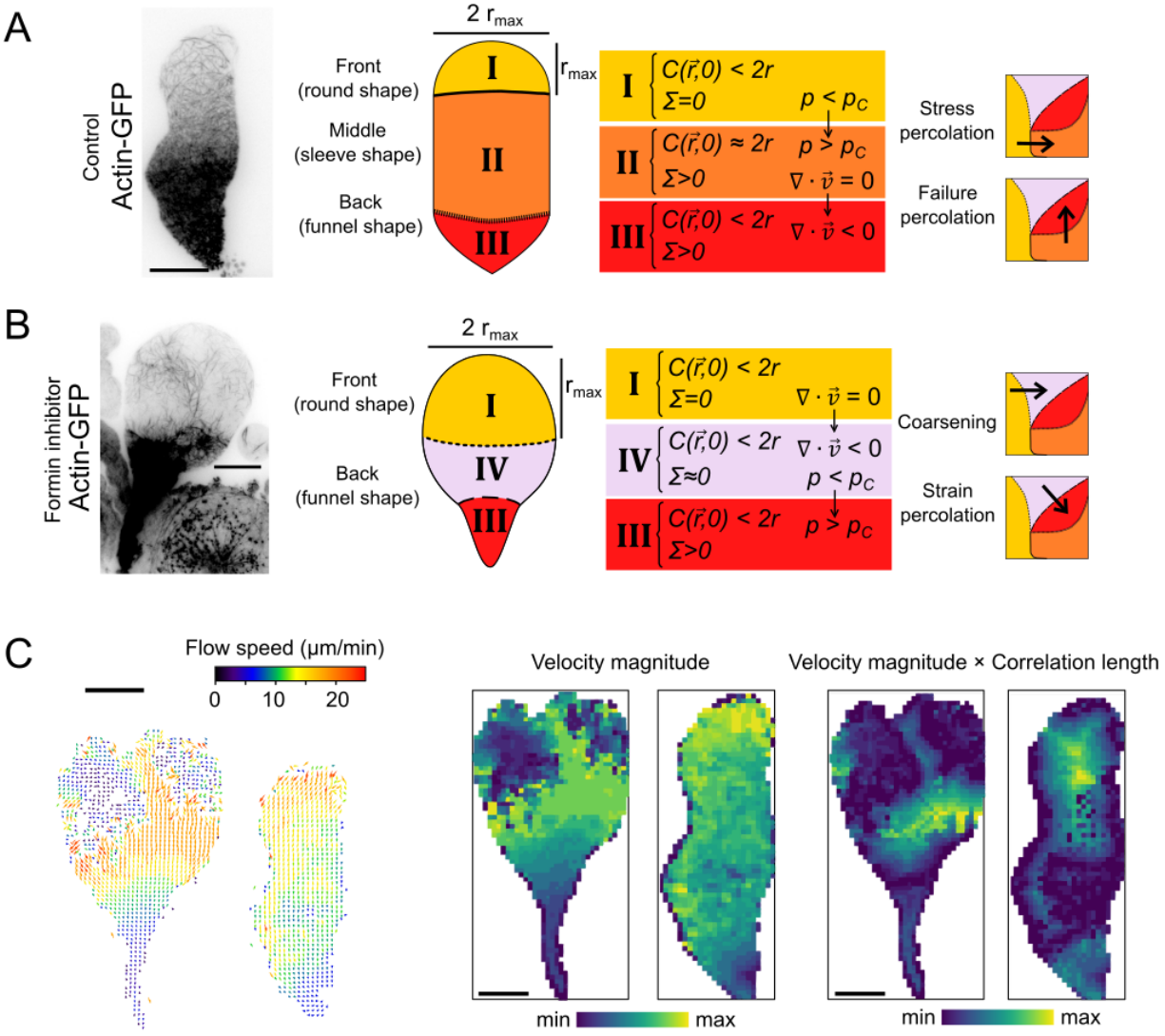

Figure 48: A: *Representative example of a confined bleb from HeLa Actin-GFP cells on high NA TIRF., showing the three cortical regimes corresponding to the shape. On the center, different descriptors (correlation length, conductivity, density) expected for each cortical regime. On the right, name of the regime transitions.* ***B:*** *Representative example of bleb in formin inhibition condition (40μM SMIFH2).* ***C:*** *PIV analysis of a single pair of frames in the blebs shown in panels A and B. On the right, velocity plot for the time time points, and velocity magnitude times correlation length, where we appreciate the transition to a global contraction. Note that the area with higher correlation spans half of the control bleb (the cylindrical area), and this is very restricted along the Y axis with formin inhibition. Scale bars: 10μm*

hour network failure events, probably due to the decreased cortex density (**Figure 48** B). In these blebs, most of the area belongs to the hemispherical cap. The interpretation of these preliminary observations is that actin density is too low to support global contraction when the motor activity increases, and therefore, we observe the formation of asters and local contraction events. At increasing densities, towards the bleb base, we observe a coordinated contraction, similar to control blebs. The time (or length) to completely crush the network into a small bleb neck is significantly reduced. These results represent the behavior observed in hundreds of blebs, but we are still working on the way to normalize and plot these characteristics in order to extract a mechanism for shape determination of motile blebs, similar to what has been proposed for other motile cells such as fish keratocytes (Keren et al., 2008). We plan to complete the quantification of cortex dynamics as a function of bleb shape and a theoretical model before the publication of the results.

Interpretation of contact guidance and actin network structure

We can reinterpret the results from the contact guidance and actin network experiments under the light of the percolation model. In the active fluid state, actin filaments are free to diffuse with a gas-like behavior. Their diffusion occurs in the plane of the membrane while they remain tightly linked. We considered in the discussion three diffusion coefficients: $D_{\parallel} \propto 1/L$, $D_{\perp} \propto 1/2L$, and $D_R \propto 1/L^3$, L being the length of the filament in monomers (Heyes, 2019; Howard, 2001). If we want to discuss the actin network's 3D organization in the whole bleb and not only the 2D network on the bottom surface, we also need to consider the arrangement of actin filaments in a curved membrane.

Bending stiffness is $K_b = EI = E_{\pi/4}a^4$, where I is the moment of inertia, and E Young's modulus of elasticity, for a rod with a circular cross-section. Persistence length l_p is related to K_b though $l_p = K_b/k_BT$. For actin, $K_b \approx 7 \cdot 10^{-26}$ and $l_p \approx 15\ \mu m$ (Bathe et al., 2008; Howard, 2001), much longer than the curvatures imposed by confinement (R = 1.5μm) or by the grooves (R=0.5μm). If the system is dominated by adhesion forces and actin bending stiffness, filaments will spontaneously diffuse and orient in the positions with lower curvature, and this effect will be more important for stiffer and longer filaments. This effect could be produced even with an active component.

The local order of filaments can introduce anisotropies in the force percolation. That is, in the direction of filament alignment (lower curvature), the conductivity percolation

threshold will be effectively lower. Actin density will need to be higher to be able to transmit forces in the direction of higher curvature. This explains why long, persistent blebs are more likely to form in the direction perpendicular to grooves, and why in regions of the bleb with higher membrane curvature we observed the formation of aligned bundles along the axis of lower curvature.

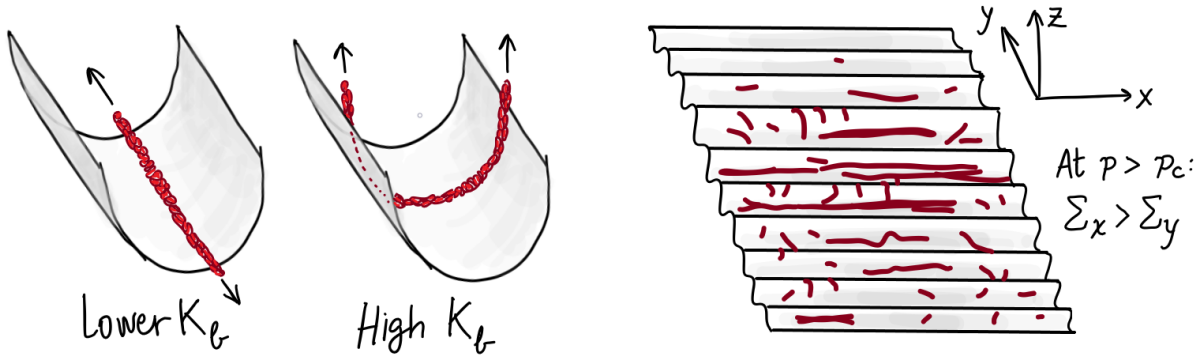

Figure 49: Possible effect of membrane curvature in the orientation of single filaments or in the network conductive at different directions.

Chapter 11: Broader perspectives and implications of the work

Perspectives in cell biology: regulation of network assembly and polarity

From the perspective of cell biology, our work contributes to understanding a novel structure used for cell migration. Our work does not study precise molecular pathways or discovers new molecular players, but it clarifies the importance of crosslinkers for bleb shape and persistence, described in the literature as essential for stable bleb migration but whose exact action mechanism was not understood. We focus on the dynamics of already known actors (mainly actin, NMIIA, and ezrin), in the context of a novel structure, the migratory bleb.

Our results suggest a shift in the main molecular mechanisms between the bleb and the lamellipodium. Regarding actin structure, the lamellipodium concentrates actin polymerization at the front, where it forms branched networks that are gradually crosslinked and bundled; the bleb polymerizes actin over a large area, accessed by actin crosslinkers, and the network assembles from sparse bundles to a dense network. Actin filaments grow tethered by nucleators to the membrane front in lamellipodia, where PIP3 enrichment prevents ezrin binding and allows membrane protrusion. Giving our results, we expect that polarity is inverted in blebs, with strong PIP2 signaling and active ezrin at the tip, as was described for transient blebs (Aoki et al., 2016; Charras, 2008). However, put in perspective, recent data from lamellipodia and other actin-rich protrusions point in the same direction: strong actin-membrane binding at the cell front inhibits membrane protrusion and impair cell migration (Bisaria et al., 2020; Welf et al., 2019).

While the molecular mechanisms are better understood in actin-rich protrusions, the biochemical regulation of protrusion persistence in blebs is not known. Future work should be directed to understand the molecular polarity in blebs and its functional consequences. We observed that, in adhesion condition (confinement of floating cells on a substrate coated with fibronectin, which allows the initial formation of blebs and then of adhesion structures after a delay), the base of the bleb could adhere and form filopodia (**Figure 50, videos available**). It is unclear if this was due to adhesion, nucleators, or differences in membrane tension. More generally, cell motility, particularly cell motility through stable blebs, has been described in many biological contexts and in a large variety of evolutionarily divergent species and cell lines (Brunet et al., 2020; Liu et al., 2015). Bleb migration is a basic potentially ancestral mode of locomotion for cells without

cell walls. Our work is a first approach to build a general model for bleb migration from a simple system driven by membrane, actin, and myosin.

Lastly, we left open an interesting question: are blebs related to the production of extracellular vesicles? Large extracellular vesicles and motile cellular fragments produced by cancer tissues may play a role in metastasis (Becker et al., 2016; Headley et al., 2016), and exosomes mediate inflammatory signaling in neutrophils (Majumdar et al., 2016). We know that blebs are rich in pro-inflammatory signaling through cPLA2, calcium (Lomakin et al., 2019), and Erk (Logue et al., 2015). We observed that blebs can easily migrate away from the cell in adhesive/friction conditions. This behavior was not directly related to the nucleus's presence, as blebs fragments could partition up to three times, each time 'dividing' into a fast motile fragment and an adhesive immotile fragment (**Figure 51, video available**). This suggests that adhesion proteins at the back mediate the fragment formation and that it could play a similar function as the recently described

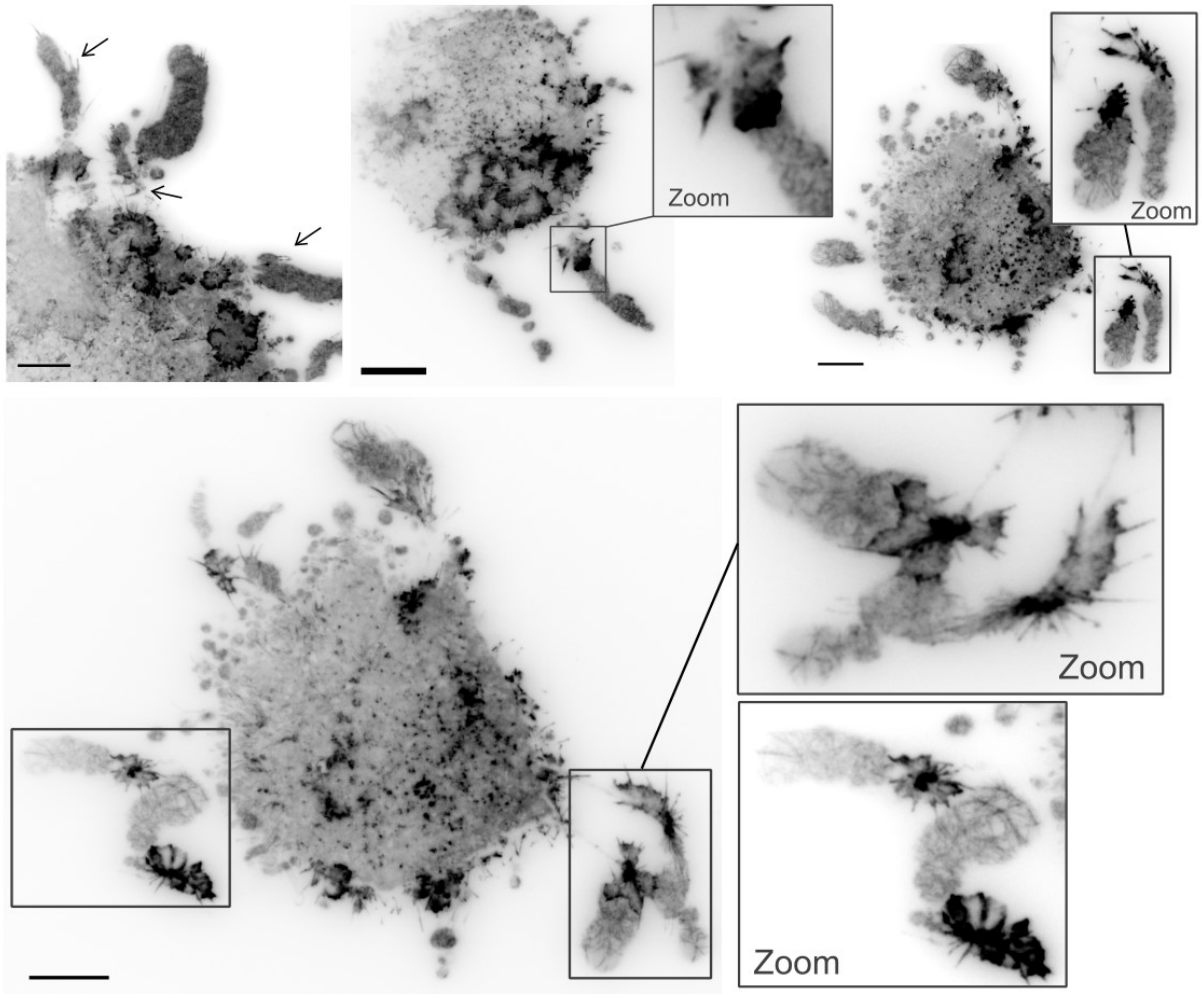

***Figure 50**: Actin-GFP confined HeLa cells on fibronectin 50µg/ml coated glass. Scale bars: 10µm.*

migrasome, with potential roles in intercellular signaling (Ma et al., 2015; Zhao et al., 2019).

Moreover, the extrusion of membrane blebs poor in adhesion proteins, and rich in signaling molecules could instantly change the migratory behavior of fragments, since the partition of elements is not symmetrical. We observed that cells that lost fragments after compression became more immobile and blebbed less. Motile fragments emanating from cancer cells have been observed in intravital microscopy in lungs (Headley et al., 2016). This represents a potential line of work to study the biological relevance of motile bleb fragments *in vivo*.

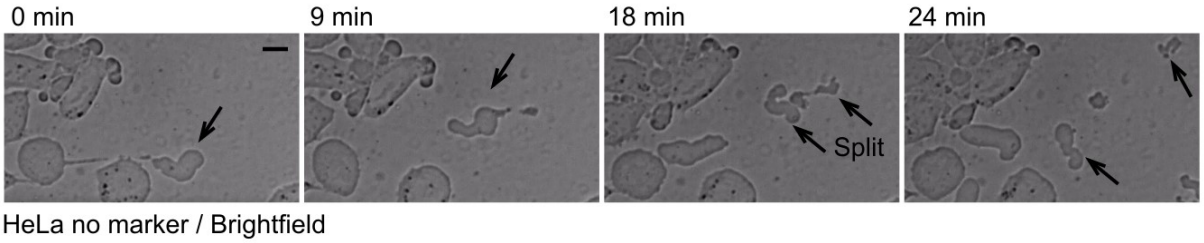

Figure 51: Time sequence of brightfield images of a bleb fragmenting from a cell, and then fragmenting again into three parts: one immovibe and two mobile 'sub-blebs'.

Perspectives in biophysics: mechanism of shape determination in motile blebs

We built on the extensive theoretical and experimental literature on bleb dynamics to propose a model for the formation and stabilization of elongated blebs. Previous models explained the transition from a homogeneous actomyosin cortex to a self-sustained polarized state driven by cortical flows (Callan-Jones and Voituriez, 2013; Liu et al., 2015; Ruprecht et al., 2015), but did not clarify the mechanism of transition and the initial steps of elongated bleb formation and flow emergence. Here we proposed that percolation theory can explain the transition between dynamic blebbing states, and that could provide a model to determine bleb shape and protrusion persistence.

More generally, our work proposes a new model system to study cell motility. The keratocyte has been used as a simplified motile cell to study lamellipodium dynamics. Through years of cumulative work, this achieved one of the most detailed models for cell shape determination and developed novel theories that clarified the relation between membrane tension and actin polymerization on the cell edges (Keren et al., 2008; Mogilner et al., 2020). Similarly, the bleb has been an intensive subject of study for

biophysicists. Its simplicity and accessibility provided key data on membrane tension, cortex assembly, and cortex composition (Charras et al., 2008, 2006; Fritzsche et al., 2013; Salbreux et al., 2012). The study of bleb motility combines these two favorite and well-established models for cell biophysics.

This work constitutes a starting point to model bleb motility from actin's molecular behavior and link molecular dynamics with large-scale cell persistence, contributing to some of the aspects proposed by the UCSP model (Maiuri et al., 2015). We did not discuss membrane tension, which might be an essential parameter to predict the bleb shape. Further work assessing the membrane tension values in blebs (or membrane tension gradients, by membrane tether pulling), measuring the filament pulling or pushing forces, and the cortex's rigidity would be needed to build a complete model with quantitative predictions. We could perform these measurements by optical traps indentation from the exterior of the cell.

The visualization of actin dynamics on the membrane in large blebs was more accessible on TIRF than on small, transient blebs. In large blebs, the membrane area in close contact with the glass is large enough to provide the right imaging conditions. Interestingly, the study of the stable bleb shape could also provide hints for the cortex dynamics in retracting blebs. The **three different cortical regimes** found **in** the **steady-state** along bleb length (active solution, prestressed gel, global contraction) are **analogous to** the **cortex's evolution during the formation and retraction of a bleb**. The tip of a stable bleb has the same state as a transient bleb that is just formed, composed of a naked membrane with incipient actin nucleation. The transition to a rigid cortex in the stable bleb is analogous to the end of membrane expansion in a transient bleb. Then, the transition from a cross-linked cortex to a contractile cortex constitutes the initiation of bleb retraction. Thus, by studying the steady-state of stable blebs, we can learn about the expansion-retraction cycle of transient blebs.

Perspectives in material science: the material properties of an elongated bleb

The bleb constitutes a dynamic, unstable material, with sequential changes in material properties from the front to the back and its lifespan: expanding and malleable, then rigid and static, to then being pulled from the back. This constitutes an excellent mechanism

to anchor to a non-adhesive porous substrate: during the expansion phase, the bleb will take the shape of the material and expand through pores. Since the expansion is mainly from the bleb front, it is possible that the bleb acquires a funnel shape, or that it expands through pores smaller than the final bleb diameter. After this, the actin cortex will reach a critical actin density and rigidify (Charras et al., 2006; Peukes and Betz, 2014), trapping the bleb in the matrix defects. When the retrograde flow starts, this “negative mold” of the matrix will be pulled. If the bleb is “locked” in the matrix like a key in a lock, this will create forces that push the rest of the cell body forward. Importantly, the front of the bleb is not contractile, just the back of the bleb, ensuring that the “negative mold” of the matrix acquired at the front remains in place to use it as an anchor. This is somewhat similar to the proposed action of transient blebs to promote cell migration, but it proposes a stable version of it in which the motility can be continuous with the malleable front, the rigid

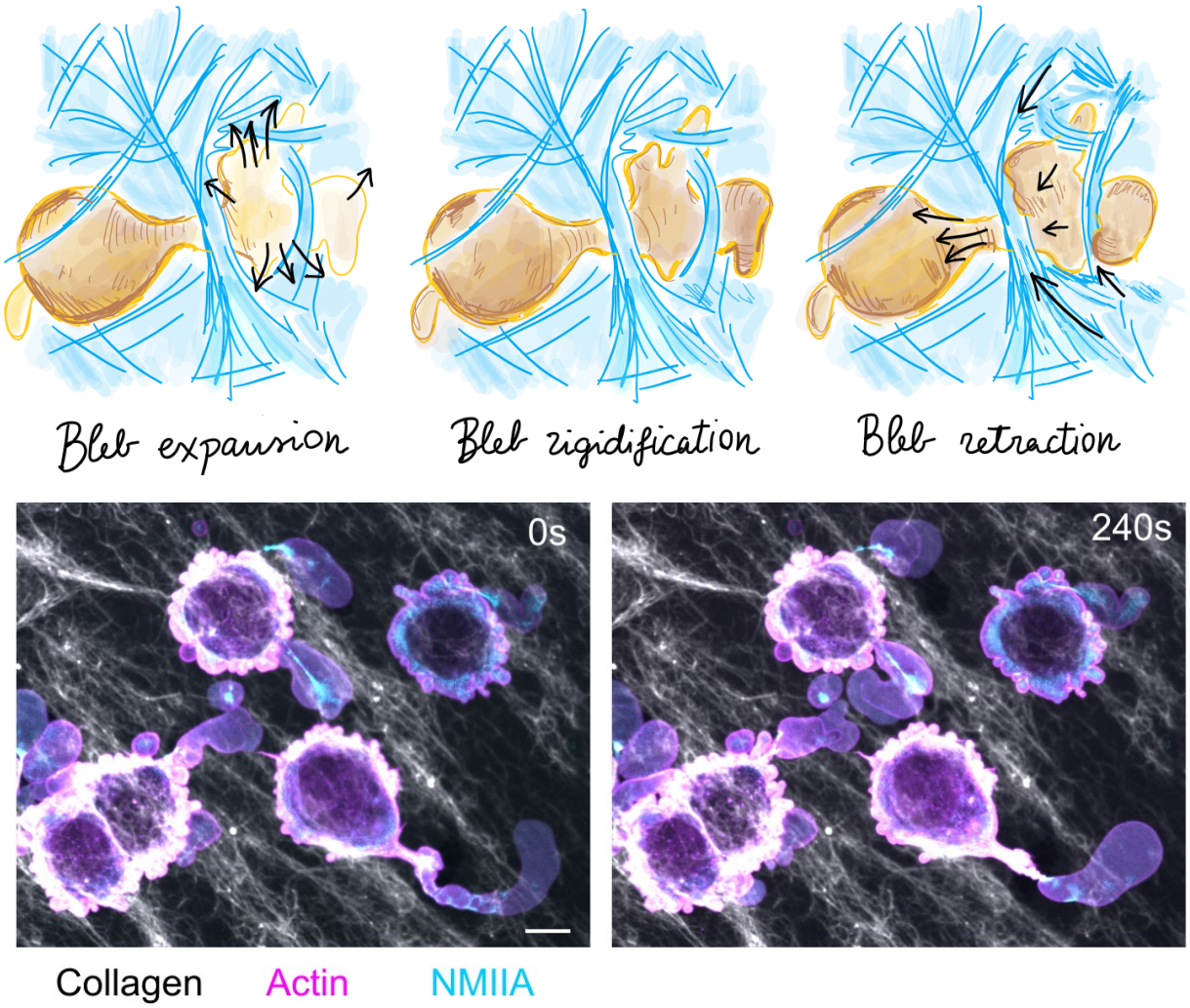

***Figure 52**: Top: phases of expansion of the bleb in a matrix: i) expansion though matrix gaps, ii) bleb rigidifies and takes the take of the sourrounding matrix as a “negative mold”, iii) retraction and adhesion-free pulling on the matrix. Bottom: Time sequence of HeLa cells embedded in rat tail 2m/ml collagen, and then confined. MYH9-eGFP / lifeact-mCherry. Scale bar: 10µm.*

middle part, and the contracting back. “Bleb trapping” could drive the migration of fast amoeboid cells or be used to anchor amoeboid cells to the matrix.

“Bleb trapping” is not analogous to the mechanism of cell migration using topological features, in which the retrograde flow of the actin cytoskeleton produces shear forces that are strong enough to drive the cell body forward in the complete absence of adhesion (Elkhatib et al., 2017; Reversat et al., 2020; Yamada and Sixt, 2019). Here we speculate that unlike round transient blebs, elongated blebs can anchor the matrix because of the spatial decoupling between contractile forces and actin cortex formation. Importantly, this effect can happen in adhesive substrates and does not rely on shear forces produced by the retrograde flow.

Conditions that decrease cortex density such as arp2/3 or formin inhibitors and prevent the formation of a solid-like cortex (regime II in **Figure 47**) between the fluid tip and the contractile back should also prevent anchoring. This anchoring hypothesis is supported by observations of blebs in collagen gels or adhesive substrates, where blebs appear blocked in the position, and a thick stress fiber is formed between the bleb and the cell, suggesting there could be a substantial force transmission (**Figure 50** and **Figure 52**).

Part V: List of references

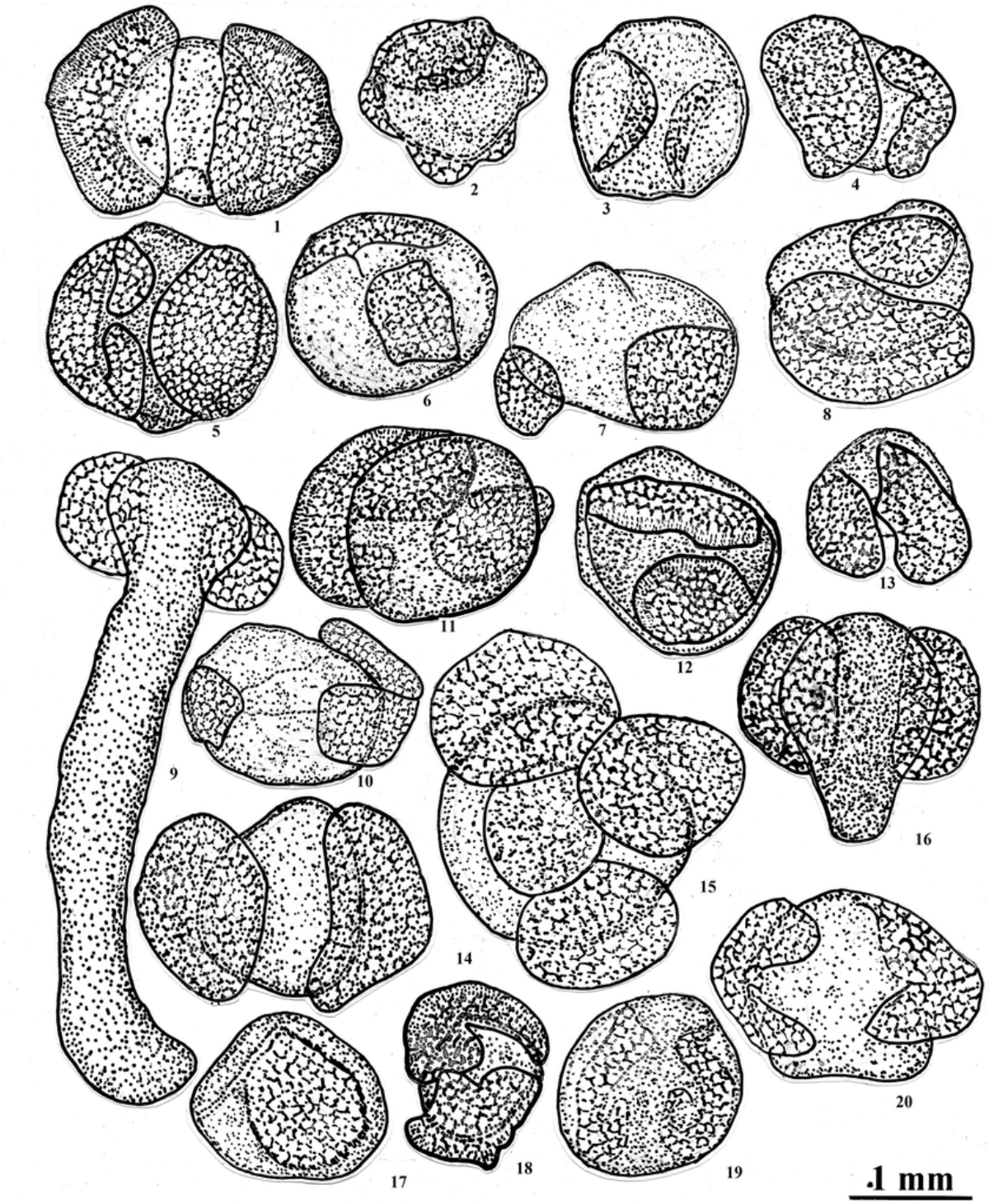

Chapter 12: List of figures and tables.

List of figures

Chapter illustrations

- Morse Code, Wikipedia.
- Astrocitos del hipocampo del cerebro humano. Cajal, de forma precisa, esquematiza la mayor parte de las propiedades de los astrocitos visualizados en un cadáver de tres horas después de la muerte. / Cortesía del Instituto Cajal, Legado Cajal, Consejo Superior de Investigaciones Científicas (CSIC)
- Image from page 195 of "The microscope: an introduction to microscopic methods and to histology" (1908)
- Review: Architecture and the Historical Imagination: Eugène-Emmanuel Viollet-le-Duc, 1814–1879, by Martin BressaniSean WeissJournal of the Society of Architectural HistoriansVol. 76 No. 2, June 2017(pp. 245-248) DOI: 10.1525/jsah.2017.76.2.245

- Dixit, Pooja & Saxena, Gauri & Kumar, Dinesh & Singh, Lav. (2016). Behavioural studies on the pollen grains of Pinus roxburghii collected from Lucknow, India–A report. Paleobotanist.
- Wikipedia, the lakes and roads of Wuhan. 武漢市都市部付近の湖（白い塊）、河川（白い帯）と道路（白い線）.
- Mozart, WA - Piano Concerto No 11 in F Major, K 413 - Piano and String Quartet - edited by Christoph Wolff. Shar Music.

Part VI: Bibliography

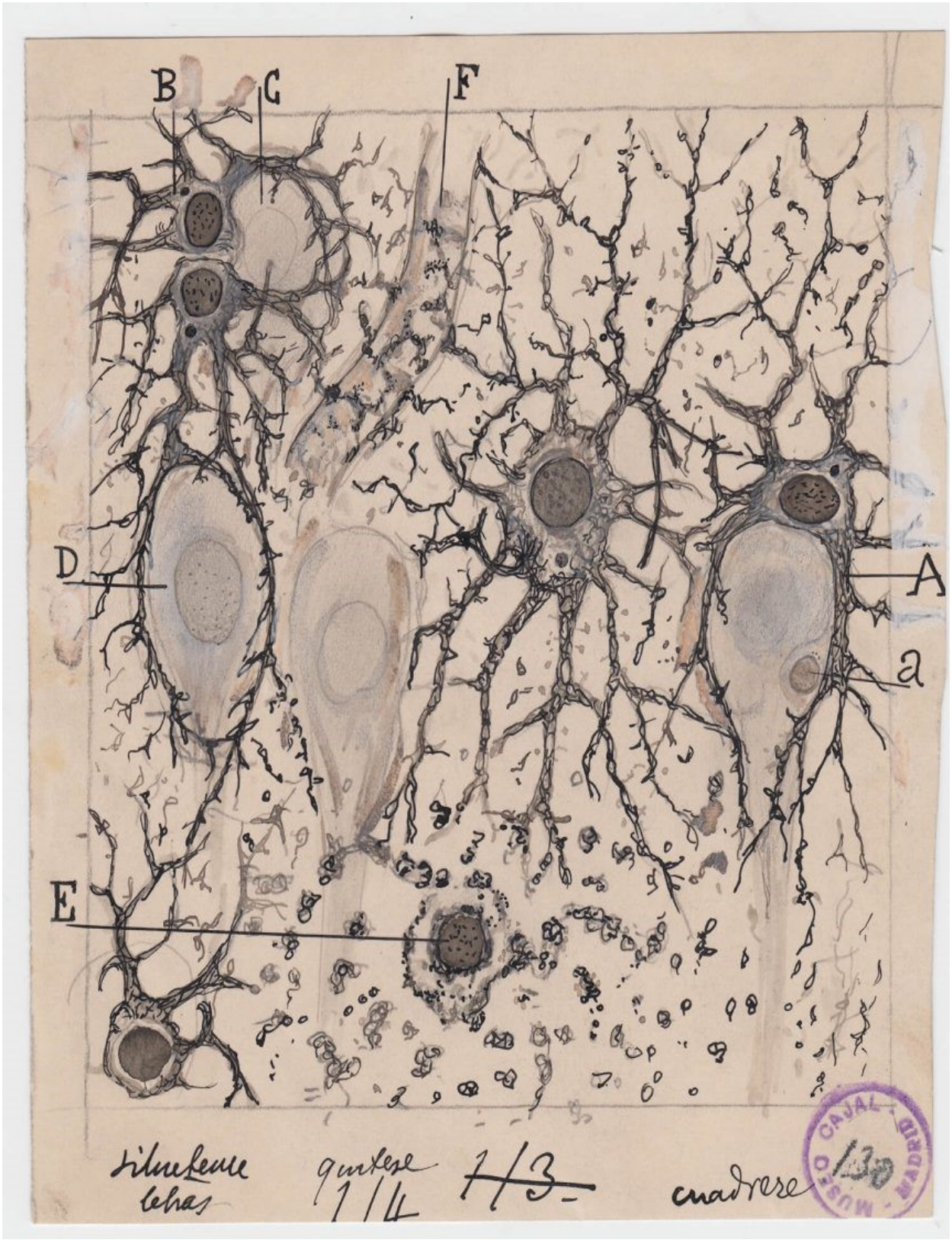

Chapter 13: Bibliography.

A. Ponuwei, G., R. Dash, P., 2019. Aquaporin 1 (AQP1) regulates plasma membrane bleb formation by facilitating bleb retraction phase in cancer cells. Integr Cancer Sci Therap 6. https://doi.org/10.15761/ICST.1000305

Abercrombie, M., Heaysman, J.E.M., 1953. Observations on the social behaviour of cells in tissue culture: I. Speed of movement of chick heart fibroblasts in relation to their mutual contacts. Experimental Cell Research 5, 111–131. https://doi.org/10.1016/0014-4827(53)90098-6

Abercrombie, M., Heaysman, J.E.M., Pegrum, S.M., 1972. Locomotion of fibroblasts in culture: V. Surface marking with concanavalin A. Experimental Cell Research 73, 536–539. https://doi.org/10.1016/0014-4827(72)90090-0

Abercrombie, M., Heaysman, J.E.M., Pegrum, S.M., 1971. The locomotion of fibroblasts in culture: IV. Electron microscopy of the leading lamella. Experimental Cell Research 67, 359–367. https://doi.org/10.1016/0014-4827(71)90420-4

Abercrombie, M., Heaysman, J.E.M., Pegrum, S.M., 1970a. The locomotion of fibroblasts in culture I. Movements of the leading edge. Experimental Cell Research 59, 393–398. https://doi.org/10.1016/0014-4827(70)90646-4

Abercrombie, M., Heaysman, J.E.M., Pegrum, S.M., 1970b. The locomotion of fibroblasts in culture: III. Movements of particles on the dorsal surface of the leading lamella. Experimental Cell Research 62, 389–398. https://doi.org/10.1016/0014-4827(70)90570-7

Abercrombie, M., Joan, E., Heaysman, M., Pegrum, S.M., 1970c. The locomotion of fibroblasts in culture: II. “Ruffling.” Experimental Cell Research 60, 437–444. https://doi.org/10.1016/0014-4827(70)90537-9

Abraham, V.C., Krishnamurthi, V., Taylor, D.L., Lanni, F., 1999. The actin-based nanomachine at the leading edge of migrating cells. Biophys. J. 77, 1721–1732. https://doi.org/10.1016/S0006-3495(99)77018-9

Abu Shah, E., Keren, K., 2014. Symmetry breaking in reconstituted actin cortices. eLife 3, e01433. https://doi.org/10.7554/eLife.01433

Abu Shah, E., Malik-Garbi, M., Keren, K., 2015. Reconstitution of cortical actin networks within water-in-oil emulsions, in: Methods in Cell Biology. Elsevier, pp. 287–301. https://doi.org/10.1016/bs.mcb.2015.01.011

Adachi, T., Stafford, S., Kayaba, H., Chihara, J., Alam, R., 2003. Myosin light chain kinase mediates eosinophil chemotaxis in a mitogen-activated protein kinase–dependent manner. Journal of Allergy and Clinical Immunology 111, 113–116. https://doi.org/10.1067/mai.2003.27

Adelstein, R.S., Conti, M.A., 1975. Phosphorylation of platelet myosin increases actin-activated myosin ATPase activity. Nature 256, 597–598. https://doi.org/10.1038/256597a0

Albrecht-Buehler, G., 1990. In Defense of “Nonmolecular” Cell Biology, in: Jeon, K.W., Friedlander, M. (Eds.), International Review of Cytology. Academic Press, pp. 191–241. https://doi.org/10.1016/S0074-7696(08)61601-0

Albrecht-Buehler, G., 1980. Autonomous movements of cytoplasmic fragments. Proceedings of the National Academy of Sciences 77, 6639–6643. https://doi.org/10.1073/pnas.77.11.6639

Alexander, S., Weigelin, B., Winkler, F., Friedl, P., 2013. Preclinical intravital microscopy of the tumour-stroma interface: invasion, metastasis, and therapy response. Current Opinion in Cell Biology 25, 659–671. https://doi.org/10.1016/j.ceb.2013.07.001

Alvarado, J., Koenderink, G.H., 2015. Chapter 6 - Reconstituting cytoskeletal contraction events with biomimetic actin–myosin active gels, in: Ross, J., Marshall, W.F. (Eds.), Methods in Cell Biology, Building a Cell from Its Component Parts. Academic Press, pp. 83–103. https://doi.org/10.1016/bs.mcb.2015.02.001

Alvarado, J., Sheinman, M., Sharma, A., MacKintosh, F.C., Koenderink, G.H., 2017. Force percolation of contractile active gels. Soft Matter 13, 5624–5644. https://doi.org/10.1039/C7SM00834A

Alvarado, J., Sheinman, M., Sharma, A., MacKintosh, F.C., Koenderink, G.H., 2013. Molecular motors robustly drive active gels to a critically connected state. Nature Phys 9, 591–597. https://doi.org/10.1038/nphys2715

Alvarez, D., Vollmann, E.H., von Andrian, U.H., 2008. Mechanisms and consequences of dendritic cell migration. Immunity 29, 325–342. https://doi.org/10.1016/j.immuni.2008.08.006

Amann, K.J., Pollard, T.D., 2001. Direct real-time observation of actin filament branching mediated by Arp2/3 complex using total internal reflection fluorescence microscopy. PNAS 98, 15009–15013. https://doi.org/10.1073/pnas.211556398

Andrade, D.M., Clausen, M.P., Keller, J., Mueller, V., Wu, C., Bear, J.E., Hell, S.W., Lagerholm, B.C., Eggeling, C., 2015. Cortical actin networks induce spatio-temporal confinement of phospholipids in the plasma membrane – a minimally invasive investigation by STED-FCS. Sci Rep 5, 1–12. https://doi.org/10.1038/srep11454

Aoki, K., Maeda, F., Nagasako, T., Mochizuki, Y., Uchida, S., Ikenouchi, J., 2016. A RhoA and Rnd3 cycle regulates actin reassembly during membrane blebbing. Proc Natl Acad Sci USA 113, E1863–E1871. https://doi.org/10.1073/pnas.1600968113

Artemenko, Y., Axiotakis, L., Borleis, J., Iglesias, P.A., Devreotes, P.N., 2016. Chemical and mechanical stimuli act on common signal transduction and cytoskeletal networks. Proc. Natl. Acad. Sci. U.S.A. 113, E7500–E7509. https://doi.org/10.1073/pnas.1608767113

Asano, Y., Nagasaki, A., Uyeda, T.Q.P., 2008. Correlated waves of actin filaments and PIP3 in Dictyostelium cells. Cell Motility 65, 923–934. https://doi.org/10.1002/cm.20314

Azioune, A., Carpi, N., Tseng, Q., Théry, M., Piel, M., 2010. Protein Micropatterns, in: Methods in Cell Biology. Elsevier, pp. 133–146. https://doi.org/10.1016/S0091-679X(10)97008-8

Barnhart, E.L., Lee, K.-C., Keren, K., Mogilner, A., Theriot, J.A., 2011. An Adhesion-Dependent Switch between Mechanisms That Determine Motile Cell Shape. PLoS Biol 9, e1001059. https://doi.org/10.1371/journal.pbio.1001059

Barry, D.J., Durkin, C.H., Abella, J.V., Way, M., 2015. Open source software for quantification of cell migration, protrusions, and fluorescence intensities. J Cell Biol 209, 163–180. https://doi.org/10.1083/jcb.201501081

Bathe, M., Heussinger, C., Claessens, M.M.A.E., Bausch, A.R., Frey, E., 2008. Cytoskeletal Bundle Mechanics. Biophysical Journal 94, 2955–2964. https://doi.org/10.1529/biophysj.107.119743

Beach, J.R., Bruun, K.S., Shao, L., Li, D., Swider, Z., Remmert, K., Zhang, Y., Conti, M.A., Adelstein, R.S., Rusan, N.M., Betzig, E., Hammer, J.A., 2017. Actin dynamics and competition for myosin monomer govern the sequential amplification of myosin filaments. Nat Cell Biol 19, 85–93. https://doi.org/10.1038/ncb3463

Becker, A., Thakur, B.K., Weiss, J.M., Kim, H.S., Peinado, H., Lyden, D., 2016. Extracellular Vesicles in Cancer: Cell-to-Cell Mediators of Metastasis. Cancer Cell 30, 836–848. https://doi.org/10.1016/j.ccell.2016.10.009

Belmonte, J.M., Leptin, M., Nédélec, F., 2017. A theory that predicts behaviors of disordered cytoskeletal networks. Mol Syst Biol 13, 941. https://doi.org/10.15252/msb.20177796

Bement, W.M., Leda, M., Moe, A.M., Kita, A.M., Larson, M.E., Golding, A.E., Pfeuti, C., Su, K.-C., Miller, A.L., Goryachev, A.B., von Dassow, G., 2015. Activator–inhibitor coupling between Rho signalling and actin assembly makes the cell cortex an excitable medium. Nat Cell Biol 17, 1471–1483. https://doi.org/10.1038/ncb3251

Bendix, P.M., Koenderink, G.H., Cuvelier, D., Dogic, Z., Koeleman, B.N., Brieher, W.M., Field, C.M., Mahadevan, L., Weitz, D.A., 2008. A Quantitative Analysis of Contractility in Active Cytoskeletal Protein Networks. Biophysical Journal 94, 3126–3136. https://doi.org/10.1529/biophysj.107.117960

Berg, H.C., 1993. Random Walks in Biology. Princeton University Press.

Berg, S., Kutra, D., Kroeger, T., Straehle, C.N., Kausler, B.X., Haubold, C., Schiegg, M., Ales, J., Beier, T., Rudy, M., Eren, K., Cervantes, J.I., Xu, B., Beuttenmueller, F., Wolny, A., Zhang, C., Koethe, U., Hamprecht, F.A., Kreshuk, A., 2019. ilastik: interactive machine learning for (bio)image analysis. Nature Methods 16, 1226–1232. https://doi.org/10.1038/s41592-019-0582-9

Bergert, M., Erzberger, A., Desai, R.A., Aspalter, I.M., Oates, A.C., Charras, G., Salbreux, G., Paluch, E.K., 2015. Force transmission during adhesion-independent migration. Nat Cell Biol 17, 524–529. https://doi.org/10.1038/ncb3134

Bettinger, C.J., Langer, R., Borenstein, J.T., 2009. Engineering Substrate Topography at the Micro- and Nanoscale to Control Cell Function. Angew. Chem. Int. Ed. 48, 5406–5415. https://doi.org/10.1002/anie.200805179

Bieling, P., Li, T.-D., Weichsel, J., McGorty, R., Jreij, P., Huang, B., Fletcher, D.A., Mullins, R.D., 2016. Force Feedback Controls Motor Activity and Mechanical Properties of Self-Assembling Branched Actin Networks. Cell 164, 115–127. https://doi.org/10.1016/j.cell.2015.11.057

Billington, N., Wang, A., Mao, J., Adelstein, R.S., Sellers, J.R., 2013. Characterization of three full-length human nonmuscle myosin II paralogs. J. Biol. Chem. 288, 33398–33410. https://doi.org/10.1074/jbc.M113.499848

Bisaria, A., Hayer, A., Garbett, D., Cohen, D., Meyer, T., 2020. Membrane-proximal F-actin restricts local membrane protrusions and directs cell migration. Science 368, 1205–1210. https://doi.org/10.1126/science.aay7794

Blaser, H., Reichman-Fried, M., Castanon, I., Dumstrei, K., Marlow, F.L., Kawakami, K., Solnica-Krezel, L., Heisenberg, C.-P., Raz, E., 2006. Migration of Zebrafish Primordial Germ Cells: A Role for Myosin Contraction and Cytoplasmic Flow. Developmental Cell 11, 613–627. https://doi.org/10.1016/j.devcel.2006.09.023

Bodor, D.L., Pönisch, W., Endres, R.G., Paluch, E.K., 2020. Of Cell Shapes and Motion: The Physical Basis of Animal Cell Migration. Developmental Cell 52, 550–562. https://doi.org/10.1016/j.devcel.2020.02.013

Bois, J.S., Jülicher, F., Grill, S.W., 2011. Pattern formation in active fluids. Phys. Rev. Lett. 106, 028103. https://doi.org/10.1103/PhysRevLett.106.028103

Bornens, M., Paintrand, M., Celati, C., 1989. The cortical microfilament system of lymphoblasts displays a periodic oscillatory activity in the absence of microtubules: implications for cell polarity. J Cell Biol 109, 1071–1083. https://doi.org/10.1083/jcb.109.3.1071

Bosk, S., Braunger, J.A., Gerke, V., Steinem, C., 2011. Activation of F-Actin Binding Capacity of Ezrin: Synergism of PIP2 Interaction and Phosphorylation. Biophys J 100, 1708–1717. https://doi.org/10.1016/j.bpj.2011.02.039

Bovellan, M., Romeo, Y., Biro, M., Boden, A., Chugh, P., Yonis, A., Vaghela, M., Fritzsche, M., Moulding, D., Thorogate, R., Jégou, A., Thrasher, A.J., Romet-Lemonne, G., Roux, P.P., Paluch, E.K., Charras, G., 2014. Cellular Control of Cortical Actin Nucleation. Current Biology 24, 1628–1635. https://doi.org/10.1016/j.cub.2014.05.069

Braunger, J.A., Brückner, B.R., Nehls, S., Pietuch, A., Gerke, V., Mey, I., Janshoff, A., Steinem, C., 2014. Phosphatidylinositol 4,5-Bisphosphate Alters the Number of Attachment Sites between Ezrin and Actin Filaments. J Biol Chem 289, 9833–9843. https://doi.org/10.1074/jbc.M113.530659

Bray, D., White, J., 1988. Cortical flow in animal cells. Science 239, 883–888. https://doi.org/10.1126/science.3277283

Brunet, T., Albert, M., Roman, W., Spitzer, D.C., King, N., 2020. A flagellate-to-amoeboid switch in the closest living relatives of animals. bioRxiv 2020.06.26.171736. https://doi.org/10.1101/2020.06.26.171736

Brzeska, H., Pridham, K., Chery, G., Titus, M.A., Korn, E.D., 2014. The Association of Myosin IB with Actin Waves in Dictyostelium Requires Both the Plasma Membrane-Binding Site and Actin-Binding Region in the Myosin Tail. PLOS ONE 9, e94306. https://doi.org/10.1371/journal.pone.0094306

Bulut, G., Hong, S.-H., Chen, K., Beauchamp, E.M., Rahim, S., Kosturko, G.W., Glasgow, E., Dakshanamurthy, S., Lee, H.-S., Daar, I., Toretsky, J.A., Khanna, C., Uren, A., 2012. Small molecule inhibitors of ezrin inhibit the invasive phenotype of osteosarcoma cells. Oncogene 31, 269–281. https://doi.org/10.1038/onc.2011.245

Cadart, C., Venkova, L., Recho, P., Lagomarsino, M.C., Piel, M., 2019. The physics of cell-size regulation across timescales. Nature Physics 15, 993–1004. https://doi.org/10.1038/s41567-019-0629-y

Cadart, C., Zlotek-Zlotkiewicz, E., Venkova, L., Thouvenin, O., Racine, V., Le Berre, M., Monnier, S., Piel, M., 2017. Fluorescence eXclusion Measurement of volume in live cells, in: Methods in Cell Biology. Elsevier, pp. 103–120. https://doi.org/10.1016/bs.mcb.2016.11.009

Callan-Jones, A.C., Ruprecht, V., Wieser, S., Heisenberg, C.P., Voituriez, R., 2016. Cortical Flow-Driven Shapes of Nonadherent Cells. Phys. Rev. Lett. 116, 028102. https://doi.org/10.1103/PhysRevLett.116.028102

Callan-Jones, A.C., Voituriez, R., 2016. Actin flows in cell migration: from locomotion and polarity to trajectories. Current Opinion in Cell Biology 38, 12–17. https://doi.org/10.1016/j.ceb.2016.01.003

Callan-Jones, A.C., Voituriez, R., 2013. Active gel model of amoeboid cell motility. New J. Phys. 15, 025022. https://doi.org/10.1088/1367-2630/15/2/025022

Cao, L., Yonis, A., Vaghela, M., Barriga, E.H., Chugh, P., Smith, M.B., Maufront, J., Lavoie, G., Méant, A., Ferber, E., Bovellan, M., Alberts, A., Bertin, A., Mayor, R., Paluch, E.K., Roux, P.P., Jégou, A., Romet-Lemonne, G., Charras, G., 2020. SPIN90 associates with mDia1 and the Arp2/3 complex to regulate cortical actin organization. Nature Cell Biology 22, 803–814. https://doi.org/10.1038/s41556-020-0531-y

Caridi, C.P., Plessner, M., Grosse, R., Chiolo, I., 2019. Nuclear actin filaments in DNA repair dynamics. Nature Cell Biology 21, 1068–1077. https://doi.org/10.1038/s41556-019-0379-1

Carlier, M.F., 1990. Actin polymerization and ATP hydrolysis. Adv. Biophys. 26, 51–73. https://doi.org/10.1016/0065-227x(90)90007-g
Carlsson, A.E., 2018. Membrane Bending by Actin Polymerization. Curr Opin Cell Biol 50, 1–7. https://doi.org/10.1016/j.ceb.2017.11.007
Carrel, A., Burrows, M.T., 1911. AN ADDITION TO THE TECHNIQUE OF THE CULTIVATION OF TISSUES IN VITRO. J Exp Med 14, 244–247.
Carrel, A., Ebeling, A.H., 1926. THE FUNDAMENTAL PROPERTIES OF THE FIBROBLAST AND THE MACROPHAGE II. THE MACROPHAGE. J Exp Med 44, 285–305. https://doi.org/10.1084/jem.44.3.285
Carvalho, K., Tsai, F.-C., Lees, E., Voituriez, R., Koenderink, G.H., Sykes, C., 2013. Cell-sized liposomes reveal how actomyosin cortical tension drives shape change. PNAS 110, 16456–16461. https://doi.org/10.1073/pnas.1221524110
Case, L.B., Waterman, C.M., 2011. Adhesive F-actin Waves: A Novel Integrin-Mediated Adhesion Complex Coupled to Ventral Actin Polymerization. PLOS ONE 6, e26631. https://doi.org/10.1371/journal.pone.0026631
Cattin, C.J., Düggelin, M., Martinez-Martin, D., Gerber, C., Müller, D.J., Stewart, M.P., 2015. Mechanical control of mitotic progression in single animal cells. Proc Natl Acad Sci USA 112, 11258–11263. https://doi.org/10.1073/pnas.1502029112
Chang, Y.-C., Nalbant, P., Birkenfeld, J., Chang, Z.-F., Bokoch, G.M., 2008. GEF-H1 couples nocodazole-induced microtubule disassembly to cell contractility via RhoA. Mol. Biol. Cell 19, 2147–2153. https://doi.org/10.1091/mbc.e07-12-1269
Charras, G., Paluch, E., 2008. Blebs lead the way: how to migrate without lamellipodia. Nat Rev Mol Cell Biol 9, 730–736. https://doi.org/10.1038/nrm2453
Charras, G.T., 2008. A short history of blebbing. Journal of Microscopy 231, 466–478. https://doi.org/10.1111/j.1365-2818.2008.02059.x
Charras, G.T., Coughlin, M., Mitchison, T.J., Mahadevan, L., 2008. Life and Times of a Cellular Bleb. Biophysical Journal 94, 1836–1853. https://doi.org/10.1529/biophysj.107.113605
Charras, G.T., Hu, C.-K., Coughlin, M., Mitchison, T.J., 2006. Reassembly of contractile actin cortex in cell blebs. J Cell Biol 175, 477–490. https://doi.org/10.1083/jcb.200602085
Charras, G.T., Yarrow, J.C., Horton, M.A., Mahadevan, L., Mitchison, T.J., 2005. Non-equilibration of hydrostatic pressure in blebbing cells. Nature 435, 365–369. https://doi.org/10.1038/nature03550
Chen, L., Iijima, M., Tang, M., Landree, M.A., Huang, Y.E., Xiong, Y., Iglesias, P.A., Devreotes, P.N., 2007. PLA2 and PI3K/PTEN pathways act in parallel to mediate chemotaxis. Dev Cell 12, 603–614. https://doi.org/10.1016/j.devcel.2007.03.005
Chen, T., Callan-Jones, A., Fedorov, E., Ravasio, A., Brugués, A., Ong, H.T., Toyama, Y., Low, B.C., Trepat, X., Shemesh, T., Voituriez, R., Ladoux, B., 2019. Large-scale curvature sensing by directional actin flow drives cellular migration mode switching. Nat. Phys. 15, 393–402. https://doi.org/10.1038/s41567-018-0383-6
Cheng, K.W., Mullins, R.D., 2020. Leading-edge VASP clusters assemble at sites containing lamellipodin and exhibit size-dependent instability. bioRxiv 2020.02.21.960229. https://doi.org/10.1101/2020.02.21.960229
Chikina, A.S., Svitkina, T.M., Alexandrova, A.Y., 2019. Time-resolved ultrastructure of the cortical actin cytoskeleton in dynamic membrane blebs. J. Cell Biol. 218, 445–454. https://doi.org/10.1083/jcb.201806075
Claessens, M.M.A.E., Bathe, M., Frey, E., Bausch, A.R., 2006. Actin-binding proteins sensitively mediate F-actin bundle stiffness. Nature Mater 5, 748–753. https://doi.org/10.1038/nmat1718

Clark, A.G., Vignjevic, D.M., 2015. Modes of cancer cell invasion and the role of the microenvironment. Current Opinion in Cell Biology 36, 13–22. https://doi.org/10.1016/j.ceb.2015.06.004
Codling, E.A., Plank, M.J., Benhamou, S., 2008. Random walk models in biology. Journal of The Royal Society Interface 5, 813–834. https://doi.org/10.1098/rsif.2008.0014
Collins, S.R., Meyer, T., 2009. Calcium Flickers Lighting the Way in Chemotaxis? Developmental Cell 16, 160–161. https://doi.org/10.1016/j.devcel.2009.01.018
Coravos, J.S., Mason, F.M., Martin, A.C., 2017. Actomyosin pulsing in tissue integrity maintenance during morphogenesis. Trends Cell Biol 27, 276–283. https://doi.org/10.1016/j.tcb.2016.11.008
Cowan, C.R., Hyman, A.A., 2007. Acto-myosin reorganization and PAR polarity in C. elegans. Development 134, 1035–1043. https://doi.org/10.1242/dev.000513
Cramer, L.P., 2010. Forming the cell rear first: breaking cell symmetry to trigger directed cell migration. Nat Cell Biol 12, 628–632. https://doi.org/10.1038/ncb0710-628
Cunningham, C.C., 1995. Actin polymerization and intracellular solvent flow in cell surface blebbing. J. Cell Biol. 129, 1589–1599. https://doi.org/10.1083/jcb.129.6.1589
Dai, J., Sheetz, M.P., 1999. Membrane Tether Formation from Blebbing Cells. Biophysical Journal 77, 3363–3370. https://doi.org/10.1016/S0006-3495(99)77168-7
Das, A., Bhat, A., Sknepnek, R., Köster, D., Mayor, S., Rao, M., 2020. Stratification relieves constraints from steric hindrance in the generation of compact actomyosin asters at the membrane cortex. Science Advances 6, eaay6093. https://doi.org/10.1126/sciadv.aay6093
de Beco, S., Vaidžiulytė, K., Manzi, J., Dalier, F., di Federico, F., Cornilleau, G., Dahan, M., Coppey, M., 2018. Optogenetic dissection of Rac1 and Cdc42 gradient shaping. Nature Communications 9, 4816. https://doi.org/10.1038/s41467-018-07286-8
Deneke, V.E., Di Talia, S., 2018. Chemical waves in cell and developmental biology. J. Cell Biol. 217, 1193–1204. https://doi.org/10.1083/jcb.201701158
Devreotes, P.N., Bhattacharya, S., Edwards, M., Iglesias, P.A., Lampert, T., Miao, Y., 2017. Excitable Signal Transduction Networks in Directed Cell Migration. Annu. Rev. Cell Dev. Biol. 33, 103–125. https://doi.org/10.1146/annurev-cellbio-100616-060739
Devreotes, P.N., Zigmond, S.H., 1988. Chemotaxis in Eukaryotic Cells: A Focus on Leukocytes and Dictyostelium. Annu. Rev. Cell. Biol. 4, 649–686. https://doi.org/10.1146/annurev.cb.04.110188.003245
Diz-Muñoz, A., Krieg, M., Bergert, M., Ibarlucea-Benitez, I., Muller, D.J., Paluch, E., Heisenberg, C.-P., 2010. Control of Directed Cell Migration In Vivo by Membrane-to-Cortex Attachment. PLOS Biology 8, e1000544. https://doi.org/10.1371/journal.pbio.1000544
Diz-Muñoz, A., Thurley, K., Chintamen, S., Altschuler, S.J., Wu, L.F., Fletcher, D.A., Weiner, O.D., 2016. Membrane Tension Acts Through PLD2 and mTORC2 to Limit Actin Network Assembly During Neutrophil Migration. PLOS Biology 14, e1002474. https://doi.org/10.1371/journal.pbio.1002474
Dmitrieff, S., Nédélec, F., 2016. Amplification of actin polymerization forces. J Cell Biol 212, 763–766. https://doi.org/10.1083/jcb.201512019
Dogterom, M., Kerssemakers, J.W., Romet-Lemonne, G., Janson, M.E., 2005. Force generation by dynamic microtubules. Current Opinion in Cell Biology 17, 67–74. https://doi.org/10.1016/j.ceb.2004.12.011

Doubrovinski, K., Kruse, K., 2011. Cell Motility Resulting from Spontaneous Polymerization Waves. Phys. Rev. Lett. 107, 258103. https://doi.org/10.1103/PhysRevLett.107.258103
Dreher, A., Aranson, I.S., Kruse, K., 2014. Spiral actin-polymerization waves can generate amoeboidal cell crawling. New J. Phys. 16, 055007. https://doi.org/10.1088/1367-2630/16/5/055007
Driscoll, M.K., Sun, X., Guven, C., Fourkas, J.T., Losert, W., 2014. Cellular Contact Guidance through Dynamic Sensing of Nanotopography. ACS Nano 8, 3546–3555. https://doi.org/10.1021/nn406637c
Dulyaninova, N.G., Bresnick, A.R., 2013. The heavy chain has its day: regulation of myosin-II assembly. Bioarchitecture 3, 77–85. https://doi.org/10.4161/bioa.26133
Elkhatib, N., Bresteau, E., Baschieri, F., Rioja, A.L., van Niel, G., Vassilopoulos, S., Montagnac, G., 2017. Tubular clathrin/AP-2 lattices pinch collagen fibers to support 3D cell migration. Science 356, eaal4713. https://doi.org/10.1126/science.aal4713
Ennomani, H., Letort, G., Guérin, C., Martiel, J.-L., Cao, W., Nédélec, F., De La Cruz, E.M., Théry, M., Blanchoin, L., 2016. Architecture and Connectivity Govern Actin Network Contractility. Current Biology 26, 616–626. https://doi.org/10.1016/j.cub.2015.12.069
Enyedi, B., Jelcic, M., Niethammer, P., 2016. The cell nucleus serves as a mechanotransducer of tissue damage-induced inflammation. Cell 165, 1160–1170. https://doi.org/10.1016/j.cell.2016.04.016
Fackler, O.T., Grosse, R., 2008. Cell motility through plasma membrane blebbing. J Cell Biol 181, 879–884. https://doi.org/10.1083/jcb.200802081
Fedier, A., Eggli, P., Keller, H.U., 1999. Redistribution of surface-bound con A is quantitatively related to the movement of cells developing polarity. Cell Motil. Cytoskeleton 44, 44–57. https://doi.org/10.1002/(SICI)1097-0169(199909)44:1<44::AID-CM4>3.0.CO;2-0
Fenix, A.M., Burnette, D.T., 2018. Assembly of myosin II filament arrays: Network Contraction versus Expansion. Cytoskeleton (Hoboken) 75, 545–549. https://doi.org/10.1002/cm.21487
Fenix, A.M., Taneja, N., Buttler, C.A., Lewis, J., Van Engelenburg, S.B., Ohi, R., Burnette, D.T., 2016. Expansion and concatenation of nonmuscle myosin IIA filaments drive cellular contractile system formation during interphase and mitosis. MBoC 27, 1465–1478. https://doi.org/10.1091/mbc.E15-10-0725
Field, C.M., Wuhr, M., Anderson, G.A., Kueh, H.Y., Strickland, D., Mitchison, T.J., 2011. Actin behavior in bulk cytoplasm is cell cycle regulated in early vertebrate embryos. Journal of Cell Science 124, 2086–2095. https://doi.org/10.1242/jcs.082263
Fievet, B.T., Gautreau, A., Roy, C., Del Maestro, L., Mangeat, P., Louvard, D., Arpin, M., 2004. Phosphoinositide binding and phosphorylation act sequentially in the activation mechanism of ezrin. J. Cell Biol. 164, 653–659. https://doi.org/10.1083/jcb.200307032
Fischer-Friedrich, E., Hyman, A.A., Jülicher, F., Müller, D.J., Helenius, J., 2014. Quantification of surface tension and internal pressure generated by single mitotic cells. Sci Rep 4, 6213. https://doi.org/10.1038/srep06213
Flynn, K.C., Pak, C.W., Shaw, A.E., Bradke, F., Bamburg, J.R., 2009. Growth cone-like waves transport actin and promote axonogenesis and neurite branching. Developmental Neurobiology 69, 761–779. https://doi.org/10.1002/dneu.20734

Footer, M.J., Kerssemakers, J.W.J., Theriot, J.A., Dogterom, M., 2007. Direct measurement of force generation by actin filament polymerization using an optical trap. Proc. Natl. Acad. Sci. U.S.A. 104, 2181–2186. https://doi.org/10.1073/pnas.0607052104

Ford, H.L., Zain, S.B., 1995. Interaction of metastasis associated Mts1 protein with nonmuscle myosin. Oncogene 10, 1597–1605.

Fotiadis, D., Scheuring, S., Müller, S.A., Engel, A., Müller, D.J., 2002. Imaging and manipulation of biological structures with the AFM. Micron 33, 385–397. https://doi.org/10.1016/S0968-4328(01)00026-9

Friedl, P., Wolf, K., 2010. Plasticity of cell migration: a multiscale tuning model. J. Cell Biol. 188, 11–19. https://doi.org/10.1083/jcb.200909003

Fritz-Laylin, L.K., Lord, S.J., Mullins, R.D., 2017a. Our evolving view of cell motility. Cell Cycle 16, 1735–1736. https://doi.org/10.1080/15384101.2017.1360655

Fritz-Laylin, L.K., Lord, S.J., Mullins, R.D., 2017b. WASP and SCAR are evolutionarily conserved in actin-filled pseudopod-based motility. J Cell Biol 216, 1673–1688. https://doi.org/10.1083/jcb.201701074

Fritzsche, M., Lewalle, A., Duke, T., Kruse, K., Charras, G., 2013. Analysis of turnover dynamics of the submembranous actin cortex. Mol Biol Cell 24, 757–767. https://doi.org/10.1091/mbc.E12-06-0485

Fritzsche, M., Thorogate, R., Charras, G., 2014. Quantitative Analysis of Ezrin Turnover Dynamics in the Actin Cortex. Biophys J 106, 343–353. https://doi.org/10.1016/j.bpj.2013.11.4499

Fujinami, N., Kageyama, T., 1975. Circus movement in dissociated embryonic cells of a teleost, Oryzias latipes. Journal of Cell Science 19, 169–182.

Funk, J., Merino, F., Venkova, L., Heydenreich, L., Kierfeld, J., Vargas, P., Raunser, S., Piel, M., Bieling, P., 2019. Profilin and formin constitute a pacemaker system for robust actin filament growth. eLife 8, e50963. https://doi.org/10.7554/eLife.50963

Garcia, M.C., Ray, D.M., Lackford, B., Rubino, M., Olden, K., Roberts, J.D., 2009. Arachidonic Acid Stimulates Cell Adhesion through a Novel p38 MAPK-RhoA Signaling Pathway That Involves Heat Shock Protein 27. J Biol Chem 284, 20936–20945. https://doi.org/10.1074/jbc.M109.020271

Gardel, M.L., Schneider, I.C., Aratyn-Schaus, Y., Waterman, C.M., 2010. Mechanical integration of actin and adhesion dynamics in cell migration. Annu. Rev. Cell Dev. Biol. 26, 315–333. https://doi.org/10.1146/annurev.cellbio.011209.122036

Gauthier, N.C., Fardin, M.A., Roca-Cusachs, P., Sheetz, M.P., 2011. Temporary increase in plasma membrane tension coordinates the activation of exocytosis and contraction during cell spreading. Proceedings of the National Academy of Sciences 108, 14467–14472. https://doi.org/10.1073/pnas.1105845108

Ghaffari, A., Hoskin, V., Turashvili, G., Varma, S., Mewburn, J., Mullins, G., Greer, P.A., Kiefer, F., Day, A.G., Madarnas, Y., SenGupta, S., Elliott, B.E., 2019. Intravital imaging reveals systemic ezrin inhibition impedes cancer cell migration and lymph node metastasis in breast cancer. Breast Cancer Research 21, 12. https://doi.org/10.1186/s13058-018-1079-7

Gibbs, D., Dellinger, O.P., 1908. The Daily Life of Amœba Proteus. The American Journal of Psychology 19, 232–241. https://doi.org/10.2307/1412761

Gierer, A., Meinhardt, H., 1972. A theory of biological pattern formation. Kybernetik 12, 30–39. https://doi.org/10.1007/BF00289234

Giese, W., Milicic, G., Schröder, A., Klipp, E., 2018. Spatial modeling of the membrane-cytosolic interface in protein kinase signal transduction. PLOS Computational Biology 14, e1006075. https://doi.org/10.1371/journal.pcbi.1006075

Goehring, N.W., Trong, P.K., Bois, J.S., Chowdhury, D., Nicola, E.M., Hyman, A.A., Grill, S.W., 2011. Polarization of PAR proteins by advective triggering of a pattern-forming system. Science 334, 1137–1141. https://doi.org/10.1126/science.1208619

Gong, M.C., Fuglsang, A., Alessi, D., Kobayashi, S., Cohen, P., Somlyo, A.V., Somlyo, A.P., 1992. Arachidonic acid inhibits myosin light chain phosphatase and sensitizes smooth muscle to calcium. J. Biol. Chem. 267, 21492–21498.

Goudarzi, M., Boquet-Pujadas, A., Olivo-Marin, J.-C., Raz, E., 2019. Fluid dynamics during bleb formation in migrating cells in vivo. PLoS One 14. https://doi.org/10.1371/journal.pone.0212699

Goudarzi, M., Tarbashevich, K., Mildner, K., Begemann, I., Garcia, J., Paksa, A., Reichman-Fried, M., Mahabaleshwar, H., Blaser, H., Hartwig, J., Zeuschner, D., Galic, M., Bagnat, M., Betz, T., Raz, E., 2017. Bleb Expansion in Migrating Cells Depends on Supply of Membrane from Cell Surface Invaginations. Developmental Cell 43, 577-587.e5. https://doi.org/10.1016/j.devcel.2017.10.030

Gov, N.S., 2018. Guided by curvature: shaping cells by coupling curved membrane proteins and cytoskeletal forces. Philosophical Transactions of the Royal Society B: Biological Sciences 373, 20170115. https://doi.org/10.1098/rstb.2017.0115

Graziano, B.R., Town, J.P., Sitarska, E., Nagy, T.L., Fošnarič, M., Penič, S., Iglič, A., Kralj-Iglič, V., Gov, N.S., Diz-Muñoz, A., Weiner, O.D., 2019. Cell confinement reveals a branched-actin independent circuit for neutrophil polarity. PLoS Biol 17, e3000457. https://doi.org/10.1371/journal.pbio.3000457

GręObecki, A., 1994. Membrane and Cytoskeleton Flow in Motile Cells with Emphasis on the Contribution of Free-Living Amoebae, in: Jeon, K.W., Jarvik, J. (Eds.), International Review of Cytology. Academic Press, pp. 37–80. https://doi.org/10.1016/S0074-7696(08)62405-5

Grewe, J., Schwarz, U.S., 2020. Mechanosensitive self-assembly of myosin II minifilaments. Phys. Rev. E 101, 022402. https://doi.org/10.1103/PhysRevE.101.022402

Gucht, J. van der, Sykes, C., 2009. Physical Model of Cellular Symmetry Breaking. Cold Spring Harb Perspect Biol 1, a001909. https://doi.org/10.1101/cshperspect.a001909

Guntas, G., Hallett, R.A., Zimmerman, S.P., Williams, T., Yumerefendi, H., Bear, J.E., Kuhlman, B., 2015. Engineering an improved light-induced dimer (iLID) for controlling the localization and activity of signaling proteins. Proc Natl Acad Sci U S A 112, 112–117. https://doi.org/10.1073/pnas.1417910112

Guo, B., Guilford, W.H., 2006. Mechanics of actomyosin bonds in different nucleotide states are tuned to muscle contraction. Proc Natl Acad Sci U S A 103, 9844–9849. https://doi.org/10.1073/pnas.0601255103

Gupton, S.L., Waterman-Storer, C.M., 2006. Spatiotemporal Feedback between Actomyosin and Focal-Adhesion Systems Optimizes Rapid Cell Migration. Cell 125, 1361–1374. https://doi.org/10.1016/j.cell.2006.05.029

Gura Sadovsky, R., Brielle, S., Kaganovich, D., England, J.L., 2017. Measurement of Rapid Protein Diffusion in the Cytoplasm by Photo-Converted Intensity Profile Expansion. Cell Rep 18, 2795–2806. https://doi.org/10.1016/j.celrep.2017.02.063

Hallett, F.R., Marsh, J., Nickel, B.G., Wood, J.M., 1993. Mechanical properties of vesicles. II. A model for osmotic swelling and lysis. Biophys. J. 64, 435–442. https://doi.org/10.1016/S0006-3495(93)81384-5

Han, W., Chen, S., Yuan, W., Fan, Q., Tian, J., Wang, X., Chen, L., Zhang, X., Wei, W., Liu, R., Qu, J., Jiao, Y., Austin, R.H., Liu, L., 2016. Oriented collagen fibers direct

tumor cell intravasation. Proc Natl Acad Sci USA 113, 11208–11213. https://doi.org/10.1073/pnas.1610347113
Hanahan, D., Weinberg, R.A., 2011. Hallmarks of Cancer: The Next Generation. Cell 144, 646–674. https://doi.org/10.1016/j.cell.2011.02.013
Hannezo, E., Dong, B., Recho, P., Joanny, J.-F., Hayashi, S., 2015. Cortical instability drives periodic supracellular actin pattern formation in epithelial tubes. Proc. Natl. Acad. Sci. U.S.A. 112, 8620–8625. https://doi.org/10.1073/pnas.1504762112
Hansen, S.D., Mullins, R.D., 2015. Lamellipodin promotes actin assembly by clustering Ena/VASP proteins and tethering them to actin filaments. Elife 4. https://doi.org/10.7554/eLife.06585
Hao, J.-J., Liu, Y., Kruhlak, M., Debell, K.E., Rellahan, B.L., Shaw, S., 2009. Phospholipase C-mediated hydrolysis of PIP2 releases ERM proteins from lymphocyte membrane. J. Cell Biol. 184, 451–462. https://doi.org/10.1083/jcb.200807047
Harris, A.R., Jreij, P., Belardi, B., Bausch, A., Fletcher, D.A., 2020. Biased localization of actin binding proteins by actin filament conformation. bioRxiv 2020.02.21.959791. https://doi.org/10.1101/2020.02.21.959791
Harrison, R.G., 1914. The reaction of embryonic cells to solid structures. J. Exp. Zool. 17, 521–544. https://doi.org/10.1002/jez.1400170403
Harrison, R.G., 1911. ON THE STEREOTROPISM OF EMBRYONIC CELLS. Science 34, 279–281. https://doi.org/10.1126/science.34.870.279
Haupt, A., Minc, N., 2018. How cells sense their own shape – mechanisms to probe cell geometry and their implications in cellular organization and function. J Cell Sci 131. https://doi.org/10.1242/jcs.214015
Havrylenko, S., Noguera, P., Abou-Ghali, M., Manzi, J., Faqir, F., Lamora, A., Guérin, C., Blanchoin, L., Plastino, J., 2015. WAVE binds Ena/VASP for enhanced Arp2/3 complex-based actin assembly. Mol. Biol. Cell 26, 55–65. https://doi.org/10.1091/mbc.E14-07-1200
Hawkins, R.J., Poincloux, R., Bénichou, O., Piel, M., Chavrier, P., Voituriez, R., 2011. Spontaneous Contractility-Mediated Cortical Flow Generates Cell Migration in Three-Dimensional Environments. Biophysical Journal 101, 1041–1045. https://doi.org/10.1016/j.bpj.2011.07.038
Headley, M.B., Bins, A., Nip, A., Roberts, E.W., Looney, M.R., Gerard, A., Krummel, M.F., 2016. Visualization of immediate immune responses to pioneer metastatic cells in the lung. Nature 531, 513–517. https://doi.org/10.1038/nature16985
Heinemann, F., Vogel, S.K., Schwille, P., 2013. Lateral Membrane Diffusion Modulated by a Minimal Actin Cortex. Biophys J 104, 1465–1475. https://doi.org/10.1016/j.bpj.2013.02.042
Hekmat, A., Künemund, V., Fischer, G., Schachner, M., 1989. Small inhibitory cerebellar interneurons grow in a perpendicular orientation to granule cell neurites in culture. Neuron 2, 1113–1122. https://doi.org/10.1016/0896-6273(89)90178-5
Hepper, I., Schymeinsky, J., Weckbach, L.T., Jakob, S.M., Frommhold, D., Sixt, M., Laschinger, M., Sperandio, M., Walzog, B., 2012. The Mammalian Actin-Binding Protein 1 Is Critical for Spreading and Intraluminal Crawling of Neutrophils under Flow Conditions. The Journal of Immunology 188, 4590–4601. https://doi.org/10.4049/jimmunol.1100878
Heyes, D.M., 2019. Translational and rotational diffusion of rod shaped molecules by molecular dynamics simulations. J. Chem. Phys. 150, 184503. https://doi.org/10.1063/1.5092958

Hind, L.E., Vincent, W.J.B., Huttenlocher, A., 2016. Leading from the Back: The Role of the Uropod in Neutrophil Polarization and Migration. Developmental Cell 38, 161–169. https://doi.org/10.1016/j.devcel.2016.06.031
Hiraiwa, T., Salbreux, G., 2016. Role of turnover in active stress generation in a filament network. Phys Rev Lett 116, 188101. https://doi.org/10.1103/PhysRevLett.116.188101
Holle, A.W., Kalafat, M., Ramos, A.S., Seufferlein, T., Kemkemer, R., Spatz, J.P., 2017. Intermediate filament reorganization dynamically influences cancer cell alignment and migration. Sci Rep 7, 45152. https://doi.org/10.1038/srep45152
Holz, D., Vavylonis, D., 2018. Building a dendritic actin filament network branch by branch: models of filament orientation pattern and force generation in lamellipodia. Biophys Rev 10, 1577–1585. https://doi.org/10.1007/s12551-018-0475-7
Hosseini, K., Sbosny, L., Poser, I., Fischer-Friedrich, E., 2020. Binding dynamics of alpha-actinin-4 in dependence of actin cortex tension. bioRxiv 2020.03.11.986935. https://doi.org/10.1101/2020.03.11.986935
Houk, A.R., Jilkine, A., Mejean, C.O., Boltyanskiy, R., Dufresne, E.R., Angenent, S.B., Altschuler, S.J., Wu, L.F., Weiner, O.D., 2012. Membrane tension maintains cell polarity by confining signals to the leading edge during neutrophil migration. Cell 148, 175–188. https://doi.org/10.1016/j.cell.2011.10.050
Howard, J., 2001. Mechanics of Motor Proteins and the Cytoskeleton. Sinauer Associates, Publishers.
Howard, J., Grill, S.W., Bois, J.S., 2011. Turing's next steps: the mechanochemical basis of morphogenesis. Nat. Rev. Mol. Cell Biol. 12, 392–398. https://doi.org/10.1038/nrm3120
Hu, S., Dasbiswas, K., Guo, Z., Tee, Y.-H., Thiagarajan, V., Hersen, P., Chew, T.-L., Safran, S.A., Zaidel-Bar, R., Bershadsky, A.D., 2017. Long-range self-organization of cytoskeletal myosin II filament stacks. Nat Cell Biol 19, 133–141. https://doi.org/10.1038/ncb3466
Huang, B., He, Y., Wang, L., Shi, J., Hu, J., Rofaani, E., Yamada, A., Chen, Y., 2020. Microfluidic channel with embedded monolayer nanofibers for cell culture and co-culture. Microelectronic Engineering 225, 111235. https://doi.org/10.1016/j.mee.2020.111235
Huang, C.-H., Tang, M., Shi, C., Iglesias, P.A., Devreotes, P.N., 2013. An Excitable Signal Integrator Couples to an Idling Cytoskeletal Oscillator to Drive Cell Migration. Nat Cell Biol 15, 1307–1316. https://doi.org/10.1038/ncb2859
Hug, C., Jay, P.Y., Reddy, I., McNally, J.G., Bridgman, P.C., Elson, E.L., Cooper, J.A., 1995. Capping protein levels influence actin assembly and cell motility in dictyostelium. Cell 81, 591–600. https://doi.org/10.1016/0092-8674(95)90080-2
Huxley, H.E., 1969. The mechanism of muscular contraction. Science 164, 1356–1365. https://doi.org/10.1126/science.164.3886.1356
Ierushalmi, N., Keren, K., 2019. Cellular Organization: Bulk Actin Network Flows Drive Ooplasm Segregation. Current Biology 29, R758–R761. https://doi.org/10.1016/j.cub.2019.06.063
Ierushalmi, N., Malik-Garbi, M., Manhart, A., Abu Shah, E., Goode, B.L., Mogilner, A., Keren, K., 2020. Centering and symmetry breaking in confined contracting actomyosin networks. eLife 9, e55368. https://doi.org/10.7554/eLife.55368
Ikenouchi, J., Aoki, K., 2017. Membrane bleb: A seesaw game of two small GTPases. Small GTPases 8, 85–89. https://doi.org/10.1080/21541248.2016.1199266
Inagaki, N., Katsuno, H., 2017. Actin Waves: Origin of Cell Polarization and Migration? Trends Cell Biol. 27, 515–526. https://doi.org/10.1016/j.tcb.2017.02.003

Inoue, T., Meyer, T., 2008. Synthetic activation of endogenous PI3K and Rac identifies an AND-gate switch for cell polarization and migration. PLoS ONE 3, e3068. https://doi.org/10.1371/journal.pone.0003068
Inoue, Y., Adachi, T., 2013. Role of the Actin–Myosin Catch Bond on Actomyosin Aggregate Formation. Cel. Mol. Bioeng. 6, 3–12. https://doi.org/10.1007/s12195-012-0265-4
Insall, R.H., Weiner, O.D., 2001. PIP3, PIP2, and Cell Movement—Similar Messages, Different Meanings? Dev Cell 1, 743.
Isogai, T., van der Kammen, R., Leyton-Puig, D., Kedziora, K.M., Jalink, K., Innocenti, M., 2015. Initiation of lamellipodia and ruffles involves cooperation between mDia1 and the Arp2/3 complex. J. Cell. Sci. 128, 3796–3810. https://doi.org/10.1242/jcs.176768
Janmey, P.A., Euteneuer, U., Traub, P., Schliwa, M., 1991. Viscoelastic properties of vimentin compared with other filamentous biopolymer networks. J. Cell Biol. 113, 155–160. https://doi.org/10.1083/jcb.113.1.155
Jasnin, M., Ecke, M., Baumeister, W., Gerisch, G., 2016. Actin Organization in Cells Responding to a Perforated Surface, Revealed by Live Imaging and Cryo-Electron Tomography. Structure 24, 1031–1043. https://doi.org/10.1016/j.str.2016.05.004
Jégou, A., Romet-Lemonne, G., 2016. Single Filaments to Reveal the Multiple Flavors of Actin. Biophys. J. 110, 2138–2146. https://doi.org/10.1016/j.bpj.2016.04.025
Jennings, H.S., 1904. Contributions to the study of the behaviour of lower organisms. Carnegie Inst. of Washington, Washington,. https://doi.org/10.5962/bhl.title.30720
Jiang, H., Kuang, Y., Wu, Y., Xie, W., Simon, M.I., Wu, D., 1997. Roles of phospholipase C β2 in chemoattractant-elicited responses. PNAS 94, 7971–7975. https://doi.org/10.1073/pnas.94.15.7971
Jiu, Y., Kumari, R., Fenix, A.M., Schaible, N., Liu, X., Varjosalo, M., Krishnan, R., Burnette, D.T., Lappalainen, P., 2019. Myosin-18B Promotes the Assembly of Myosin II Stacks for Maturation of Contractile Actomyosin Bundles. Current Biology 29, 81-92.e5. https://doi.org/10.1016/j.cub.2018.11.045
Johnson, H.E., King, S.J., Asokan, S.B., Rotty, J.D., Bear, J.E., Haugh, J.M., 2015. F-actin bundles direct the initiation and orientation of lamellipodia through adhesion-based signaling. J Cell Biol 208, 443–455. https://doi.org/10.1083/jcb.201406102
Jülicher, F., Kruse, K., Prost, J., Joanny, J.-F., 2007. Active behavior of the Cytoskeleton. Physics Reports, Nonequilibrium physics: From complex fluids to biological systems III. Living systems 449, 3–28. https://doi.org/10.1016/j.physrep.2007.02.018
Karuri, N.W., 2004. Biological length scale topography enhances cell-substratum adhesion of human corneal epithelial cells. Journal of Cell Science 117, 3153–3164. https://doi.org/10.1242/jcs.01146
Katsuno, H., Toriyama, M., Hosokawa, Y., Mizuno, K., Ikeda, K., Sakumura, Y., Inagaki, N., 2015. Actin Migration Driven by Directional Assembly and Disassembly of Membrane-Anchored Actin Filaments. Cell Reports 12, 648–660. https://doi.org/10.1016/j.celrep.2015.06.048
Keller, H.U., Wilkinson, P.C., Abercrombie, M., Becker, E.L., Hirsch, J.G., Miller, M.E., Scottramsey, W., Zigmond, S.H., 1977. A proposal for the definition of terms related to locomotion of leucocytes and other cells. Clin Exp Immunol 27, 377–380.
Keren, K., Pincus, Z., Allen, G.M., Barnhart, E.L., Marriott, G., Mogilner, A., Theriot, J.A., 2008. Mechanism of shape determination in motile cells. Nature 453, 475–480. https://doi.org/10.1038/nature06952

Kim, D.-H., Han, K., Gupta, K., Kwon, K.W., Suh, K.-Y., Levchenko, A., 2009. Mechanosensitivity of fibroblast cell shape and movement to anisotropic substratum topography gradients. Biomaterials 30, 5433–5444. https://doi.org/10.1016/j.biomaterials.2009.06.042

Kim, D.-H., Lipke, E.A., Kim, P., Cheong, R., Thompson, S., Delannoy, M., Suh, K.-Y., Tung, L., Levchenko, A., 2010. Nanoscale cues regulate the structure and function of macroscopic cardiac tissue constructs. Proceedings of the National Academy of Sciences 107, 565–570. https://doi.org/10.1073/pnas.0906504107

Korn, E.D., Carlier, M.F., Pantaloni, D., 1987. Actin polymerization and ATP hydrolysis. Science 238, 638–644. https://doi.org/10.1126/science.3672117

Kortholt, A., King, J.S., Keizer-Gunnink, I., Harwood, A.J., Van Haastert, P.J.M., 2007. Phospholipase C Regulation of Phosphatidylinositol 3,4,5-trisphosphate-mediated Chemotaxis. MBoC 18, 4772–4779. https://doi.org/10.1091/mbc.e07-05-0407

Koseki, K., Taniguchi, D., Yamashiro, S., Mizuno, H., Vavylonis, D., Watanabe, N., 2019. Lamellipodium tip actin barbed ends serve as a force sensor. Genes Cells 24, 705–718. https://doi.org/10.1111/gtc.12720

Koudehi, M.A., Rutkowski, D.M., Vavylonis, D., 2019. Organization of Associating or Crosslinked Actin Filaments in Confinement. Cytoskeleton (Hoboken) 76, 532–548. https://doi.org/10.1002/cm.21565

Kovar, D.R., Pollard, T.D., 2004. Insertional assembly of actin filament barbed ends in association with formins produces piconewton forces. Proc Natl Acad Sci U S A 101, 14725–14730. https://doi.org/10.1073/pnas.0405902101

Kozlov, M.M., Mogilner, A., 2007. Model of Polarization and Bistability of Cell Fragments. Biophys J 93, 3811–3819. https://doi.org/10.1529/biophysj.107.110411

Kress, A., Wang, X., Ranchon, H., Savatier, J., Rigneault, H., Ferrand, P., Brasselet, S., 2013. Mapping the Local Organization of Cell Membranes Using Excitation-Polarization-Resolved Confocal Fluorescence Microscopy. Biophys J 105, 127–136. https://doi.org/10.1016/j.bpj.2013.05.043

Kreten, F.H., Hoffmann, Ch., Riveline, D., Kruse, K., 2018. Active bundles of polar and bipolar filaments. Phys. Rev. E 98, 012413. https://doi.org/10.1103/PhysRevE.98.012413

Krueger, D., Quinkler, T., Mortensen, S.A., Sachse, C., De Renzis, S., 2019. Cross-linker–mediated regulation of actin network organization controls tissue morphogenesis. J Cell Biol 218, 2743–2761. https://doi.org/10.1083/jcb.201811127

Kühne, W., Kühne, 1864. Untersuchungen über das Protoplasma und die Contractilität. W. Engelmann.

Kwon, K.W., Park, H., Song, K.H., Choi, J.-C., Ahn, H., Park, M.J., Suh, K.-Y., Doh, J., 2012. Nanotopography-Guided Migration of T Cells. J.I. 189, 2266–2273. https://doi.org/10.4049/jimmunol.1102273

Lamb, R.F., Ozanne, B.W., Roy, C., McGarry, L., Stipp, C., Mangeat, P., Jay, D.G., 1997. Essential functions of ezrin in maintenance of cell shape and lamellipodial extension in normal and transformed fibroblasts. Current Biology 7, 682–688. https://doi.org/10.1016/S0960-9822(06)00295-8

Lämmermann, T., Bader, B.L., Monkley, S.J., Worbs, T., Wedlich-Söldner, R., Hirsch, K., Keller, M., Förster, R., Critchley, D.R., Fässler, R., Sixt, M., 2008. Rapid leukocyte migration by integrin-independent flowing and squeezing. Nature 453, 51–55. https://doi.org/10.1038/nature06887

Lämmermann, T., Sixt, M., 2009. Mechanical modes of 'amoeboid' cell migration. Current Opinion in Cell Biology 21, 636–644. https://doi.org/10.1016/j.ceb.2009.05.003

Langridge, P.D., Kay, R.R., 2006. Blebbing of Dictyostelium cells in response to chemoattractant. Experimental Cell Research 312, 2009–2017. https://doi.org/10.1016/j.yexcr.2006.03.007

Laplaud, V., Levernier, N., Pineau, J., Roman, M.S., Barbier, L., Saez, P.J., Lennon, A.M., Vargas, P., Kruse, K., Roure, O. du, Piel, M., Heuvingh, J., 2020. Pinching the cortex of live cells reveals thickness instabilities caused by Myosin II motors. bioRxiv 2020.09.28.316729. https://doi.org/10.1101/2020.09.28.316729

Laporte, D., Ojkic, N., Vavylonis, D., Wu, J.-Q., 2012. α-Actinin and fimbrin cooperate with myosin II to organize actomyosin bundles during contractile-ring assembly. MBoC 23, 3094–3110. https://doi.org/10.1091/mbc.e12-02-0123

Laurent, V.M., Kasas, S., Yersin, A., Schäffer, T.E., Catsicas, S., Dietler, G., Verkhovsky, A.B., Meister, J.-J., 2005. Gradient of rigidity in the lamellipodia of migrating cells revealed by atomic force microscopy. Biophys. J. 89, 667–675. https://doi.org/10.1529/biophysj.104.052316

Lavi, I., Goudarzi, M., Raz, E., Gov, N.S., Voituriez, R., Sens, P., 2019. Cellular Blebs and Membrane Invaginations Are Coupled through Membrane Tension Buffering. Biophysical Journal 117, 1485–1495. https://doi.org/10.1016/j.bpj.2019.08.002

Lawson, M.J., Drawert, B., Khammash, M., Petzold, L., Yi, T.-M., 2013. Spatial Stochastic Dynamics Enable Robust Cell Polarization. PLOS Computational Biology 9, e1003139. https://doi.org/10.1371/journal.pcbi.1003139

Le Berre, M., Zlotek-Zlotkiewicz, E., Bonazzi, D., Lautenschlaeger, F., Piel, M., 2014. Methods for Two-Dimensional Cell Confinement, in: Methods in Cell Biology. Elsevier, pp. 213–229. https://doi.org/10.1016/B978-0-12-800281-0.00014-2

Lee, S., Shen, Z., Robinson, D.N., Briggs, S., Firtel, R.A., 2010. Involvement of the cytoskeleton in controlling leading-edge function during chemotaxis. Mol. Biol. Cell 21, 1810–1824. https://doi.org/10.1091/mbc.e10-01-0009

Leithner, A., Eichner, A., Müller, J., Reversat, A., Brown, M., Schwarz, J., Merrin, J., de Gorter, D.J.J., Schur, F., Bayerl, J., de Vries, I., Wieser, S., Hauschild, R., Lai, F.P.L., Moser, M., Kerjaschki, D., Rottner, K., Small, J.V., Stradal, T.E.B., Sixt, M., 2016. Diversified actin protrusions promote environmental exploration but are dispensable for locomotion of leukocytes. Nat Cell Biol 18, 1253–1259. https://doi.org/10.1038/ncb3426

Lewis, W.H., 1923. MESENCHYME AND MESOTHELIUM. J. Exp. Med. 38, 257–262. https://doi.org/10.1084/jem.38.3.257

Lewis, W.H., Gregory, P.W., 1929. Cinematographs of Living Developing Rabbit-Eggs. Science 69, 226–229. https://doi.org/10.1126/science.69.1782.226-a

Li, Z.-H., Spektor, A., Varlamova, O., Bresnick, A.R., 2003. Mts1 Regulates the Assembly of Nonmuscle Myosin-IIA. Biochemistry 42, 14258–14266. https://doi.org/10.1021/bi0354379

Lieber, A.D., Schweitzer, Y., Kozlov, M.M., Keren, K., 2015. Front-to-Rear Membrane Tension Gradient in Rapidly Moving Cells. Biophys J 108, 1599–1603. https://doi.org/10.1016/j.bpj.2015.02.007

Lieber, A.D., Yehudai-Resheff, S., Barnhart, E.L., Theriot, J.A., Keren, K., 2013. Membrane Tension in Rapidly Moving Cells Is Determined by Cytoskeletal Forces. Current Biology 23, 1409–1417. https://doi.org/10.1016/j.cub.2013.05.063

Liu, Y., Belkina, N.V., Park, C., Nambiar, R., Loughhead, S.M., Patino-Lopez, G., Ben-Aissa, K., Hao, J.-J., Kruhlak, M.J., Qi, H., von Andrian, U.H., Kehrl, J.H., Tyska, M.J., Shaw, S., 2012. Constitutively active ezrin increases membrane tension, slows migration, and impedes endothelial transmigration of lymphocytes in vivo in mice. Blood 119, 445–453. https://doi.org/10.1182/blood-2011-07-368860

Liu, Y.-J., Le Berre, M., Lautenschlaeger, F., Maiuri, P., Callan-Jones, A., Heuzé, M., Takaki, T., Voituriez, R., Piel, M., 2015. Confinement and Low Adhesion Induce Fast Amoeboid Migration of Slow Mesenchymal Cells. Cell 160, 659–672. https://doi.org/10.1016/j.cell.2015.01.007

Lo, C.-M., Wang, H.-B., Dembo, M., Wang, Y., 2000. Cell Movement Is Guided by the Rigidity of the Substrate. Biophysical Journal 79, 144–152. https://doi.org/10.1016/S0006-3495(00)76279-5

Loeb, J., 1898. Biological lectures delivered at the Marine Biological Laboratory of Wood's Holl [sic]. Ginn & Co., Boston,.

Loeb, J., 1893. Biological lectures delivered at the Marine Biological Laboratory of Wood's Holl [sic]. Ginn & Co., Boston.

Logue, J.S., Cartagena-Rivera, A.X., Baird, M.A., Davidson, M.W., Chadwick, R.S., Waterman, C.M., 2015. Erk regulation of actin capping and bundling by Eps8 promotes cortex tension and leader bleb-based migration. eLife 4, e08314. https://doi.org/10.7554/eLife.08314

Logue, J.S., Morrison, D.K., 2012. Complexity in the signaling network: insights from the use of targeted inhibitors in cancer therapy. Genes Dev. 26, 641–650. https://doi.org/10.1101/gad.186965.112

Loison, O., Weitkunat, M., Kaya-Çopur, A., Alves, C.N., Matzat, T., Spletter, M.L., Luschnig, S., Brasselet, S., Lenne, P.-F., Schnorrer, F., 2018. Polarization-resolved microscopy reveals a muscle myosin motor-independent mechanism of molecular actin ordering during sarcomere maturation. PLOS Biology 16, e2004718. https://doi.org/10.1371/journal.pbio.2004718

Lomakin, A.J., Cattin, C.J., Cuvelier, D., Alraies, Z., Molina, M., Nader, G., Srivastava, N., Garcia-Arcos, J.M., Zhitnyak, I.Y., Bhargava, A., Driscoll, M.K., Welf, E.S., Fiolka, R., Petrie, R.J., Manel, N., Lennon-Duménil, A.M., Müller, D.J., Piel, M., 2019. The nucleus acts as a ruler tailoring cell responses to spatial constraints. bioRxiv 863514. https://doi.org/10.1101/863514

Lomakin, A.J., Cattin, C.J., Cuvelier, D., Alraies, Z., Molina, M., Nader, G.P.F., Srivastava, N., Saez, P.J., Garcia-Arcos, J.M., Zhitnyak, I.Y., Bhargava, A., Driscoll, M.K., Welf, E.S., Fiolka, R., Petrie, R.J., Silva, N.S.D., González-Granado, J.M., Manel, N., Lennon-Duménil, A.M., Müller, D.J., Piel, M., 2020. The nucleus acts as a ruler tailoring cell responses to spatial constraints. Science 370. https://doi.org/10.1126/science.aba2894

Lomakin, A.J., Lee, K.-C., Han, S.J., Bui, D.A., Davidson, M., Mogilner, A., Danuser, G., 2015. Competition for actin between two distinct F-actin networks defines a bistable switch for cell polarization. Nat. Cell Biol. 17, 1435–1445. https://doi.org/10.1038/ncb3246

Lorentzen, A., Bamber, J., Sadok, A., Elson-Schwab, I., Marshall, C.J., 2011. An ezrin-rich, rigid uropod-like structure directs movement of amoeboid blebbing cells. Journal of Cell Science 124, 1256–1267. https://doi.org/10.1242/jcs.074849

Lou, S.S., Diz-Muñoz, A., Weiner, O.D., Fletcher, D.A., Theriot, J.A., 2015. Myosin light chain kinase regulates cell polarization independently of membrane tension or Rho kinase. J Cell Biol 209, 275–288. https://doi.org/10.1083/jcb.201409001

Luxton, G.G., Gomes, E.R., Folker, E.S., Worman, H.J., Gundersen, G.G., 2011. TAN lines. Nucleus 2, 173–181. https://doi.org/10.4161/nucl.2.3.16243

Ma, L., Janetopoulos, C., Yang, L., Devreotes, P.N., Iglesias, P.A., 2004. Two Complementary, Local Excitation, Global Inhibition Mechanisms Acting in Parallel Can Explain the Chemoattractant-Induced Regulation of PI(3,4,5)P3 Response in

Dictyostelium Cells. Biophysical Journal 87, 3764–3774. https://doi.org/10.1529/biophysj.104.045484
Ma, L., Li, Y., Peng, J., Wu, D., Zhao, X., Cui, Y., Chen, L., Yan, X., Du, Y., Yu, L., 2015. Discovery of the migrasome, an organelle mediating release of cytoplasmic contents during cell migration. Cell Res 25, 24–38. https://doi.org/10.1038/cr.2014.135
Machacek, M., Hodgson, L., Welch, C., Elliott, H., Pertz, O., Nalbant, P., Abell, A., Johnson, G.L., Hahn, K.M., Danuser, G., 2009. Coordination of Rho GTPase activities during cell protrusion. Nature 461, 99–103. https://doi.org/10.1038/nature08242
Maeda, Y.T., Inose, J., Matsuo, M.Y., Iwaya, S., Sano, M., 2008. Ordered Patterns of Cell Shape and Orientational Correlation during Spontaneous Cell Migration. PLOS ONE 3, e3734. https://doi.org/10.1371/journal.pone.0003734
Maître, J.-L., Niwayama, R., Turlier, H., Nédélec, F., Hiiragi, T., 2015. Pulsatile cell-autonomous contractility drives compaction in the mouse embryo. Nat Cell Biol 17, 849–855. https://doi.org/10.1038/ncb3185
Maiuri, P., Rupprecht, J.-F., Wieser, S., Ruprecht, V., Bénichou, O., Carpi, N., Coppey, M., De Beco, S., Gov, N., Heisenberg, C.-P., Lage Crespo, C., Lautenschlaeger, F., Le Berre, M., Lennon-Dumenil, A.-M., Raab, M., Thiam, H.-R., Piel, M., Sixt, M., Voituriez, R., 2015. Actin Flows Mediate a Universal Coupling between Cell Speed and Cell Persistence. Cell 161, 374–386. https://doi.org/10.1016/j.cell.2015.01.056
Maiuri, P., Terriac, E., Paul-Gilloteaux, P., Vignaud, T., McNally, K., Onuffer, J., Thorn, K., Nguyen, P.A., Georgoulia, N., Soong, D., Jayo, A., Beil, N., Beneke, J., Hong Lim, J.C., Pei-Ying Sim, C., Chu, Y.-S., Jiménez-Dalmaroni, A., Joanny, J.-F., Thiery, J.-P., Erfle, H., Parsons, M., Mitchison, T.J., Lim, W.A., Lennon-Duménil, A.-M., Piel, M., Théry, M., 2012. The first World Cell Race. Current Biology 22, R673–R675. https://doi.org/10.1016/j.cub.2012.07.052
Majumdar, R., Tavakoli Tameh, A., Parent, C.A., 2016. Exosomes Mediate LTB4 Release during Neutrophil Chemotaxis. PLoS Biol 14, e1002336. https://doi.org/10.1371/journal.pbio.1002336
Malawista, S., 1982. The cytokineplast: purified, stable, and functional motile machinery from human blood polymorphonuclear leukocytes. The Journal of Cell Biology 95, 960–973. https://doi.org/10.1083/jcb.95.3.960
Malik-Garbi, M., Ierushalmi, N., Jansen, S., Abu-Shah, E., Goode, B.L., Mogilner, A., Keren, K., 2019. Scaling behaviour in steady-state contracting actomyosin networks. Nat Phys 15, 509–516. https://doi.org/10.1038/s41567-018-0413-4
Marion, S., Hoffmann, E., Holzer, D., Clainche, C.L., Martin, M., Sachse, M., Ganeva, I., Mangeat, P., Griffiths, G., 2011. Ezrin Promotes Actin Assembly at the Phagosome Membrane and Regulates Phago-Lysosomal Fusion. Traffic 12, 421–437. https://doi.org/10.1111/j.1600-0854.2011.01158.x
Martin, K., Reimann, A., Fritz, R.D., Ryu, H., Jeon, N.L., Pertz, O., 2016. Spatio-temporal co-ordination of RhoA, Rac1 and Cdc42 activation during prototypical edge protrusion and retraction dynamics. Scientific Reports 6, 21901. https://doi.org/10.1038/srep21901
Maugis, B., Brugues, J., Nassoy, P., Guillen, N., Sens, P., Amblard, F., 2010. Dynamic instability of the intracellular pressure drives bleb-based motility. Journal of Cell Science 123, 3884–3892. https://doi.org/10.1242/jcs.065672
Mavrakis, M., Azou-Gros, Y., Tsai, F.-C., Alvarado, J., Bertin, A., Iv, F., Kress, A., Brasselet, S., Koenderink, G.H., Lecuit, T., 2014. Septins promote F-actin ring

formation by crosslinking actin filaments into curved bundles. Nature Cell Biology 16, 322–334. https://doi.org/10.1038/ncb2921
Mayer, M., Depken, M., Bois, J.S., Jülicher, F., Grill, S.W., 2010. Anisotropies in cortical tension reveal the physical basis of polarizing cortical flows. Nature 467, 617–621. https://doi.org/10.1038/nature09376
McMahon, H.T., Boucrot, E., 2015. Membrane curvature at a glance. Journal of Cell Science 128, 1065–1070. https://doi.org/10.1242/jcs.114454
Medeiros, N.A., Burnette, D.T., Forscher, P., 2006. Myosin II functions in actin-bundle turnover in neuronal growth cones. Nat Cell Biol 8, 216–226. https://doi.org/10.1038/ncb1367
Mehidi, A., Rossier, O., Schaks, M., Chazeau, A., Binamé, F., Remorino, A., Coppey, M., Karatas, Z., Sibarita, J.-B., Rottner, K., Moreau, V., Giannone, G., 2019. Transient Activations of Rac1 at the Lamellipodium Tip Trigger Membrane Protrusion. Current Biology 29, 2852-2866.e5. https://doi.org/10.1016/j.cub.2019.07.035
Meinhardt, H., Gierer, A., 1974. Applications of a Theory of Biological Pattern Formation Based on Lateral Inhibition. Journal of Cell Science 15, 321–346.
Menshykau, D., Blanc, P., Unal, E., Sapin, V., Iber, D., 2014. An interplay of geometry and signaling enables robust lung branching morphogenesis. Development 141, 4526–4536. https://doi.org/10.1242/dev.116202
Meyers, J., Craig, J., Odde, D.J., 2006. Potential for control of signaling pathways via cell size and shape. Curr. Biol. 16, 1685–1693. https://doi.org/10.1016/j.cub.2006.07.056
Miao, Y., Bhattacharya, S., Banerjee, T., Abubaker-Sharif, B., Long, Y., Inoue, T., Iglesias, P.A., Devreotes, P.N., 2019. Wave patterns organize cellular protrusions and control cortical dynamics. Mol Syst Biol 15. https://doi.org/10.15252/msb.20188585
Miao, Y., Bhattacharya, S., Edwards, M., Cai, H., Inoue, T., Iglesias, P.A., Devreotes, P.N., 2017. Altering the threshold of an excitable signal transduction network changes cell migratory modes. Nat Cell Biol 19, 329–340. https://doi.org/10.1038/ncb3495
Milo, R., Phillips, R., 2016. Cell biology by the numbers. Garland Science, Taylor & Francis Group, New York, NY.
Miyoshi, T., Watanabe, N., 2013. Can filament treadmilling alone account for the F-actin turnover in lamellipodia? Cytoskeleton 70, 179–190. https://doi.org/10.1002/cm.21098
Mogilner, A., Barnhart, E.L., Keren, K., 2020. Experiment, theory, and the keratocyte: An ode to a simple model for cell motility. Seminars in Cell & Developmental Biology, REGENERATION OF VERTEBRATE ORGANS 100, 143–151. https://doi.org/10.1016/j.semcdb.2019.10.019
Mogilner, A., Oster, G., 2003. Force Generation by Actin Polymerization II: The Elastic Ratchet and Tethered Filaments. Biophys J 84, 1591–1605.
Mogilner, A., Oster, G., 1996. Cell motility driven by actin polymerization. Biophys. J. 71, 3030–3045. https://doi.org/10.1016/S0006-3495(96)79496-1
Montaville, P., Jégou, A., Pernier, J., Compper, C., Guichard, B., Mogessie, B., Schuh, M., Romet-Lemonne, G., Carlier, M.-F., 2014. Spire and Formin 2 Synergize and Antagonize in Regulating Actin Assembly in Meiosis by a Ping-Pong Mechanism. PLOS Biology 12, e1001795. https://doi.org/10.1371/journal.pbio.1001795
Morris, C.E., Homann, U., 2001. Cell Surface Area Regulation and Membrane Tension. J. Membrane Biol. 179, 79–102. https://doi.org/10.1007/s002320010040

Mosby, L.S., Hundt, N., Young, G., Fineberg, A., Polin, M., Mayor, S., Kukura, P., Köster, D.V., 2020. Myosin II Filament Dynamics in Actin Networks Revealed with Interferometric Scattering Microscopy. Biophysical Journal 0. https://doi.org/10.1016/j.bpj.2020.02.025

Mullins, R.D., 2010. Cytoskeletal Mechanisms for Breaking Cellular Symmetry. Cold Spring Harb Perspect Biol 2, a003392. https://doi.org/10.1101/cshperspect.a003392

Mullins, R.D., Bieling, P., Fletcher, D.A., 2018. From solution to surface to filament: actin flux into branched networks. Biophys Rev 10, 1537–1551. https://doi.org/10.1007/s12551-018-0469-5

Munro, E., Bowerman, B., 2009. Cellular symmetry breaking during Caenorhabditis elegans development. Cold Spring Harb Perspect Biol 1, a003400. https://doi.org/10.1101/cshperspect.a003400

Munro, E., Nance, J., Priess, J.R., 2004. Cortical flows powered by asymmetrical contraction transport PAR proteins to establish and maintain anterior-posterior polarity in the early C. elegans embryo. Dev. Cell 7, 413–424. https://doi.org/10.1016/j.devcel.2004.08.001

Nagata, I., Kawana, A., Nakatsuji, N., 1993. Perpendicular contact guidance of CNS neuroblasts on artificial microstructures. Development 117, 401–408.

Nagata, Isao, Kawana, A., Nakatsuji, N., 1993. Perpendicular Contact Guidance of CNS Neuroblasts on Artificial Microstructures. Development (Cambridge, England) 117.

Nakagawa, H., Terasaki, A.G., Suzuki, H., Ohashi, K., Miyamoto, S., 2006. Short-term retention of actin filament binding proteins on lamellipodial actin bundles. FEBS Letters 580, 3223–3228. https://doi.org/10.1016/j.febslet.2006.04.082

Neuhaus, J.M., Wanger, M., Keiser, T., Wegner, A., 1983. Treadmilling of actin. J. Muscle Res. Cell. Motil. 4, 507–527. https://doi.org/10.1007/bf00712112

Nguyen, T.T.T., Park, W.S., Park, B.O., Kim, C.Y., Oh, Y., Kim, J.M., Choi, H., Kyung, T., Kim, C.-H., Lee, G., Hahn, K.M., Meyer, T., Heo, W.D., 2016. PLEKHG3 enhances polarized cell migration by activating actin filaments at the cell front. Proc. Natl. Acad. Sci. U.S.A. 113, 10091–10096. https://doi.org/10.1073/pnas.1604720113

Niederman, R., Pollard, T.D., 1975. Human platelet myosin. II. In vitro assembly and structure of myosin filaments. J. Cell Biol. 67, 72–92. https://doi.org/10.1083/jcb.67.1.72

Nishikawa, M., Naganathan, S.R., Jülicher, F., Grill, S.W., 2017. Controlling contractile instabilities in the actomyosin cortex. eLife 6, e19595. https://doi.org/10.7554/eLife.19595

Oakes, P.W., Bidone, T.C., Beckham, Y., Skeeters, A.V., Juan, G.R.R.-S., Winter, S.P., Voth, G.A., Gardel, M.L., 2018. Lamellipodium is a myosin-independent mechanosensor. PNAS 115, 2646–2651. https://doi.org/10.1073/pnas.1715869115

Okimura, C., Taniguchi, A., Nonaka, S., Iwadate, Y., 2018. Rotation of stress fibers as a single wheel in migrating fish keratocytes. Scientific Reports 8, 10615. https://doi.org/10.1038/s41598-018-28875-z

Olguin-Olguin, A., Aalto, A., Maugis, B., Boquet-Pujadas, A., Hoffmann, D., Ermlich, L., Betz, T., Gov, N.S., Reichman-Fried, M., Raz, E., 2021. Chemokine-biased robust self-organizing polarization of migrating cells in vivo. PNAS 118. https://doi.org/10.1073/pnas.2018480118

Olson, M.F., Sahai, E., 2008. The actin cytoskeleton in cancer cell motility. Clin Exp Metastasis 26, 273. https://doi.org/10.1007/s10585-008-9174-2
O'Neill, P.R., Castillo-Badillo, J.A., Meshik, X., Kalyanaraman, V., Melgarejo, K., Gautam, N., 2018. Membrane Flow Drives an Adhesion-Independent Amoeboid Cell Migration Mode. Developmental Cell 46, 9-22.e4. https://doi.org/10.1016/j.devcel.2018.05.029
Osterhout, W.J.V., 2011. Biographical Memoir Of Jacques Loeb, 1859-1924: Biographical Memoirs V13, Fourth Memoir. Literary Licensing, LLC.
Otto, A., Collins-Hooper, H., Patel, A., Dash, P.R., Patel, K., 2011. Adult skeletal muscle stem cell migration is mediated by a blebbing/amoeboid mechanism. Rejuvenation Res 14, 249–260. https://doi.org/10.1089/rej.2010.1151
Paluch, E.K., Aspalter, I.M., Sixt, M., 2016. Focal Adhesion–Independent Cell Migration. Annu. Rev. Cell Dev. Biol. 32, 469–490. https://doi.org/10.1146/annurev-cellbio-111315-125341
Paluch, E.K., Raz, E., 2013. The role and regulation of blebs in cell migration. Current Opinion in Cell Biology 25, 582–590. https://doi.org/10.1016/j.ceb.2013.05.005
Pandit, N.G., Cao, W., Bibeau, J., Johnson-Chavarria, E.M., Taylor, E.W., Pollard, T.D., Cruz, E.M.D.L., 2020. Force and phosphate release from Arp2/3 complex promote dissociation of actin filament branches. PNAS 117, 13519–13528. https://doi.org/10.1073/pnas.1911183117
Parent, C.A., Blacklock, B.J., Froehlich, W.M., Murphy, D.B., Devreotes, P.N., 1998. G protein signaling events are activated at the leading edge of chemotactic cells. Cell 95, 81–91. https://doi.org/10.1016/s0092-8674(00)81784-5
Parent, C.A., Devreotes, P.N., 1999. A Cell's Sense of Direction. Science 284, 765–770. https://doi.org/10.1126/science.284.5415.765
Pasternak, C., Spudich, J.A., Elson, E.L., 1989. Capping of surface receptors and concomitant cortical tension are generated by conventional myosin. Nature 341, 549–551. https://doi.org/10.1038/341549a0
Pauly, P.J., 1987. Controlling Life: Jacques Loeb and the Engineering Ideal in Biology. Oxford University Press.
Pernier, J., Shekhar, S., Jegou, A., Guichard, B., Carlier, M.-F., 2016. Profilin Interaction with Actin Filament Barbed End Controls Dynamic Instability, Capping, Branching, and Motility. Developmental Cell 36, 201–214. https://doi.org/10.1016/j.devcel.2015.12.024
Peskin, C.S., Odell, G.M., Oster, G.F., 1993. Cellular motions and thermal fluctuations: the Brownian ratchet. Biophys J 65, 316–324.
Petitjean, L., Reffay, M., Grasland-Mongrain, E., Poujade, M., Ladoux, B., Buguin, A., Silberzan, P., 2010. Velocity Fields in a Collectively Migrating Epithelium. Biophys J 98, 1790–1800. https://doi.org/10.1016/j.bpj.2010.01.030
Petrie, R.J., Gavara, N., Chadwick, R.S., Yamada, K.M., 2012. Nonpolarized signaling reveals two distinct modes of 3D cell migration. J. Cell Biol. 197, 439–455. https://doi.org/10.1083/jcb.201201124
Peukes, J., Betz, T., 2014. Direct Measurement of the Cortical Tension during the Growth of Membrane Blebs. Biophysical Journal 107, 1810–1820. https://doi.org/10.1016/j.bpj.2014.07.076
Pietuch, A., Brückner, B.R., Janshoff, A., 2013. Membrane tension homeostasis of epithelial cells through surface area regulation in response to osmotic stress. Biochim. Biophys. Acta 1833, 712–722. https://doi.org/10.1016/j.bbamcr.2012.11.006

Pincus, Z., Theriot, J.A., 2007. Comparison of quantitative methods for cell-shape analysis. J Microsc 227, 140–156. https://doi.org/10.1111/j.1365-2818.2007.01799.x
Pinot, M., Steiner, V., Dehapiot, B., Yoo, B.-K., Chesnel, F., Blanchoin, L., Kervrann, C., Gueroui, Z., 2012. Confinement induces actin flow in a meiotic cytoplasm. PNAS 109, 11705–11710. https://doi.org/10.1073/pnas.1121583109
Pipathsouk, A., Brunetti, R.M., Town, J.P., Breuer, A., Pellett, P.A., Marchuk, K., Tran, N.-H.T., Krummel, M.F., Stamou, D., Weiner, O.D., 2019. WAVE complex self-organization templates lamellipodial formation. bioRxiv 836585. https://doi.org/10.1101/836585
Pollard, T.D., 2016. Actin and Actin-Binding Proteins. Cold Spring Harb Perspect Biol 8. https://doi.org/10.1101/cshperspect.a018226
Pollard, T.D., 1986. Rate constants for the reactions of ATP- and ADP-actin with the ends of actin filaments. J. Cell Biol. 103, 2747–2754. https://doi.org/10.1083/jcb.103.6.2747
Pollard, T.D., Blanchoin, L., Mullins, R.D., 2000. Molecular Mechanisms Controlling Actin Filament Dynamics in Nonmuscle Cells. Annual Review of Biophysics and Biomolecular Structure 29, 545–576. https://doi.org/10.1146/annurev.biophys.29.1.545
Pollard, T.D., Borisy, G.G., 2003. Cellular motility driven by assembly and disassembly of actin filaments. Cell 112, 453–465. https://doi.org/10.1016/s0092-8674(03)00120-x
Pollard, T.D., Korn, E.D., 1973a. Acanthamoeba myosin. I. Isolation from Acanthamoeba castellanii of an enzyme similar to muscle myosin. J. Biol. Chem. 248, 4682–4690.
Pollard, T.D., Korn, E.D., 1973b. Acanthamoeba myosin. II. Interaction with actin and with a new cofactor protein required for actin activation of Mg 2+ adenosine triphosphatase activity. J. Biol. Chem. 248, 4691–4697.
Purcell, E.M., 1977. Life at low Reynolds number. American Journal of Physics 45, 3–11. https://doi.org/10.1119/1.10903
Quemeneur, F., Sigurdsson, J.K., Renner, M., Atzberger, P.J., Bassereau, P., Lacoste, D., 2014. Shape matters in protein mobility within membranes. Proc Natl Acad Sci U S A 111, 5083–5087. https://doi.org/10.1073/pnas.1321054111
Rall, J.A., 2018. Generation of life in a test tube: Albert Szent-Gyorgyi, Bruno Straub, and the discovery of actin. Advances in Physiology Education 42, 277–288. https://doi.org/10.1152/advan.00189.2017
Ramkumar, N., Baum, B., 2016. Coupling changes in cell shape to chromosome segregation. Nature Reviews Molecular Cell Biology 17, 511–521. https://doi.org/10.1038/nrm.2016.75
Rangamani, P., Lipshtat, A., Azeloglu, E.U., Calizo, R.C., Hu, M., Ghassemi, S., Hone, J., Scarlata, S., Neves, S.R., Iyengar, R., 2013. Decoding Information in Cell Shape. Cell 154, 1356–1369. https://doi.org/10.1016/j.cell.2013.08.026
Raucher, D., Sheetz, M.P., 1999. Characteristics of a Membrane Reservoir Buffering Membrane Tension. Biophysical Journal 77, 1992–2002. https://doi.org/10.1016/S0006-3495(99)77040-2
Raucher, D., Stauffer, T., Chen, W., Shen, K., Guo, S., York, J.D., Sheetz, M.P., Meyer, T., 2000. Phosphatidylinositol 4,5-Bisphosphate Functions as a Second Messenger that Regulates Cytoskeleton–Plasma Membrane Adhesion. Cell 100, 221–228. https://doi.org/10.1016/S0092-8674(00)81560-3

Rauzi, M., Lenne, P.-F., Lecuit, T., 2010. Planar polarized actomyosin contractile flows control epithelial junction remodelling. Nature 468, 1110–1114. https://doi.org/10.1038/nature09566

Raz-Ben Aroush, D., Ofer, N., Abu-Shah, E., Allard, J., Krichevsky, O., Mogilner, A., Keren, K., 2017. Actin Turnover in Lamellipodial Fragments. Current Biology 27, 2963-2973.e14. https://doi.org/10.1016/j.cub.2017.08.066

Renkawitz, J., Schumann, K., Weber, M., Lämmermann, T., Pflicke, H., Piel, M., Polleux, J., Spatz, J.P., Sixt, M., 2009. Adaptive force transmission in amoeboid cell migration. Nat Cell Biol 11, 1438–1443. https://doi.org/10.1038/ncb1992

Reversat, A., Gaertner, F., Merrin, J., Stopp, J., Tasciyan, S., Aguilera, J., Vries, I. de, Hauschild, R., Hons, M., Piel, M., Callan-Jones, A., Voituriez, R., Sixt, M., 2020. Cellular locomotion using environmental topography. Nature 1–4. https://doi.org/10.1038/s41586-020-2283-z

Reversat, A., Merrin, J., Hauschild, R., de Vries, I., Piel, M., Callan-Jones, A., Voituriez, R., Sixt, M., 2019. Adhesion-free cell migration by topography-based force transduction (preprint). Cell Biology. https://doi.org/10.1101/793919

Ricketson, D., Johnston, C.A., Prehoda, K.E., 2010. Multiple tail domain interactions stabilize nonmuscle myosin II bipolar filaments. PNAS 107, 20964–20969. https://doi.org/10.1073/pnas.1007025107

Risca, V.I., Wang, E.B., Chaudhuri, O., Chia, J.J., Geissler, P.L., Fletcher, D.A., 2012. Actin filament curvature biases branching direction. Proceedings of the National Academy of Sciences 109, 2913–2918. https://doi.org/10.1073/pnas.1114292109

Romet-Lemonne, G., Jégou, A., 2013. Mechanotransduction down to individual actin filaments. Eur. J. Cell Biol. 92, 333–338. https://doi.org/10.1016/j.ejcb.2013.10.011

Rosenberger, H., 1929a. A Standard Microcinematographic Apparatus. Science 69, 672–674. https://doi.org/10.1126/science.69.1800.672

Rosenberger, H., 1929b. Micro-Cinematography in Medical Research: Journal of Dental Research. https://doi.org/10.1177/00220345290090030501

Rouven Brückner, B., Pietuch, A., Nehls, S., Rother, J., Janshoff, A., 2015. Ezrin is a Major Regulator of Membrane Tension in Epithelial Cells. Scientific Reports 5, 14700. https://doi.org/10.1038/srep14700

Ruprecht, V., Wieser, S., Callan-Jones, A., Smutny, M., Morita, H., Sako, K., Barone, V., Ritsch-Marte, M., Sixt, M., Voituriez, R., Heisenberg, C.-P., 2015. Cortical Contractility Triggers a Stochastic Switch to Fast Amoeboid Cell Motility. Cell 160, 673–685. https://doi.org/10.1016/j.cell.2015.01.008

Sahai, E., 2007. Illuminating the metastatic process. Nat Rev Cancer 7, 737–749. https://doi.org/10.1038/nrc2229

Sahai, E., Marshall, C.J., 2003. Differing modes of tumour cell invasion have distinct requirements for Rho/ROCK signalling and extracellular proteolysis. Nat Cell Biol 5, 711–719. https://doi.org/10.1038/ncb1019

Salbreux, G., Charras, G., Paluch, E., 2012. Actin cortex mechanics and cellular morphogenesis. Trends Cell Biol. 22, 536–545. https://doi.org/10.1016/j.tcb.2012.07.001

Sandquist, J.C., Swenson, K.I., DeMali, K.A., Burridge, K., Means, A.R., 2006. Rho Kinase Differentially Regulates Phosphorylation of Nonmuscle Myosin II Isoforms A and B during Cell Rounding and Migration. J. Biol. Chem. 281, 35873–35883. https://doi.org/10.1074/jbc.M605343200

Schaeffer, A.A. (Asa A., 1920. Ameboid movement. Princeton : Princeton University Press.

Schiffhauer, E.S., Luo, T., Mohan, K., Srivastava, V., Qian, X., Griffis, E.R., Iglesias, P.A., Robinson, D.N., 2016. Mechanoaccumulative Elements of the Mammalian Actin Cytoskeleton. Curr. Biol. 26, 1473–1479. https://doi.org/10.1016/j.cub.2016.04.007

Schmick, M., Bastiaens, P.I.H., 2014. The Interdependence of Membrane Shape and Cellular Signal Processing. Cell 156, 1132–1138. https://doi.org/10.1016/j.cell.2014.02.007

Scholey, J.M., Taylor, K.A., Kendrick-Jones, J., 1980. Regulation of non-muscle myosin assembly by calmodulin-dependent light chain kinase. Nature 287, 233–235. https://doi.org/10.1038/287233a0

Selmeczi, D., Mosler, S., Hagedorn, P.H., Larsen, N.B., Flyvbjerg, H., 2005. Cell Motility as Persistent Random Motion: Theories from Experiments. Biophys J 89, 912–931. https://doi.org/10.1529/biophysj.105.061150

Sens, P., Plastino, J., 2015. Membrane tension and cytoskeleton organization in cell motility. J Phys Condens Matter 27, 273103. https://doi.org/10.1088/0953-8984/27/27/273103

Servant, G., Weiner, O.D., Neptune, E.R., Sedat, J.W., Bourne, H.R., 1999. Dynamics of a Chemoattractant Receptor in Living Neutrophils during Chemotaxis. Mol Biol Cell 10, 1163–1178.

Sha'afi, R.I., Molski, T.F.P., 1988. Activation of the Neutrophil (Part 1 of 4). Membrane Activation in Immunologically Relevant Cells 42, 1–16. https://doi.org/10.1159/000318681

Sheetz, M.P., Sable, J.E., Döbereiner, H.-G., 2006. Continuous membrane-cytoskeleton adhesion requires continuous accommodation to lipid and cytoskeleton dynamics. Annu. Rev. Biophys. Biomol. Struct. 35, 417–434. https://doi.org/10.1146/annurev.biophys.35.040405.102017

Shekhar, S., Pernier, J., Carlier, M.-F., 2016. Regulators of actin filament barbed ends at a glance. J Cell Sci 129, 1085–1091. https://doi.org/10.1242/jcs.179994

Shi, Z., Graber, Z.T., Baumgart, T., Stone, H.A., Cohen, A.E., 2018. Cell Membranes Resist Flow. Cell 175, 1769-1779.e13. https://doi.org/10.1016/j.cell.2018.09.054

Shutova, M.S., Svitkina, T.M., 2018. Mammalian nonmuscle myosin II comes in three flavors. Biochem. Biophys. Res. Commun. 506, 394–402. https://doi.org/10.1016/j.bbrc.2018.03.103

Sinha, B., Köster, D., Ruez, R., Gonnord, P., Bastiani, M., Abankwa, D., Stan, R.V., Butler-Browne, G., Vedie, B., Johannes, L., Morone, N., Parton, R.G., Raposo, G., Sens, P., Lamaze, C., Nassoy, P., 2011. Cells Respond to Mechanical Stress by Rapid Disassembly of Caveolae. Cell 144, 402–413. https://doi.org/10.1016/j.cell.2010.12.031

Skruber, K., Read, T.-A., Vitriol, E.A., 2018. Reconsidering an active role for G-actin in cytoskeletal regulation. J Cell Sci 131. https://doi.org/10.1242/jcs.203760

Small, J.V., 1981. Organization of actin in the leading edge of cultured cells: influence of osmium tetroxide and dehydration on the ultrastructure of actin meshworks. J. Cell Biol. 91, 695–705. https://doi.org/10.1083/jcb.91.3.695

Soares e Silva, M., Depken, M., Stuhrmann, B., Korsten, M., MacKintosh, F.C., Koenderink, G.H., 2011. Active multistage coarsening of actin networks driven by myosin motors. PNAS 108, 9408–9413. https://doi.org/10.1073/pnas.1016616108

Solinet, S., Mahmud, K., Stewman, S.F., Ben El Kadhi, K., Decelle, B., Talje, L., Ma, A., Kwok, B.H., Carreno, S., 2013. The actin-binding ERM protein Moesin binds to and stabilizes microtubules at the cell cortex. J Cell Biol 202, 251–260. https://doi.org/10.1083/jcb.201304052

Somlyo, A.P., Somlyo, A.V., 2003. Ca2+ sensitivity of smooth muscle and nonmuscle myosin II: modulated by G proteins, kinases, and myosin phosphatase. Physiol. Rev. 83, 1325–1358. https://doi.org/10.1152/physrev.00023.2003

Sonal, S., Ganzinger, K.A., Vogel, S.K., Mücksch, J., Blumhardt, P., Schwille, P., 2018. Myosin-II activity generates a dynamic steady state with continuous actin turnover in a minimal actin cortex. J. Cell. Sci. 132. https://doi.org/10.1242/jcs.219899

Sorce, B., Escobedo, C., Toyoda, Y., Stewart, M.P., Cattin, C.J., Newton, R., Banerjee, I., Stettler, A., Roska, B., Eaton, S., Hyman, A.A., Hierlemann, A., Müller, D.J., 2015. Mitotic cells contract actomyosin cortex and generate pressure to round against or escape epithelial confinement. Nat Commun 6. https://doi.org/10.1038/ncomms9872

Srinivasan, S., Wang, F., Glavas, S., Ott, A., Hofmann, F., Aktories, K., Kalman, D., Bourne, H.R., 2003. Rac and Cdc42 play distinct roles in regulating PI(3,4,5)P3 and polarity during neutrophil chemotaxis. J. Cell Biol. 160, 375–385. https://doi.org/10.1083/jcb.200208179

Srivastava, N., Traynor, D., Piel, M., Kabla, A.J., Kay, R.R., 2020. Pressure sensing through Piezo channels controls whether cells migrate with blebs or pseudopods. Proc. Natl. Acad. Sci. U.S.A. 117, 2506–2512. https://doi.org/10.1073/pnas.1905730117

Stankevicins, L., Ecker, N., Terriac, E., Maiuri, P., Schoppmeyer, R., Vargas, P., Lennon-Duménil, A.-M., Piel, M., Qu, B., Hoth, M., Kruse, K., Lautenschläger, F., 2020. Deterministic actin waves as generators of cell polarization cues. Proc Natl Acad Sci USA 117, 826–835. https://doi.org/10.1073/pnas.1907845117

Stauffer, D., Aharony, A., Aharony, A., 1994. Introduction To Percolation Theory: Second Edition. Taylor & Francis. https://doi.org/10.1201/9781315274386

Stramer, B.M., Dunn, G.A., 2015. Cells on film - the past and future of cinemicroscopy. Journal of Cell Science 128, 9–13. https://doi.org/10.1242/jcs.165019

Suarez, C., Carroll, R.T., Burke, T.A., Christensen, J.R., Bestul, A.J., Sees, J.A., James, M.L., Sirotkin, V., Kovar, D.R., 2015. Profilin Regulates F-Actin Network Homeostasis by Favoring Formin over Arp2/3 Complex. Developmental Cell 32, 43–53. https://doi.org/10.1016/j.devcel.2014.10.027

Sugiyama, T., Pramanik, Md.K., Yumura, S., 2015. Microtubule-Mediated Inositol Lipid Signaling Plays Critical Roles in Regulation of Blebbing. PLoS One 10. https://doi.org/10.1371/journal.pone.0137032

Svitkina, T.M., Verkhovsky, A.B., McQuade, K.M., Borisy, G.G., 1997. Analysis of the Actin–Myosin II System in Fish Epidermal Keratocytes: Mechanism of Cell Body Translocation. J Cell Biol 139, 397–415. https://doi.org/10.1083/jcb.139.2.397

Swaney, K.F., Huang, C.-H., Devreotes, P.N., 2010. Eukaryotic Chemotaxis: A Network of Signaling Pathways Controls Motility, Directional Sensing, and Polarity. Annual Review of Biophysics 39, 265–289. https://doi.org/10.1146/annurev.biophys.093008.131228

Symposium on Locomotion of Tissue Cells, 1973. Locomotion of tissue cells. Elsevier, Amsterdam; New York.

Szent-Györgyi, A., 1942. The contraction of myosin threads. Stud. Inst. Med.Chem. Univ. Szeged., I :17 –26.

Szent-Györgyi, A.G., 1968. The role of actin-myosin interaction in contraction. Symp. Soc. Exp. Biol. 22, 17–42.

Taloni, A., Kardash, E., Salman, O.U., Truskinovsky, L., Zapperi, S., La Porta, C.A.M., 2015. Volume Changes During Active Shape Fluctuations in Cells. Phys. Rev. Lett. 114, 208101. https://doi.org/10.1103/PhysRevLett.114.208101

Tan, T.H., Malik-Garbi, M., Abu-Shah, E., Li, J., Sharma, A., MacKintosh, F.C., Keren, K., Schmidt, C.F., Fakhri, N., 2018. Self-organized stress patterns drive state transitions in actin cortices. Sci. Adv. 4, eaar2847. https://doi.org/10.1126/sciadv.aar2847

Taneja, N., Burnette, D.T., 2019. Myosin IIA drives membrane bleb retraction. Mol. Biol. Cell 30, 1051–1059. https://doi.org/10.1091/mbc.E18-11-0752

Taylor, D.L., Condeelis, J.S., Moore, P.L., Allen, R.D., 1973. THE CONTRACTILE BASIS OF AMOEBOID MOVEMENT. J Cell Biol 59, 378–394.

te Boekhorst, V., Preziosi, L., Friedl, P., 2016. Plasticity of Cell Migration In Vivo and In Silico. Annu. Rev. Cell Dev. Biol. 32, 491–526. https://doi.org/10.1146/annurev-cellbio-111315-125201

Teixeira, A.I., Abrams, G.A., Bertics, P.J., Murphy, C.J., Nealey, P.F., 2003. Epithelial contact guidance on well-defined micro- and nanostructured substrates. Journal of Cell Science 116, 1881–1892. https://doi.org/10.1242/jcs.00383

Theriot, J.A., Mitchison, T.J., Tilney, L.G., Portnoy, D.A., 1992. The rate of actin-based motility of intracellular Listeria monocytogenes equals the rate of actin polymerization. Nature 357, 257–260. https://doi.org/10.1038/357257a0

Thoresen, T., Lenz, M., Gardel, M.L., 2011. Reconstitution of Contractile Actomyosin Bundles. Biophysical Journal 100, 2698–2705. https://doi.org/10.1016/j.bpj.2011.04.031

Tibes, U., Hinder, M., Scheuer, W., Friebe, W.G., Schramm, S., Kaiser, B., 1999. Phospholipase A2 is involved in chemotaxis of human leukocytes. Adv. Exp. Med. Biol. 469, 189–197. https://doi.org/10.1007/978-1-4615-4793-8_29

Tickle, C., Trinkaus, J.P., 1977. Some clues as to the formation of protrusions by Fundulus deep cells. J. Cell. Sci. 26, 139–150.

Tinevez, J.-Y., Schulze, U., Salbreux, G., Roensch, J., Joanny, J.-F., Paluch, E., 2009. Role of cortical tension in bleb growth. Proceedings of the National Academy of Sciences 106, 18581–18586. https://doi.org/10.1073/pnas.0903353106

Tjhung, E., Marenduzzo, D., Cates, M.E., 2012. Spontaneous symmetry breaking in active droplets provides a generic route to motility. Proceedings of the National Academy of Sciences 109, 12381–12386. https://doi.org/10.1073/pnas.1200843109

Toriyama, M., Shimada, T., Kim, K.B., Mitsuba, M., Nomura, E., Katsuta, K., Sakumura, Y., Roepstorff, P., Inagaki, N., 2006. Shootin1: a protein involved in the organization of an asymmetric signal for neuronal polarization. J Cell Biol 175, 147–157. https://doi.org/10.1083/jcb.200604160

Totsukawa, G., Yamakita, Y., Yamashiro, S., Hartshorne, D.J., Sasaki, Y., Matsumura, F., 2000. Distinct Roles of Rock (Rho-Kinase) and Mlck in Spatial Regulation of Mlc Phosphorylation for Assembly of Stress Fibers and Focal Adhesions in 3t3 Fibroblasts. J Cell Biol 150, 797–806.

Trinkaus, J.P., 1973. Modes of Cell Locomotion in vivo, in: Ciba Foundation Symposium 14 - Locomotion of Tissue Cells. John Wiley & Sons, Ltd, pp. 233–249. https://doi.org/10.1002/9780470719978.ch11

Tseng, Q., 2011. Etude d'architecture multicellulaire avec le microenvironnement contrôlé (phdthesis). Université de Grenoble.

Tseng, Q., Duchemin-Pelletier, E., Deshiere, A., Balland, M., Guillou, H., Filhol, O., Théry, M., 2012. Spatial organization of the extracellular matrix regulates cell–cell junction positioning. PNAS. https://doi.org/10.1073/pnas.1106377109

Tseng, Y., Kole, T.P., Lee, J.S.H., Fedorov, E., Almo, S.C., Schafer, B.W., Wirtz, D., 2005. How actin crosslinking and bundling proteins cooperate to generate an

enhanced cell mechanical response. Biochemical and Biophysical Research Communications 334, 183–192. https://doi.org/10.1016/j.bbrc.2005.05.205
Turing, A.M., 1952. The Chemical Basis of Morphogenesis. Philosophical Transactions of the Royal Society of London. Series B, Biological Sciences 237, 37–72.
Ullo, M.F., Logue, J.S., 2018. Re-thinking preclinical models of cancer metastasis. Oncoscience 5, 9–10.
Valon, L., Marín-Llauradó, A., Wyatt, T., Charras, G., Trepat, X., 2017. Optogenetic control of cellular forces and mechanotransduction. Nature Communications 8, 14396. https://doi.org/10.1038/ncomms14396
van Haastert, P.J., Konijn, T.M., 1982. Signal transduction in the cellular slime molds. Mol. Cell. Endocrinol. 26, 1–17. https://doi.org/10.1016/0303-7207(82)90002-8
van Haastert, P.J.M., Keizer-Gunnink, I., Kortholt, A., 2007. Essential role of PI3-kinase and phospholipase A2 in Dictyostelium discoideum chemotaxis. J. Cell Biol. 177, 809–816. https://doi.org/10.1083/jcb.200701134
Vavylonis, D., Yang, Q., O'Shaughnessy, B., 2005. Actin polymerization kinetics, cap structure, and fluctuations. Proceedings of the National Academy of Sciences 102, 8543–8548. https://doi.org/10.1073/pnas.0501435102
Veltman, D.M., Keizer-Gunnik, I., Van Haastert, P.J.M., 2008. Four key signaling pathways mediating chemotaxis in Dictyostelium discoideum. J Cell Biol 180, 747–753. https://doi.org/10.1083/jcb.200709180
Venkova, L., 2019. Cell volume regulation in response to deformations (phdthesis). Université Paris-Saclay.
Venturini, V., Pezzano, F., Castro, F.C., Häkkinen, H.-M., Jiménez-Delgado, S., Colomer-Rosell, M., Marro, M., Tolosa-Ramon, Q., Paz-López, S., Valverde, M.A., Weghuber, J., Loza-Alvarez, P., Krieg, M., Wieser, S., Ruprecht, V., 2020. The nucleus measures shape changes for cellular proprioception to control dynamic cell behavior. Science 370. https://doi.org/10.1126/science.aba2644
Venturini, V., Pezzano, F., Castro, F.C., Häkkinen, H.-M., Jiménez-Delgado, S., Colomer-Rosell, M., Sánchez, M.M., Tolosa-Ramon, Q., Paz-López, S., Valverde, M.A., Loza-Alvarez, P., Krieg, M., Wieser, S., Ruprecht, V., 2019. The nucleus measures shape deformation for cellular proprioception and regulates adaptive morphodynamics. bioRxiv 865949. https://doi.org/10.1101/865949
Verkhovsky, A.B., Svitkina, T.M., Borisy, G.G., 1999. Self-polarization and directional motility of cytoplasm. Current Biology 9, 11-S1. https://doi.org/10.1016/S0960-9822(99)80042-6
Verkhovsky, A.B., Svitkina, T.M., Borisy, G.G., 1995. Myosin II filament assemblies in the active lamella of fibroblasts: their morphogenesis and role in the formation of actin filament bundles. J. Cell Biol. 131, 989–1002. https://doi.org/10.1083/jcb.131.4.989
Vicker, M.G., 2002. Eukaryotic Cell Locomotion Depends on the Propagation of Self-Organized Reaction–Diffusion Waves and Oscillations of Actin Filament Assembly. Experimental Cell Research 275, 54–66. https://doi.org/10.1006/excr.2001.5466
Vignaud, T., Copos, C., Leterrier, C., Tseng, Q., Blanchoin, L., Mogilner, A., Théry, M., Kurzawa, L., 2020. Stress fibers are embedded in a contractile cortical network. bioRxiv 2020.02.11.944579. https://doi.org/10.1101/2020.02.11.944579
Vogel, S.K., Petrasek, Z., Heinemann, F., Schwille, P., 2013. Myosin motors fragment and compact membrane-bound actin filaments. eLife 2, e00116. https://doi.org/10.7554/eLife.00116

Vogel, S.K., Wölfer, C., Ramirez-Diaz, D.A., Flassig, R.J., Sundmacher, K., Schwille, P., 2020. Symmetry Breaking and Emergence of Directional Flows in Minimal Actomyosin Cortices. Cells 9. https://doi.org/10.3390/cells9061432
Wagner, A.R., Luan, Q., Liu, S.-L., Nolen, B.J., 2013. WISH/DIP/SPIN90 proteins form a class of Arp2/3 complex activators that function without preformed actin filaments. Curr Biol 23, 1990–1998. https://doi.org/10.1016/j.cub.2013.08.029
Wang, X., Kress, A., Brasselet, S., Ferrand, P., 2013. High frame-rate fluorescence confocal angle-resolved linear dichroism microscopy. Rev Sci Instrum 84, 053708. https://doi.org/10.1063/1.4807318
Wang, Y., Chen, C.-L., Iijima, M., 2011. Signaling Mechanisms for Chemotaxis. Dev Growth Differ 53, 495–502. https://doi.org/10.1111/j.1440-169X.2011.01265.x
Wedlich-Soldner, R., Altschuler, S., Wu, L., Li, R., 2003. Spontaneous cell polarization through actomyosin-based delivery of the Cdc42 GTPase. Science 299, 1231–1235. https://doi.org/10.1126/science.1080944
Weigelin, B., Bakker, G.-J., Friedl, P., 2012. Intravital third harmonic generation microscopy of collective melanoma cell invasion: Principles of interface guidance and microvesicle dynamics. IntraVital 1, 32–43. https://doi.org/10.4161/intv.21223
Weiner, O.D., Marganski, W.A., Wu, L.F., Altschuler, S.J., Kirschner, M.W., 2007. An Actin-Based Wave Generator Organizes Cell Motility. PLOS Biology 5, e221. https://doi.org/10.1371/journal.pbio.0050221
Weiner, O.D., Neilsen, P.O., Prestwich, G.D., Kirschner, M.W., Cantley, L.C., Bourne, H.R., 2002. A PtdInsP(3)- and Rho GTPase-mediated positive feedback loop regulates neutrophil polarity. Nat. Cell Biol. 4, 509–513. https://doi.org/10.1038/ncb811
Weiner, O.D., Rentel, M.C., Ott, A., Brown, G.E., Jedrychowski, M., Yaffe, M.B., Gygi, S.P., Cantley, L.C., Bourne, H.R., Kirschner, M.W., 2006. Hem-1 Complexes Are Essential for Rac Activation, Actin Polymerization, and Myosin Regulation during Neutrophil Chemotaxis. PLOS Biology 4, e38. https://doi.org/10.1371/journal.pbio.0040038
Weiss, P., 1945. Experiments on cell and axon orientation in vitro: The role of colloidal exudates in tissue organization. J. Exp. Zool. 100, 353–386. https://doi.org/10.1002/jez.1401000305
Weiss, P., 1934. In vitro experiments on the factors determining the course of the outgrowing nerve fiber. Journal of Experimental Zoology 68, 393–448. https://doi.org/10.1002/jez.1400680304
Weisswange, I., Bretschneider, T., Anderson, K.I., 2005. The leading edge is a lipid diffusion barrier. Journal of Cell Science 118, 4375–4380. https://doi.org/10.1242/jcs.02551
Welch, M.D., Mullins, R.D., 2002. Cellular Control of Actin Nucleation. Annual Review of Cell and Developmental Biology 18, 247–288. https://doi.org/10.1146/annurev.cellbio.18.040202.112133
Welch, M.D., Way, M., 2013. Arp2/3-mediated actin-based motility: a tail of pathogen abuse. Cell Host Microbe 14, 242–255. https://doi.org/10.1016/j.chom.2013.08.011
Welf, E.S., Driscoll, M.K., Sapoznik, E., Murali, V.S., Weems, A., Roh-Johnson, M., Dean, K.M., Fiolka, R., Danuser, G., 2020. Worrying drives cell migration in mechanically unrestrained environments. bioRxiv 2020.11.09.372912. https://doi.org/10.1101/2020.11.09.372912
Welf, E.S., Miles, C.E., Huh, J., Driscoll, M.K., Isogai, T., Noh, J., Weems, A.D., Chi, J., Pohlkamp, T., Dean, K., Fiolka, R., Mogilner, A., Danuser, G., 2019. A unified role

for membrane-cortex detachment during cell protrusion initiation (preprint). Cell Biology. https://doi.org/10.1101/696211
Wessels, D., Soll, D.R., Knecht, D., Loomis, W.F., De Lozanne, A., Spudich, J., 1988. Cell motility and chemotaxis in Dictyostelium amebae lacking myosin heavy chain. Dev. Biol. 128, 164–177. https://doi.org/10.1016/0012-1606(88)90279-5
Wilson, C.A., Tsuchida, M.A., Allen, G.M., Barnhart, E.L., Applegate, K.T., Yam, P.T., Ji, L., Keren, K., Danuser, G., Theriot, J.A., 2010. Myosin II contributes to cell-scale actin network treadmilling via network disassembly. Nature 465, 373–377. https://doi.org/10.1038/nature08994
Wintrebert, P., 1931. La rotation immédiate de l'oeuf pondu et la rotation d'activation chez Discoglossus pictus Otth. C. R. Soc. Biol. 106, 439-442. 2.
Wolf, K., Mazo, I., Leung, H., Engelke, K., von Andrian, U.H., Deryugina, E.I., Strongin, A.Y., Bröcker, E.-B., Friedl, P., 2003. Compensation mechanism in tumor cell migration mesenchymal–amoeboid transition after blocking of pericellular proteolysis. J Cell Biol 160, 267–277. https://doi.org/10.1083/jcb.200209006
Wollrab, V., Belmonte, J.M., Baldauf, L., Leptin, M., Nédeléc, F., Koenderink, G.H., 2019. Polarity sorting drives remodeling of actin-myosin networks. J Cell Sci 132, jcs219717. https://doi.org/10.1242/jcs.219717
Xiong, Y., Huang, C.-H., Iglesias, P.A., Devreotes, P.N., 2010. Cells navigate with a local-excitation, global-inhibition-biased excitable network. PNAS 107, 17079–17086. https://doi.org/10.1073/pnas.1011271107
Xu, B., Kang, H.-W., Jilkine, A., 2019. Comparison of Deterministic and Stochastic Regime in a Model for Cdc42 Oscillations in Fission Yeast. Bull. Math. Biol. 81, 1268–1302. https://doi.org/10.1007/s11538-019-00573-5
Yam, P.T., Wilson, C.A., Ji, L., Hebert, B., Barnhart, E.L., Dye, N.A., Wiseman, P.W., Danuser, G., Theriot, J.A., 2007. Actin–myosin network reorganization breaks symmetry at the cell rear to spontaneously initiate polarized cell motility. J Cell Biol 178, 1207–1221. https://doi.org/10.1083/jcb.200706012
Yamada, K.M., Sixt, M., 2019. Mechanisms of 3D cell migration. Nature Reviews Molecular Cell Biology 20, 738–752. https://doi.org/10.1038/s41580-019-0172-9
Yanai, M., Kenyon, C.M., Butler, J.P., Macklem, P.T., Kelly, S.M., 1996. Intracellular pressure is a motive force for cell motion in Amoeba proteus. Cell Motility 33, 22–29. https://doi.org/10.1002/(SICI)1097-0169(1996)33:1<22::AID-CM3>3.0.CO;2-K
Yip, A.K., Chiam, K.-H., Matsudaira, P., 2015. Traction stress analysis and modeling reveal that amoeboid migration in confined spaces is accompanied by expansive forces and requires the structural integrity of the membrane–cortex interactions. Integr. Biol. 7, 1196–1211. https://doi.org/10.1039/C4IB00245H
Yolland, L., Burki, M., Marcotti, S., Luchici, A., Kenny, F.N., Davis, J.R., Serna-Morales, E., Müller, J., Sixt, M., Davidson, A., Wood, W., Schumacher, L.J., Endres, R.G., Miodownik, M., Stramer, B.M., 2019. Persistent and polarized global actin flow is essential for directionality during cell migration. Nat Cell Biol 21, 1370–1381. https://doi.org/10.1038/s41556-019-0411-5
Yoshida, K., Soldati, T., 2006. Dissection of amoeboid movement into two mechanically distinct modes. J. Cell. Sci. 119, 3833–3844. https://doi.org/10.1242/jcs.03152
Yu, Q., Li, J., Murrell, M.P., Kim, T., 2018. Balance between Force Generation and Relaxation Leads to Pulsed Contraction of Actomyosin Networks. Biophysical Journal 115, 2003–2013. https://doi.org/10.1016/j.bpj.2018.10.008

Zatulovskiy, E., Tyson, R., Bretschneider, T., Kay, R.R., 2014. Bleb-driven chemotaxis of Dictyostelium cells. The Journal of Cell Biology 204, 1027–1044. https://doi.org/10.1083/jcb.201306147

Zhao, X., Lei, Y., Zheng, J., Peng, J., Li, Y., Yu, L., Chen, Y., 2019. Identification of markers for migrasome detection. Cell Discov 5, 1–4. https://doi.org/10.1038/s41421-019-0093-y

Part VII: Annexes

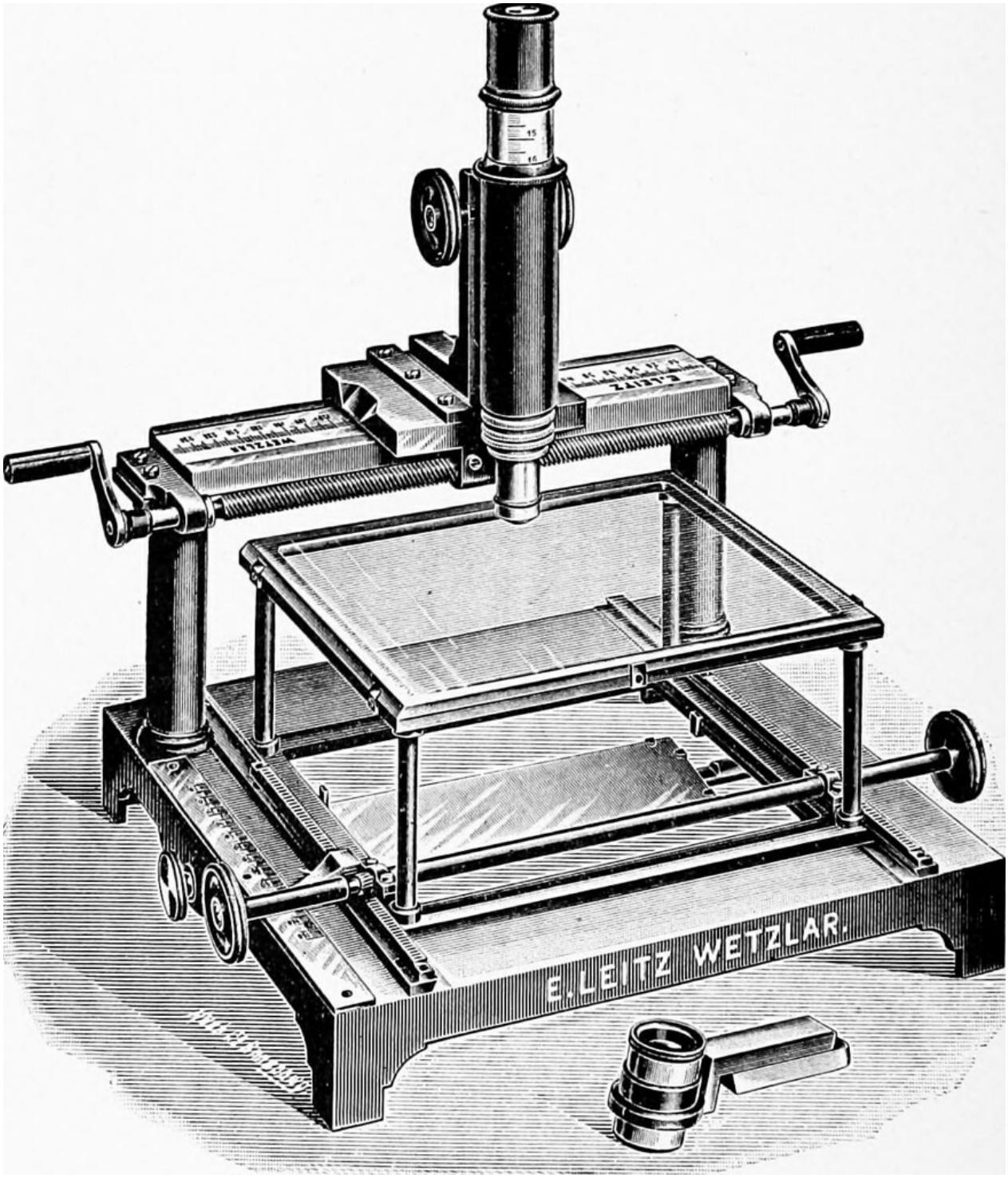

Chapter 14: History of science. Standing on the shoulders of giants

Isaac Newton wrote in 1675: "If I have seen further it is by standing on the shoulders of Giants". This expression was first attributed to Bernard de Chartres (Latin: Bernardus Carnotensis) and means that our intellectual progress is based on the understanding gained by major thinkers in the past. Whereas it is extremely difficult to trace all intellectual roots to the ideas I use in this manuscript, I want to mention a few which I hold with high regard.

Early research on single-cell migration

We start the journey in the times of Newton, with Robert Hooke (1635-1703). He used compound microscopes with two convex lenses to describe biological samples. Hooke coined the word “cell” for the first time after he observed **cork** and published a book called “*Micrographia: or Some Physiological Descriptions of Minute Bodies Made by Magnifying Glasses. With Observations and Inquiries Thereupon*”. Published in January 1665, the first major publication of the Royal Society, it became the first scientific best-seller. Antonie van Leeuwenhoek (1632-1723) was a Dutch businessman and scientist from Delft who made extensive descriptions of microbial life with his single-lensed microscope. He disputes Hooke the title of being the first to observe cells. His design consisted of **a small glass bead that could achieve up to 300x magnification**. The same idea was taken by some modern devices, such as the Foldscope, a simple low-cost optical microscope that can be assembled from a sheet of plasticized paper and a small spherical lens. Microscopes did not improve significantly until the 19th century and the work of Carl Zeiss (1816-1888), Otto Schott, and Ernst Abbe (1840-1905) in Germany. Meanwhile, the cell theory started to achieve consensus thanks to the work of Theodor Schwann, Matthias Jakob Schleiden, Robert Remak, Rudolf Virchow, Albert Kolliker, Santiago Ramón y Cajal, and many others.

Jacques Loeb (1859-1924) was a German-born American physiologist and biologist, a pioneer in the field of cell migration. Loeb moved to the US in 1891 and the University of Chicago in 1892 as an assistant professor of physiology and experimental biology, while later becoming an associate professor in 1895 and professor of physiology in 1899. During these years he began spending summers at the MBL in Woods Hole, where he demonstrated in 1899 artificial parthenogenesis in sea urchin eggs. His lecture notes from Woods Hole describe his observation of bleb formation upon hypotonic shock, or the **migration of single pigmented epithelial cells in *Fundulus* embryonic yolk sac**

(Loeb, 1898, 1893). Since the embryo was transparent and the cells were black and red, he could describe the migration, attracted by blood vessels, that gives rise to its distinctive tiger stripes pattern (**Figure 53**). He described a similar process happening in the rest of the embryo later, similar to that in the yolk sac. Jacques Loeb became a well-known scientist and left a mark over a generation of biologists (Osterhout, 2011; Pauly, 1987).

Amoebae were from the beginning a popular model organism for cell migration, due to its size and easy culture. **The term "amoeboid movement" was common in the scientific literature at the turn of the century**. Gibbs and Dellinger, from Carnegie institution, described in 1908 the "*daily life of Amoeba"* in a journal dedicated to psychology. They mention that amoeba is *"the best-studied animal and other colleagues in zoology, biology […] find it convenient to start with Amoeba*" (Gibbs and Dellinger, 1908). They observed *Amoeba proteus* and proposed a walking locomotion mechanism where the motion is driven by a **contractile layer called the *ectoplasm*, which we would nowadays call the cortex** (**Figure 54**). Jennings observed particles of carmine adhered to the surface (**Figure 54**) and proposed that forward ectoplasm flow is the main driver for migration (Jennings, 1904). Older models from Berthold (1886), Butschili (1894), and Rhumbler (1898) proposed a fountain flow from the endoplasm (cytosol) to the ectoplasm (cortex), by which the endoplasm will have a sol-gel transition and create new ectoplasm in the front of the cell. Inspiration from this model came from the forward cytoplasmic flow observed in amoeba. The quantitative work of the American scientist Asa Arthur Schaeffer (Schaeffer, 1920) also marked a modern precedent.

Figure 53: Stages of migration of single pigmented epithelial cells in Fundulus embryonic yolk sac. *From left to right: pigmented epithelial cells gradually become more restricted to blood vessels, actively migrating towards them. At the end of the process, cells cover so well the vessels that they are indistinguishable, only for the color. Jacques Loeb. Biological lectures delivered at the Marine Biological Laboratory of Woods Hole 1898 (6). Boston, Ginn and co.*

A pioneer in the use of video microscopy for research was Jean Comandon, who developed the technique to film syphilis bacteria as part of his doctoral thesis at Institut Pasteur in 1909. However, it remained for a long time used just for vulgarization purposes, not as a means to gather qualitative or quantitative data. **Early works on microscopy and cell migration were done primarily in fish embryos at marine biology centers such as station Biologique de Roscoff** in northern France **or Marine Biological Laboratory (MBL)** at Woods Hole in Cape Cod, US. At that time, it was much easier to work with marine samples, since their growth conditions were known better, and it was easy to gather new specimens. It was not until later, when mammalian cell culture was discovered and improved that the first movies of mammalian cells started to be produced, often coming from chick or rabbit embryos.

Mammalian cell culture was developed in the early 20th century by Ross G. Harrison (Yale University), Alexis Carrel (Rockefeller Institute of Medical Research), and Montrose T. Burrows (also at Rockefeller). Harrison was one of the first to experiment with substrates of different topology and discovered what we call today contact guidance. He **plated chick embryonic cells onto cellulose fibers or spider webs and described how cells move and adhere parallel to these structures.** (Harrison, 1914, 1911). In parallel, Carrel and Burrows also did similar experiments with embryonic and tumor

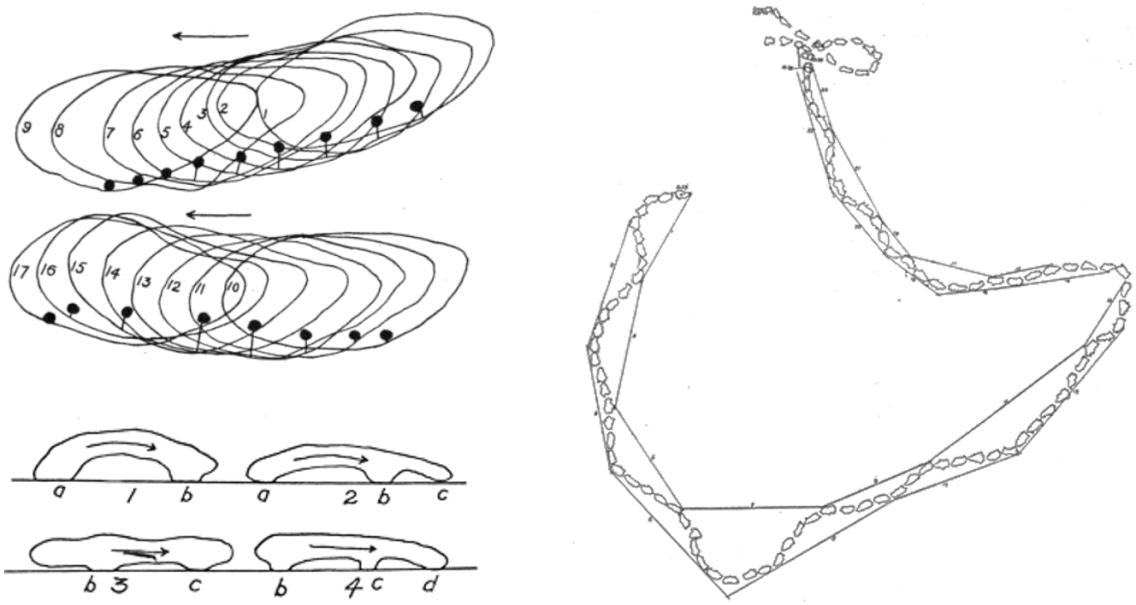

Figure 54: Description of the migration of Amoeba. *Left top: illustration of the cortical flows in Amoeba sphaeronucleosus. The forward surface flow is higher in the middle of the amoeba than on the edge. Left bottom: illustration of the movements of Amoeba proteus, with characteristic protrusion-adhesion cycles. Right: trajectory analysis of Amoeba bigemma. The author notes the regular waves that describe the trajectory of the cell. Extracted from Gibbs and Dellinger 1908 and Jennings 1904.*

tissues (Carrel and Burrows, 1911). Paul Weiss, a collaborator of Harrison from the University of Chicago who went to New York to work with him, described electrical, physical or topological, and chemical factors determining the growth of sectioned nerve fibers from brain fragments or spinal ganglia of chick embryos (Weiss, 1945, 1934).

Alexis Carrel's lab was a pioneer in mammalian cell culture combined with filming and published a methods article in *Science* in 1929 describing the technique (**Figure 55**). The person who produced Carrel's movies was his technical assistant, Heinz Rosenberger, who later kept working on the subject and tried to convince scientists *''who have not yet realized the great possibilities of the motion-picture camera in research laboratories''* (Carrel and Ebeling, 1926; Rosenberger, 1929a, 1929b). Researchers, later on, started to realize of its potential to extract quantitative information from these movies, such as the embryologist Warren Lewis or the pioneer Ronald Canti, a pathologist who worked at St Bartholomew's Hospital in London. **Canti used videos to address experimental questions related to the effect of radiation in cells** and made a series of videos named 'The Cultivation of Living Tissue', which became famous even outside academic

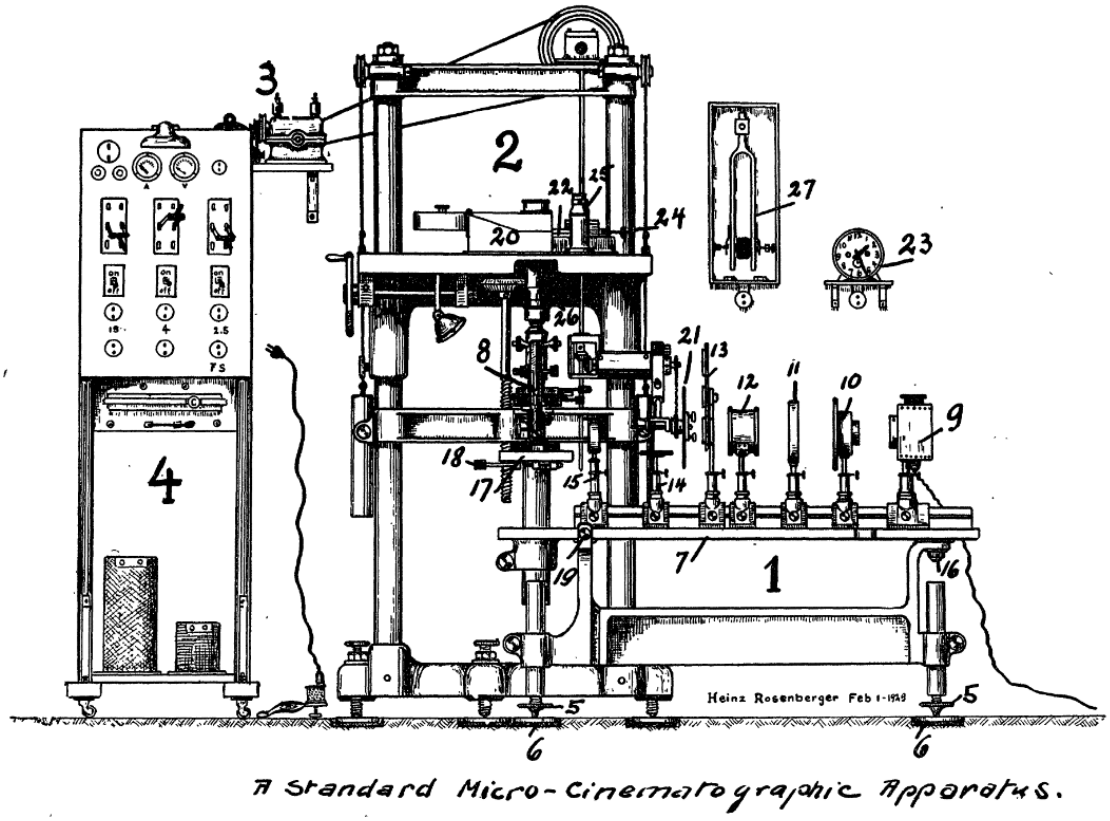

Figure 55: A standard microcinematographic apparatus. *First published design of a video microscope by Heinz Rosenberger, published on the journal* Science *on June 28th,1929.*

environments. Remarkably, Canti received funding from the parent foundation of what is nowadays Cancer Research UK to develop his technique. Canti passed away in 1936 leaving an extensive oeuvre of films that are nowadays remastered and published on YouTube by the Wellcome Trust (Stramer and Dunn, 2015).

Warren Lewis and colleagues from Carnegie Institution in Washington began experimenting with rabbit embryos in the late 1920s (Lewis and Gregory, 1929). Further development of tissue culture and microscopy allowed for the observation of much smaller cells, such as leucocytes. **Lewis proposed already in 1939 that leukocytes have, like amoebae, a "superficial layer of plasmagel" that provides forces for cell locomotion and division** (Bray and White, 1988). Around these years we find the first mention of the word "cytoskeleton" (*cytosquelette*) made by Paul Wintrebert, a French embryologist and a theoretician of developmental biology (Wintrebert, 1931).

After WWII, Michael Abercrombie (1912-1979), a British cell biologist and embryologist, emerged as one of the leading researchers in the field. Abercrombie's major contributions include the description of **contact inhibition in 1953** (Abercrombie and Heaysman,

	Chick cells		Mouse cells	
	Mean	S.D.	Mean	S.D.
Displacement, μm/min	0.60	0.32	0.68	0.61
Fluctuations/100 min	23	9	23	6
Protrusion distance, μm	5.3	1.6	6.0	1.9
Withdrawal distance, μm	3.6	1.0	4.1	0.5
% of time stationary	50	12	48	15
Speed while moving, protrusion, μm/min	5.0	1.4	5.0	0.8
Speed while moving withdrawal, μm/min	4.7	1.0	4.9	0.5
% of time moving forward	31	7	32	13
% of time moving backward	19	9	19	6

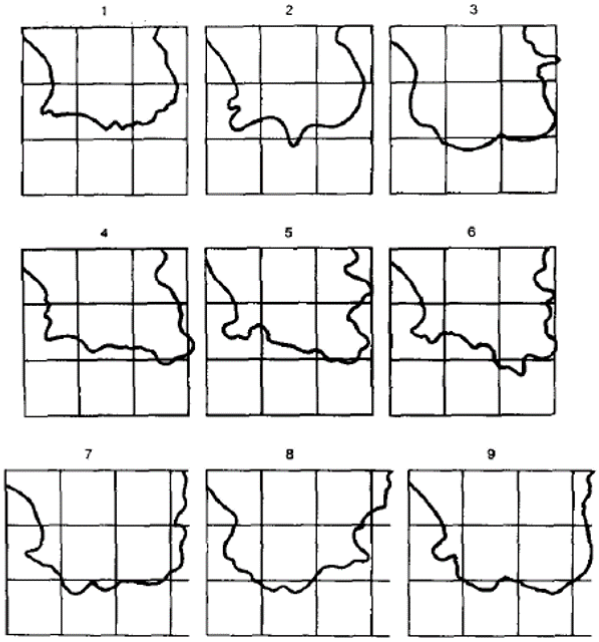

Figure 56: Study of leading edge dynamics in fibroblasts. *Left: Measurements, with standard deviations, on the leading edges of 13 chick heart and 7 mouse muscle fibroblast-like cells. Right: outline of the edge of a leading lamella at 30 seconds intervals. The superimposed grid is of squares of approximately 10μm sides. Adapted from Abercrombie, M., Heaysman, J.E.M., Pegrum, S.M., 1970. The locomotion of fibroblasts in culture I. Movements of the leading edge. Experimental Cell Research 59, 393–398.*

1953), which is the fact that cultured cells moving on a petri dish will halt if they come in contact with another, except for cancer cells. **Abercrombie is also well-known for his**

model of mesenchymal cell migration based on his observation of embryonic fibroblasts, in which he described the different steps in the process of locomotion: formation of lamellipodia, adhesion, displacement of the cell body, protrusion. He and his colleagues built the first comprehensive model of cell migration with a series of publications on “The locomotion of fibroblasts in culture” (Abercrombie et al., 1972, 1971, 1971, 1970a, 1970a, 1970c, 1970b). He also worked on the differences between collective and single-cell migration as well as on the chemotaxis of leukocytes (Keller et al., 1977). His beautiful work is characterized by an effort to quantitatively measure and represent cellular trajectories and edge dynamics (**Figure 56**). The collection of his movies is available online at the Wellcome Library YouTube channel surprises by the quality and resolution: even though they were taken 60 years ago with a standard 16-mm film they resemble what we obtain with the modern-day phase microscopes.

Michael Abercrombie chaired the first dedicated symposium on the subject in summer 1972 held at the Ciba Foundation in London (Symposium on Locomotion of Tissue Cells, 1973). This meeting gathered all the experts at that time working on the subject and laid the foundation for the modern, quantitative study of cell migration. The notes of the discussions of the meeting reveal that some current ideas in the field were already discussed at that time, like the complementarity of amoeboid versus mesenchymal migration, the influence of physical and chemical cues, the influences of genetic programs or cell differentiation in migration, and the role of blebs.

John Philip Trinkaus (1918-2003) an American embryologist and one of the world's leading experts on *in vivo* cell motility at his time, was also present at the 1972 symposium organized by Abercrombie. Like Jacques Loeb, **Trinkaus worked on the embryonic development of the fish *Fundulus heteroclitus***, taking advantage of its transparent shell and embryo and its epithelial pigmented cells. He spent many years performing his research at Marine Biological Laboratory, Woods Hole, Massachusetts, and the Station Marine, Roscoff. He was one of the first to precisely describe single-cell migration in vivo using modern video microscopy techniques (Trinkaus, 1973). Trinkaus was interested in the chemical and physical factors that guide cell migration in the developing organisms, where often cells need to migrate throughout the entire embryo efficiently. He also studied the movement of epithelial sheets *in vitro* and *in vivo* and contact inhibition of single cells. Some quotes from his presentation in 1972 seem incredibly relevant such as this one describing bleb-based migration “*cells seem to displace other cells by thrusting out blebs and flowing into them. Locomotion occurs us the bleb is forming, in the direction of the long axis of the cell, with the bleb leading the*

way". **Trinkaus recognized the effect of cell adhesion on cell migration, and the cooperation of blebs and lamellipodia,** which is something that only now is being established in the cell biology community: "*If it adheres weakly, the slight pull of an adhering bleb could be sufficient to displace it and the bleb would become an organ of locomotion. If the cell body adheres more firmly, it would not be displaced immediately and as a consequence the bleb might continue spreading against the substratum, forming a lamellipodium."*

Günter Albrecht-Bühler (Northwestern University Medical School, Chicago) was also present in that meeting. His seminal **work on cell biology and particularly on cell fragments** in the 1970s and 1980s opened a lot of questions of the nature of the different cell morphologies (e.g.: of "blebbing" versus "ruffling") and its biochemical regulation (Albrecht-Buehler, 1980). Cell fragments obtained from flushing cytochalasin B-treated human skin fibroblasts could display after recovery very different phenotypes (**Figure 57**). These cell fragments could show a blebbing phenotype with dynamic blebs on the surface of the cell retracting and protruding, a lamellipodia phenotype with dynamic ruffles, or stable filopodia fragments.

Albrecht-Bühler and colleagues hypothesized that these random fragments, which were about 2% of the total cell volume, inherited different molecular types of machinery from the cell. This argues that although a cell type often shows only one migration phenotype, it contains all the elements necessary for different migration modes. In their own words: "*The design of the cytoplasmic matrix is complex enough to sustain this variety of expressions of cell motility locally and autonomously*". Local heterogeneity is used in all

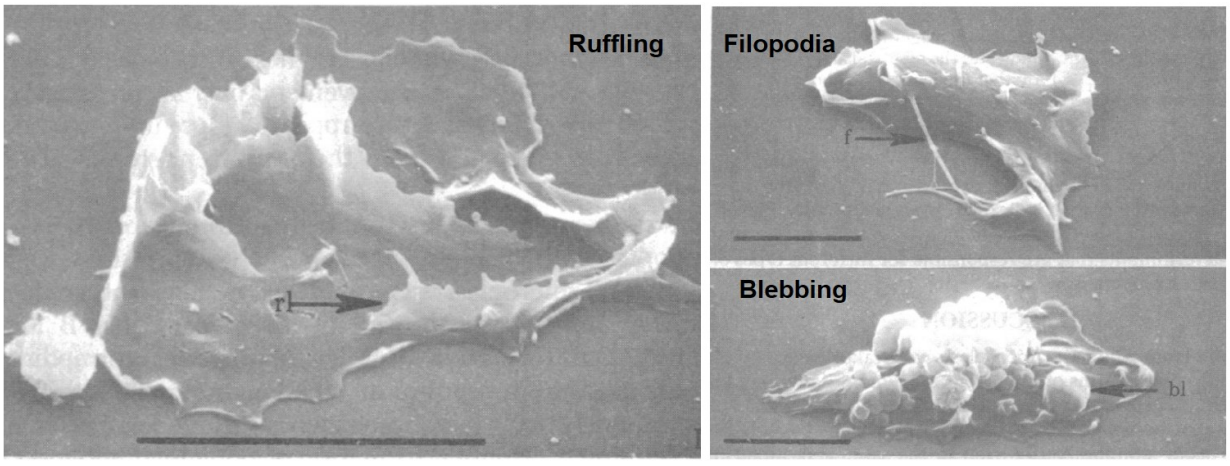

Figure 57: Morphology of fibroblasts fragments taken by electron microscopy replicas. *All scale bars = 5 µm. Adapted (labels added) from Albrecht-Buehler Proc. Natl. Acad. Sci. USA 1980.*

migrating cells to establish a front-back polarity. Without polarizing, cells would not be able to direct the motion in one direction. This experiment also shows that migration is an autonomous property of some parts of the cytoplasm and does not require a full cell at short timescales (hours). For example, confined blebbing cells can lose blebs that break away. Blebs would detach from the main body of the cell and migrate alone, recapitulating the same shape and dynamics of a whole cell (Liu et al., 2015). Similarly, keratocytes can spontaneously detach cytoplasmic fragments that move with speed, shape, and persistence similar to cells (Verkhovsky et al., 1999).

Later on, Albrecht-Bühler wrote an essay describing the ideas of the cell biology school he represented, titled “In Defense of “Nonmolecular” Cell Biology” (Albrecht-Buehler, 1990). He argued against the applicability of molecular explanations to whole-cell functions. His statements were a response to a time where cell biology was dominated by the extreme success of molecular biology and genetics and tried to highlight the role of biophysics and systems biology in a more holistic understanding of cell behavior.

Thanks to the cumulated work of these scientists and many others we can nowadays make our contributions and walk together towards a better understanding of nature. While reading all these inspiring works, some of them written more than a century ago, I often fell into the realization that **ideas are often born out of a scientific community, discussions, and from people walking on the shoulders of giants, and not from isolated minds.**

Chapter 15: Early works on cell polarity and chemotaxis

Mathematical basis of polarity and morphogenesis

The English and polymath Alan Turing wrote the founding ideas of biological polarity theory in a book named **"The chemical basis of morphogenesis" (Turing, 1952)**, just two years before his premature death. Inspired by previous work on morphogenesis from Sir **D'Arcy (1942)** and the enzymatic kinetics from **Michaelis and Menten (1913),** he proposed elegant models for pattern formation in complex systems. Nowadays, solutions of Turing-like reaction-diffusion equations are called Turing patterns. Emerging from initial homogeneous uniform states and varying different parameters, they can form fronts, hexagons, spirals, stripes, and rolling waves. Another pioneer was **Hans Meinhardt (1938-2016)**, a theoretical biologist that developed theories on morphogenesis with Alfred Gierer, inspired by oscillations and chemotaxis in the slime mold *Dictyostelium*. His work united two ideas of the field of cybernetics: that **positive feedback amplifies small deviations** in a range of systems from economy to embryogenesis, and the **importance of local activation and global inhibition** (Gierer and Meinhardt, 1972; Meinhardt and Gierer, 1974).

In their work, Meinhardt and Gierer **predicted well the pattern formation of a range of morphogenetic processes but lacked any precise molecular data on the origin of these patterns**. Compared to the work of Turing, they showed that only a certain class of reactions can give rise to patterns and only if the local autocatalysis/global inhibition condition is satisfied. They described the two possible ways systems with two components could self-organize: the **activator/inhibitor and** the **substrate-depletion models**. The activator/inhibitor model (equations 1 and 2) is composed of two substances: a, the short-range autocatalytic substance or the activator, and h, the long-range antagonist or inhibitor (abbreviation for *Hemmstoff*, inhibitor in German). The first equation describes the change of activator concentration over time. The first term on the right describes the production rate of the activator which depends in a non-linear fashion on the activator concentration (a^2) and is slowed down by the inhibitor ($1/h$). The next term represents the decay, which is proportional to a decay rate (μ_a) and the number of activator molecules present (a). The third term is the exchange of molecules which is assumed to happen by diffusion ($D_a\,\partial^2 a/\partial x^2$) and the last term is an activator-independent production of the activator, necessary to trigger autocatalysis at very low activator concentration (ρ_a). The second set describes in similar ways the inhibitor

dynamics. A low baseline production of the inhibitor ρ_h in equation 2 can lead to a stable non-patterned state that is “asleep” until the system is perturbed.

$$(Eq.1) \quad \frac{\partial a}{\partial t} = \rho \frac{a^2}{h} - \mu_a a + D_a \frac{\partial^2 a}{\partial x^2} + \rho_a \quad (Eq.2) \quad \frac{\partial h}{\partial t} = \rho a^2 - \mu_h h + D_h \frac{\partial^2 h}{\partial x^2} + \rho_h$$

The **substrate-depletion model is an alternative for the formation of such patterns without the presence of an inhibitor.** The long-range antagonistic effect can occur from the depletion of a substrate s that is consumed when the autocatalytic activator a is produced (equations 3 and 4). The substrate is produced everywhere with the same rate (δ). An important condition is that diffusion of the substrate must be much higher than that of the activator.

$$(Eq.3) \quad \frac{\partial a}{\partial t} = \rho s a^2 - \mu_a a + D_a \frac{\partial^2 a}{\partial x^2} + \rho_0 \quad (Eq.4) \quad \frac{\partial s}{\partial t} = \delta - \rho s a^2 - \mu_s s + D_s \frac{\partial^2 s}{\partial x^2}$$

A simple and elegant application of the substrate-depletion is pattern formation within a cell. Consider an activation autocatalytic process happening at the cell membrane from a cytoplasmic precursor. The precursor can freely diffuse in the cytoplasm but the activator is restricted to the membrane. In this case, the activator becomes restricted to only a part of the membrane. In other words, the cell polarizes. It is easy to argue that cytoplasmic molecules have a much higher diffusion coefficient than membrane-bound molecules, which would satisfy the condition for the substrate-depletion model.

Application of the LEGI model in chemotaxis

The context for early research on cell polarity was chemotaxis, even though nowadays the concepts from Meinhardt and Gierer, with modifications, are applied to explain polarity in many biological models: blebbing migration, embryogenesis, signaling waves, etc. In the 1980s, chemotactic factors and mechanisms began to be understood well, so it presented a good opportunity to investigate the signal transduction arising from the Meinhardt and Gierer model, termed also “**LEGI**” (**Local Excitation, Global Inhibition**). This **laid the foundations for the experimental application of these theories** into the fields of cell migration and cell polarity. Chemotaxis is the cell motion directed by an external chemical gradient. It has been reported for a wide range of eukaryotic cells: from neutrophils going towards inflammation sites to endothelial cells attracted by growth factors to rebuild tissues or fibroblasts migrating to wound sites to secrete and remodel extracellular matrix. Chemotaxis is indeed an excellent case to study cell polarity: cells

rapidly polarize or reorient their polarity axis according to external stimuli, which can be controlled experimentally in a spatiotemporal manner.

Mainly, two biological models were used: **leukocytes** and amoeba. On one hand, **neutrophils** migrate towards inflammation sites, and can be attracted by N-formylated peptides such as f-Met-Leu-Phe, leukotriene B4 (LTB4), platelet-activating factor, and a cleavage product of complement component 5 (C5a) (Sha'afi and Molski, 1988). On the other hand, the amoeba ***Dictyostelium discoideum*** is found in nature in soil or moist litter. It is attracted by the folic acid produced by bacteria such as *Escherichia coli*, its primary diet. *D. discoideum* also aggregates to form multicellular bodies in conditions of starvation. To do so, their enzyme adenylyl cyclase produces cyclic AMP, which serves as a chemoattractant for cell aggregation (van Haastert and Konijn, 1982).

Models of chemotaxis tried to accommodate several observations made experimentally. First, cells have a **remarkable sensitivity**: they can direct the movement with only a 2% difference in concentration between the front and the back of the cell. Second, the ability of cells to **regulate polarity dynamically or desensitize**. And third, the **independence of the chemotactic response system and the actin cytoskeleton**: directional sensing is not essential for movement, and chemotactic signaling can occur without actin (Parent et al., 1998; Parent and Devreotes, 1999). Due to the decoupling of motility and directional sensing, authors have distinguished three different processes: directional sensing, motility, and polarity. Directional sensing is the molecular machinery that reads the direction of the gradient of a chemoattractant and provides biased cues to guide the migration. Motility can occur in the absence of chemotaxis, and it is based on the extension of protrusions that result in cell locomotion. Polarity is a morphological state of the cell where a leading front and a lagging back are defined by the preferential localization of some molecules and cellular activities (Devreotes et al., 2017; Swaney et al., 2010).

The addition of chemoattractant causes similar effects in *D. discoideum* and leukocytes: cell orientation and pseudopod extension towards the chemoattractant, polarization, chemokinesis (increased rate of locomotion after addition of a chemoattractant), adhesion, secretion, and pinocytosis (Devreotes and Zigmond, 1988). These **physiological responses are reverted when the chemoattractant is removed**. G protein-coupled receptors (GPCRs) are the transducers of the chemoattractant signals, which also share common downstream effects in *D. discoideum* and leukocytes such as nucleotidic signaling (Wang et al., 2011) calcium influx (Collins and Meyer,

2009), receptor remodeling (Servant et al., 1999), phospholipase C activation (Jiang et al., 1997; Kortholt et al., 2007), phospholipase A2 activation, arachidonic acid production (Tibes et al., 1999; van Haastert et al., 2007), and myosin light chain phosphorylation (Adachi et al., 2003).

How do GPCRs transduce extracellular signals to produce a sharp local response? Strikingly, **GPCRs are distributed uniformly on the cell surface**. GPCRs targeted with GFP cover the finest protrusions, and do not redistribute upon the addition of a chemoattractant. This is consistent with the fact that both *D. discoideum* and leukocytes can sense a chemotactic gradient at any point of the cell perimeter. However, the actin and actin-binding proteins that create a pseudopod accumulate preferentially at the leading edge of chemotactic cells. In cells lacking the functional part of the GPCRs, the subunit Gβ, cells still localize actin and all associated proteins to the leading edge. Mutations or depletions of key cytoskeletal proteins such as myosin II in amoeba lead to a defect in motility but not to a defect in directional sensing. Therefore, **the signal localizing the site for protrusions must occur upstream of the cytoskeletal modification**.

Small GTPases of the Rho family are the mediators of this signaling, such as the Rho exchange factors Cdc42 and Rac. Many of them have Pleckstrin homology domains (PH domains) that mediate their interaction with GPCRs and membranes. PH domains are key players in intracellular signaling and membrane recruitment. They can bind to phosphatidylinositol lipids such as phosphatidylinositol-(3,4,5)-*bis*-phosphate (**PIP_2**) or phosphatidylinositol-(3,4,5)-*tris*-phosphate (**PIP_3**), receptors such as GPCR βγ-subunits

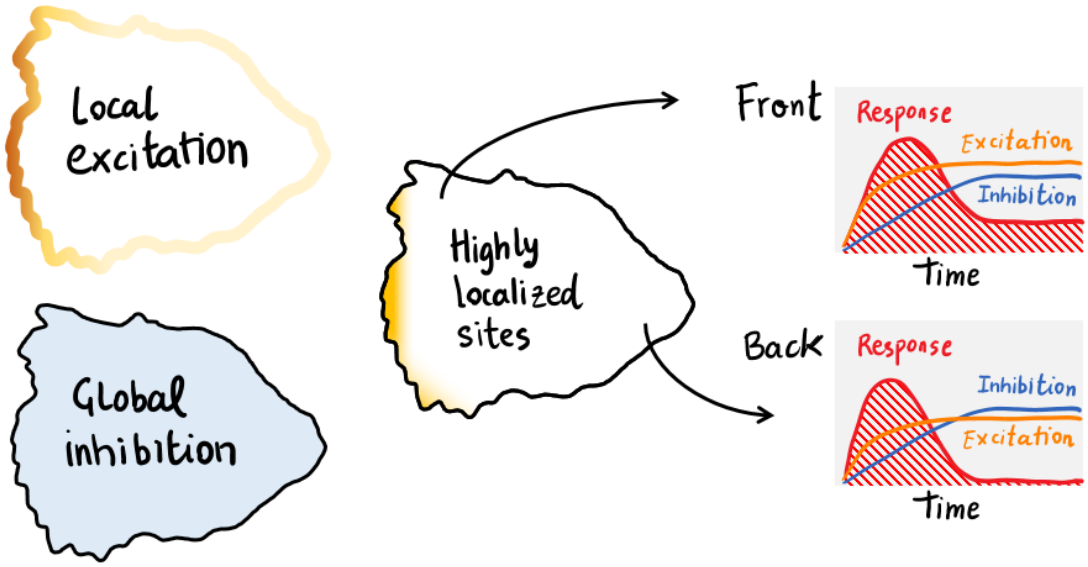

Figure 58: Representation of the LEGI model. *Adapted from (Parent and Devreotes, 1999).*

and enzymes such as and protein kinase C. Individual **PH domains possess specificities related to the function of a certain protein (e.g. binding preferentially to PIP_3 but not to PIP_2).** Researchers have tagged PH domains of relevant proteins involved in chemotaxis to understand its regulation and visualize the subcellular sites of GPCRs activation, such as adenylyl cyclase protein (CRAC) or protein kinase B (PKB). Even if GPCRs are distributed uniformly in chemotactic cells, these PH domains bind only locally on the inner side of the membrane facing the higher concentration, and their localization is sharper than downstream effectors such as actin. The dynamics of different PH domains in chemotactic cells can shed light on the mechanism of cell polarization during chemotaxis:

1. The **intensity of the response does not depend on the absolute concentration of the signal, but on the sharpness of the gradient**.
2. In the absence of gradient or cell lacking GPCRs, the leading edge remains unlabeled.
3. Cytoskeleton and cell motility are not necessary to be able to respond to a gradient.
4. **As long as the gradient persists, the polarity is maintained**: the response decays only when the gradient is perturbed.
5. **Homogeneous addition of chemoattractants gives rise to transient responses in cells.**

This behavior can be explained using a LEGI model, where the excitatory signals are determined by the local occupancy of receptors and the inhibitory signals are determined by the average occupancy in the whole cell. Let's imagine a cell placed in a gradient that suddenly experiences a general increase of chemoattractant that then remains constant. The front and the back will have a different concentration, but since both experience an increase, they will activate GPCRs everywhere. However, the front of the cell will have a higher average occupancy than the back and therefore the signal will be able to persist (Figure 58). In the back the signal will eventually decay to zero since the occupancy of receptors is below the cell average (Parent and Devreotes, 1999).

Cell behavior conceptualized as excitable networks

The system establishing cell polarity after chemotaxis has been conceptualized as an excitable network. First, the **signaling operates with multiple parallel pathways** that can compensate each other, so we need to treat it as a network. **Disruption of some**

individual nodes such as PIP_3 production **has no major consequence** for migration but their activation has relevant phenotypes. For this reason, inhibition of multiple parallel pathways is required to have an inhibitory phenotype (Artemenko et al., 2016; Chen et al., 2007; Veltman et al., 2008). As a consequence, we need to think conceptually as a network, and question the utility of the classical knockout approach to discover the function of regulators in cell biology. While this proved useful, we can also learn interesting properties of biological systems by tuning gradually knobs or regulators of these excitable networks. **Second, signal transduction events display features of biochemical excitability**, typically happening at neuronal impulses: i) at saturating concentrations of chemoattractant, the response is the same independently of the duration of the stimulus; ii) even if the cell can have a dose-response, individual patches on the membrane have an all-or-nothing behavior; iii) refractory periods appear after excitation and inhibit or decrease temporarily the response to a new input; iv) annihilation events that occur when waves cross each other. Traveling waves of chemical activities are believed to be a major organizing tool for morphogenesis and signaling in biological systems (Deneke and Di Talia, 2018).

The network and excitable behavior are not exclusive of the chemotactic response but are also present in cytoskeletal signaling and actin waves. **The cytoskeletal organization could provide the feedback loops necessary for persistent migration**, and can play a role in directing the migration in the absence of chemotactic cues (Devreotes et al., 2017). The actin cytoskeleton is intrinsically excitable in ways that can be independent of upstream signaling (Huang et al., 2013). Many of the regulatory mechanisms of actin polymerization are not linear, and together with the long-range inhibitory effect of membrane tension, a polarization mechanism analogous to the one achieved by chemotactic cues and the signal transduction network can be established.

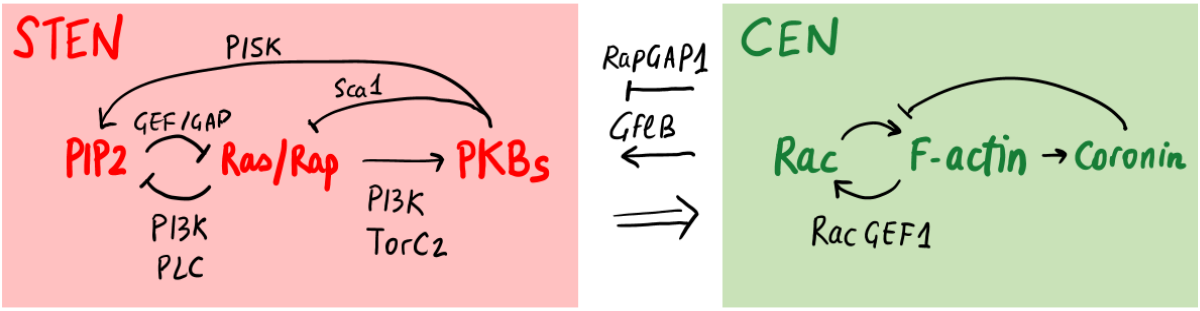

Figure 59: Biochemical pathways giving rise to the excitable feedback loops in the signal transduction excitable network (STEN) and the cytoskeleton excitable network (CEN). *Adapted from (Miao et al., 2019)*

For this reason, researchers have described **at least two interacting excitable networks** n *D. discoideum* cells. The first one encompasses the signal transducers such as Rap and Ras, PIP_3, and PKB and a second one is cytoskeleton dependent, including activated Rac, RacGEF1, F-actin, and coronin (Figure 59). They have been conceptualized as the **signal transduction excitable network (STEN) and the cytoskeleton excitable network (CEN),** respectively (Devreotes et al., 2017; Ma et al., 2004; Miao et al., 2019, 2017). STEN is the best studied in terms of molecular details and overall behavior. An expansion of this model was termed **LEGI-BEN (local excitation–global inhibition–biased excitable network**), accounting for the interactions of the LEGI mechanism of CEN and STEN with other regulatory networks proposed in the cell (Xiong et al., 2010) (Figure 12).

Chapter 16: Reconstitution of cell migration at a glance.

My role in this work was to design the scope and structure of the review, the visual identity of the accompanying poster, write parts of the manuscript, and review and assemble the contributions from other authors. Renaud Chabrier, the co-first author, made the illustrations of the accompanying poster and co-designed the poster.

Article type: Review. **Journal**: J Cell Sci. 2019 Feb 11;132(4):jcs225565. doi: 10.1242/jcs.225565.

Authors: **Juan Manuel Garcia-Arcos***, Renaud Chabrier*, Mathieu Deygas, Guilherme Nader, Lucie Barbier, Pablo José Sáez, Aastha Mathur, Pablo Vargas, Matthieu Piel. *Co-first authors.

Abstract: Single cells migrate in a myriad of physiological contexts, such as tissue patrolling by immune cells, and during neurogenesis and tissue remodeling, as well as in metastasis, the spread of cancer cells. To understand the basic principles of single-cell migration, a reductionist approach can be taken. This aims to control and deconstruct the complexity of different cellular microenvironments into simpler elementary constrains that can be recombined together. This approach is the cell microenvironment equivalent of in vitro reconstituted systems that combine elementary molecular players to understand cellular functions. In this Cell Science at a Glance article and accompanying poster, we present selected experimental setups that mimic different events that cells undergo during migration in vivo These include polydimethylsiloxane (PDMS) devices to deform whole cells or organelles, micro patterning, nano-fabricated structures like grooves, and compartmentalized collagen chambers with chemical gradients. We also outline the main contribution of each technique to the understanding of different aspects of single-cell migration.

Keywords: Cell migration; In vitro assay; Microfabrication; Microfluidics; Micropatterning.

Chapter 17: Heterochromatin-driven nuclear softening protects the genome against mechanical stress-induced damage.

My role in this work was to perform preliminary experiments, provide the confinement devices, and train the autors in the use of the confinement.

Article type: Research paper. **Journal**: Cell. 2020 May 14;181(4):800-817.e22. doi: 10.1016/j.cell.2020.03.052. Epub 2020 Apr 16.

Authors: Michele M Nava, Yekaterina A Miroshnikova, Leah C Biggs, Daniel B Whitefield, Franziska Metge, Jorge Boucas, Helena Vihinen, Eija Jokitalo, Xinping Li, **Juan Manuel García Arcos**, Bernd Hoffmann, Rudolf Merkel, Carien M Niessen, Kris Noel Dahl, Sara A Wickström

Abstract: Tissue homeostasis requires maintenance of functional integrity under stress. A central source of stress is mechanical force that acts on cells, their nuclei, and chromatin, but how the genome is protected against mechanical stress is unclear. We show that mechanical stretch deforms the nucleus, which cells initially counteract via a calcium-dependent nuclear softening driven by loss of H3K9me3-marked heterochromatin. The resulting changes in chromatin rheology and architecture are required to insulate genetic material from mechanical force. Failure to mount this nuclear mechanoresponse results in DNA damage. Persistent, high-amplitude stretch induces supracellular alignment of tissue to redistribute mechanical energy before it reaches the nucleus. This tissue-scale mechanoadaptation functions through a separate pathway mediated by cell-cell contacts and allows cells/tissues to switch off nuclear mechanotransduction to restore initial chromatin state. Our work identifies an unconventional role of chromatin in altering its own mechanical state to maintain genome integrity in response to deformation.

Keywords: DNA damage; chromatin; heterochromatin; mechanoprotection; mechanotransduction; nuclear architecture; nuclear lamina; nuclear mechanics; stem cells.

Chapter 18: The nucleus acts as a ruler tailoring cell responses to spatial constraints.

My role in this work was to analyze the cortical accumulation of myosin on the AFM experiments, make experiments with cytoplasts, transcription/translation inhibition, and protein extractions from confined cells

Article type: Research paper. **Journal**: Science. 2020 Oct 16;370(6514):eaba2894. doi: 10.1126/science.aba2894. PMID: 33060332.

Authors: Lomakin AJ, Cattin CJ, Cuvelier D, Alraies Z, Molina M, Nader GPF, Srivastava N, Sáez PJ, **Garcia-Arcos JM**, Zhitnyak IY, Bhargava A, Driscoll MK, Welf ES, Fiolka R, Petrie RJ, De Silva NS, González-Granado JM, Manel N, Lennon-Duménil AM, Müller DJ, Piel M.

Abstract: The microscopic environment inside a metazoan organism is highly crowded. Whether individual cells can tailor their behavior to the limited space remains unclear. In this study, we found that cells measure the degree of spatial confinement by using their largest and stiffest organelle, the nucleus. Cell confinement below a resting nucleus size deforms the nucleus, which expands and stretches its envelope. This activates signaling to the actomyosin cortex via nuclear envelope stretch-sensitive proteins, up-regulating cell contractility. We established that the tailored contractile response constitutes a nuclear ruler-based signaling pathway involved in migratory cell behaviors. Cells rely on the nuclear ruler to modulate the motive force that enables their passage through restrictive pores in complex three-dimensional environments, a process relevant to cancer cell invasion, immune responses, and embryonic development.

Chapter 19: Data and code repositories.

Supplementary Videos are archived on Figshare.com:

GARCIA ARCOS, Juan Manuel; Piel, Matthieu (2021): Supplementary Videos. figshare. Media. https://doi.org/10.6084/m9.figshare.14053964.v1

Data and original files are available upon request to: (juanmagarciaarcos@gmail.com; matthieu.piel@curie.fr) and archived on Figshare.com under the following project:

Title: **Stabilization and motility mechanism of blebs in cancer cells**

https://figshare.com/projects/Stabilization_and_motility_mechanism_of_blebs_in_cancer_cells/98747

Chapter 20: Teaching and outreach activities.

I like to place my research in society and communicate, not only with fellow scientists, but also to the general public and researchers from very different disciplines (e.g., art, architecture).

Along my PhD research I participated in many teaching and science communication activities, which enriched me and also provided motivation at times when the experiments were not working! All the information is available on my personal website **openscienceschool.org**. I will mention below some of them:

- **Development of DI-lambda, the open hardware spectrophotomter.** DIλ is an Open Hardware modular spectrophotometer, designed to be accurate, easy to modify, and extremely cheap. We achieve this by using LEDs instead of an optical refraction system.
- **Water quality workshops**. Water Watchers is an educational kit for high schools. In water watchers, students measure water quality of their area, learn about colorimetry and water quality analysis and critically analyze and debate over water quality data.
- **Co-lab workshops**. Co-lab is a movement, a format of workshop, and a philosophy to achieve interdisciplinary collaboration. We work with universities, NGOs or science labs in all the world to spread this methodology. We did a workshop in the scope of the microfluidics conference organized by IPGG.
- **Les bactéries de compagnie**. "The bacterial pets" workshop was designed in partnership with the National Museum of Modern Art in Paris (Centre Pompidou) to teach kids 6-12 years old about synthetic biology and DNA design.
- **The impact of humans on Earth**. Short course doculenting the impact of humans of Earth based on scientific evidence and serves as an introduction to ecology and to green politics. This was done for the bachelor program at CRI Paris.

KOI SCIENCE
spectrophotometer

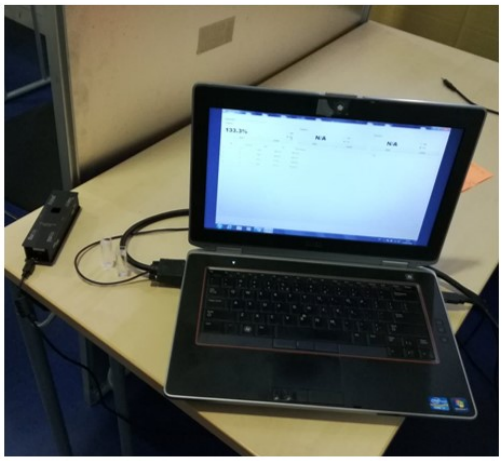

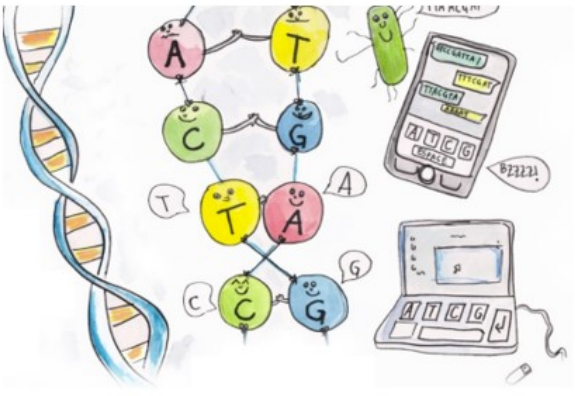

コ•ラボ co-lab

interdisciplinary workshops

ateliers interdisciplinaires

Brainstorming workshop

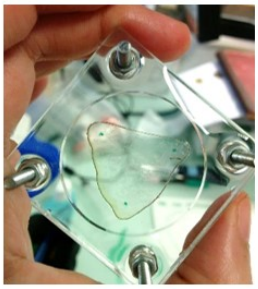

INSTITUT PIERRE-GILLES DE GENNES
Pour la microfluidique

CRI

Chapter 21: Résumé substantiel en français

Historiquement décrits comme une caractéristique de l'apoptose, les *blebs* se sont avérés être également essentiels à la migration amiboïde dont usent les cellules cancéreuses.

Les *blebs* (ou bourgeonnements) sont des structures dynamiques qui se forment suite au détachement de la membrane plasmique vis-à-vis du cortex d'actomyosine. Lorsqu'ils se rétractent, ils génèrent des forces de friction suffisantes pour mettre en mouvement les cellules. Au cours de la dernière décennie, quelques études indépendantes ont montré que soumettre des cellules à des contraintes de confinement en absence d'adhésion, permettait l'apparition de blebs des dimensions importantes et stables dans le temps. Ceci met en évidence que ces cellules sont capables de prévenir la rétractation du bleb et de le maintenir dans le temps. Ceci amène à un mode de motilité (*bleb-based)* qui diffère de la migration mésanchymateuse faisant intervenir les **filipodes** et **les lamellipodes.** Il est retrouvé aussi bien chez les amibes, les choanoflagellés que chez les cellules immortalisées ou issues de culture primaire. Au sein d'une cellule, une compétition peut avoir lieu entre plusieurs blebs nouvellement formés et amène à la sélection d'un bleb qui sera à l'origine de la migration. Ainsi, il est essentiel de déterminer comment les blebs uniques se stabilisent afin de comprendre comment les cellules amiboides se polarisent. Plus généralement, des flux d'actomyosine stables constituent la base d'une migration rapide dans de nombreux types de cellules, y compris les cellules immunitaires.

La première partie de mon travail décrit la morphogenèse des blebs suite au confinement de cellules. En fonction de la forme, de l'organisation de l'actomyosine et de la durée de vie des blebs individuels, nous avons classé les blebs en deux groupes : les blebs **ronds** et les blebs **allongés**. Tandis que les premiers se forment immédiatement après le confinement, les seconds n'apparaissent qu'après un certain délai (~15s). La dynamique des blebs ronds ainsi que leur faible durée de vie reflètent celles de l'actomyosine, précédemment décrites pour les blebs rétractiles (Bovellan et al., 2014 ; Charras et al., 2008 ; Cunningham, 1995 ; Tinevez et al., 2009). Les blebs allongés se vident progressivement de l'actomyosine à leur avant jusqu'à la formation d'un gradient stable, comparable à celui observé lors de la formation à la surface des cellules polarisées et confinées des larges blebs (Callan-Jones et Voituriez, 2013). Ces derniers, décrits récemment par notre laboratoire et d'autres, forment des gradients d'actomyosine en raison d'un flux rétrograde soutenu qui concentre l'actomyosine et les protéines liées au

cortex à l'arrière de la cellule (Bergert et al., 2015 ; Liu et al., 2015 ; Logue et al., 2015 ; Ruprecht et al., 2015).

Nous proposons un modèle de travail pour la morphogenèse des blebs dans lequel le phénotype final (bleb rétractile ou stable) est déterminé par le temps relatif de la formation du cortex par rapport à la contraction de la myosine, quelle que soit la forme initiale du bleb. En effet, un bleb ayant accumulé de l'actine à l'avant suite à la formation *de novo* du cortex, se rétracte suite à la contraction de la myosine tandis qu'un bleb dépourvu de cette actine se maintient dans le temps. Autrement dit, si la contraction se produit avant que le cortex ne soit complètement formé, le bleb atteint un état d'équilibre caractérisé par un gradient d'actomyosine. De manière systématique, nous avons constaté que l'activation optogénétique de la myosine dans les blebs stables profite à leur stabilité, alors qu'elle accélère la rétraction des blebs rétractiles.

Dans la littérature, plusieurs régimes ou modes de *blebbing* ont été décrits : *persistent blebbing* (Liu et al., 2015 ; Ruprecht et al., 2015), *circus blebbing* provoqué par un détachement de la membrane qui se déplace autour de la cellule (Charras et al, 2008 ; Fujinami et Kageyama, 1975 ; Graziano et al., 2019), ainsi que *unstable blebbing*, fréquents notamment chez D. discoideum (Fackler et Grosse, 2008 ; Srivastava et al., 2020 ; Zatulovskiy et al., 2014). Cependant, aucune étude n'a caractérisé les différences fondamentales et les transitions possibles entre ces différents régimes. Nous avons identifié quels facteurs influencent la stabilité des blebs et la prévalence relative des différents régimes de *blebbing,* et ce grâce à différentes techniques afin d'exercer des perturbations des blebs : optogénétique pour contrôler l'activité de RhoA, Cdc42 ou Rac1, ainsi que pharmacologique ou physique. Notre apport conceptuel consiste que les blebs peuvent passer d'un état stable dynamique à un autre (persistant, sinueux, instable) en fonction de l'interaction entre la membrane au front du bleb et sa base se contractant,à travers le réseau d'actine.

Les blebs persistants conservent une forme constante et lisse, et les *winding* blebs se forment lors de cycles séquentiels de formation de bleb et de cortex. Ces trois états d'équilibre stables et l'état de rétraction peuvent se produire tant au sein des blebs, qu'en celui de fragments (cellulaires) mobiles et isolés issus du détachement d'un bleb de sa cellule.

La fréquence des blebs et fragments cellulaires persistants peut être augmentée soit en altérant les interactions entre les filaments d'actine avec la membrane plasmique, soit en

réduisant la quantité d'actine présente au front du bleb. De plus, les analyses de corrélation temporelle entre la densité d'actine au front et sa vélocité suggèrent que la densité actine corticale empêche la protusion de la membrane *via* un effet de seuil. Ceci peut être expliqué par l'existence d'interactions physiques entre l'actine et la membrane au niveau du front de bleb, qui vont ainsi contrôler les passages entre différents états d'équilibre. Par conséquent, un découplage mécanique complet entre les filaments d'actine et la membrane au niveau du front doit se produire pour permettre la formation de blebs persistants.

Au moyen d'expériences de confinement réalisées avec un microscope de fluorescence par réflexion totale interne (*TIRF)* à haute aperture numérique, nous avons pu caractériser en détail la dynamique du cortex d'actine au sein d'un bleb, depuis sa nucléation et l'assemblage du réseau en son front jusqu'à la contraction et au désassemblage du réseau à sa base. Nous avons ainsi pu identifier trois régimes de cortex dans les blebs : I) un cortex contractile à la base du bleb, enrichi en NMIIA, avec des flux convergents où se produit le désassemblage du réseau d'actine ; II) un cortex réticulé au centre du bleb, exempt de contractions, qui transmet les forces depuis sa base à son front; et III) un cortex fluide au front du bleb, composé de filaments simples faiblement attachés à la membrane ou d'un réseau lâche d'actine. Nos résultats présentent un rôle négatif de l'attachement actine-membrane sur la persistance de la protrusion et sont soutenus par d'autres travaux récents (Bisaria et al., 2020 ; Welf et al., 2019). Ils introduisent également un rôle supplémentaire pour la contractilité du NMIIA, qui est essentiel pour maintenir la pression intracellulaire et retirer l'actine du front cellulaire. Nos résultats expliquent également la fonction des réticulants dans l'assemblage des réseaux, précédemment identifiée comme essentielle pour une migration stable des bleb (Logue et al., 2015). Les réticulants créent le réseau réticulé intermédiaire non contractile, qui est responsable de la forme longue des blebs.

Ces observations rappellent la dynamique de percolation des réseaux d'actine contractile reconstitués in vitro, mais n'ont pas encore été directement observées dans un système vivant (Abu Shah et Keren, 2014 ; Alvarado et al., 2013 ; Bendix et al., 2008 ; Ierushalmi et al., 2020 ; Malik-Garbi et al., 2019 ; Tan et al., 2018). Même dans les systèmes in vitro, les expériences n'ont pas encore pu établir de lien entre les régimes de percolation et la densité des filaments au niveau moléculaire. La théorie prévoit que selon la connectivité ou l'activité motrice, les gels contractiles actifs peuvent acquérir différents régimes : solutions actives, gels précontraints, contraction locale ou contraction globale. Selon les densités d'actine et de myosine, le cortex des blebs peut récapituler ces régimes : le

cortex contractile à la base correspond à un régime de contraction globale, le cortex réticulé correspond à un régime de gel précontraint, et le cortex fluide lâche au front des blebs correspond au régime de solutions actives. Le seuil de densité de conductivité détermine la forme en état d'équilibre des blebs persistants et peut expliquer les états intermédiaires entre persistant et rétractile qui n'étaient pas pris en compte par les précédents modèles de migration basés sur les blebs. La description d'un processus cellulaire expliqué par la théorie de la percolation au niveau moléculaire constitue une nouvelle contribution à la biophysique cellulaire et au champ du cytosquelette.

Du point de vue de la biologie cellulaire, nos travaux contribuent à la compréhension d'une nouvelle structure exploitée lors de la migration cellulaire. Bien que notre travail ne détaille pas les voies moléculaires sous-jacentes, il clarifie l'importance des réticulants pour la forme et la persistance des blebs, décrits dans la littérature comme essentiels pour une migration stable des bleb mais dont le mécanisme d'action n’avait jusqu’alors pas été compris.

Plus généralement, nos travaux proposent un nouveau système modèle pour étudier la motilité des cellules. Le kératocyte a été utilisé comme une cellule motile simplifiée pour étudier la dynamique du lamellipodium. Grâce à des années de travail cumulé, nous avons obtenu l'un des modèles les plus détaillés pour la détermination de la forme des cellules et développé de nouvelles théories qui ont permis de clarifier la relation entre la tension membranaire et la polymérisation de l'actine sur le front des cellules (Keren et al., 2008 ; Mogilner et al., 2020). De même, le bleb a été un sujet d'étude intensif pour les biophysiciens. Sa simplicité et son accessibilité ont fourni des données essentielles sur la tension membranaire, l'assemblage du cortex et la composition du cortex (Charras et al., 2008, 2006 ; Fritzsche et al., 2013 ; Salbreux et al., 2012). L'étude de la motilité des bleb combine ces deux modèles favoris et bien établis pour la biophysique cellulaire.